Electrical and thermal diagnostics for a better understanding of the energy balance of species in technological plasmas

Dissertation

zur Erlangung des Doktorgrades
der Mathematisch-Naturwissenschaftlichen Fakultät
der Christian-Albrechts-Universität zu Kiel

Vorgelegt von:

Felix M. W. Schlichting

Kiel, 2023

Supervisor and 1st examiner:
Prof Dr. Holger Kersten

2nd examiner:
Prof Dr. Hermann Kohlstedt

Oral examination date: 12.10.2023
Print approval date: 12.10.2023

Abstract

This doctoral thesis explores the investigation of the energy balance of species in technological plasmas through the application of electrical and thermal diagnostics. The fundamental principles of plasma physics theory, including plasma states, different discharge applications and energy balance at a surface exposed to plasma, are outlined to establish a theoretical foundation for the conducted experiments.

The research focuses on advancing the understanding of the energy balance of species in plasmas by employing electrical, thermal, and optical diagnostics. Three previously published works are presented, highlighting the use of thermal and electrical diagnostics to analyze magnetron-sputtered thin films with highly specific applications. These publications demonstrate the significance of accurate diagnostic techniques in evaluating the behaviour of plasma-generated species and their effect on thin film properties such as morphology and structure.

Additionally, a novel combined diagnostic approach is introduced, combining a thermal probe with a retarding field energy analyzer (RFEA). In this technique, the thermal probe serves as the collector for the RFEA, allowing simultaneous thermal and electrical measurements. The thesis describes the development of a prototype that provides proof of principle for the combined diagnostic and outlines the challenges and limitations encountered during the initial implementation.

Furthermore, a new design for the combined diagnostic is presented in a fourth publication, showcasing improvements over the prototype. The new design addresses the limitations identified in the earlier stage and provides enhanced capabilities for studying plasma energy balance. The thesis thoroughly discusses the experimental setup, methodology, and data analysis procedures associated with the new combined diagnostic, illustrating its potential for advancing our understanding of species behaviour in technological plasmas.

Overall, this doctoral thesis extensively explores electrical and thermal diagnostics for a better understanding of the energy balance of species in the ever-expanding field of technological plasmas. The research contributes to the area of plasma physics by expanding our knowledge of plasma parameters, discharge applications, and energy interactions at plasma-surface interfaces. Moreover, developing the combined diagnostic technique offers new avenues for characterising plasma-generated species and holds promising implications for various plasma-based applications.

Kurzfassung

Diese Doktorarbeit untersucht den Energiehaushalt von Spezies in technologischen Plasmen durch den Einsatz von elektrischer und thermischer Diagnostik. Es wird eine theoretische Grundlage für die durchgeführten Experimente geschaffen, indem die grundlegenden Prinzipien der Plasmaphysik erläutert werden, einschließlich der Plasmazustände, unterschiedlicher Entladungsanwendungen und des Energiehaushalts an einer plasmaexponierten Oberfläche.

Die Forschung konzentriert sich auf die Weiterentwicklung des Verständnisses des Energiehaushalts von Spezies in Plasmen durch den Einsatz von elektrischer, thermischer und optischer Diagnostik. Es werden drei zuvor veröffentlichte Arbeiten präsentiert, die den Einsatz von thermischer und elektrischer Diagnostik zur Analyse von magnetronbeschichteten Dünnschichten mit hochspezifischen Anwendungen verdeutlichen. Diese Veröffentlichungen zeigen die Bedeutung genauer Temperaturmessungen und elektrischer Charakterisierungstechniken zur Untersuchung des Verhaltens von plasmaerzeugten Spezies auf.

Darüber hinaus wird ein neuartiger kombinierter diagnostischer Ansatz vorgestellt, bei dem eine thermische Sonde mit einem retarding field energy analyzer (RFEA) kombiniert wird. In dieser Technik dient die thermische Sonde als Kollektor für den RFEA und ermöglicht gleichzeitige thermische und elektrische Messungen. Die Arbeit beschreibt die Entwicklung eines Prototyps, der den Machbarkeitsnachweis für die kombinierte Diagnostik liefert, und erläutert die Herausforderungen und Einschränkungen, die während der anfänglichen Umsetzung aufgetreten sind.

Des Weiteren wird ein neues Design für die kombinierte Diagnostik in einer vierten Veröffentlichung präsentiert, das Verbesserungen gegenüber dem Prototypen aufzeigt. Das neue Design adressiert die in der frühen Entwicklungsphase identifizierten Einschränkungen und bietet erweiterte Möglichkeiten zur Untersuchung des Energiehaushalts von Spezies in technologischen Plasmen. Die Arbeit diskutiert ausführlich den experimentellen Aufbau, die Methodik und die Datenanalyseverfahren im Zusammenhang mit der neuen kombinierten Diagnostik und veranschaulicht ihr Potenzial zur Weiterentwicklung unseres Verständnisses des Speziesverhaltens in technologischen Plasmen.

Insgesamt präsentiert diese Doktorarbeit eine umfamgreiche Untersuchung der elektrischen und thermischen Diagnostik zur besseren Erfassung der Energiebilanz einzelner Spezies im ständig wachsenden Bereich der technologischen Plasmen. Die Forschung trägt zur Plasmaphysik bei, indem sie unser Wissen über Plasmaparameter, Entladungsanwendungen und Energiewechselwirkungen an Plasma-Oberflächen-Schnittstellen erweitert. Darüber hinaus bietet die Entwicklung der kombinierten Diagnostik neue Möglichkeiten zur Charakterisierung von plasmaerzeugten Spezies und birgt vielversprechende Implikation für zahlreiche Plasma-basierten Anwendungen.

List of publications

This thesis is partially based upon the following peer-reviewed papers that are either already published or submitted for publication.

1. F. Zahari, **F. Schlichting**, J. Strobel, S. Dirkmann, J. Cipo, S. Gauter, J. Trieschmann, R. Marquardt, G. Haberfehlner, G. Kothleitner, L. Kienle, T. Mussenbrock, M. Ziegler, H. Kersten, H. Kohlstedt; Correlation between sputter deposition parameters and I-V characteristics in double-barrier memristive devices. Journal of Vacuum Science & Technology B 1 November 2019; 37 (6): 061203.
2. R. Marquardt, J. Cipo, **F. Schlichting**, G. Kolhatkar, H. Kohlstedt, H. Kersten; Correlation between properties of direct current magnetron sputtered thin niobium nitride films and plasma parameters, Thin Solid Films, Volume 742, 2022, 139046.
3. **F. Schlichting**, L. Thormählen, J. Cipo, D. Meyners, H. Kersten; Energy-dependent film growth of Cu and NiTi from a tilted DC magnetron sputtering source determined by calorimetric probe analysis, Surface and Coatings Technology, Volume 450, 2022, 129000.
4. **F. Schlichting**, H. Kersten; A retarding field thermal probe for combined plasma diagnostics, European Physical Journal Techniques & Instrumentation (submitted), 2023

Contents

1 Introduction

In the past decades, the development of technological plasmas has undergone remarkable advancements, revolutionizing various industries and enabling cutting-edge applications. Technological plasmas, such as those employed in thin film deposition, etching and material processing, have become indispensable tools in modern industry, providing unique capabilities for fabricating and manipulating materials at the atomic and molecular scales. A comprehensive understanding of the underlying energy balance is crucial to optimise and control these highly complex plasma processes. This thesis focuses on the importance of electrical and thermal diagnostics in elucidating the energy transfer mechanisms within technological plasmas and enhancing process efficiency.

Over the last 30 to 50 years, technological plasmas have been implemented in industries such as microelectronics, aerospace, medicine, and energy production. They have facilitated the miniaturization of electronic devices, improved energy conversion efficiencies and enabled advancements in materials science. By leveraging the properties of plasmas, diverse applications such as physical vapour deposition (PVD), plasma-enhanced chemical vapour deposition (PECVD), plasma etching and plasma-assisted material synthesis have been developed. These processes rely on intricate interactions between charged particles, neutral species and electromagnetic and magnetic fields, making it imperative to characterize the plasma parameters and energy transfer pathways precisely.

To achieve optimal control and performance, advanced diagnostics are essential for tailoring complex plasma processes. Electric diagnostics, including Langmuir probes, retarding field energy analyzers, microwave interferometry and electric field probes, provide critical information about plasma parameters such as electron density, electron temperature, ion energy distribution and electric fields. These measurements offer insights into charged species' spatial and temporal distribution and their interaction with external fields. Similarly, thermal diagnostics, including calorimetric probes, optical emission spectroscopy and infrared thermography, allow for determining plasma parameters, energy flux densities and energy distribution. Combined with electric diagnostics, these techniques enable a holistic understanding of energy transfer and losses in technological plasmas.

The introduction of increasingly sophisticated diagnostics into plasma processes poses several challenges. Technological plasmas are often complex, involving non-equilibrium conditions, high temperatures and rapid timescales. This complexity necessitates the development of diagnostic techniques capable of capturing the transient and spatially varying nature of the plasma parameters. Additionally, integrating non-intrusive diagnostics into industrial plasma systems while maintaining their reliability and accuracy is a significant engineering challenge. Overcoming these hurdles requires the collaboration of researchers, engineers and industry experts to devise innovative diagnostic tools and strategies.

This thesis gives a comprehensive overview of the capabilities and shortcomings of various diagnostics in a wide range of plasma discharges, including radio frequency plasma, ion beam sources and magnetron sputtering devices. It also introduces a new combination of a retarding field energy analyzer and a passive thermal probe enabling the simultaneous measurement of ion energy distributions and energy flux densities. The combination yields information neither probe diagnostic can deliver on its own.

Capacitively coupled radio frequency (rf) plasmas find extensive use in both industrial applications and scientific research due to their versatile capabilities for material processing, surface modification and plasma diagnostics. These plasmas are used in plasma etching processes, such as reactive ion etching (RIE) and plasma-enhanced chemical vapour deposition (PECVD) for surface modification. Furthermore, they are used for surface cleaning and activation, removing organic contaminants, oxides and particles from surfaces, enabling improved adhesion, wettability and surface energy properties [1]. Introducing precursor gases into the plasma allows thin polymer films with tailored properties to be deposited onto substrates. This enables the creation of functional coatings, adhesion promotion layers and biomaterial surfaces with desired properties, such as hydrophobicity, hydrophilicity or bioactivity [2].

Ion beam sources have widespread applications in modern industry and scientific research, offering unique material processing, surface modification, and analysis capabilities. These sources provide a controlled and focused beam of ions tailored to specific requirements, enabling precise manipulation of materials at the atomic and molecular scales. The versatility and precision offered by ion beams make them valuable tools across various fields, enabling advancements in materials science, electronics, energy, and fundamental research [3].

Magnetron sputtering is a widely used physical vapour deposition (PVD) technique in which a high-density plasma is created using a magnetic field to enhance sputtering efficiency. It is a necessary industrial process for many applications ranging from the deposition of hard coatings to the deposition of functional layers for electronic applications. The process allows for thin film deposition onto various substrates with excellent control over film properties. It involves bombarding a target material with energetic ions to dislodge atoms or molecules from the target surface. The target material is typically a solid metal or compound material. A magnetron is placed behind the target, creating a magnetic field that traps electrons near the target surface. The magnetic field enhances the plasma density and helps confine the plasma near the target, resulting in a higher sputtering yield [4].

In conclusion, this thesis highlights the significance of electric and thermal diagnostics in unravelling the energy balance within technological plasmas. These non-conventional diagnostics optimise and control complex plasma processes by providing a comprehensive understanding of the plasma parameters and energy transfer mechanisms, leading to enhanced efficiency and improved outcomes. The challenges associated with introducing diagnostics into plasma systems underscore the need for continuous research and innovation to advance diagnostic capabilities and realize the full potential of technological plasmas in various industrial applications.

2 Definitions and Fundamentals of Low Temperature Plasma

This chapter explores the theoretical background and definitions concerning the plasma state of matter which are relevant for this work. The term 'plasma' refers to the ionized gaseous state of a substance where ions and electrons coexist in a limited space. It is sometimes called the 'fourth state of matter' after solid, liquid and gaseous [5]. The term 'plasma' itself originates in the 1920s when Irving Langmuir investigated ionized gases at low pressures and high temperatures [6]. Similar to the transition energies needed for a substance to change from a solid state to a liquid state (enthalpy of fusion) and from liquid to gaseous (enthalpy of vaporization), the ionization energy is needed to create a plasma from a gas.

In laboratory plasmas, there is a general distinction between low-temperature plasma (LTP) and high-temperature plasma (HTP). This is detailed in table 2.1. In HTPs electrons and ions roughly have the same temperature which may exceed 10^7 K [7]. This is the case in fusion devices like tokamaks or stellarators. LTPs, in turn, are divided into two categories, thermal and non-thermal LTP. An example of thermal plasmas is arc discharges, where ions and electrons roughly have the same temperature, which, however, is much smaller than in HTPs. In non-thermal LTPs, the electron temperature far exceeds the ion temperature, resulting in an imbalance between their thermal velocity and ability to react to electric and magnetic fields.

Low Temperature Plasma		High Temperature Plasma
thermal	non-thermal	
$T_e \approx T_i \lesssim 2 \cdot 10^4$ K	$T_i \approx 300$ K $T_i \ll T_e \lesssim 10^5$ K	$T_i \approx T_e \gtrsim 10^7$ K

Table 2.1: Subdivision of laboratory plasmas and their respective electron and ion temperatures. Taken from [7].

This work focuses on non-thermal LTPs and the different ways of generating which are discussed in chapter 3.

In the following, the basic properties and phenomena of the non-thermal low temperature plasma are discussed in a short overview.

2.1 Quasineutrality and Debye-shielding

The concept of quasineutrality in a plasma arises from the fact that plasmas are made up of both positively charged ions and negatively charged electrons which display collective behaviour. At a microscopic scale, the plasma can be highly non-neutral, with localized regions of positive and negative charge imbalances. However, at a macroscopic scale, these charge imbalances tend to average out, resulting in a net charge of zero. This macroscopic balance of charge is what is meant by quasineutrality. Mathematically this can be described as [8]:

$$e_0 n_e + \sum_j q_j n_j \approx \sum_k q_k n_k \tag{2.1}$$

Here e_0 is the elementary charge and n_e is the number density of electrons. The indexes j and k represent negative and positive ions, respectively, with the corresponding number densities n_j and n_k and valencies q_j and q_k. Negative ions only occur in electronegative gas discharges, which this work will not address. Therefore, when only looking at single-charged ions, eq. 2.1 can be reduced to $n_e \approx n_i$.

At a microscopic scale, neutrality cannot be retained due to the finite expansion of the particles and their respective attraction or repulsion, leading to non-neutral space charge zones. The Debye length λ_D is a measure of the distance over which charges in the plasma are screened by other charges [9]:

$$\frac{1}{\lambda_D} = \sqrt{\frac{e_0^2 n_e}{\epsilon_0 k_B T_e} + \frac{e_0^2 n_i}{\epsilon_0 k_b T_i}} \tag{2.2}$$

with ϵ_0 the permittivity in vacuum, k_B the Boltzmann constant and $T_{e,i}$ the electron and ion temperature, respectively. When introducing an external positive charge Q into a plasma, electrons will be attracted while ions will be repelled. The external charge is thereby shielded from the plasma. Other than the Coulomb potential in a vacuum, the resulting potential Φ around Q in the distance r drops following the Debye-Hückel relation [10]:

$$\Phi(r) = \frac{Q}{4\pi\epsilon_0 r} \exp\left(-\frac{r}{\lambda_D}\right) \tag{2.3}$$

In low temperature plasmas, where $T_i \ll T_e$ the electron velocity is much higher than the ion velocity and, therefore, electrons are mainly responsible for the shielding mechanism. Eq. 2.2 can be separated by ions and electrons with the electron Debye length λ_{De}

$$\lambda_{De} = \left(\frac{\epsilon_0 k_B T_e}{e_0^2 n_e} \right)^{1/2} \tag{2.4}$$

defining the length scale at which eq. 2.3 has dropped by at least 1/e times the (not shielded) Coulomb potential and the condition for quasineutrality is met. The number density of electrons inside the so-called Debye-sphere determines the plasma parameter N_d:

$$N_{de} = \frac{4}{3} \pi n_e \lambda_{De} \tag{2.5}$$

The time scale of the shielding process is defined by the response time $\tau_{e,i} = \lambda_{De,Di}/u_{e,i}$ of the electrons and ions. In case of a small disturbing charge Q with an equally small potential, the electron and ion velocities $u_{e,i} \approx (k_B T_{e,i}/m_{e,i})^{1/2}$ corresponds approximately to their thermal velocity ($m_{e,i}$ is the electron and ion mass). In common, the inverse of the response time is used to estimate the time scale of the shielding possibility of a plasma. This is called the plasma frequency ω_p:

$$\omega_{pe,pi} = \frac{u_{e,i}}{\lambda_{De,Di}} = \sqrt{\frac{e_0^2 n_{e,i}}{\epsilon_0 m_{e,i}}}. \tag{2.6}$$

As with the Debye length, the electrons play the dominant role because of their smaller mass compared with ions. This means that only electrons react fast enough to external electrical disturbances with frequencies $\gg \omega_{pi}$ and shielding is maintained by electrons.

In summary, for plasma to show collective behaviour and achieve quasineutrality the following criteria must be fulfilled:

- The dimension L must be: $L \gg \lambda_D$
- The plasma parameter must be: $N_{de} \gg 1$
- The plasma must exist much longer than the response time τ

2.2 Energy and velocity distribution

In a plasma, the free charge carriers possess a wide range of energies and velocities. The distribution of these energies and velocities can be described using statistical mechanics and the principles of thermodynamics. Here, the concept of entropy plays a crucial role in understanding the distributions. Entropy S represents the measure of disorder in a system. In a state of thermodynamic equilibrium, entropy reaches a maximum. In a system with N particles with total energy E, in which every particle N_i can occupy an energy E_i, entropy is written as [9]:

$$S = -k_B \sum_i n_i \ln n_i \tag{2.7}$$

$n_i = N_i/N$ is not a particle density, but the relative frequency of particles that occupy the energy E_i. By maximizing the entropy of the system subject to constraints such as fixed particle number, energy, and volume, one can use the method of Lagrange multipliers to derive the distribution that corresponds to the most probable energy state. The resulting distribution is the Maxwell-Boltzmann distribution, which describes the statistical behavior of particles in equilibrium [2]:

$$f_M(v) = 4\pi v^2 \left(\frac{m}{2\pi k_B T}\right)^{3/2} \exp\left(-\frac{mv^2}{2k_B T}\right) \tag{2.8}$$

Here, m is the mass of the described particles, ions or electrons, and their respective temperature T and velocity $v = |\mathbf{v}|$. From the first and second momentum of the distribution the thermal velocity v_{th} and the averaged thermal energy $\langle E_{th}\rangle$ can be derived:

$$v_{th} = \int_0^\infty f_M(v) v \mathrm{d}v = \left(\frac{8k_B T}{\pi m}\right)^{1/2} \tag{2.9}$$

$$\langle E_{th}\rangle = \frac{m}{2n} \int_0^\infty f_M(v) v^2 \mathrm{d}v = \frac{3}{2} k_B T \tag{2.10}$$

Using energy conversation and following $E_{th} = E_{kin} = \frac{1}{2}mv^2$ the velocity distribution can be written as energy distribution [11]

$$f_M(E) = \frac{2n}{\sqrt{\pi}} \frac{1}{(k_B T)^{3/2}} E^{1/2} \exp\left(-\frac{E}{k_B T}\right) \tag{2.11}$$

which conserves the number of particles in a certain velocity and energy interval, $f_M(v)dv = f_M(E)\mathrm{d}E$ with $\mathrm{d}E = mv\mathrm{d}v$.

It is important to note that the Maxwell-Boltzmann distribution applies to a system of non-interacting particles in equilibrium. In reality, plasmas often exhibit complex interactions and deviate from strict equilibrium conditions. Nonetheless, the Maxwell-Boltzmann distribution serves as a valuable approximation for characterizing the energy and velocity distribution of charge carriers in many plasma scenarios.

2.3 Sheath Formation

The concept of shielding not only applies to external charges but to neutral surfaces as well. On Earth plasmas only exist in confined spaces, resulting in inevitable contact with the containing material such as a vacuum chamber. Assuming an electrically floating wall, electrons, due to their higher mobility, will reach such a surface first leading to a negative charge. The electrons are assumed to have a Maxwellian energy distribution in the plasma. The resulting electric field, in turn, repels electrons and attracts ions until a positive *space charge sheath*, or simply *sheath*, is established as illustrated in Figure 2.1. The net charge on the wall (and any surface inside the vacuum chamber that can carry a charge) is called the *floating potential* Φ_{fl}. It is negative with respect to the electrical potential inside the plasma, which is called the *plasma potential* Φ_{pl}.

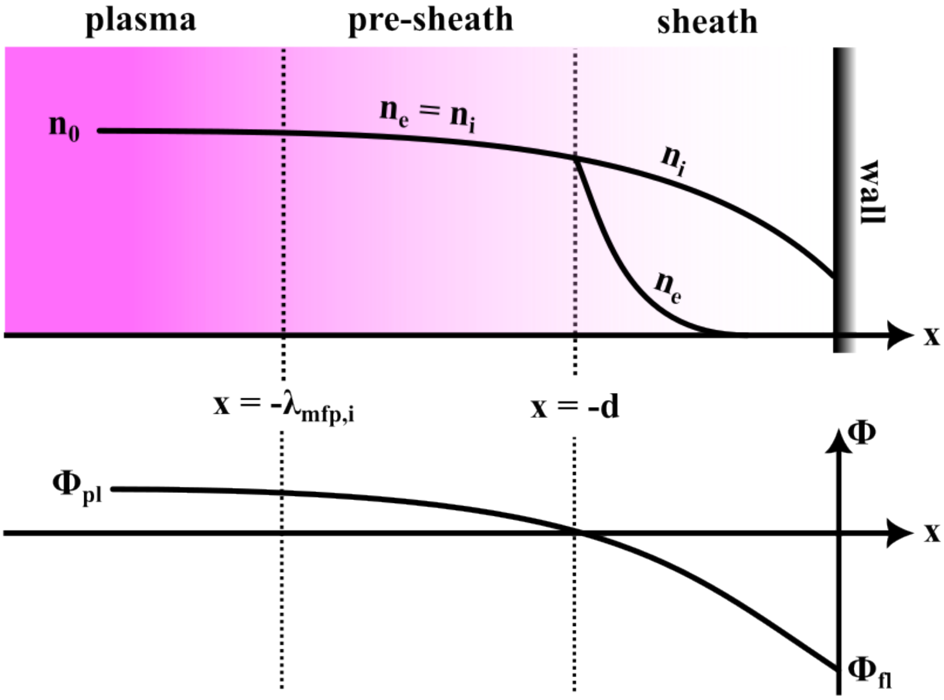

Figure 2.1: (Top) Electron and ion densities n_e and n_i, respectively, across bulk plasma to the pre-sheath and sheath. (Bottom) Potential distribution in the sheath region with plasma potential Φ_{pl} and floating potential Φ_{fl}.

In the sheath, quasineutrality is not upheld and only restored at the *sheath edge*. The sheath expansion is roughly equal to the ion mean free path $\lambda_{mfp,i}$, which includes the sheath and *pre-sheath*. The sheath itself expands roughly over the Debye length λ_D.

To be able to escape the plasma bulk, ions are accelerated in the pre-sheath to the so-called Bohm velocity v_B, which is defined as [12]:

$$v_B = \sqrt{\frac{k_B T_e}{m_i}} \tag{2.12}$$

In the pre-sheath quasineutrality is still given, although ion and electron density slowly decreases. In a collisionless sheath, the ions gain kinetic energy during transit in relation to the potential drop between their origin (plasma bulk) and the wall:

$$E_{kin,i} = e_0(\Phi_{pl} - \Phi_{fl}) \tag{2.13}$$

However, if the surrounding walls or surfaces inside the chamber are conducting or even biased, a different potential drop develops across the sheath. The sheath dimension, as well as the ion and electron densities, are thereby influenced. In case of a high negative bias, the electrons are pushed further into the plasma bulk and ion density can be assumed constant. This is the so-called *matrix-sheath*. The approximation of a constant ion density can only be true for potential differences ΔU far greater than $k_B T_e / e_0$ and for small time spans, in which ions due to their inertia can still be assumed as stationary. These conditions, for example, are found in plasma-immersion ion implantation (PIII) experiments [13].

If that is not the case, the Child-Langmuir law [14, 15] is applicable to sheath formation. Using Poisson's equation and assuming a collisionless sheath, the potential distribution $\Phi(x)$ in the sheath can be described as [9]:

$$\Phi(x) = \left(\frac{3}{2}\right)^{4/3} \left(\frac{m_i}{2e_0}\right)^{1/3} \left(\frac{j_i}{\epsilon_0}\right) (x+d)^{4/3} \tag{2.14}$$

With this the potential drop $U = \Phi(-d) - \Phi(0)$ can be calculated and from it the ion current density j_i in a collisionless sheath:

$$j_i = \frac{4}{9}\epsilon_0 \sqrt{\frac{2e_0}{m_i}} \frac{U^{3/2}}{d^2} \tag{2.15}$$

The ion current at the sheath edge is defined by the Bohm velocity and the ion density n_0 in the plasma bulk like

$$j_i = e_0 n_0 v_B, \tag{2.16}$$

hence, the sheath thickness d can be calculated as follows [1]:

$$d = \frac{\sqrt{2}}{3}\lambda_D\left(\frac{2e_0V}{k_BT_e}\right)^{3/4} \tag{2.17}$$

In reality, the ions undergo collisions in the sheath since the ion mean free path $\lambda_{mfp,i}$ is usually considerably lower than the sheath thickness. To describe the collisional sheath equation 2.15 has to be adjusted to account for the energy conversation condition. In the intermediate pressure regime, the ion mean free path is considered to be independent of their mobility μ_i and can be assumed constant [16]. Equation 2.15 is then modified to:

$$j_i = \frac{2}{3}\left(\frac{5}{3}\right)^{3/2}\epsilon_0\sqrt{\frac{2e_0\lambda_{mfp,i}}{\pi m_i}}\frac{U^{3/2}}{d^{5/2}} \tag{2.18}$$

In case of higher pressure, the probability of collisions rises and the ion mobility itself is then found to be independent of their velocity. This results in the Child-Langmuir law for highly collisional sheaths:

$$j_i = \frac{9}{8}\epsilon_0\mu_i\frac{U^2}{d^3} \tag{2.19}$$

2.4 Particle Collisions

When looking at a plasma as a mixture of charged particles combined with a neutral background gas, in reality, plasmas will always have a variation of density, a gradient across the plasma region. This leads to diffusion and, consequently, collisions between the involved particles. Particle collisions in a plasma encompass a range of interactions, including, but not limited to, ionization collisions, elastic and inelastic scattering, binary collisions, dissociation, recombination and charge exchange collisions. Each type of collision has its distinct consequences on plasma behaviour, influencing energy transfer, momentum exchange, and the excitation/ionization of particles. Understanding and characterizing these collision processes are essential for comprehending plasma dynamics and developing plasma-based technologies. Important quantities in describing collisions are the mean free path λ_{mfp}, the cross section σ and the collision frequency ν_{coll} of the involved particles. The macroscopic probability $\omega(z)$ for a particle to travel a distance z without any collisions is $\omega(z) = \exp(-z/\lambda_{mfp})$ [9]. Mean free path, cross section and collision frequency are defined by:

$$\lambda_{mfp} = (n_a \sigma)^{-1} \tag{2.20}$$

$$\nu_{coll} = \sigma v n_a \tag{2.21}$$

with v the velocity of the particles and n_a the density of their collision 'partners' (i.e. atoms).

Ionisation

In plasma generation, as well as maintaining the plasma state, electron impact ionization plays a crucial role. It is an inelastic collision process where high-energy electrons collide with a neutral atom, ejecting one or more electrons from the atom and forming a positively charged ion. Inelastic collisions lead to the reduction of the overall kinetic energy of the involved particles [1]. The ionization cross section σ_i generally depends on the electron's energy, the target atom's ionization potential, and the specific atomic or molecular structure. It tends to increase with increasing electron energy and is typically higher for atoms with lower ionization potentials [17]. σ_i shows a minimum for small electron energies of a few eV (Ramsauer effect [18]). The calculation of electron-impact ionization of atoms and molecules is fairly difficult [19, 20] and experimental data of cross sections can be used to verify and/or serve as a benchmark for the theoretical considerations [21].

Elastic scattering

Elastic collisions in a plasma involve interactions between particles, where there is an exchange of momentum and energy, but no change in their internal energy states. They can be electron-electron, ion-electron or ion-ion collisions. These collisions are relevant in plasma dynamics and thermalization processes [22]. This is because kinetic energy is generally exchanged between particles, while the total kinetic energy is conserved. If the kinetic energy is not conserved the collision is inelastic. Coulomb forces dominate the interactions between charged particles during elastic collisions in a plasma. Coulomb collisions are primarily relevant in fully ionized hot plasmas.

Charge exchange collisions

Charge exchange collisions occur when an ion captures an electron from a neutral particle, resulting in the ionization of the neutral particle and the formation of an energetic neutral atom. Charge transfer, electron exchange, electron transfer and electron capture are often used synonymously when referring to charge exchange collisions. In typical radio frequency (rf) and direct current (dc) discharges, resonant charge exchange is the dominant ion collision process, with a comparable cross section to small-angle elastic scattering, but a much higher effect on ion momentum [23].

The understanding of these collisions is essential when looking at etching rates, surface modification, thin film deposition, plasma heating and damage in sputtering discharges as well as ion implantation and ion penetration in technological plasmas and plasma processing systems [23]. The various forms of plasma surface interactions relevant to this work will be discussed in detail in section 2.5.

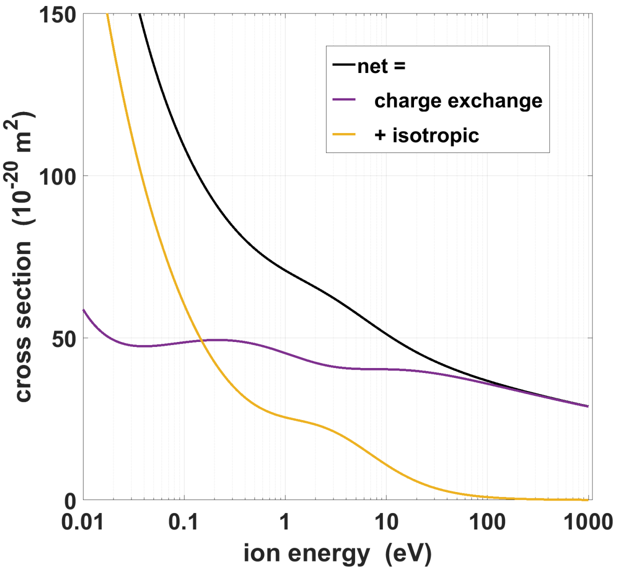

Figure 2.2: Collision cross sections for ion-atom collisions after [23] and used in [24].

The charge exchange cross section σ_{ce} is highly dependent on the energy of the impacting ion. According to [23], the differential cross section $\sigma_{net}(\Theta, E_i)$ of the dominating elastic collisions can be idealized as the sum of the charge exchange cross section $\sigma_c e(\Theta, E_i)$ and an isotropic scattering cross section $\sigma_i(\Theta, E_i)$. Θ is the scattering angle and E_i the ion energy.

Figure 2.2 shows the angle-integrated cross sections $\sigma_{ce}(E_i)$ and $\sigma_i(E_i)$ as well as the net cross section $\sigma_{net}(, E_i) = \sigma_{ce}(E_i) + \sigma_i(E_i)$ [24]. For ion energies $E_i > 100$ eV, isotropic scattering becomes irrelevant. The charge exchange collisions of highly energetic ions with neutral gas atoms produce neutral atoms with high kinetic energy in the direction of the scattering ion. These energetic neutrals can not be detected with electrostatic diagnostics, but still play a vital role in the energy balance of the plasma-surface interaction. This is especially true when looking at ion beam experiments as will be discussed in more detail in chapter 7.

2.5 Energy Balance at the Surface

In technological plasmas, which are used for thin film deposition, etching, surface modification, plasma catalysis or material synthesis, the plasma-surface interaction, or plasma-wall interaction, strongly influences the outcome of the processes [25, 26]. The surfaces themselves can be metals, dielectrics, polymers or even biological matter [27]. The interactions involve very complex mechanisms, in which the plasma parameters influence the surface parameters and vice versa. When looking at the influence of the plasma on the surface, generally, there are three types of interaction, namely, chemical modification, physical modification and energy exchange (energy balance). Chemical reactions induced by plasma processing on surfaces are used in surface cleaning or activation. Physical modification of a surface involves implantation, sputtering and secondary electron emission. Third, the energy exchange between plasma and surface, involving, of course, the aforementioned chemical and physical reactions, as well as any other plasma-surface interaction, is described by the energy flux of particles and radiation. Since all these processes are interconnected and, mostly, happen simultaneously, it is very hard to give a comprehensive overview. For a much more detailed description of possibilities and limitations in plasma processing of surfaces a small excerpt of literature is given in [27–30]. In the following, the focus is on the key surface processes relevant to this work.

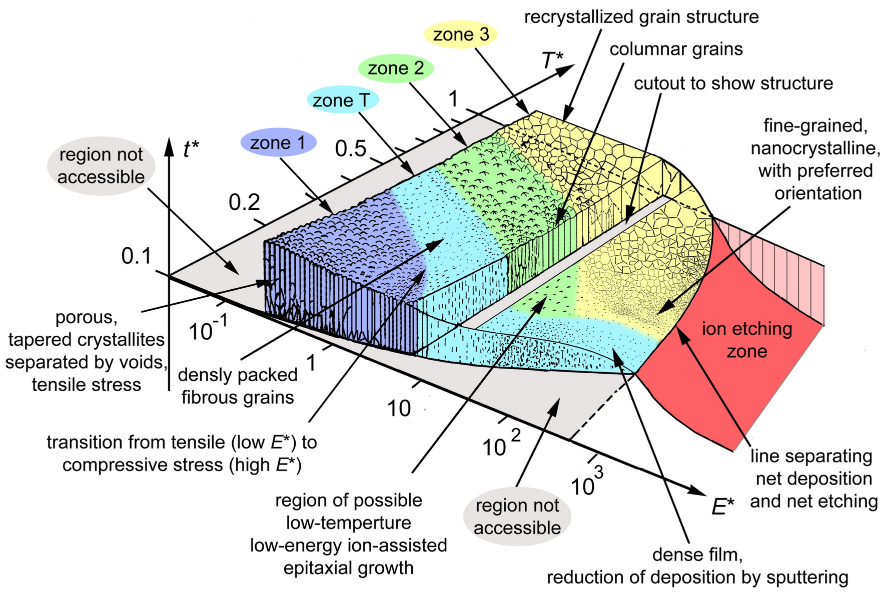

Figure 2.3: Structure zone diagram showing the influence of temperature and energy flux on thickness and structure of thin films formed by energetic deposition. Taken with permission from [31]

When considering the energy exchange or transfer from a plasma to a surface, the understanding of the individual contributions is crucial. It allows for tailoring of these processes since small changes in the plasma parameters can lead to a whole new set of characteristics of the processed materials. In the vastly diverse and ever-growing field of thin film deposition, this is especially important.

Figure 2.3 shows the extended structure zone diagram (SZD) by A. Anders [31], detailing the influence of energy flux and correlated substrate temperature on the film structure and deposition rate.

The total energy flux J_{in} towards a surface (or substrate) is the sum of different contributions coming from the kinetic energy of the involved particles J_{part} impinging on the surface, surface processes J_{surf} like adsorption, film formation or recombination, radiation J_{rad} from the plasma or the surface and loss processes J_{loss} like particle emission and radiation [32]:

$$J_{in} = J_{part} + J_{surf} + J_{rad} + J_{loss} \tag{2.22}$$

Figure 2.4 shows the different interactions between the plasma bulk, species inside the plasma and exposed surfaces leading to the energy balance at the plasma-surface interface.

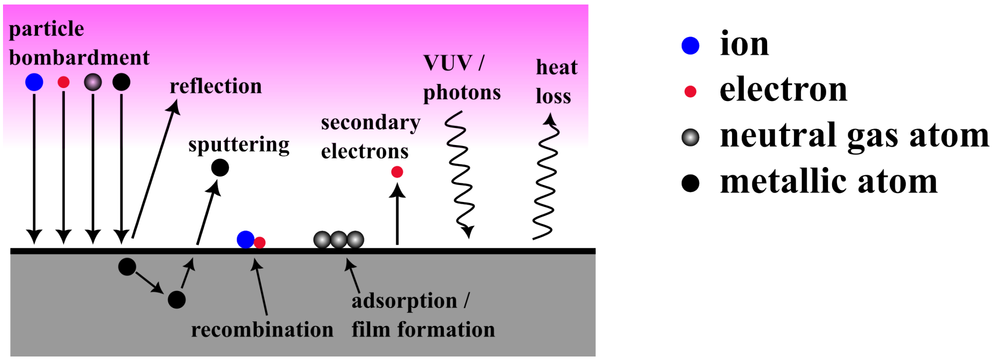

Figure 2.4: Particles, surface processes, radiation and loss processes involved in the plasma-surface interaction.

In the following, the individual contributions to the total energy flux will be discussed.

2.5.1 Kinetic energy of particles

Particles impinging on a surface can transfer their kinetic energy to that surface, either totally, by sticking to it, or partially, by reflecting on it. This can be electrons, ions and neutrals. Assuming that all particles stick to a surface and transfer all their kinetic energy, the energy flux J_{part} of these particles is

$$J_{part} = \Gamma_{part}\bar{E}_{kin} \tag{2.23}$$

with $\Gamma_{part} = j_{part}/e_0$ the particle flux density, j_{part} the particle current density and $\bar{E}_{kin}$ the mean kinetic energy of the particles.

Assuming a thermodynamic equilibrium and a collision frequency independent of velocity, a Maxwellian electron energy distribution function (EEDF) can be used to describe the energy flux of electrons J_e as [32]:

$$J_e = n_e\sqrt{\frac{k_B T_e}{2\pi m_e}}\, 2k_B T_e \exp(-\xi)\, 2k_B T_e = \frac{j_e}{e_0} \tag{2.24}$$

with j_e the electron current density and $\xi = (\Phi_{pl} - \Phi_s)/(k_B T_e)$ describing the potential difference between the plasma and the substrate in relation to the electron temperature T_e. Assuming a constant collisional cross section, electrons are better described by a Druyvesteyn EEDF [33] leading to electron energy flux of:

$$J_e = n_e\sqrt{\frac{k_B T_e}{2\pi m_e}} k_B T_e(-\xi \exp(-0.25\xi) + (1.79 + 0.89\xi^2) erf(0.5\xi)) \tag{2.25}$$

In the case of a mono-energetic electron beam the electron energy flux is:

$$J_e = n_e\sqrt{\frac{k_B T_e}{2\pi m_e}}\, k_B T_e\, 2\pi(1 - \xi)^2 \tag{2.26}$$

As previously discussed the kinetic energy of positive ions is mainly determined by the voltage drop across the sheath in front of the substrate Φ_{sh}. In process plasmas, the ion energy and angular distributions arriving at a substrate are crucial in determining ion anisotropy and etch rate [34]. In a discharge at high density and low pressure, one can assume a collisionless sheath since the sheath thickness is much smaller than the ion mean free path. Then the energy flux of ions simply is

$$J_i = j_i\Phi_{sh} \tag{2.27}$$

with $j_i = e_0 n_i v_B \approx 0.61 n_0 v_B$ the ion current density with n_i the ion density at the sheath edge, n_0 the ion density in the plasma bulk and v_B the Bohm velocity. However, at lower pressure collisions occur in the sheath and the ion flux density must be adjusted. For low pressure applications with pressure $p \leq 10$ Pa it is best described by the Bohm flux and for $p \leq 1$ Pa, the Child-Langmuir law is applicable [32]:

$$j_i = \begin{cases} n_e \sqrt{\dfrac{k_B T_e}{m_i}} \exp(-0.5) & \text{Bohm flux} \\ \dfrac{4}{9} \dfrac{\epsilon_0}{e_0} \sqrt{\dfrac{e_0}{m_i}} \dfrac{\Phi_{sh}^{3/2}}{d_{sh}^2} & \text{Child-Langmuir sheath} \end{cases} \tag{2.28}$$

So, depending on the plasma environment, the kinetic energy of ions will drastically be affected depending on pressure, driving power and many other factors. This in turn affects the ion energy distribution function (IEDF). The IEDF will be discussed in more detail in chapter 4.1.2.

In many technological plasma negative ions are produced, either by admixture of electronegative gases or at a target surface in reactive magnetron sputter discharges. Negative ions produced in the plasma bulk, tend to stay there since their low kinetic energy and local attachment in the dense region to the positive plasma potential do not allow for them to overcome the potential barrier of the sheath. On the other hand, if they are produced at the target electrode or in the sheath in front of a highly negatively biased electrode, they experience strong electric fields and gain high kinetic energy. Although these negative ions can reach the substrate and usually have a small current density, they can seriously alter or even damage surfaces or deposited films [35].

As for the kinetic energy of neutrals, it is less complicated to describe a theoretical model, since their flux density is independent of energetic fields and potentials. Their contribution to the energy flux can also be described by their flux density Γ_n and mean kinetic energy $\bar{E}_{kin}$:

$$J_n = \Gamma_n \bar{E}_{kin,n} \tag{2.29}$$

However, their detection by diagnostic probes proves to be more complicated, especially considering fast neutrals originating in charge exchange collisions or sputtered atoms coming from a target. More to the experimental determination of the neutral flux contribution to the overall energy flux will be discussed in chapter 6 and 7.

2.5.2 Sputtering

Sputtering occurs when a highly energetic ion or neutral bombards the surface of a solid material (metal, insulator or semiconductor) and, thereby, evaporates it releasing single particles, molecules or even particle clusters. It is a long-known phenomenon [36] that nowadays is used in plasma-based physical vapour deposition (PVD) for thin film deposition or in the semiconductor industry where the evaporation of material is used to etch complex structures and devices [37].

The process itself is very complicated since the bombardment with fast ions or neutrals can trigger a variety of processes. These include elastic and inelastic collisions inside the material, the reflection of the impinging particles and the release of atoms, ions and clusters or radiation coming from the surface and coming from excited particles [38]. The bombarded material is referred to as the target. The mechanism of how particles are sputtered from a target (the momentum transfer) can be divided into three categories depending on the energy of the bombarding particles E_{in} and the mass ratio between incident ions and target atoms [39]:

1. **Single knock-on:** target atoms gain sufficient energy from collisions to escape the surface, but a collision cascade is not triggered ($E_{in} \leq 1$ keV).
2. **Linear cascade**: energy transferred by collision to target atoms is sufficiently high, so even more atoms can be displaced by collisions (E_{in} up to 100 keV).
3. **Spike regime**: the density of displaced atoms gets so high that collisions between recoiled atoms start to dominate and most of the target atoms in the spike region are in motion ($E_{in} > 100$ keV).

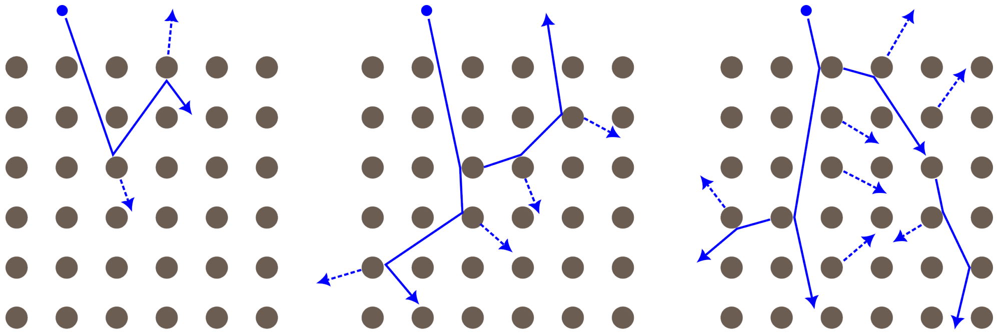

Figure 2.5: Illustration of the different sputter mechanisms after [39]: (Left) single knock-on, (Middle) linear cascade and (Right) spike regime.

The sputter yield Y denotes the relation of sputtered particles to incident particles. In PVD processes the usual sputter yield is in the range of 0.1 and up to 2 [40, 41].

The free software package SRIM (Stopping and Range of Ions in Matter) [42] provides a useful tool to estimate sputter yields by simulation.

And although the kinetic energy of the incident particles is usually very high, most of it is lost in the collision cascade and only a small fraction is deposited. Therefore, the change in the energy balance at the surface of the target by sputtering is also very small. A detailed depiction of the possible mechanism during sputtering is shown in figure 2.5.

In PVD processes a substrate is placed in front of the target as a basis for i.e. thin film growth. Sputtered neutrals coming from the target usually have a kinetic energy of several 10 eV and sometimes up to 100 eV. This kinetic energy is then deposited onto the surface as described in the previous section.

The experimental setup used in magnetron sputter PVD processes will be discussed in more detail in chapter 3.4.

2.5.3 Secondary Electron Emission

When the surface of a metal or metal oxide is bombarded by energetic particles (electrons and ions) or by photons with sufficient kinetic energy secondary electrons can be emitted from the surface. This effect is called secondary electron emission (SEE). It is a vital process in plasma generation since only a sufficient amount of secondary electrons released from the cathode can account for the loss of primary electrons of the plasma bulk at the anode and the surrounding walls. SEE also affects the potential drop in the sheath, making it more positive with respect to the plasma potential [43]. This is important for the deposition process of thin films and also for Hall thrusters and fusion devices.

Secondary electrons (SE) are produced by electron impact or ion impact. When a primary electron (PE) is responsible for SEE there are two kinds of released electrons in the so-called δ-process. The SEE coefficient δ describes the SEE yield by electron impact. It can be written as [44]:

$$\delta = \int n(x, E_{pe}) p(x) dx \tag{2.30}$$

where $n(x, E_{pe})dx$ is the average number of SEs produced at a certain depth x below the surface dependent on the energy of the PE E_{pe}.

The reflected SEs have roughly the same energy as the PE and, therefore, do not significantly attribute to a change in the energy balance between plasma and surface. True secondary electrons on the other hand usually have a thermal energy distribution function [45]. To actually be released from the surface, the SE has to overcome the electron work function E_{wf} which is dependent on the surface material. It is the energy needed to raise an electron from the Fermi level, which is the maximum energy of the electrons in the conduction band (their electrochemical potential), to the potential energy level in vacuum [46]. Table 2.2 lists the work function for a few selected metals.

metal	E_{wf} (eV)
Ni	4.9
Ti	4.46
Cu	4.26
Nb	4.27

Table 2.2: Electron work function E_{wf} for selected metals, taken from [47].

Using equation 2.30 the energy lost by a PE per unit path length under the surface is $-dE_{ep}/dx$. Divided by E_{wf} gives the number of SEs produced per incident PE and unit path length.

In case SEE is triggered by impacting ions the SEE coefficient γ_{see} is used [1]:

$$\gamma_{see} \approx 0.016(E_{ion} - 2E_{wf}) \tag{2.31}$$

with E_{ion} being the ionization energy of the impacting ions. The release of SEs from the surface takes away energy comprised of E_{wf} and its kinetic energy $E_{kin,see}$:

$$J_{see} = \Gamma_{see}(E_{wf} + E_{kin,see}) \tag{2.32}$$

The flux of secondary electrons Γ_{see} also is material dependent and governed by the secondary electron emission coefficient.

2.5.4 Surface processes

The different surface processes occurring, especially, in thin film deposition technologies, can either add to or subtract from the total energy flux onto a surface. When thin films are formed on a substrate in PVD processes, the sputtered particles impinging on the substrate bond to the surface. This bond either is weakly coupled by van-der-Waals forces (physisorbed) or strongly coupled by ionic or covalent bonds (chemisorbed) [48]. The adsorption of a target species on a substrate releases a maximum energy $E_{ad,max}$ depending on the kinetic energy $E_{kin,in}$ of the impinging species [48]:

$$E_{ad,max} = E_{kin,in}\frac{4m_{in}m_s}{(m_{in}m_s)^2} \tag{2.33}$$

This energy is added to the integral energy flux on top of the kinetic energy of the sputtered particles:

$$J_{sub} = \Gamma_{sp} E_{ad,max} \tag{2.34}$$

Γ_{sp} denotes the flux density of sputtered particles onto the surface that contributes to the film formation.

The process of adsorption often is a two-step process, where an adsorbate first is physisorbed to the surface. In this weakly coupled state, it still has high mobility and diffuses on the surface. This is beneficial in film growth since it increases the chance of it getting chemisorbed at a suitable site on the growing film surface. Chemisorption is the formation of a chemical bond by the transfer of electrons between atoms.

Another contribution to the energy flux comes from ion-electron recombination on the surface. Whether the surfaces (or chamber walls) are grounded, conductive or floating, there will always be enough electrons for ions to recombine with. In order to recombine the electron has to overcome the electron work function E_{wf}. If the process is assumed to take place directly at the surface the energy flux by recombination is:

$$J_{rec} = \Gamma_i (E_{ion} - E_{wf}) \tag{2.35}$$

with E_{ion} the ionization energy of the participating ion.

2.5.5 Radiation

The energy coming from radiation can have different sources. There is line radiation by the plasma species themselves or heat radiation coming from hot surfaces inside the processing chamber. In LTPs, the contribution of line radiation from excited species (ranging from infra-red (IR) to ultraviolet (UV) light) has a rather small contribution, ranging from $5\% - 10\%$ in inductively coupled rf discharges [32] to $20\% - 30\%$ in cylindrical magnetron sputtering [49]. The heat radiation from a surface onto a substrate can be estimated using the Boltzmann formula [32]:

$$J_{rad} = \sigma(\epsilon_{rad} T_{rad}^4 - \epsilon_s T_s^4), \tag{2.36}$$

with $\sigma = 5.67 \cdot 10^{-8} \mathrm{W/(m^2K^4)}$ the Stefan-Boltzmannn constant and the spectral emissisivities ϵ_{rad}, ϵ_s and temperatures T_{rad}, T_s of the radiating surface and the substrate, respectively.

3 Laboratory plasmas

In this chapter, the various plasma discharges used in this work will be presented. First, a more general overview of plasma generation will be given. How the plasma is generated in the experiments specifically will be discussed in the individual sections. Afterwards, the radio frequency capacitively coupled plasma (rf-ccp) chamber is presented which was specially designed to embed different plasma diagnostics into the grounded electrode. The diagnostics themselves will be discussed in chapter 4. Next, the two ion beam setups are presented. There is a vertical and a horizontal ion beam which both use an identical ion source where the plasma is generated with microwaves in an electron cyclotron resonance (ECR) heating process. Last, the magnetron sputtering (MS) mechanism is explained in more detail and the various forms from direct current (DC-MS) to rf-MS to high-power impulse magnetron sputtering (HiPIMS) are introduced.

3.1 Plasma generation

In technological plasmas, a cathode and an anode are placed inside a vacuum chamber. The anode either is an actual electrode of some form inside the chamber or the grounded chamber walls serve as the anode. In order to generate a plasma, a power source is needed such as a DC power supply. A working gas, for example, argon (Ar), is introduced into the chamber. Free electrons are accelerated by the electrical field generated with the power supply and gain enough kinetic energy $E_{kin,e}$ to overcome the ionization energy of the atoms $E_{ion,a}$ and ionize the atoms of the working gas upon collision ($E_{kin,e} > E_{ion}$) [9]. The electron impact ionization produces ions and, consequently, more electrons:

$$e^- + Ar \rightarrow Ar^+ + 2e^- \tag{3.1}$$

which in turn leads to an ionization avalanche that best be described by the Townsend coefficient α [1]:

$$\alpha = \frac{\nu_i}{v_d} = \lambda_i^{-1} \tag{3.2}$$

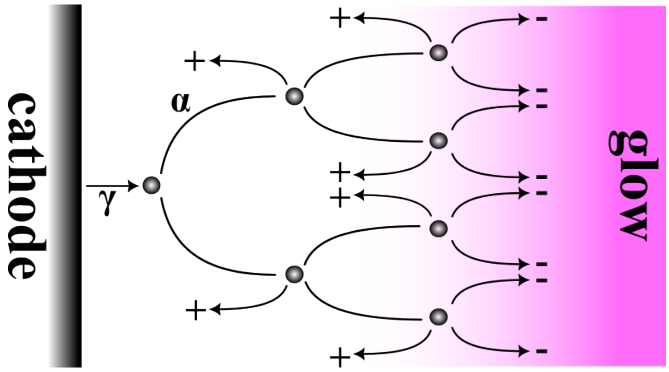

Figure 3.1: Illustration after [9] of the ionization avalanche triggered by secondary electron emission. The electron is released and accelerated away from the cathode. This leads to electron impact ionization with a probability α which in turn produces more electrons.

with ν_i the ionization frequency, v_d the drift velocity of the electrons and λ_i the mean free path of ionization. At the anode, electrons are lost due to recombination. To maintain the avalanche ionization process depicted in Figure 3.1, enough electrons must be produced at the cathode by ion impact emission (i.e. SEE). This is necessary since not only electrons are lost to the walls, but ions as well.

As was discussed in the previous chapter, the yield of SEE by ion impact is described by γ_{see}. In order to get a self-sustained discharge Townsend's stationary law has to be fulfilled [8]:

$$\gamma(\exp(\alpha d) - 1) = 1 \tag{3.3}$$

Here, d is the distance between the electrodes (see Figure...). In a self-sustained discharge and with a growing discharge power supply the gas begins to glow and a sharp drop in the voltage is reached (gas breakdown voltage V_{bd}). The necessary conditions to get a gas breakdown are described by the so-called Paschen law [1]:

$$V_{bd} = \frac{Bpd}{\ln(Apd) - \ln[\ln(1 + 1/\gamma_{see})]} \tag{3.4}$$

It is dependent on the pressure p of the working gas, the distance d between the electrodes and two gas-specific constants A and B. Figure 3.2 shows exemplarily the Paschen curve for Ar, Xe, He and air. The constants A and B were taken from [1] for Ar, Xe and He. For air the constants were taken from [50]. SEE yield was chosen as $\gamma_{see} = 0.1$ for all gases.

After the gas breakdown, the so-called normal glow regime is reached. With increasing power, the current density is evenly distributed over the cathode until the

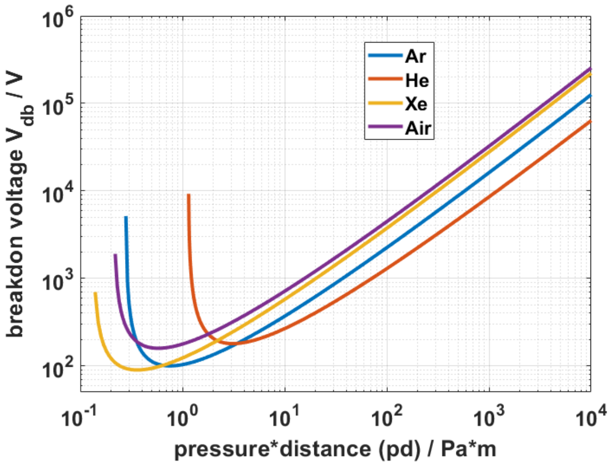

Figure 3.2: Paschen curve for Ar, Xe, He [1] and air [50] showing the dependence of the breakdown voltage on the pressure-distance product.

ion bombardment covers the whole cathode and current density and voltage increase. This is called the abnormal glow regime. These discharge conditions are used in plasma processing, such as sputtering or etching. Further, an increase in power results in the thermionic emission of electrons from the cathode resulting in a sharp voltage drop while maintaining high current densities. This is the arc discharge regime. These conditions are used for example for cathodic arc deposition [51]. The different regimes are illustrated in Figure 3.3.

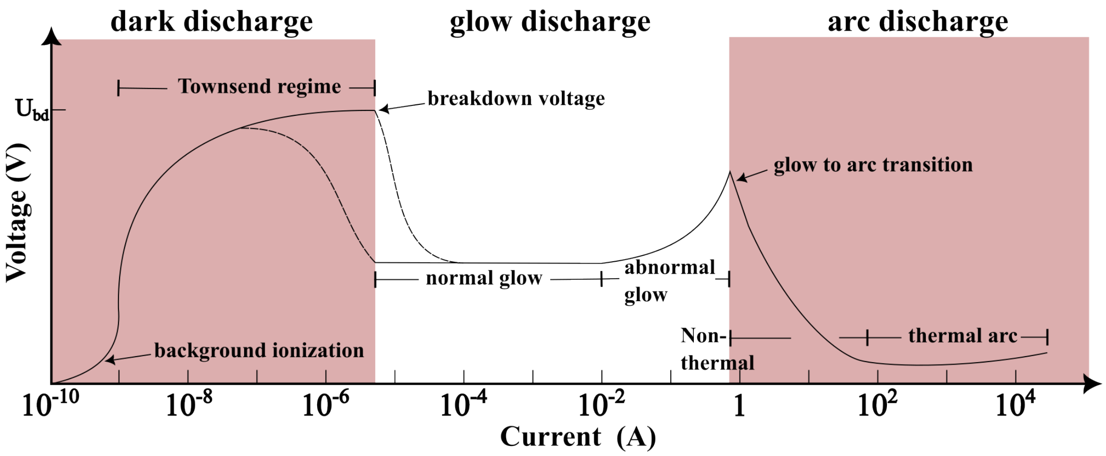

Figure 3.3: Illustration after [52] of the different discharge regimes of a DC plasma depending on the current.

3.2 RF discharges

Radio frequency (rf) discharges, sometimes called high frequency (hf) discharges, are widely used in plasma etching and deposition processes. The limits of a normal DC discharge with respect to the charge-up of insulating surfaces inside the chamber can be overcome by powering the discharge through radio frequency excitation with frequencies between 1 MHz and 100 MHz. Typical frequencies used are $\omega_{rf} = 13.56$ MHz and its first and second harmonic (27.12 MHz and 40.68 MHz). Assuming a mean particle density of $n_{e,i} \approx 10^{15}$ m^{-3} in an argon gas atmosphere ($m_i = 40$ amu) and using equation 2.6 the plasma frequencies of electrons and ions in a 13.56 MHz discharge come to:

$$\omega_{pe} \approx 16.6\,\mathrm{GHz} \tag{3.5}$$

$$\omega_{pi} \approx 1.8\,\mathrm{MHz} \tag{3.6}$$

This means that only electrons can follow the alternating electric field while the ions stay practically stationary. So electrons are accelerated sufficiently to induce impact ionization of the working gas. The alternating electric field leads to an also alternating electron cloud moving against the static ion background. This also has an effect on the sheath in front of the electrodes. In the negative half-cycle of the rf, the electrons are pushed away from the electrode leading to sheath expansion. In the positive half cycle, the electrons are accelerated towards the electrode. This leads to a collapse of the sheath in front of the electrodes and an indirect contact between electrode and plasma [53].

There are two types of rf discharges, symmetric and asymmetric. In the symmetric case, both electrodes are powered simultaneously. More widely used is the asymmetric case. Here the rf power is supplied from a frequency generator to the cathode (or powered electrode) via a matchbox and a capacitor.

As counterpart serves either an opposite grounded electrode or the grounded chamber walls. The matchbox is a network of inductors and impedances used to adjust the impedance of the frequency generator to the impedance of the vacuum chamber so that no power is reflected in the generator. To galvanically isolate the powered electrode a capacitance is added between the matchbox and electrode.

The following concentrates on the Plasma Interface Diagnostic EXperiment (PIDEX) chamber that was specially designed to embed different diagnostics (passive thermal probe, retarding field energy analyser) into the grounded electrode of an asymmetric rf-ccp discharge. In [54] a setup with the grounded electrode opposite the powered one with adjustable spacing between them was developed that was placed inside the chamber. The rf power was delivered to the powered electrode via an insulated cable in the chamber. This led to the problem of plasma generation between the

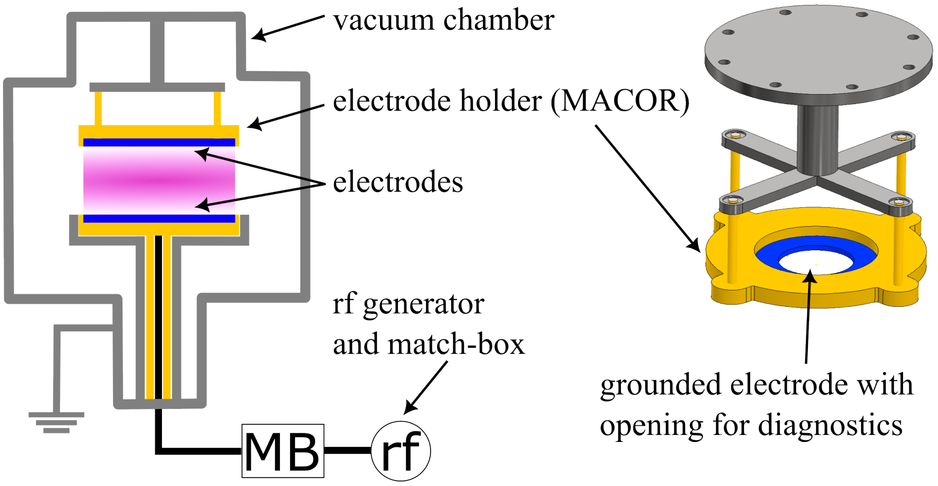

Figure 3.4: (Left) Schematic drawing of the experimental chamber and the driven and grounded electrodes mounted in MACOR holders. (Right) CAD drawing of the upper flange holding the grounded electrode in which diagnostics can be embedded.

two electrodes and in the rest of the chamber since the cable could not be insulated sufficiently and served as an antenna for the rf power. The setup design was changed in a way that the power supply is better insulated and both the changeable distance between the electrodes as well as the embedment of the diagnostics are still feasible. The setup is shown in figure 3.4. The rf feedthrough is insulated inside a MACOR tube and directly connected to the powered electrode. The grounded electrode is suspended from the upper lid of the chamber. Here, the distance between the electrodes can be changed and the various cables of the diagnostics can be led out through the flanges in the upper lid.

3.3 Ion beam experiments

In chapter 6 and 7 measurements are presented of which some were done in two different ion beam discharges. A Vertical Ion Beam EXperiment (VIBEX) and a Horizontal Ion Beam EXperiment (HIBEX). Both of them use an identical ion source as first presented in [55]. The only difference is the grid system used to propagate the broad ion beam into the vacuum chamber. Figure 3.5 shows the cylinder in which high-energy ions are generated.

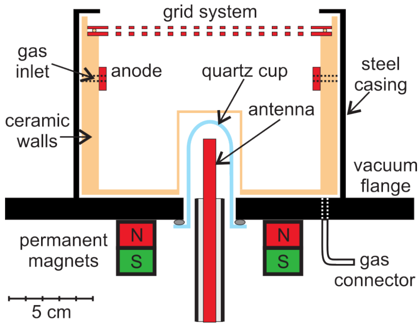

Figure 3.5: ECR ion source setup taken from [56].

An antenna emits microwaves into the source chamber ($P_{mw} \approx 360$ W and $\omega_{mw} = 2.45$ GHz). A superimposed steady magnetic field provides a volume where the electron cyclotron frequency $\omega_{e,c} = e_0 B/m_e$ resonates with the excitation frequency ω_{wf} and a component of the electric field is perpendicular to the magnetic field. B is the magnetic field strength and m_e the electron mass. Here, the electrons are accelerated and ionize the working gas. This process is called electron cyclotron resonance (ECR) heating. The result is a low-pressure, almost collisionless plasma, that can be changed from a weakly to a highly-ionized state by changing the working gas pressure and microwave power [57]. This and the fact that no electrodes are needed to generate the plasma makes it a steadily operating type of ion source that is often used in plasma processing, such as etching and surface modification.

An anode ring (also seen in Figure 3.5) around the discharge is used to elevate the ion potential energy. Voltages of up to $V_{an} = 1200$ V can be applied. The grid system is made up of two molybdenum grids which are used to extract and accelerate the ions from the ion source. The inner grid is floating and the outer grid usually has a potential of $U_{grid} = -300$ V.

VIBEX

In the VIBEX experimental chamber, the ion source is located on the top. It is housed in a cylinder with a diameter of $2r_1 = 25$ cm and a height of $h_1 = 20$ cm. This in turn is put on a slightly bigger cylinder ($2r_2 = 30$ cm and $h_2 = 40$ cm) with four openings of which two are opposite each other, respectively. Here, the vacuum pumping system and pressure measurements are installed on two of them, while the other two have ISO KF-160 flanges to give access to diagnostic probes. The setup is schematically drawn in figure 3.6 where, additionally, it is shown how different diagnostics can be

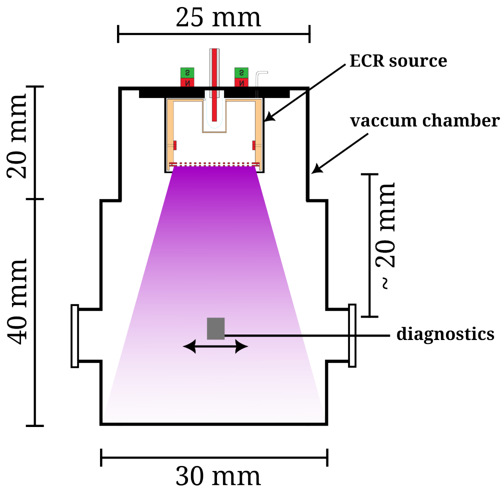

Figure 3.6: Schematic drawing of the experimental chamber VIBEX with dimensions and the placing of diagnostics in the beam.

placed in the ion beam and horizontally moved through the chamber.

HIBEX

The HIBEX chamber is a stainless steel cylinder with an inner diameter of $d = 65$ cm and a length of $l = 160$ cm. The ion source is centered along the horizontal axis and the ion beam travels along this axis approximately 140 cm until it reaches the beam dump on the opposite end. Figure 3.7 shows schematically how the ion source and diagnostics are located in the chamber.

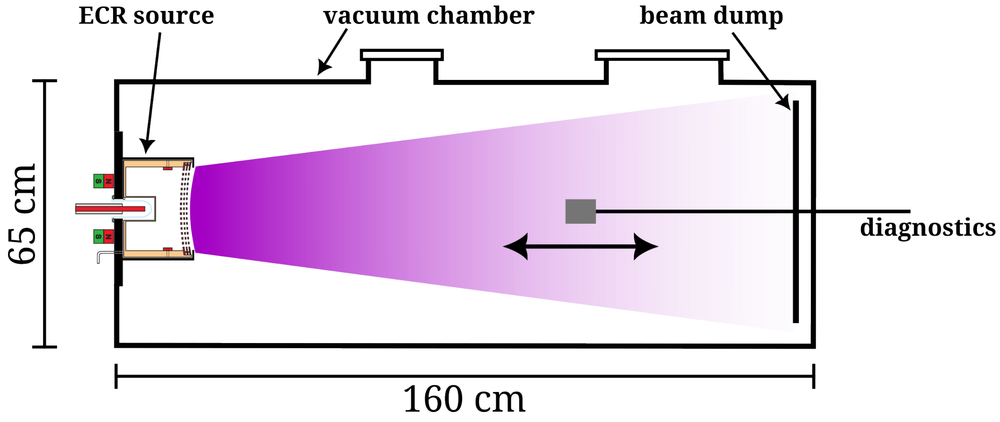

Figure 3.7: The HIBEX chamber schematically shown as a top view, with the ion source, ion bema and beam dump after [58]. Diagnostics can be inserted from the side flanges or opposite the ion source.

In contrast to the ion source used in VIBEX, the grid system has three spherically curved molybdenum grids to extract, accelerate and focus the ion beam [58]. Otherwise, the source is operated as described above.

3.4 Magnetron sputtering

A series of different sputter devices are examined in this thesis. The individual setup is detailed in the respective publication. Now, the general technique of sputtering from a target with the help of magnetrons will be discussed.

The use of magnetrons to deposit thin films onto a substrate goes as far back as the 1960s [59]. It uses a combination of magnetic and electrical fields to confine the plasma in front of the target similarly as described in the previous section. Ions from the plasma are accelerated toward the target leading to the sputtering of target atoms, molecules or clusters. These sputtered particles travel across the chamber onto the substrate where they are deposited. Figure 3.8 shows the typical arrangement of magnets, target, cathode and anode in a circular planar configuration, as well as the substrate.

On the left, the magnetic field is closed above the cathode. This is referred to as a balanced magnetron [60]. The electric field lines point vertically from the cathode. In the region where the electric ($\vec{E}$) and magnetic ($\vec{B}$) fields are perpendicular to each other most ionization takes place. Here, the electrons are trapped due to the Lorentz force

$$\vec{F}_L = e_0(\vec{E} + \vec{v}\text{x}\vec{B}) \tag{3.7}$$

leading to higher ionization rates in that region. $\vec{v}$ is the velocity of the electrons. In this torus-shaped region, the plasma density is especially high which leads to a more pronounced glow and also extensive sputtering beneath it. The so-called race track is formed. This actually is a disadvantage of the planar configuration, since it leads to non-uniform sputtering of the target. This target abrasion can force the user to frequently change the targets which, especially, in the industry process can become very costly and does not guarantee reproducibility. Furthermore, the confinement of the plasma in front of the target limits the possibility of charged particles reaching the substrate which is wanted for the formation of dense coatings or to improve adhesion [31]. An example of the effect of the race track on film properties is publication 1 in chapter 5. For that purpose, the configuration of the magnetic field can be altered as is shown in the middle and on the right in figure 3.8.

This configuration is unbalanced since the magnetic field is not closed above the target. Some electrons can escape the confinement and plasma can be created away

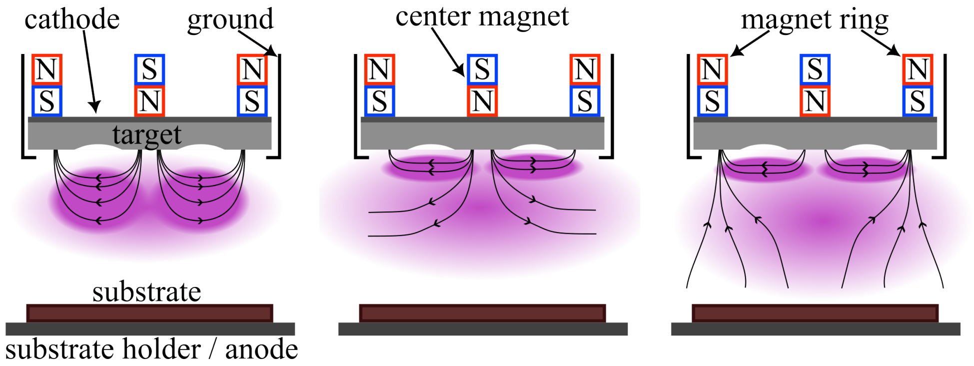

Figure 3.8: Schematic drawing of a typical magnetron configuration including anode and cathode, target, substrate, substrate holder and the magnetic field lines. (Left) balanced configuration, (Middle) unbalanced type 1, (Right) unbalanced type 2.

from the target. This ultimately leads to better transport of charged particles towards the substrate. The formation of the race track, however, remains. There is a distinction between type 1 unbalanced and type 2 unbalanced configurations. Type 1: magnetic field lines originate from the centre magnet and the field is not closed. Type 2: magnetic field lines originate from the magnet ring and, also, the field is not closed with the centre magnet.

The electric field $\vec{E}$ can either be created by a direct current (referred to as dcMS) or a radio frequency (rfMS) power supply. Planar dcMS sources are generally operated in a low-pressure range of $0.2-4$ Pa with a cathode voltage of $300-700$ V. At these low pressures backward diffusion of the target atoms is reduced which increases the deposition rate [60]. The ionization rate of the sputtered target atoms is very low (2% – 3%) and the secondary electrons emitted from the target by the impinging working gas ions are trapped by the dense plasma in front of the cathode. This means that substrate heating is relatively low under these conditions which makes them ideal for working with heat-sensitive substrates.

With an rfMS setup, the ionization rate of the sputtered target atoms can be increased. Furthermore, it is possible to sputter from insulating target materials. However, the deposition rate for dielectric films is generally very low [60].

In many reactive PVD processes where the admixture of reactive gas (nitrogen or oxygen) to the inert working gas is used to deposit dielectric or insulating films and also semiconductors [61]. With conventional planar magnetrons this leads to target poisoning and arc development and instabilities in the process [62]. Especially the formation of an insulating layer on top of the target surface leads to forming a positive charge and, consequently, lowering the sputter yield. To address this issue, the pulsed magnetron sputter deposition was developed. There is the bipolar pulsed operating mode, symmetric and asymmetric. The target voltage is alternated between negative and positive with square waveforms. In the asymmetric case, the negative voltage pulse is higher than the positive and applied for more extended periods. The positive pulse amplitude and its length roughly are $10\% - 20\%$ of the negative amplitude and length [63]. During the negative pulse sputtering takes place. The short application of the positive pulse cleans the insulating target surface by neutralizing its net positive charge and even charging it negatively. So when the pulse is reversed again, sputtering ions can reach the surface better and remove the compound fraction of the target surface.

For high power densities and high ion current to the target high power impulse magnetron sputtering was developed (HiPIMS) [64]. Unipolar high-power pulses with short duty cycles ($\leq 10\%$) are applied with a low frequency (around 500 Hz) and short pulse lengths ($50 - 200\,\mu$s) [65]. This leads to a very high ionization degree (up to 90%) while not heating up the target too much. Peak powers of up to a few MW/pulse and average powers of ≈ 20 kW can be achieved [66]. The energy flux density to the target reaches $1 - 3\,\mathrm{kW}/cm^2$ compared to the $1 - 10\,\mathrm{W}/cm^2$ in the conventional dcMS.

4 Plasma diagnostics

A combination of experimental diagnostic techniques is employed to accurately characterize the plasma parameters and the energy fluxes at a substrate surface. Langmuir probes are versatile tools for measuring plasma properties, including electron temperature T_e, plasma potential Φ_{pl} and electron energy distribution. Retarding field analysers allow for the measurement of the ion energy distribution (IED) and ion flux onto the substrate surface. Thermal probes, such as the passive thermal probe, provide the integral energy flux density towards a surface exposed to a plasma source.

By utilizing these diagnostic techniques, researchers can comprehensively understand the energy balance in the plasma and at the substrate surface. This knowledge is vital for optimizing plasma processes in various technological applications, enabling better control over surface interactions, material modification, and overall plasma performance.

The following chapter is divided into three parts considering all diagnostic techniques used in this work. First, the two electrical probes, the Langmuir probe (LP) and the retarding field energy analyser (RFEA) are presented. Then the passive thermal probe (PTP) is discussed, followed by the surface diagnostics utilized in the magnetron sputtering experiments in chapter 5 done at the Faculty of Engineering of Kiel University.

4.1 Electrical probes

The different kinds of electrical probes for plasma diagnostics are amongst the oldest used probe techniques. From Langmuir probes to Hairpin probes to electric and magnetic field probes to retarding field energy analysers they enable the determination of plasma parameters and the energy spectrum of charge carriers or electric and magnetic field strengths and directions. The long-lasting use of these kinds of probes can be attributed to their simplicity in terms of design and implementation and their cost-effectiveness compared to other sophisticated diagnostic techniques. They can be easily incorporated into experimental setups, allowing real-time measurements and providing valuable feedback for plasma control and optimization. Additionally, the extensive historical use of these probes has led to a wealth of knowledge and understanding of their limitations and calibration procedures, making them highly reliable and well-established tools in the field of plasma physics.

4.1.1 The Langmuir probe

Its simplicity in setup and measurement technique makes the Langmuir probe one of the most used tools in plasma diagnostics. It was first introduced in 1926 by H.M. Mott-Smith and I. Langmuir [67]. A metallic wire or small platelet is introduced into the plasma. This disturbance leads to the formation of a sheath around the probe as described in section 2.3. By biasing the probe with a voltage V_p the flux of charge carriers to the probe can be influenced. A voltage sweep is applied and measuring the resulting current yields the typical I-V characteristic which can be used to determine the plasma and floating potentials, Φ_{pl} and Φ_{fl}, the electron and ion density $n_{e,i}$ and their respective temperatures $T_{e,i}$. Furthermore, the ion flux and electron energy distribution function (EEDF) can be determined.

The probe itself can have different geometries. The cylindrical and the planar probe are the most common and used in this work. Spherical probe geometries are not used as frequently. A typical I-V characteristic is shown in figure 4.1 for a cylindrical probe (length: 6 mm, diameter: 100 μm). It is taken from measurements inside an rf plasma operated at 3 Pa argon pressure and 100 W power. Floating potential Φ_{fl} and plasma potential Φ_{pl} are also indicated. Furthermore, the theoretical current-voltage course for a planar, cylindrical and spherical probe is displayed on the right.

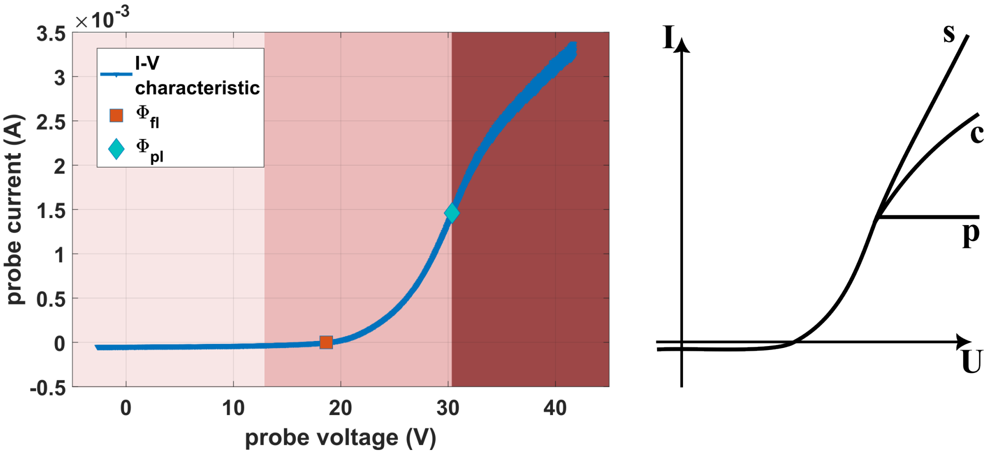

Figure 4.1: (Left) Example of a typical I-V measurement with a cylindrical probe in an rf plasma (Ar, 3 Pa, 100 W). Floating and plasma potential are indicated. (Right) Theoretical I-V course for a planar (p), cylindrical (c) and spherical probe (s) [9].

As indicated by the red shading in figure 4.1, the I-V characteristic can be divided into three parts:

> **1. Ion saturation regime:** For high negative voltages, the electrons are repelled from the probe and only ions can reach it. The measured current is the ion saturation current $I_{i,sat}$. In theory, this is constant for even higher negative potentials. However, with higher negative potentials, the sheath expands, making it possible for more ions to be collected.
>
> **2. Electron retardation regime:** With more and more positive potential electrons start to reach the probe. The point where the net current to the probe is $I_p = 0$ A is the floating potential Φ_{fl}. The electron current rises exponentially until it reaches an inflexion point. The probe has the plasma potential Φ_{pl}.
>
> **3. Electron saturation regime:** The high positive potential of the probe only allows for electrons to reach it. The measured current at the plasma potential is the electron saturation current $I_{e,sat}$.

To be able to determine the plasma parameters mentioned above from the I-V characteristic, a model is needed to describe the measured current depending on the applied voltage. For this, an ideal gas is assumed with its particles having a Maxwellian distribution of their velocities.

If the probe potential Φ_p is highly negative with respect to the plasma potential, only ions with Bohm velocity v_B (equation 2.12) can reach it. The ion saturation current is given by [1]:

$$I_{i,sat} = n_{i,sh} e_0 v_B A_p \approx 0.61 n_i e_0 A_p \sqrt{\frac{k_B T_e}{m_i}} \tag{4.1}$$

A_p is the probe surface. $n_{i,sh}$ is the ion density at the sheath edge and n_i the ion density in the unperturbed plasma. This gives a relation with which the ion density can be calculated if electron temperature T_e and $I_{i,sat}$ are known. In contrast to the ions which reach the surface with the same directional velocity, electrons can only reach the surface if their kinetic energy is sufficient to overcome the potential barrier of the applied voltage, $E_{kin,e} \geq -e_0 V_p$. The direction in which electrons reach the surface is put as z-direction. So it applies:

$$E_{kin,e} = \frac{1}{2} m_e v_z^2 \geq -e_0 V_p \tag{4.2}$$

With this, the minimal velocity v_{min} of the electrons reaching the surface is:

$$v_{min} = \sqrt{-\frac{2e_0 V_p}{m_e}} \tag{4.3}$$

with m_e the electron mass. Using equation 2.8 and substituting the sphere surface ($4\pi v^2$) with the probe surface A_p, the electron current depending on the probe potential $I_e(V_p)$ can be calculated:

$$I_e(V_p) = -e_0 n_e A_p \int v_z f(\vec{v}) d^3 v \tag{4.4}$$

$$= -\frac{1}{4} n_e A_p \sqrt{\frac{8k_B T_e}{\pi m_e}} \exp\left(\frac{e_0 V_p}{k_B T_e}\right) \tag{4.5}$$

If the probe potential is related to the plasma potential, $V_p = \Phi_{pl} - \Phi_p$, the electron saturation current is described as:

$$I_{e,sat} = I_e(0) = -\frac{1}{e} n_e A_p \sqrt{\frac{8k_B T_e}{\pi m_e}} \tag{4.6}$$

For a planar probe, this current is theoretically constant for probe voltages higher than the plasma potential. However, if the probe is just a cylindrical wire immersed in the plasma, more and more electrons will be diverted towards the surface with rising probe voltage. This leads to a rising current which can be described using the *orbital motion limit* introduced by J. E. Allen [68]. It gives a relation between the probe radius r_p and the effective radius h_p:

$$\frac{h_p}{r_p} = \sqrt{1 + \frac{e_0 V_p}{k_B T_e}} \tag{4.7}$$

h_p is the effective radius of the sectional plane within which an electron will reach the surface of the probe. Multiplying equation 4.7 with the electron saturation current yields the electron current beyond the plasma potential:

$$I_e(V_p \geq \Phi_{pl}) = I_{e,sat} \sqrt{1 + \frac{e_0 V_p}{k_B T_e}} \tag{4.8}$$

Using these considerations, the electron and ion density, floating and plasma potential and electron temperature can be obtained using the I-V characteristic shown in figure 4.1.

The floating potential and the ion and electron saturation currents can be observed directly. The plasma potential is at the inflexion point of the exponentially rising electron current. Therefore, it is found at the maximum of the first derivative of the current. And using the exponential rise of the current in the electron retardation regime, the electron temperature can be calculated using a linear fit to the slope m of the logarithmic plot of the current. This is clear by taking the logarithm of equation 4.5:

$$\ln\left(\frac{|I_e|}{A_p}\right) = \ln\left(\frac{|I_{e,sat}|}{A_p}\right) + \frac{e_0}{k_B T_e} V_p \tag{4.9}$$

With the electron temperature T_e and the ion saturation current, the electron and ion densities (assuming that $n_e = n_i$) can be calculated using equation 4.1.

When the LP is operated in an rf plasma, the rf voltage will superimpose on the measured current. The plasma potential fluctuates with the frequency of the rf amplitude and the floating potential will be shifted by roughly the amplitude to a more negative value. In this work, this is compensated using a passive pick-up electrode. It consists of an additional wire connected to a series of four parallel resonant circuits. Each circuit consists of an inductor (2.2 μH) and a changeable capacitor ($5.5 - 20$ pF). The first two circuits are used to compensate for the fundamental wave of the rf voltage (13.56 MHz) and the other two for the first harmonic (27.12 MHz). This enables the pick-up electrode to resonate with the rf. The probe wire and pick-up electrode are additionally coupled by a capacitance of 10 pF to avoid current flow from the probe to the pick-up electrode.

4.1.2 The retarding field energy analyser

The principle of the retarding field energy analyser (RFEA) is relatively simple. The energy distribution of charged species is obtained by extracting them from the plasma and measuring the resulting current after they passed a retarding field (potential barrier). First and foremost it is used to measure the ion energy distribution (IED). A multigrid system of three (or sometimes four) grids plus a collector is used to discriminate ion flux depending on the applied voltage sweep. This is schematically shown in figure 4.2.

The orifice faces the plasma and allows a sample of the ions arriving through the sheath into the RFEA for analysis. The entrance grid G1 (screen grid) has a sufficiently high negative bias to prevent plasma electrons (and also negative ions if present) to enter the RFEA. A positive voltage sweep U_{scan} is applied to the discriminator grid G2 (scan grid). Here only ions with enough kinetic energy can overcome the potential barrier formed by the applied voltage $\Phi_{scan} = q(U_{scan} - \Phi_{pl})$ [69]. The ion flux passing the scan grid is measured at the collector plate C. It has a small negative

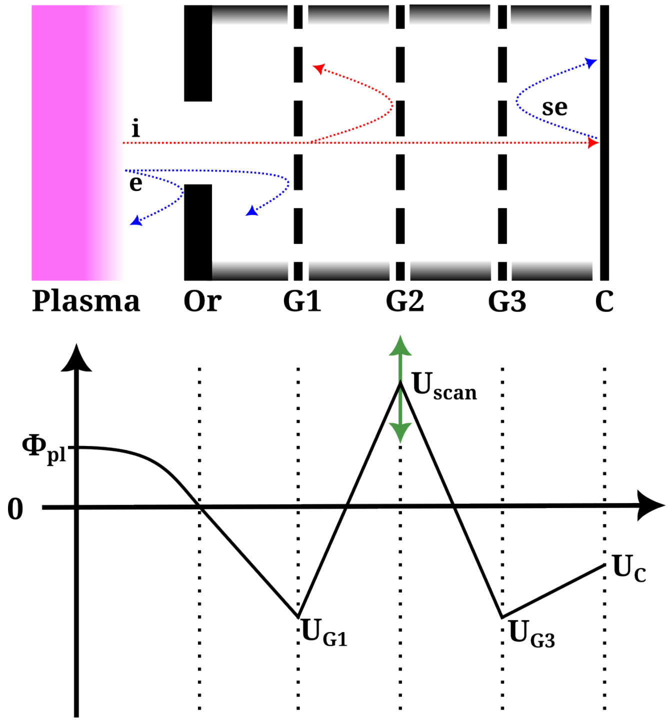

Figure 4.2: (Top) Schematic drawing of the grid constellation of a typical RFEA system with possible paths of ions (i) and electrons (e) and secondary electrons (se) emitted from the collector. (Bottom) Respective biasing scheme applied to the individual grids.

bias to draw ions towards it but not accelerate them too much to cause secondary electron emission. Still, upon impact, the ions can have sufficient energy to cause secondary electron emission from the collector [70]. The SEs are diverted back to the collector by grid G3 (SE repeller) in order not to distort the measured current. It also ensures that no SEs coming from the scan or screen grid are detected by the collector. The SE repeller, therefore, has to be more negatively biased than the collector and at least as negative as the screen grid. Sometimes it is advisable to use a grounded fourth grid G0 in front of the screen grid. It can be used to reduce the sampling area open to the plasma and minimize the disturbance to the sheath electric field.

The IED can be obtained by differentiating the collector current measured in dependence of the scan grid voltage [71]. Figure 4.3 shows exemplarily the current-voltage characteristic and the resulting IED obtained by differentiating the current. For low scan grid voltage, all ions can pass to the collector. With rising scan grid voltage the ions are repelled until the current goes to zero. The first derivative of the current yields the IED.

With appropriate bias of the grids, it is also possible to examine negatively charged

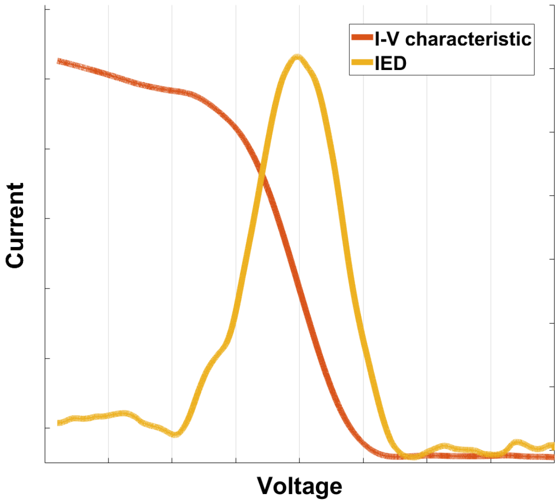

Figure 4.3: Exemplary measurement of the I-V characteristic and its derivative yielding the ion energy distribution (IED).

species. By repelling the ions with a positive screen grid voltage and applying a negative voltage sweep at the scan grid, electron energy distribution can be obtained. In plasmas generated with electronegative gases, one would get electrons and negative ions. To separate the electrons from the ions, a magnetic field in front of the orifice can be used to deflect the electrons and hinder them from entering the RFEA [72].

Chapters 6 and 7 will go into more detail regarding the design of the probe itself, the electronics and software used for the measurements and the software used to evaluate the data. In these chapters, the combination of the RFEA with a passive thermal probe is also presented.

4.2 Thermal probes

Thermal or calorimetric probes are used for the characterization of the energy balance of surfaces. There are heat flux probes used mostly in astrophysics [73, 74] and nuclear fusion devices [75, 76] and thin-film calorimeters that consist of a highly sensitive piezoelectric resonator with a good thermal conductivity that exhibits a change in electrical resistance or temperature in response to energy deposition. It detects phase transformation temperatures and enthalpies of thin films [77, 78]. At the same time, they can serve as substrates for a thin film to be examined. Another example is Gardon sensors [79] which uses the temperature change of a membrane exposed to a heat source and deduces the total energy flux towards it [80].

The principle of the passive thermal probe as it is used in this work was first introduced as a plasma diagnostic by Thornton in 1978 [49]. It utilizes a substrate surface that is exposed to an energy source (plasma). Attached to it is a thermocouple that detects a temperature change in the substrate in relation to the net power coming from the plasma. With this, a total energy flux towards the substrate can be determined.

The passive thermal probe

The passive thermal probe (PTP) as it was developed by Kersten [81] and later refined in the workgroup Plasmatechonogie [82] has been proven a versatile tool in a great variety of different plasma environments and applications. From rf plasmas [83] to ion beam sources [24], dcMS experiments and HiPIMS [84] to atmospheric plasma jets [85] and surface dielectric barrier discharges (DBD) [86] and even a gas aggregation source [87] it allows for a broad understanding of the energy balance at surfaces exposed to all kinds of different energy sources and species. The ability to bias the probe with an external voltage also allows for the distinction between charge carriers and their respective energy flux as well as the detection of SEE as was done in a plasma immersion ion implantation (PIII) experiment [88]. Most recently an atmospheric pressure DC microplasma discharge has been developed for in-situ TEM diagnostics where two PTPs are used as anode and cathode, respectively, to measure the power transferred to the electrodes [89, 90].

The measurement principle, as well as the design, electronics and software utilized with this plasma diagnostic, has been covered in many peer-reviewed articles, including the four publications pertaining to this work, and also PhD theses from our working group [91]. For a comprehensive description of the mathematical model as well as the design, measurement principle, calibration of the probe and evaluation of the acquired data the reader is referred to the PhD theses by F. Haase and S. Gauter [92, 93].

Because of the wide coverage of this probe, the description of it will not go into too much detail regarding the underlying mathematical model and evaluation methods. Especially, since the measurement and evaluation principle is described in the following chapters within the publications. However, to give the reader a basic understanding of how it works, prior to presenting the results of different studies, the following elaborations are made.

A type K thermocouple is spot welded to the back of a substrate dummy which usually is a copper platelet with an 11 mm diameter and a 100μm thickness, depending on the operating conditions. Additionally, a shielded copper wire is also spot welded in order to bias the probe. This is necessary for calibration and sometimes useful for measurements as charged species can be kept away from the probe. The ability to bias the probe also opens up new opportunities in its usage. It can be used as a planar Langmuir probe (as done in publication 1). Later it will be shown in chapter 6 and

7 that it can be used as the collector in an RFEA system opening up a whole new understanding of the energy balance of species in different plasma environments.

The substrate platelet, thermocouple and bias wire are housed in a stainless steel container with the front of the substrate facing the plasma. The setup is shown schematically in figure 4.4. If the power source is switched on, i.e. the plasma ignited, all the particles, radiation and surface processes discussed in chapter 2 will lead to a change in enthalpy H of the PTP. Enthalpy is a measure of the total amount of energy or heat stored in a thermodynamic system. By adding more power P_{in} to the probe than subtracting from it (P_{out}), its temperature rises. The temperature rises as an integral energy flux of mostly particles (depending on the examined plasma environment) arrives at the probe. This is called the heating phase.

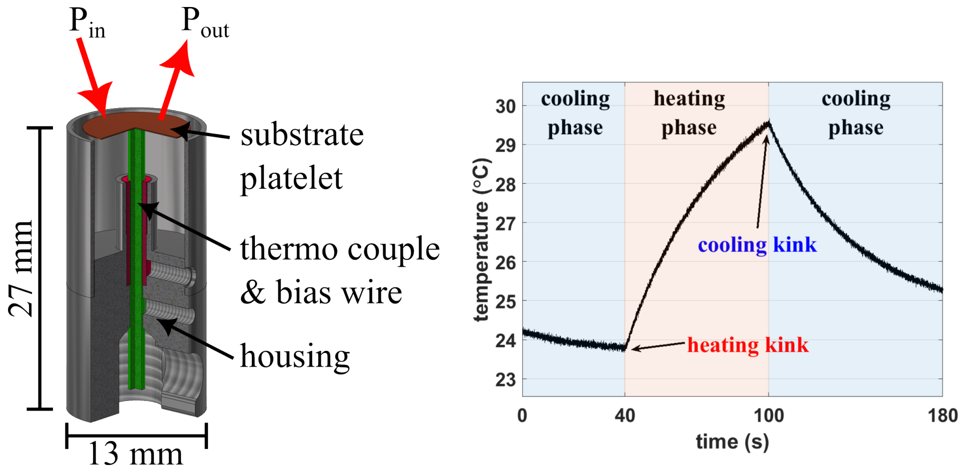

Figure 4.4: (Left) Schematic drawing of the PTP showing substrate, thermo couple and bias wire and the stainless steel housing which can be mounted orthogonally or perpendicularly. (Right) Example of a typical temperature course during measurements. The heating kink and cooling kink mark the time of 'plasma on' and 'plasma off', respectively.

The energy flux can be separated in contributions by the kinetic energies of the particles, line radiation and surface processes like absorption or particle emission which can change instantly when the plasma is turned off or its parameters are changed. Furthermore, heat conduction and heat radiation contribute to the energy flux but in a more continuous fashion, as they are more dependent on the temperature of the probe itself rather than time. This will be beneficial when evaluating the temperature course which is shown on the right in figure 4.4.

When the power source is switched off, the probe cools down. Hence, this is called the cooling phase. The change in temperature over time, given that the power source is constant, is dependent on the energy flux density coming towards the probe as well as the heat capacity of the probe. The heat capacity of the probe is calibrated in an electron beam experiment especially designed for this purpose. A detailed description of it is given in [82]. By evaluating the temperature course the integral energy flux density can be determined. The evaluation can be done by looking at the two phases separately.

The onset of the plasma exposure marks a sharp, exponential rise in temperature. This is called the heating kink. When the plasma is switched off or the probe is moved away from the power source, a sharp drop in temperature occurs. This is the cooling kink. With these distinct points in the temperature course, it can be separated easily as is shown in figure 4.4.

There are mainly two ways to evaluate such a temperature course. Either one looks at short time periods around the two kinks and uses a linear fit to determine the temperature changes in the two phases. This allows for the examination of short time periods but needs a sufficient sample rate and good signal-to-noise ratio when acquiring the data. Another way is to plot the change in temperature $\mathrm{d}T$ over the temperature. The heating and cooling phases are now represented linearly and the energy flux density can be calculated directly by their distance. This method does not require such high sample rates since the evaluation regime is fairly long but therefore needs a stable environment without any changes in i.e. the plasma parameters.

4.3 Surface diagnostics

The following gives a brief overview of the surface diagnostics involved in the measurements discussed in chapter 5. Here, these diagnostics enable an ex-situ determination of the morphology, structure or surface roughness of deposited thin films and the effect of the changing of external (e.g. pressure or power) and (subsequent) internal plasma parameters (e.g. species temperature or plasma potential) had on them. Thus, providing a valuable addition to the plasma diagnostics in the determination of the outcome of plasma-surface interactions.

4.3.1 Electron microscopy

Scanning electron microscopy (SEM) and transmission electron microscopy (TEM) are popular material characterization techniques used both in industry and research.

Both SEM and TEM use a collimated electron beam accelerated by high voltages and focused via a series of electromagnetic lenses that either scan (SEM) or travel through (TEM) the examined sample.

TEM works in a way similar to conventional light microscopy. After the electron beam is transmitted through the sample it is focused onto a fluorescent screen. A limitation of TEM is the fact that the electrons have to travel through the sample which only allows for very thin samples (≤ 100 nm) and makes it impossible to examine structures on solid surfaces. Sample preparation can be very difficult and strongly affects the outcome of the image.

With SEM an electron beam is scanned across the surface of the sample. Depending on its topography and local composition the number of backscattered electrons and/or secondary electrons generated by the beam emerging from the surface changes. They are collected by an electron collector and an image is produced depending on the location of the beam. It can be used on most surfaces but typically has a lower resolution (> 1 nm) than TEM.

SEM and TEM offer complementary capabilities for plasma diagnostics and materials characterization. They enable researchers to observe plasma-affected materials at different length scales, from the micrometer range in SEM to the sub-nanometer range in TEM. By combining these techniques with other plasma diagnostics, such as spectroscopy or surface analysis, a comprehensive understanding of plasma-material interactions, plasma-induced processes and material properties can be achieved. For a more detailed description of the principle, usage and limitations the reader is referred to standard textbooks such as [94–96].

4.3.2 X-ray diffraction

High-energy X-Ray tubes or synchrotron radiation are used to investigate the diffraction pattern produced by the scattering of the X-rays from the crystal lattice of a sample. The electric field of the incoming X-Ray beam interacts with the electrons of the crystal atoms what leads to scattering The diffraction pattern allows conclusions about the arrangement of atoms and molecules in the lattice regarding their positions and distances. Other structural parameters like average grain size, crystallinity, strain and crystal defects can also be characterized. The diffraction relies on Bragg's law which describes the relationship between the angle of incidence, the angle of diffraction and the spacing of crystal planes [97]. The diffraction pattern is formed by constructive and destructive interference of the X-Rays with the sample under a specific angle Θ. Constructive interference (Bragg reflection) takes place when the phase delay between waves scattered from neighbouring planes is an integer multiple n of the wavelength λ: $n\lambda = 2d\,sin\Theta$. d is the distance between two neighbouring lattice planes in the crystal. This is appears as a peak in the diffraction pattern. By destructive interference

4.3.3 Atomic force microscopy

Atomic force microscopy (AFM) can be used on both conducting and insulating materials. It uses a sharp metal tip at the end of a cantilever to mechanically scan a sample. The tip is dragged across the surface and an atomic force F between the tip and surface deflects the cantilever by Δz: $F = C\Delta z$. These forces include Coulomb and van-der-Waals forces and quantum-mechanical repulsion on the basis of the Pauli exclusion principle. Depending on the force constant C of the cantilever the deflection is detected, often by using the back of the cantilever as a reflector for a laser beam [46]. The reflection of the laser is imaged with a photodiode array. Another way is using force sensors like utilizing a scanning tunnelling microscope tip, an interferometer or a piezoelectric element embedded in the tip [98]. However, the optical lever became the most widely used design in today's AFMs because of its high sensitivity to very small movements and cheap and easy build.

Piezoelectric components control the movement of the probe tip. There are also setups where the probe is fixed and the sample is moved beneath it. The piezoelectric components are arranged in a complex manner allowing for a displacement in the x, y and z directions. One way to operate an AFM is to drag the tip across the surface and detect its deflection. This gives an image of the topography of the surface but can also damage it. Another way is the non-contact or intermittent-contact mode where long-ranging forces like van-der-Waals are detected and the tip either hovers above the sample or oscillates with a specific frequency near the resonant frequency of the cantilever. The forces between the tip and sample shift that resonant frequency which in turn is detected and used to create an image [46].

4.3.4 Focused ion beam imaging

The focused ion beam (FIB) setup is similar to the SEM. Instead of electrons, an ion beam is used to generate a surface image. It can be operated in two ways. With a low beam current, the primary ions lead to very little emission of particles (atoms, ions and electrons) and electromagnetic radiation. These are detected to generate a surface image. The low sputter rate reduces the risk of excessive material removal and beam-induced damage. It is suitable for imaging delicate or sensitive samples, such as biological specimens, soft materials or grain growth in thin films [99]. With high beam currents, sample material can be sputtered and removed faster which makes it useful for milling, shaping and material deposition. High currents are advantageous for applications such as sample preparation for transmission electron microscopy (TEM), creating cross-sections, or fabricating microstructures on a sample surface. Most modern FIB instruments are supplemented with an additional SEM column to become a versatile "dual-beam" setup used for imaging, material removal and deposition [100].

5 Experiments in magnetron sputtering discharges

In collaboration with the Faculty of Engineering, three measurement campaigns were conducted comprising different magnetron sputter discharges used for thin film deposition of complex film structures, requirements and geometrical setups. The following chapter is divided into three parts by the publications that came out of these studies. In all three studies, a PTP was used to measure the energy flux density to the substrates in different geometrical setups and discharge conditions. The measurements once more show the versatility and flexibility of the probe, especially in connection with surface diagnostics revealing the correlation between morphological, topographical and structural variances and the energy balance at the substrate. In publication 1 the PTP was also used as a planar Langmuir probe yielding additional information about the plasma parameters and their spatial distribution across the target area and their influence on the thin film deposition.

Publications 1 and 2 pertain to very specific applications in the field of functional thin film deposition. In the first one, the switching mechanism of the metal oxide layer in a memristive device is studied in dependence of the location on the 100 mm Si wafer the films are deposited on and the plasma parameters during reactive DC magnetron sputtering. In the second publication, superconducting thin niobium nitride (NbN) films are studied by systematic power, pressure and distance variation. The superconducting properties of the films are correlated to these variations and the change in plasma parameters and energy balance they bring with them. Publication 3 is a more general study of the spatially resolved energy flux density coming from a tilted DC magnetron sputtering device where 4 targets are located rotationally symmetrical and with a fixed angle of 45° above a circular, rotating substrate with a 200 mm diameter. The film properties of copper (Cu) and nickel-titanium (NiTi) thin films deposited across the substrate area can directly be correlated to the respective energy flux density and resulting deposition rate.

5.1 Double-barrier memristive devices

Publication 1

Correlations between sputter deposition parameters and I-V characteristics in double-barrier memristive devices

Authors:	F. Zahari, F. Schlichting, J. Strobel, S. Dirkmann, J. Cipo, S. Gauter, J. Trieschmann, R. Marquardt, G. Haberfehlner, G. Kothleitner, L. Kienle, T. Mussenbrock, M. Ziegler, H. Kersten, H. Kohlstedt
Journal:	Journal of Vaccum Science and Technology B [101]
Technique:	Electrical diagnostic and energy flux measurements, scanning transmission electron microscopy, simulations
Own contribution:	approximately 25%

Experimental Setup:

Reactive DC magnetron sputtering was used to deposit the NbO_x thin film. An Ar/O_2 working gas mixture with 7 sccm Ar and 23 sccm O_2 gas flow was used at a total pressure of 1.21×10^{-2} mbar. The Nb target was operated in poisoned mode with an unbalanced magnetic field configuration and the discharge power was regulated to 100 W. The PTP was radially moved across the target area in steps of 10 mm and the probe-to-target distance was 60 and 80 mm.

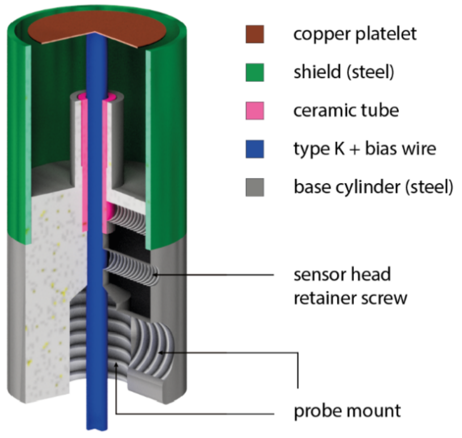

A subfigure

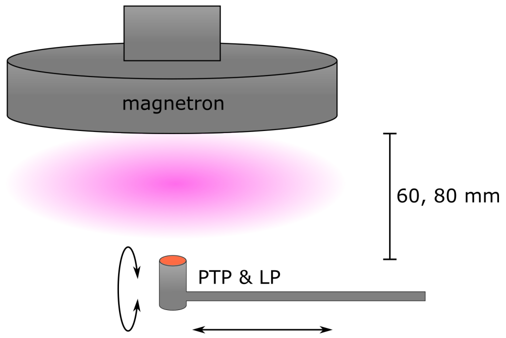

A subfigure

Motivation:

This work aimed to unravel the difference in the electrical behaviour of multiple (5336) double-barrier memristive devices produced on 100 mm Si wafers and structured within an area of 40 mm radius. These are multilayered devices with the layer sequence Nb/Al/AL_2O_3/NbO_x/Au where the niobium oxide acts as the active layer. Here, charge defects and the oxygen ions allow for switching between a high and low resistance state depending on the externally applied electric field (sweep between a positive and negative bias). The analog resistive switching mechanism was not uniform across the substrate area with a significant difference in the I-V characteristics of the devices. The desired rectifying property and hysteresis are only present within a 25 mm radius from the center of the wafer. Outside of that the devices show no hysteresis in the I-V characteristic and have a constant resistivity regardless of the applied voltage.

Main Results:

Within the inner area (25 mm radius) the floating potential resembles the resistivity pattern for positive bias. Especially the measurements in 60 mm distance can well be correlated to the electrical behaviour of the devices. The electron temperature and plasma potential increase within this area reaching a maximum at the position of the race track of the target. This increase can be correlated to the broadening of the hysteresis but does not explain it on its own because in the maximum (race track, 30 mm position) the devices have high resistance and no memristive behaviour. The measured energy flux density has a Gaussian-like shape around the center of the target and seems mainly governed by the flux of positive ions. The energy flux drops significantly towards the egde of the target. Since it plays a crucial role for film properties like stochiometry, morphology and film density, it is believed to superimpose with the other plasma parameters in order to form the desired properties of the NbO_x layer.

Additionally, scanning TEM electron energy-loss spectrometry investigations were conducted showing strong differences in the chemical structure for samples from the center and under the race track. The oxidation state is much higher in the center of the target where there is high energy flux density, floating potential and electron temperature. The oxidation state is believed to be essential for the switching mechanism. Kinetic Monte Carlo Simulations show the dependence of the I-V hysteresis on the oxidation state as well as the defect concentration within the NbO_x layer.

Correlation between sputter deposition parameters and *I-V* characteristics in double-barrier memristive devices

Finn Zahari,[1,a)] Felix Schlichting,[2] Julian Strobel,[3] Sven Dirkmann,[4] Julia Cipo,[2]
Sven Gauter,[2] Jan Trieschmann,[5] Richard Marquardt,[1] Georg Haberfehlner,[6]
Gerald Kothleitner,[6,7] Lorenz Kienle,[3] Thomas Mussenbrock,[5] Martin Ziegler,[8]
Holger Kersten,[2] and Hermann Kohlstedt[1,b)]
[1]*Nanoelectronics, Faculty of Engineering, Kiel University, 24143 Kiel, Germany*
[2]*Institute of Experimental and Applied Physics, Kiel University, 24098 Kiel, Germany*
[3]*Synthesis and Real Structure, Faculty of Engineering, Kiel University, 24143 Kiel, Germany*
[4]*Kooperation Elmos Semiconductor AG/Fraunhofer-Gesellschaft IMS, 47057 Duisburg, Germany*
[5]*Electrodynamics and Physical Electronics Group, Brandenburg University of Technology Cottbus-Senftenberg, 03046 Cottbus, Germany*
[6]*Institute of Electron Microscopy and Nanoanalysis, Graz University of Technology, 8010 Graz, Austria*
[7]*Graz Centre for Electron Microscopy, 8010 Graz, Austria*
[8]*Department of Micro- and Nanoelectronic Systems, TU Ilmenau, 98693 Ilmenau, Germany*

(Received 15 July 2019; accepted 24 September 2019; published 16 October 2019)

Sputter deposition is one of the most important techniques for the fabrication of memristive devices. It allows us to adjust the concentration of defects within the fabricated metal-oxide thin film layers. The defect concentration is important for those memristive devices whose resistance changes during device operation due to the drift of ions within the active layer while an electric field is applied. Reversible change of the resistance is an important property for devices used in neuromorphic circuits to emulate synaptic behavior. These novel bioinspired hardware architectures are ascertained in terms of advantageous features such as lower power dissipation and improved cognitive capabilities compared to state-of-the-art digital electronics. Thus, memristive devices are intensively studied with regard to neuromorphic analog systems. Double-barrier memristive devices with the layer sequence Nb/Al/Al_2O_3/NbO_x/Au are promising candidates to emulate analog synaptic behavior in hardware. Here, the niobium oxide acts as the active layer, in which charged defects can drift due to an applied electric field causing analog resistive switching. In this publication, crucial parameters of the process plasma for thin film deposition, such as floating potential, electron temperature, and the energy flux to the substrate, are correlated with the *I-V* characteristics of the individual memristive devices. The results from plasma diagnostics are combined with microscopic and simulation methods. Strong differences in the oxidation state of the niobium oxide layers were found by transmission electron microscopy. Furthermore, kinetic Monte Carlo simulations indicate the impact of the defect concentration within the NbO_x layer on the *I-V* hysteresis. The findings may enable a new pathway for the development of plasma-engineered memristive devices tailored for specific application. *Published by the AVS.* https://doi.org/10.1116/1.5119984

I. INTRODUCTION

Today's computer science is characterized by a time of upheaval.[1] The extremely successful downscaling of CMOS devices and circuit integration during the last decades will soon face physical and economical limits.[1,2] The predictable end of Moore's Law puts advanced electronic and ionic devices paired with conceptually new non-Boolean architectures, such as cellular automata, quantum computer, or neuromorphic circuits, increasingly into the spotlight of research institutions and industry.[3–8] Worldwide research activities encompass a broad spectrum of topics ranging from advanced electronic device concepts to entirely new circuit designs.

In this context, the advent of memristive devices offers opportunities to extend CMOS technology or might even lead to entirely novel computing architectures inspired by biological information pathways in nervous systems.[9–13] A memristive device in its simplest form consists of a metal-insulator-metal (MIM) capacitorlike layer structure. By applying a sufficiently large bias voltage, structural and/or electronic changes within the insulator (I) or a either metal insulator (MI) interface lead to a remnant dc device resistance, which justifies the term "memresistive."[11,14–16] We would like to emphasize that another portmanteau "memristor" as coined by Leon Chua refers to the theoretical background of the effect, i.e., to establish a fourth electric lumped circuit element, besides resistors, capacitors, and inductors.[17] Because the theoretical concept of the memristor is heavily debated, we use the (emotionally) less occupied and (experimentally) favored term "memristive" throughout the manuscript.[18–20]

During the last two decades, a plethora of different memristive MIM devices has been investigated. In recent overviews, the involved material combinations and device parameters such as layer thickness and area are summarized.[16,21] A number of

---

[a)] Electronic mail: fnz@tf.uni-kiel.de

[b)] Electronic mail: hko@tf.uni-kiel.de

2166-2746/2019/37(6)/061203/10/$30.00

mechanisms were identified, which led to a more or less acceptable explanation for the cause of the observed resistance change and memory effect. Indeed, memristive switching encompasses a broad range of different physical mechanisms.

To adapt the electrical parameters of memristive devices, such as switching voltage, high resistance state (HRS), low resistance state (LRS), or the switching dynamics, to a particular application, engineered approaches are welcome. Indeed, correlating thin film deposition parameters to the electronic interfacial structure enables the route of "memristive devices by design."

The present work focuses in particular on the correlation between plasma parameters during film deposition by sputtering and the memristive device properties. Indeed, instability and insufficient reproducibility of electrical characteristics present two major problems in deposition of material and practical use of memristive devices. The characteristics of amorphous and microcrystalline nanostructures are strongly dependent on the manufacturing technique. Common plasma techniques with their respective applications and merits to fabricate samples are plasma-enhanced chemical vapor deposition,[22–25] ion beam sputtering,[26,27] or magnetron sputtering,[28,29] respectively. Well-studied metal oxides (TiO_{2-x}, NbO_x) are typical base materials for active memristive media. The amorphous state of the resulting coatings is affected by varying the deposition temperature at unvaried intrinsic deposition rate, residual gas pressure, and obtained film thickness.

At present, NbO_x films have received growing interest because of their electrical properties, which make them suitable semiconductor materials for memristive devices[30] with the potential to be used in neuromorphic architectures.[31] One of the most important challenges for the circuit performance is the fabrication of hundreds and more similar memristive devices on one and the same substrate. Thus, the control and improvement of the plasma grown metal-oxide films is a key requirement for the development of neuromorphic circuits based on NbO_x films.

For the optimization of such sputter deposition techniques, knowledge of the energy balance at the substrate surface is important, since it significantly influences the resulting properties of the deposited films.[32,33] The energy balance is determined by heating processes caused by impinging particles, surface reactions, and incoming radiation as well as loss processes such as heat conduction and convection through the surrounding gas and by emitted radiation.[33] Calorimetric probes have been proven to be flexible and versatile tools for the characterization of energy fluxes and thermal balance of surfaces in different kinds of low-temperature plasmas (see Refs. 34–37 and references therein). The principle of the calorimetric or thermal probes being used in plasma science is based on Thornton's original design from 1978.[34] They are powerful especially in complex systems where the total energy influx is the sum of many different contributions originating from charge carriers, neutral particles, various surface processes, and radiation.[35,38] However, a quantitative calculation of all the contributions is not possible because of too many unknown variables, such as secondary electron emission and sticking coefficients, neutral particle fluxes and energy distributions, plasma radiation, etc. Various investigations concerning the energy flux in a plasma system and the different types of calorimetric probes have led to a well-understood diagnostic technique. In recent years, it has been used in many different magnetron sputtering processes, such as DC magnetron sputtering,[35] high power impulse magnetron sputtering,[36] or plasma immersion ion implantation.[37]

The magnitude of the different heating and cooling processes depends on the used deposition technique, on the deposition device and experimental conditions (gas flow, mixture and pressure, electric and magnetic field, and substrate position). Consequently, the influence of different parameters is of essential interest: gas flow rates and the resulting pressures have a strong influence on the particle energies, which determine structure and density as well as the electrical and optical properties of the deposited films.[33,39] Also, the gas composition itself has a strong effect, as it determines chemical reactions in the gas phase and at surfaces (target, substrate), which also determine stoichiometry and other properties of the films. Furthermore, the structure and strength of the magnetic field as well as the amplitude and form of the discharge have a strong impact. Last but not least, the substrate position and orientation affects the film structure and properties, because particle fluxes and plasma potentials, which determine the ion energy, may show strong spatial inhomogeneities.[35,37,39,40]

The importance of the defect concentration within filamentary based metal-oxide memristive devices has been already investigated. For example, substoichiometric HfO_x is widely used due to its CMOS-compatibility.[41,42] Adjusting the oxygen stoichiometry in HfO_x has been shown to influence the forming voltage,[43–45] the switching mode[45] (i.e., bipolar switching, unipolar switching, threshold switching, and complementary switching), and shows evidence leading toward multilevel memristive quantum devices.[45]

The aim of this work is to correlate the plasma properties with the energetic conditions at the surface which are related to structural characteristics and ultimately to electrical film properties. This can lead a way toward the plasma engineering of analog memristive devices whose properties can be adjusted with respect to the requirements of particular applications by tailoring the oxygen vacancy concentration within a metal-oxide layer.

II. METHODS

A. Device fabrication

The device fabrication, which was developed in Refs. 46 and 47, is sketched in Fig. 1. The memristive devices were deposited on 100 mm Si wafers (0.5 mm thick) passivated by 400 nm thermally oxidized SiO_2. The layers were deposited using DC magnetron sputtering without breaking the vacuum. The base pressure constituted less than 5×10^{-7} mbar. The potential of the substrate was floating with respect to the common ground of the sputtering system. The Al_2O_3 tunnel barrier was produced by sputtering an Al layer, which was thermally oxidized at room temperature. The NbO_x was sputtered in a reactive Ar/O_2 gas mixture with a total pressure of

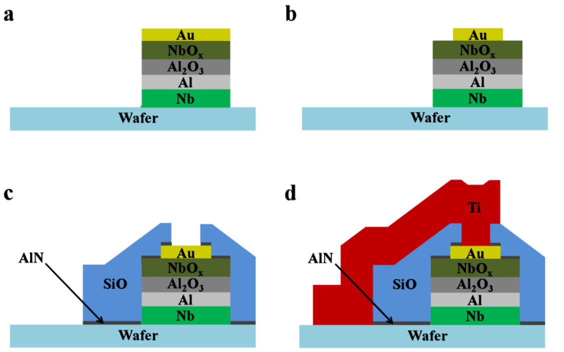

FIG. 1. Sketch of the production steps of one device (described in more detail in Refs. 46 and 47). (a) Sputtering of all layers and subsequent lift-off process. (b) Etching of the Au top electrode. (c) Insulation: sputtering of AlN as an adhesion promoter for the subsequent evaporation of SiO. (d) Sputtering of Ti wiring. To contact the bottom electrode, its area is bigger than the area of the other layers.

1.21×10^{-2} mbar in poisoned mode (7 sccm Ar, 23 sccm O_2) using an Nb target with an unbalanced magnetic field configuration, and the discharge power was regulated to 100 W. The distance between the target and the substrate was adjusted to 53 mm during NbO_x deposition. The device patterning was performed by standard optical lithography and lift-off processes [cf. Fig. 1(a)]. The device area was defined as 400 μm^2 by etching the Au top electrode in potassium iodide [cf. Fig. 1(b)]. For the subsequent deposition of 720 nm SiO by thermal evaporation, a 10 nm thin AlN layer was sputtered as an adhesion promoter [cf. Fig. 1(c)]. These layers serve as an insulation layer for the following sputtering of Ti wiring [cf. Fig. 1(d)]. The area of the Nb bottom electrode is bigger than the area of the other layers and it is covered with Ti wiring as well, so that it can be easily contacted.

B. Measurement of plasma parameters

To measure the internal plasma parameters during NbO_x deposition, a planar probe was used in two measurement modes, namely, as a passive thermal probe (PTP)[34,35] and as a Langmuir probe (LP).[48,49] The probe consists of a sensor copper plate with a diameter of 11 mm and a thickness of 100 μm [cf. Fig. 2(b)]. On the back, a type K thermocouple for temperature measurement (40 μV/K) and a copper bias wire were spot-welded. A stainless steel shield surrounds the probe to restrict the measurements of energy flux toward the normal plane. The wires are placed upon a base cylinder, which can be mounted on a vacuum feed-through. Furthermore, the cables are fed through the base via a ceramic tube. This updated design was recently developed.[35] In Fig. 2(a), the experimental setup to measure the plasma parameters is sketched. To get the radial distribution beneath the target, the probe was mounted on a moveable rod and introduced into the vacuum chamber by a vacuum flange. Starting in the center of the sputtering target, the probe was moved to one edge and back through the center to the other edge and back to the center again, enabling to measure each

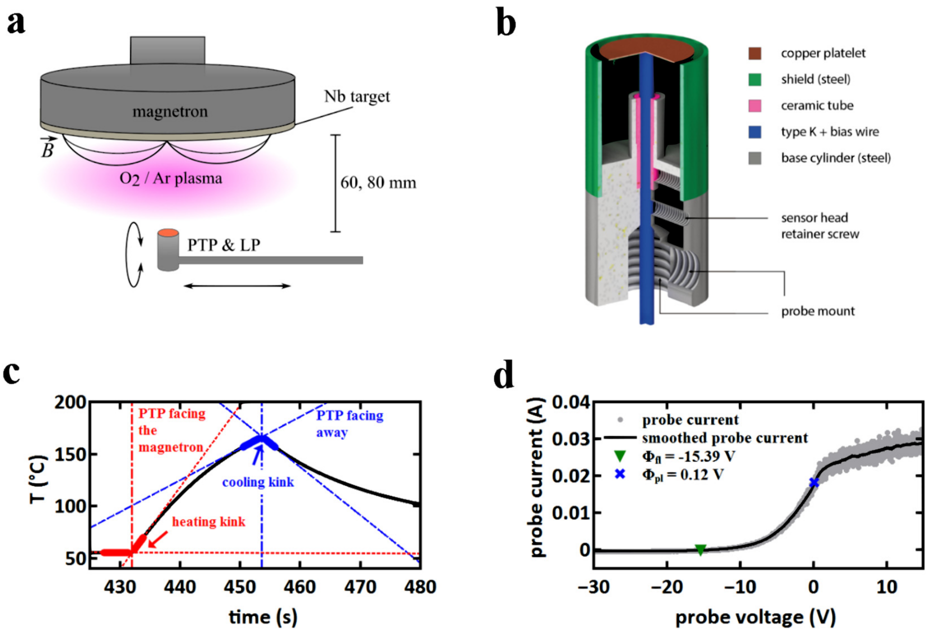

FIG. 2. Measurement of the plasma parameters: (a) Experimental setup of *in situ* measurement. (b) Probe design [used with permission from S. Gauter, F. Haase, and H. Kersten, Thin Solid Films **669**, 8 (2019)]. (c) Example of a passive thermal probe measurement curve at 0 mm radial position and 60 mm target to probe distance (measurement: black soild line, asymptotes of heating/cooling kink: red/blue doted/dashed lines, respectively) (d) Example of an *I-V* curve of a Langmuir probe measurement at 0 mm radial position and 60 mm target to probe distance (measured current: grey dots, smoothed current: black solid line, evaluation of floating potential and plasma potential: green triangle and blue cross, respectively).

position twice (the center position three times) to allow for the detection of possible parameter drifts.

Upon exposure to an energy flux, the probe surface temperature T_S rises (heating phase), whereas it falls when the plasma is switched off (cooling phase), as is shown in Fig. 1(c). The overall change in enthalpy $\dot{H}$ and the resulting change in temperature $\dot{T}_S$ by these two phases can be described by[38]

$$\dot{H}_h = C_s \dot{T}_{s,h} = P_{in} - P_{out,h}, \tag{1}$$

$$\dot{H}_c = C_s \dot{T}_{s,c} = -P_{out,c}, \tag{2}$$

with the heat capacity of the probe C_S and the incoming power P_{in} during the heating process. Because it can be assumed that the outgoing power (heat loss) during both phases is equal ($P_{out,h} = P_{out,c}$), the above equations can be combined to calculate the incoming power to the probe,

$$P_{in} = C_s(\dot{T}_{s,h} - \dot{T}_{s,c}) = -P_{out,h}. \tag{3}$$

Therefore, the incoming energy flux J_{in} to the probe is

$$J_{in} = \frac{C_s}{A_s}(\dot{T}_{s,h} - \dot{T}_{s,c}), \tag{4}$$

where A_S is the surface area of the probe. The assumption $P_{out,h} = P_{out,c}$ is valid only for environments where the energy flux coming from sources other than the investigated heat source is constant during measurements. This can be achieved by evaluating only short time periods. For the executed measurements, the kink-method[35] was chosen, whereby a linear fit is used for the heating and the cooling kink as exemplarily demonstrated in Fig. 1(c). Further, the slopes of the two linear fits can be subtracted, obtaining $\dot{T}_{S,h} - \dot{T}_{S,c}$. Since the other two parameters of Eq. (4), namely, the heat capacitance C_S (0.03 J/K—calibrated with an electron beam before the measurements were performed) and the probe area A_S (95 mm^2), are known, the incoming energy flux J_{in} can be calculated. A detailed description of the evaluation methods of the PTP measurements is given in the literature.[35] During the measurements, the plasma source was constantly operating. The heating and cooling phase of the PTP were realized by facing the magnetron and turning the probe 180° away from the source, respectively. A 20 s heating phase (probe facing the target) was followed by a 20 s cooling phase (probe facing away from the target). The potential of the PTP was floating with respect to the common ground of the sputtering system.

It was also possible to use the PTP as a planar Langmuir probe.[38] By the additional bias wire, a voltage sweep was applied to the probe while the current was measured. From the *I-V* Langmuir probe characteristic, the floating and plasma potential, Φ_{fl} and Φ_{pl}, the electron temperature T_e, and the current of positively charged ions to the probe can be determined. There are different methods to evaluate LP measurements. In this work, the electron temperature was acquired using a semilogarithmic plot of the *I-V* curve [cf. Fig. 1(d)]. According to the probe theory,[50] T_e is found as the slope of a linear fit of the curve. The plasma potential is determined as the maximum of the first derivative, and the floating potential is the zero crossing of the Langmuir curve. Furthermore, using the resulting electron temperature in combination with the Bohm-sheath criterion, the current density j_{ion} of positive ions can be calculated.[51] For each measurement with the Langmuir probe, the voltage was swept in 3 s from −30 V to +15 V.

The radial scans using the LP and the PTP were obtained at two target-to-probe distances of 60 and 80 mm, respectively.

C. Transmission electron microscopy

Scanning transmission electron microscopy (STEM) investigations were conducted on a monochromated and spherical aberration corrected FEI Titan^3 60–300 at the Graz Centre for Electron Microscopy equipped with a GIF Quantum spectrometer for electron energy-loss spectrometry (EELS). The acceleration voltage during investigation was 300 kV with an approximate dose rate of 10^6 e nm^{-2} s^{-1}. High-resolution transmission electron microscopy (HRTEM) was used to record real space images of the layers on a FEI Tecnai G^2 Stwin microscope with an acceleration voltage of 300 kV. Samples were prepared via scanning electron microscopy based focused ion beam milling in a Fischione Model 1040 NanoMill® system and refined by low-energy argon ion polishing.

D. *I-V* measurements

All *I-V* measurements were performed on a HP 4156A parameter analyzer. Voltage was applied to the top electrode while the bottom electrode was grounded. The current was measured simultaneously. The resistance values were computed by utilizing Ohm's law. All 5336 devices on one wafer were measured by using an automatic probe station with the result that the *I-V* characteristics can be evaluated dependent on the position on the wafer.

E. Simulations

The kinetic Monte Carlo (kMC) simulation of the conceptual device was performed as described in Ref. 52. The device is mimicked by the layer sequence Al/Al_2O_3/NbO_x/Au taken from the actual experiment. We assume that the NbO_x layer can be modeled as an ionic/electronic mixed conductor. It is depicted as a solid-state electrolyte in which mobile negative oxygen ions can drift under the influence of an electrical field. Of course, charge neutrality has to be guaranteed within the simulation domain. Therefore, the mobile negative oxygen ions are compensated by immobile stationary positive oxygen ions (O^{2+}). These positive oxygen ions are distributed randomly within the NbO_x layer. In fact, it is this defect distribution and concentration that ultimately controls the *I-V* characteristics of the device. The *I-V* characteristic itself is calculated from a lumped element circuit model that consists of three distinct elements: (1) a tunnel barrier (the Al_2O_3 layer) described by a voltage controlled current source based on Simmons formula,[53] (2) the NbO_x/Au interface which is described by the Schottky contact model,[54] and (3) the NbO_x

layer which is modeled as an ohmic resistance depending on its inner atomic structure.[52] As mentioned above, within the latter, the transport of ions under the influence of the externally applied electric field and the Coulomb field due to the ions themselves is of particular importance. The transport is calculated using a kMC approach in which the most important processes are taken into account, i.e., diffusion of negative oxygen ions within the solid-state electrolyte as well as adsorption and desorption at the respective interfaces of the layer.

The two distinct models, i.e., the lumped element circuit model and the kMC model, are consistently coupled in such a way that Kirchhoff's voltage and current laws for the circuit model are satisfied at all instances of time. Applying Kirchhoff's current law, which states that the current through the device is constant, the individual voltage drops across the tunnel barrier and the Schottky contact and the current itself can be calculated.

III. RESULTS AND DISCUSSIONS

A. Double-barrier memristive devices

The investigated double-barrier memristive devices consist of the layer sequence Nb/Al/Al_2O_3/NbO_x/Au.[46] The ultrathin memristive layer (2.2 nm) is bounded between a Schottky-like contact to the Au top electrode and an Al_2O_3 tunnel barrier (1.3 nm). A characteristic *I-V* curve can be seen in Fig. 3(c) with a typical hysteresis, a high *I-V* nonlinearity, and a great rectifying property. Here, a linear voltage sweep was applied to the top electrode, while the bottom electrode was grounded. By applying a positive bias, the resistance decreases and the LRS can be reached. The resistance can be changed by more than two orders of magnitude for a read voltage V_R of 0.5 V. To reset the device to the HRS, a negative voltage has to be applied. The switching occurs gradually so that an analog switching is performed. The resistance change is assumed to be based on oxygen ions (or vacancies) moving according to the electric field. Furthermore, interfacial trap states may be filled and emptied during the switching process. Hence, the interfacial properties [e.g., energy barriers, density of states (DOSs), and barrier thicknesses] at the Schottky-like contact and at the tunnel barrier are varied. Thus, the functionality of the devices is based on interfacial processes rather than on filaments produced and ruptured during switching. Therefore, there is no electro forming needed, and the current distribution is highly uniform over the device area. The physical mechanisms of this analog switching have been described in

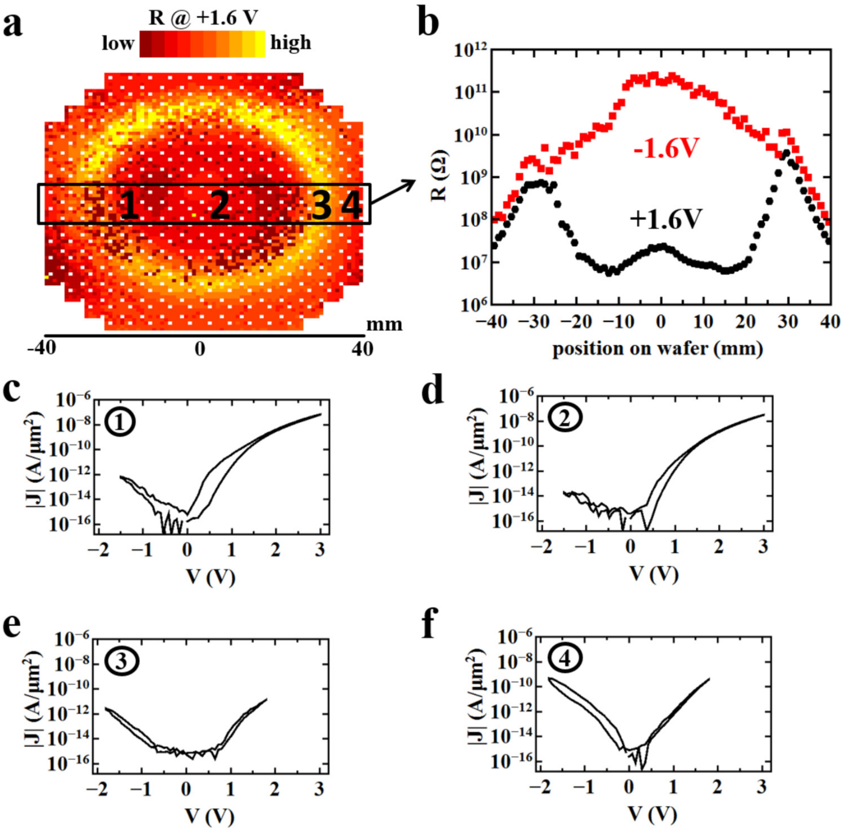

FIG. 3. Electrical characterization of double-barrier memristive devices at different positions on the wafer: (a) Resistance map of a whole wafer measured at 1.6 V ($VR = 1.6$ V). (b) Resistance of devices dependent on radial position (black dots: $VR = +1.6$ V; red squares: $VR = -1.6$ V). (c)–(f) *I-V* curves at different radial positions 1 to 4 (−25, +5, +30, and +35 mm).

previous publications in more detail.[46,52] It is worth mentioning that significant switching takes place only when the voltage exceeds a threshold of about 2 V. Furthermore, it is favorable to integrate memristive devices in dense crossbar arrays to realize neuromorphic networks in hardware.[55] This requires a strong non-linearity in the *I-V* characteristics or an additonal acces device for each integrated memristive device decreasing the density of the network.[56] Moreover, the voltage drop accross the wires in big arrays can lead to failures in the filament formation, i.e., in the electro-forming, of filamentary-based memristive devices. However, it has been shown in Ref. 31 that the integration of double-barrier memristive devices in selector-less crossbar arrays is possible. This is founded in the high *I-V* non-linearity, the recification property and no required electro-forming.

This work focuses on the deposition conditions during the NbO_x DC magnetron sputtering and correlates the plasma parameters to the resulting electronic properties of the devices. Thereby, a new pathway for the development of plasma-engineered analog memristive devices shall be enabled. The layers are deposited on a 100 mm wafer and structured within an area of 40 mm radius. In Fig. 3(a), the resistance map for a read voltage of +1.6 V is shown. Here, 5336 devices with a contact area of $400\,\mu m^2$ are measured. The inner red circle, which has a radius of about 25 mm, has a relatively low resistance for the positive bias. In this area, the devices are working, as described above. Typical *I-V* curves are shown in Figs. 3(c)–3(d). Here, the analog *I-V*-hysteresis and the rectification are existent. The rectification is also shown in Fig. 3(b) in dependence of the radial position on the wafer. Therein, the resistance values averaged over ten devices for each position for $V_R = +1.6$ V (black squares) and $V_R = -1.6$ V (red dots) are plotted. A difference in the resistance of up to four orders of magnitude for positive and negative biases in the radial positions from −25 to +25 mm is apparent. Defective devices, i.e., those that are short circuited or not properly connected to the wiring, and the test structures [gray squares in Fig. 3(a)] are not taken into account for averaging. The yellow ring in Fig. 3(a), starting at about 30 mm away from the center, contains devices with a relatively high resistance. As can be seen in Fig. 3(e), the *I-V* characteristics differ significantly from the devices in the center (i.e., no rectification and no hysteresis). In this area, the race track of the magnetron is located. In the outer red area, the *I-V* curves are as shown in Fig. 3(f). Here, the resistance is rather low, but no rectification and no hysteresis are apparent. The voltage is swept to lower positive values in the outer areas compared to Figs. 3(c)–3(d), because the devices are burning out for higher voltages here. In the following, the radial positions −25, +5, +30, and +35 mm are denoted as positions 1, 2, 3, and 4, respectively [cf. Fig. 3(a)].

B. Plasma parameters

To correlate the internal plasma parameters during NbO_x deposition to the electrical properties of the memristive devices, the energy flux to the substrate [Fig. 4(a)], the electron temperature in the plasma [Fig. 4(b)], the floating potential of the substrate [Fig. 4(c)], the plasma potential [Fig. 4(d)], and the current of the positively charged ions flowing to the probe [Fig. 4(e)] were recorded. The

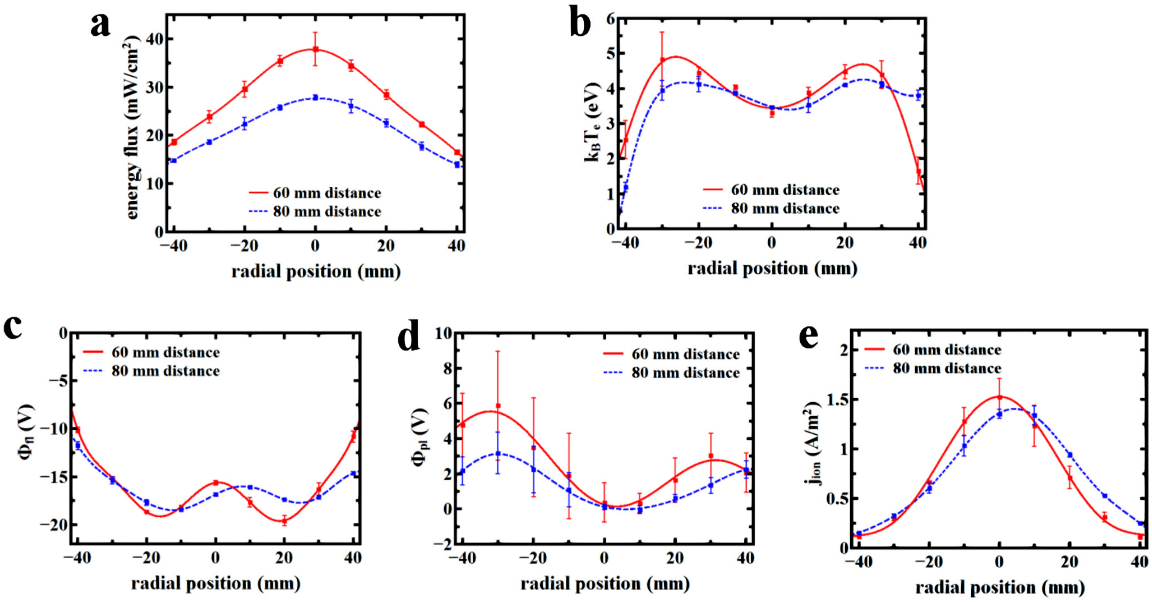

Fig. 4. Plasma parameters dependent on the radial position-the mean values and the standard deviations obtained from the two measurement points for each position (three for the center position) are depicted (squares with error bars). The solid and dashed lines show fits of the mean values (60 and 80 mm target to probe distance, respectively). (a) Energy flux, (b) electron temperature, (c) floating potential of probe, (d) plasma potential, and (e) current of positive ions.

rectification shown in Fig. 3(b) is compared to these plasma parameters. In the case of the double-barrier memristive devices investigated, the rectification is a sufficient condition for memristive behavior. In general, the shape of the floating potential, the plasma potential, and the electron temperature [especially for a distance of 60 mm—red curves in Figs. 4(b)–4(d)] can be correlated to the electronic device behavior for radial position between −25 and +25 mm. In particular, the floating potential resembles the resistivity for positive bias voltage. It varies between −20 V in the center and about −15 V at the edge of the inner area. Within this inner area, the increasing electron temperature and the decreasing floating potential toward the edge of the wafer are correlated additionally to the broadening of the *I-V* hysteresis [cf. Figs. 3(c) and 3(d)]. In the center, the electron temperature constitutes 3.5 eV, while for a more pronounced hysteresis at −25 mm radial position, the electron temperature constitutes almost 5 eV. Also, the plasma potential varies between 1 V in the center and up to 6 V at the edge of the inner area. Having a closer look at the electron temperature and the plasma potential, it is found that their maxima are right at the position of the race track. Here, however, the devices have a relatively high resistance and no memristive behavior. Thus, the increasing electron temperature and plasma potential do not explain the broadening of the *I-V* hysteresis by themselves but other effects have to be taken into account.

In contrast to the hitherto mentioned parameters, the energy flux and the current of positive ions have a Gaussian-like shape centered at the center of the wafer. The Gaussian shape of the positive ions j_{ion} is typical for an unbalanced magnetron and is reflected by the energy flux. It is known that the energy at the substrate surface during sputter deposition plays a crucial role for film properties like film density, stoichiometry, morphology, etc.[32,33,39] The energy decreases from the center (37.5 mW/cm^2) to ±25 mm radial position (27.5 mW/cm^2) by 27%. It drops almost linearly with increasing distance from the center down to 18 mW/cm^2 at the edge of the investigated area. We believe that the effect of energy superimposes with the other plasma parameters to form the NbO_x in the needed properties (e.g., oxidation state and defect concentrations). This is supported by analyzing the electron temperature and the floating potential at a radial position of around 35 mm. Both parameters show values comparable to those closer to the center of the target. Nevertheless, the electronic behavior [cf. Fig. 3(f)] differs strongly from those devices in the center of the wafer [cf. Figs. 3(c) and 3(d)].

Another important parameter for the film growth in a reactive sputter deposition process in an electronegative gas is the density of negatively charged ions. Since more than 75% of the process gas is O_2, the target surface gets completely poisoned. This leads to the formation of negative oxygen ions. These negative oxygen ions are accelerated by the electric field toward the substrate, hitting it at an angle of almost 90° for uneroded targets. This can cause crystallographic defects or stress in deposited films due to the high energy of the ions.[40,57] Further, the radial distribution, the energy, and the impinge angle of these negative ions depend on the erosion state of the target and the discharge voltage. The geometrical influence of the target on the nonuniformity of the resistivity of thin oxide films has been studied in Refs. 40 and 58. The correlation between the target age (i.e., the erosion at the race track position) and the radial distribution of the negative ions has been confirmed, and the changed electrical properties of the thin films have been traced back to the negative ions causing radiation damage to the deposited films. This might lead to defects within the amorphous NbOx film. Even though there is no long-range order in amorphous films, defects like dangling bonds or those comparable to vacancies and interstitials in crystalline structures are possible, for example.[59] It is also conceivable that resputtering is induced by heavier negative Nb ions. In Ref. 60, the existence of negatively charged metal ions within a plasma sputtering process and the possibility of building negative metal ion sources by this method is shown. Since the formation probability of Nb^- ions is lower than that of the negative oxygen ions, one can disregard the effect of the negative metal ions in the present study.[57] Furthermore, the existence of stable NbO_x^- ions within a vacuum process is discussed in Ref. 61, but the probability of their formation is expected to be much lower like it is experimentally shown in Ref. 62 for several reactive sputtered metal oxides like ZnO_x and InO_x. Thus, the impact of negatively charged ions, especially oxygen ions, might influence the electronic behavior of the devices shown in this publication as well. In particular, the devices underneath the race track (i.e., at 30 mm radial position), which show no memristive behavior, might be affected by the negative ions. In addition, the pressure of the deposition is rather high, i.e., 1.21×10^{-2} mbar, leading to a mean free path of less than 1 cm. Thus, several scattering events can be expected during material transport to the substrate. Nevertheless, the energy and material transport is dominated by the magnetic and electric fields as can be seen in the plasma parameters which show the expected qualitative behavior of an unbalanced magnetron source.

C. Transmission electron microscopy

In order to investigate how the different plasma characteristics affect the deposition of Nb oxide, HRTEM and STEM-EELS investigations of the deposited layers were conducted. To this end, samples were extracted from the center of the wafer (position 2) and from a position beneath the race track (comparable to position 3), where the device resistance was found to be higher and where the devices lost their rectifying and memristive characteristics. In Fig. 5, real space images recorded by HRTEM and an elemental map of the Nb-M_{45} edge extracted from a STEM-EELS spectrum image are shown for both samples. In both cases, the deposited layers present themselves as smooth uniform thin films with a surface roughness well below 1 nm. The determined thickness for the NbO_x layer extracted from the center is around 2.2 nm, while the layer extracted from the edge of the wafer has a thickness of 2.1 nm, both with a standard deviation of about 0.2 nm. Accordingly, the observed difference in

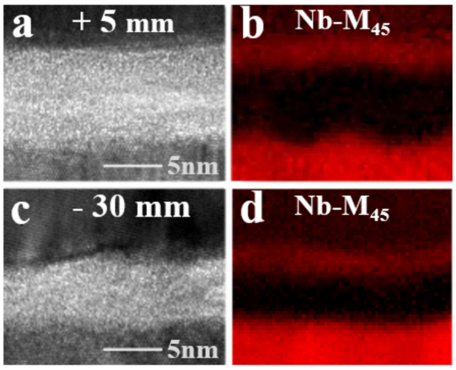

Fig. 5. Real space imaging of the deposited layers: Layers at the center (position 2) of the wafer imaged by HRTEM (a) and STEM-EELS showing the distribution of Nb through the Nb-M45 edge (b). Layers at the −30 mm radial position (comparable to position 3) imaged by HRTEM (c) and STEM-EELS (d).

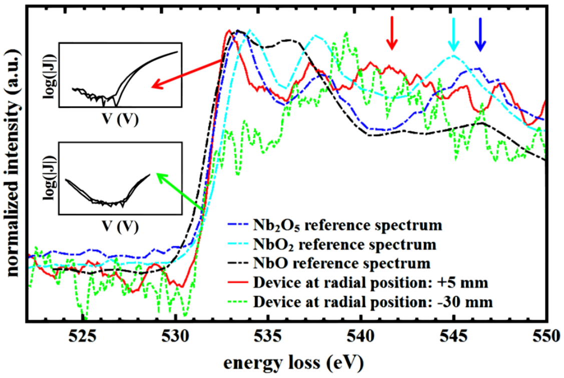

Fig. 6. EELS analysis of the O-K edge of Nb oxide layers from the center of the wafer (+5 mm—red solid line) and beneath the race track of the target (+30 mm—green dotted line) in comparison to reference spectra taken from Ref. 63 (dashed-dotted lines). Measured spectra (solid and dotted lines) were averaged over several positions in the respective samples. The insets show the *I-V* curves of devices at the respective positions.

thickness of around 0.1 nm (or 5%) is smaller than the standard deviation. In order to better evaluate this result, the thickness of an underlying Al oxide layer has been determined, showing a difference in thickness of around 16% between positions 2 and 3. A similar stack containing Hf oxide showed a difference in thickness of up to 20%. In both cases—Al and Hf oxide—the absolute difference in thickness was larger than the standard deviation, thus supporting the significance of this result. The decrease in the thickness of sputtered layers toward the edges of the wafer is a common phenomenon in magnetron sputtering due to the involved magnetic field and, therefore, inhomogeneous utilization of the target. Other prepared devices with thinner NbO$_x$ layers as investigated here show memristive behavior. Thus, the 0.1 nm thinner layer at the edge of the wafer is not responsible for the difference in electronic properties.

In a second step, the oxidation state of the Nb oxide from the two positions was analyzed by STEM-EELS. The results are displayed in Fig. 6. The insets show the *I-V* characteristics of devices at the respective positions. All spectra have been background-subtracted. As the low-loss spectrum was not recorded simultaneously with the spectra, the position of peaks between experimental data and reference spectra[63] can be compared only qualitatively. Nonetheless, the O-K edge from the center device shows good congruency with either NbO$_2$ or Nb$_2$O$_5$ up to around 538 eV energy loss. The arrows in Fig. 6 mark the position of the first local maximum after 538 eV where strong deviations between the spectra arise. Specifically, the position of the experimentally determined maximum is 541 eV, while NbO$_2$ and Nb$_2$O$_5$ have local maxima at 545 and 546 eV, respectively. While it has been demonstrated in the literature in several studies that the conduction band minimum in NbO$_2$ is formed by Nb 4d t_{2g} (between 531 and 534 eV in these spectra) and $e_{g\sigma}$ (between 535 and 539 eV) orbitals,[64] no data were found on the empty orbitals above those. The electronic structure of Nb(V) oxide is expected to be similar, which is also reflected in the similarity between their EEL spectra. The increased empty DOSs above 540 eV in the experimentally determined spectra can, thus, not be attributed to a specific orbital but potentially arises due to the amorphous character of Nb oxide. The oxidation state of Nb in the deposited layers is expected to be similar to either of the two oxides. The off-center sample of the −30 mm radial position [cf. position 3 in Fig. 3(a)] on the other hand cannot be assigned to any known Nb oxide. First of all, the O-K signal recorded on these oxides was much weaker, which can also be seen in the lower signal-to-noise ratio in the spectrum. Secondly, unlike the previously discussed cases, this spectrum does not contain a strong peak at the onset of the edge and instead has its maximum around 8 eV behind the edge. The small recorded O-K edge signal intensity hints toward a lower oxidation state. The difference in edge shape underlines these differences, as the electronic structure apparently strongly deviates from the known Nb oxide stoichiometries.

The results of nanoscopic investigations indicate that the reactive sputtering resulted in a highly oxidized—and thus insulating—amorphous Nb oxide with an oxidation between +4 and +5 in the center of the wafer. Beneath the race track, however, a Nb suboxide is formed, of which the oxidation state could not be determined by STEM-EELS. This infers, moreover, that the oxidation state is not that of a known Nb oxide, i.e., +2, +4, or +5. Due to the generally very weak O-K signal, we conclude that a low oxidized Nb suboxide has been formed. It is known that the lower oxidation states of Nb are acting as a metallic conductor.[63] As can be seen in the *I-V* curve of these devices [cf. Fig. 3(e)], no Schottky-like barrier is formed. This is another hint for the lower oxidation state of the NbO$_x$ underneath the race track of the target.

D. Kinetic Monte Carlo simulations

In order to understand better the actual resistive switching mechanism of the device and particularly the influence of the structure of NbO$_x$ layer, kinetic Monte Carlo simulations have been performed. As is shown in Fig. 7, the *I-V* curve depends

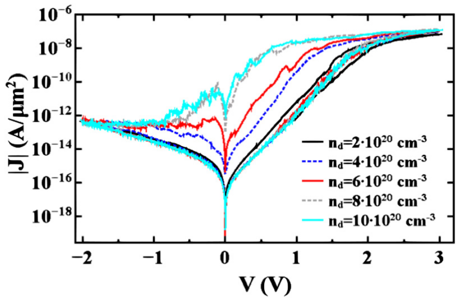

FIG. 7. Simulated *I-V* characteristic of the double-barrier memristive devices dependent on the defect concentration (n_d) within the NbO_x layer. The simulations are performed with a 1.25 nm tunnel barrier thickness and a 0.9 eV Schottky-barrier height to show *I-V* characteristics comparable to device behavior at position 1 and position 2 (cf. Fig. 3).

strongly on the defect concentration (i.e., immobile oxygen vacancies O^{2+} and mobile negatively charged oxygen ions) in the NbO_x layer. With a higher defect concentration, the hysteretic or memristive behavior of the device is getting more pronounced. According to this finding, it might be a good idea to adjust the memristive behavior of the device by controlling the defect concentration within the NbO_x layer already during the processing of the structure. Having a closer look at the different *I-V* characteristics within the inner area of the wafer, correlations between the plasma parameters and the width of the hysteresis (i.e., the defect concentration) are visible. Here, a higher electron temperature, a higher plasma potential, and a lower floating potential at around the −25 mm radial position [position 1—cf. Fig. 3(c)] are correlated to a more pronounced hysteresis compared to the position of around +5 mm [position 2—cf. Fig. 3(d)], as is described in more detail in Sec. III B. A qualitative correlation between the plasma parameters and the defect concentration within the NbO_x layer, as well as the impact of negative ions on the film properties, has to be addressed in further investigations.

To explain the electronic behavior of the devices at +30 mm, which shows no memristive behavior [position 3—cf. Fig. 3(e)], the tunnel barrier width and the Schottky-barrier height are varied within the simulations. It is found that a device with a tunnel barrier of 1.6 nm thickness (compared to 1.25 nm in the center) and a decreased Schottky-barrier of 0.7 eV (compared to 0.9 eV in the center) is showing comparable *I-V* curves as the device at position 3. Thus, the NbO_x has a higher conductance and significant lower voltage drops across the solid-state electrolyte. Therefore, the electric field is too small to move charged defects within the layer. These simulation results are in good agreement with the EELS measurements showing a lower oxidation state of the NbO_x at the position of −30 mm.

IV. SUMMARY

The variation of *I-V* characteristics across a 100 mm wafer of magnetron-sputtered double-barrier memristive devices was investigated. The functionality of the analog resistive switching devices is dependent on the position on the wafer. The correlations of the differences in electronic behavior with the internal plasma deposition parameters of the reactive sputtering process of NbO_x are depicted. Strong differences in the chemical structure were found by STEM-EELS investigations, which suggest that a high oxidation state of the niobium is essential for resistive switching. Kinetic Monte Carlo simulations show a crucial dependence of the *I-V* hysteresis on the defect concentration within the NbO_x layer and on the oxidation state. These findings are correlated to the energy conditions on the sample surface and to the electron temperature and the floating potential. The impact of the magnetic field strength of the sputter cathode, the target geometry, and the distribution of high energetic oxygen ions within the plasma has to be addressed in further investigations. The reported results show that a reactive magnetron sputtering process with the same target and substrate geometry and size is not sufficient to deposit a homogenous metal oxide layer across a whole 100 mm wafer. Nevertheless, the integration of the double-barrier memristive devices into crossbar arrays and their possibility to be used in neuromorphic circuits have already been shown.[31] Furthermore, the deposition technique allows us to investigate the impact of the plasma process parameters on the chemical and electrical properties of a metal oxide layer and on the performance of the devices obtained in one and the same deposition process.

ACKNOWLEDGMENTS

The authors gratefully acknowledge financial support provided by the Deutsche Forschungsgemeinschaft (DFG) in the frame of Research Unit RU 2093 “Memristive Devices for Neural Systems.” This project has received funding from the European Union’s Horizon 2020 research and innovation program under Grant Agreement No. 823717—ESTEEM3. J.S. and L.K. thank Ferdinand Hofer for enabling STEM investigations.

[1] B. Hoefflinger, *CHIPS 2020*, edited by B. Höfflinger (Springer International Publishing, Cham, 2016), Vol. **2**, pp. 189–200.
[2] G. E. Moore, *Cramming More Components onto Integrated Circuits* (McGraw-Hill, New York, 1965).
[3] M. Inubushi and K. Yoshimura, Sci. Rep. **7**, 10199 (2017).
[4] L. Appeltant, M. C. Soriano, G. Van der Sande, J. Danckaert, S. Massar, J. Dambre, B. Schrauwen, C. R. Mirasso, and I. Fischer, Nat. Commun. **2**, 468 (2011).
[5] H. Zenil, Complex Syst. **19**, 1 (2010).
[6] U. Rueckert, *CHIPS 2020*, edited by B. Höfflinger (Springer International Publishing, Cham, 2016), Vol. **2**, pp. 249–274.
[7] N. D. Mermin, *Quantum Computer Science: An Introduction* (Cambridge University Press, Cambridge, 2007).
[8] A. Alaghi and J. P. Hayes, ACM Trans. Embed. Comput. Syst. **12**, 1 (2013).
[9] D. S. Jeong, R. Thomas, R. S. Katiyar, J. F. Scott, H. Kohlstedt, A. Petraru, and C. S. Hwang, Rep. Prog. Phys. **75**, 076502 (2012).
[10] D. S. Jeong and C. S. Hwang, Adv. Mater. **30**, 1704729 (2018).
[11] D. Ielmini and R. Waser, *Resistive Switching: From Fundamentals of Nanoionic Redox Processes to Memristive Device Applications* (Wiley-VCH Verlag GmbH & Co. KGaA, Weinheim, 2016).
[12] S.-C. Liu, *Event-Based Neuromorphic Systems* (John Wiley & Sons, Ltd, Chichester, 2015).
[13] M. Ziegler, Ch. Wenger, E. Chicca, and H. Kohlstedt, J. Appl. Phys. **124**, 152003 (2018).

[14] R. Tetzlaff, *Memristors and Memristive Systems* (Springer, New York, 2014).
[15] R. Kozma, R. E. Pino, and G. E. Paziena, *Advances in Neuromorphic Memristor Science and Applications* (Springer, New York, 2012).
[16] Y. Li, Z. Wang, R. Midya, Q. Xia, and J. J. Yang, J. Phys. Appl. Phys. **51**, 503002 (2018).
[17] A. Adamatzky and L. Chua, *Memristor Networks* (Springer, London, 2014).
[18] F. Z. Wang, L. Li, L. Shi, H. Wu, and L. O. Chua, J. Appl. Phys. **125**, 054504 (2019).
[19] I. Abraham, Sci. Rep. **8** (2018).
[20] P. Meuffels and R. Soni (2012), e-print arXiv: 1207-7319.
[21] X. Hong, D. J. Loy, P. A. Dananjaya, F. Tan, C. Ng, and W. Lew, J. Mater. Sci. **53**, 8720 (2018).
[22] J. J. Yang, N. P. Kobayashi, J. P. Strachan, M.-X. Zhang, D. A. A. Ohlberg, M. D. Pickett, Z. Li, G. Medeiros-Ribeiro, and R. S. Williams, Chem. Mater. **23**, 123 (2011).
[23] H. Zhang, N. Aslam, M. Reiners, R. Waser, and S. Hoffmann-Eifert, Chem. Vap. Depos. **20**, 282 (2014).
[24] S. Porro, A. Jasmin, K. Bejtka, D. Conti, D. Perrone, S. Guastella, C. F. Pirri, A. Chiolerio, and C. Ricciardi, J. Vac. Sci. Technol. A **34**, 01A147 (2015).
[25] C. Giovinazzo, C. Ricciardi, C. F. Pirri, A. Chiolerio, and S. Porro, Appl. Phys. A **124**, 686 (2018).
[26] A. Kumar, M. Das, V. Garg, B. S. Sengar, M. T. Htay, S. Kumar, A. Kranti, and S. Mukherjee, Appl. Phys. Lett. **110**, 253509 (2017).
[27] M. Das, A. Kumar, R. Singh, M. T. Htay, and S. Mukherjee, Nanotechnology **29**, 055203 (2018).
[28] H. Jiang and Q. Xia, Appl. Phys. Lett. **104**, 153505 (2014).
[29] J. Domaradzki, A. Wiatrowski, T. Kotwica, and M. Mazur, Mater. Sci. Semicond. Process. **94**, 9 (2019).
[30] H. Mähne, H. Wylezich, F. Hanzig, S. Slesazeck, D. Rafaja, and T. Mikolajick, Semicond. Sci. Technol. **29**, 104002 (2014).
[31] M. Hansen, F. Zahari, H. Kohlstedt, and M. Ziegler, Sci. Rep. **8**, 8914 (2018).
[32] H. Kersten, G. M. W. Kroesen, and R. Hippler, Thin Solid Films **332**, 282 (1998).
[33] H. Kersten, H. Deutsch, H. Steffen, G. M. W. Kroesen, and R. Hippler, Vacuum **63**, 385 (2001).
[34] J. A. Thornton, Thin Solid Films **54**, 23 (1978).
[35] S. Gauter, F. Haase, and H. Kersten, Thin Solid Films **669**, 8 (2019).
[36] S. Gauter, M. Fröhlich, W. Garkas, M. Polak, and H. Kersten, Plasma Sources Sci. Technol. **26**, 065013 (2017).
[37] F. Haase, D. Manova, D. Hirsch, S. Mändl, and H. Kersten, Plasma Sources Sci. Technol. **27**, 044003 (2018).
[38] S. Bornholdt and H. Kersten, Eur. Phys. J. D **67**, 176 (2013).
[39] S. Bornholdt, N. Itagaki, K. Kuwahara, H. Wulff, M. Shiratani, and H. Kersten, Plasma Sources Sci. Technol. **22**, 025019 (2013).
[40] T. Minami, T. Miyata, T. Yamamoto, and H. Toda, J. Vac. Sci. Technol. A **18**, 1584 (2000).
[41] H. Y. Lee *et al.*, *2008 IEEE International Electron Devices Meeting*, 15–17 December 2008 (IEEE, San Francisco, CA, 2008).
[42] D. Walczyk, Ch. Walczyk, T. Schroeder, T. Bertaud, M. Sowińska, M. Lukosius, M. Fraschke, B. Tillack, and Ch. Wenger, Microelectron. Eng. **88**, 1133 (2011).
[43] L. Zhao, S. Clima, B. Magyari-Köpe, M. Jurczak, and Y. Nishi, Appl. Phys. Lett. **107**, 013504 (2015).
[44] S. U. Sharath *et al.*, Appl. Phys. Lett. **104**, 063502 (2014).
[45] S. U. Sharath *et al.*, Adv. Funct. Mater. **27**, 1700432 (2017).
[46] M. Hansen, M. Ziegler, L. Kolberg, R. Soni, S. Dirkmann, T. Mussenbrock, and H. Kohlstedt, Sci. Rep. **5**, 13753 (2015).
[47] M. Hansen, M. Ziegler, and H. Kohlstedt, *IEEE International Conference on Rebooting Computing (ICRC 2016)*, San Diego, CA, 17–19 October 2016 (IEEE, San Diego, CA, 2016).
[48] H. M. Mott-Smith and I. Langmuir, Phys. Rev. **28**, 727 (1926).
[49] B. E. Cherrington, Plasma Chem. Plasma Process. **2**, 113 (1982).
[50] R. Piejak, V. Godyak, B. Alexandrovich, and N. Tishchenko, Plasma Sources Sci. Technol. **7**, 590 (1998).
[51] A. Piel, *Plasma Physics: An Introduction to Laboratory, Space, and Fusion Plasmas* (Springer, Berlin, 2010).
[52] S. Dirkmann, M. Hansen, M. Ziegler, H. Kohlstedt, and T. Mussenbrock, Sci. Rep. **6**, srep35686 (2016).
[53] J. G. Simmons, J. Appl. Phys. **34**, 1793 (1963).
[54] S. M. Sze and K. K. Ng, *Physics of Semiconductor Devices* (Wiley, Hoboken, NJ, 2007).
[55] C. Kügeler, M. Meier, R. Rosezin, S. Gilles, and R. Waser, Solid State Electron. **53**, 1287 (2009).
[56] G. W. Burr, R. S. Shenoy, K. Virwani, P. Narayanan, A. Padilla, B. Kurdi, and H. Hwang, J. Vac. Sci. Technol. B **32**, 040802 (2014).
[57] K. Ellmer and T. Welzel, J. Mater. Res. **27**, 765 (2012).
[58] T. Welzel and K. Ellmer, Surf. Coat. Technol. **205**, S294 (2011).
[59] M. Popescu, Thin Solid Films **121**, 317 (1984).
[60] Y. Mori, Rev. Sci. Instrum. **63**, 2357 (1992).
[61] J. W. J. Wu, R. Moriyama, M. Nakano, K. Ohshimo, and F. Misaizu, Phys. Chem. Chem. Phys. **19**, 24903 (2017).
[62] T. Welzel and K. Ellmer, Vak. Forsch. Prax. **25**, 52 (2013).
[63] D. Bach, "EELS investigations of stoichiometric niobium oxides and niobium-based capacitors," dissertation (University of Karlsruhe, 2009).
[64] V. Eyert, Europhys. Lett. **58**, 851 (2002).

5.2 Superconducting NbN thin films

Publication 2

Correlation between properties of direct current magnetron sputtered thin niobium nitride films and plasma parameters

Authors:	R. Marquardt, J. Cipo, F. Schlichting, G. Kolkhatkar, H. Kohlstedt, H. Kersten
Journal:	Thin Solid Films [102]
Technique:	Electrical diagnostic and energy flux measurements, X-ray diffraction, atomic force microscopy
Own contribution:	approximately 20%

Experimental Setup:

DC magnetron sputtering from a 2-inch NbN target in Ar atmosphere deposited NbN layers onto square Si-substrates. Depositions were carried out with a variation of pressure, target-substrate distance and power. Each parameter was varied separately. In the same manner, PTP and Langmuir probe measurements were done. For the power and pressure variation, the two Diagnostics were mounted into the vacuum chamber from the side. Distance variation was done using the bottom flange of the vacuum chamber.

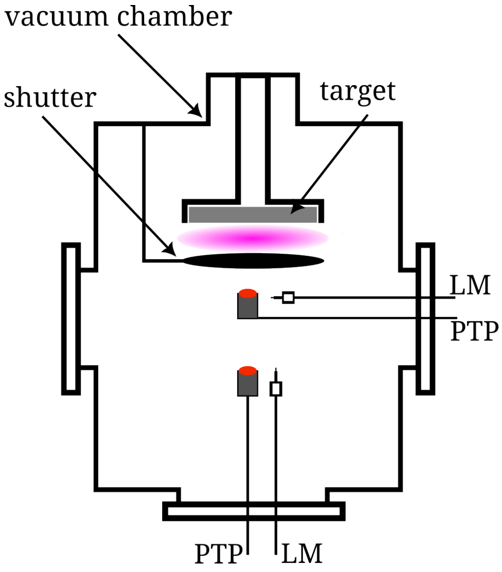

Motivation:

Niobium nitride (NbN) as a superconducting compound exhibits a large transition temperature and superconducting energy gap. Previous studies on NbN in its thin film form established a clear dependence of its superconducting properties on the parameters such as film thickness, deposition rate and pressure. However, knowledge of the influence of the internal plasma parameters like electron temperature, plasma potential, ion current density and energy flux density can help develop a more refined approach to optimising thin films for specific applications. Using the plasma diagnostics to sort of map out the plasma parameters in the deposition chamber and comparing them with the obtained thin films allows for a way to anticipate their film properties which would lower the need of having to extensively analyze them ex-situ with complex techniques like TEM or X-ray diffraction.

Main Results:

Pressure variation ($0.5 - 4.5$ Pa) revealed the correlation of ion current density and electron temperature to crystallinity and grain size. With increasing pressure electron and ion densities rise while their kinetic energy drops due to the increased collision rates with the gas atoms. This leads to a decrease in grain size and a lower crystallization rate, which can be correlated to the decrease in the critical temperature T_c. The highest crystallinity and critical temperature were observed for 1 Pa.

While adjusting the distance ($5 - 40$ mm) between the target and substrate/ probe a higher T_c, grain size and crystallinity are observed for greater distances while the energy flux density and deposition rate decrease. The residual resistivity ratio (RRR) shows no dependence on distance variation which suggests that it is not determined by the grain size. The mean free path of the neutrals is around 33 mm. A probe-to-target distance smaller than that induces a higher energy flux and lower transition temperatures.

As expected, the energy flux density and deposition rate increase with increasing discharge power ($20 - 100$ W) at a distance of 37 mm and gas pressure 0.5 Pa. Here, the electron temperature and plasma potential display a similar course with an increasing trend towards higher discharge power. This is due to the close proximity to the magnetic field of the magnetron which entraps more electrons and in turn results in a low floating potential.

Thin Solid Films 742 (2022) 139046

Contents lists available at ScienceDirect

Thin Solid Films

journal homepage: www.elsevier.com/locate/tsf

Correlation between properties of direct current magnetron sputtered thin niobium nitride films and plasma parameters

Richard Marquardt [a,*], Julia Cipo [b], Felix Schlichting [b], Gitanjali Kolhatkar [a],
Hermann Kohlstedt [a], Holger Kersten [b]

[a] Nanoelectronics, Faculty of Engineering, Kiel University, Kiel 24143, Germany
[b] Institute of Experimental and Applied Physics, Kiel University, Kiel 24098, Germany

ARTICLE INFO

Keywords:
Niobium nitride
Thin films
Superconductor
Langmuir probe
Passive thermal probe
Atomic force microscopy
Grazing incidence X-ray diffraction

ABSTRACT

Superconducting thin films of NbN on SiO_2 are prepared at ambient temperature by direct current magnetron sputtering with varying external deposition parameters, i.e. pressure, target-substrate distance, and power. Internal deposition parameters such as the plasma properties are determined with both a Langmuir probe and a calorimetric probe providing insight regarding the energy flux, the electron temperature, the plasma potential, and the ion current density of the plasma. Grazing incident x-ray diffraction and atomic force microcopy measurements reveal that the thin films have cubic polycrystalline structures with grain sizes of up to 51 Å, which define the superconducting behavior. Structural and electrical properties are related to the plasma parameters, showing a high correlation between the ion current density and the superconducting properties of the films. The results attest to the potential of plasma characterization as a powerful tool to optimize the deposition of thin NbN films and to predict their film properties.

1. Introduction

Niobium nitride (NbN) is a refractory Bardeen-Cooper-Schrieffer-type superconductor compound, exhibiting a large transition temperature and superconducting energy gap. In its thin film form, NbN is exploited in numerous applications, such as bolometers, single-photon detectors, superconductor-insulator-superconductor tunnel junctions for millimeter wave detectors, superconducting Quantum interference devices, radio frequency (RF) cavities [1–6] as well as non-superconductive applications, e.g. in tribological engineering [7]. NbN is commonly deposited by direct current (DC-) or RF-magnetron sputtering in an Ar/N_2(85%/15%) atmosphere and reaches a transition temperature of up to 14.2 K when deposited in ambient temperature on a structurally suitable substrate [8,9]. In previous studies, a relation between the deposition rate, pressure and nitrogen partial pressure and the transition temperature as well as the hardness, the stoichiometry and density of NbN could already be established [10]. In addition, the film thickness influences the orientation and structure of the NbN layer and, therefore, also its superconducting properties [11,12]. Although extensive information and studies on the influence of the deposition conditions on the layer properties of NbN have already been reported, the present work focuses on plasma engineered thin NbN films. By exploring the relation between plasma parameters and film properties, a high degree of flexibility in the production of NbN thin films can be achieved. To extract relevant plasma properties during sputtering, two different diagnostics are exploited, i.e. a Langmuir probe (LP) and a passive thermal probe (PTP). While the former offers the opportunity to monitor the electron temperature, the plasma potential and the ion current density of the plasma, the latter measures the energy flux density from plasma to the wafer surface [13]. We show that the structural and electrical properties of the deposited NbN thin films are clearly related to the plasma parameters. In more general terms, the work presented here demonstrates that the tool box offered by plasma diagnostic is a powerful approach to optimize thin films towards particular applications.

2. Material and methods

2.1. Sputtering conditions and thin film diagnostics

All NbN films were deposited on a silicon substrate using a home-made DC magnetron sputtering system. In this system, a high vacuum

---

[*] Correspondence author.
E-mail addresses: rvm@tf.uni-kiel.de (R. Marquardt), julia.cipo@isit.fraunhofer.de (J. Cipo).

https://doi.org/10.1016/j.tsf.2021.139046
Received 30 April 2021; Received in revised form 15 November 2021; Accepted 7 December 2021

was obtained using a mechanical pump (Vacuubrand, MD 4 NT) in combination with a turbo-molecular pump (Leybold, Turbovac 350i). The pressure was precisely controlled by adjusting the angle of the throttle valve of the turbo-molecular pump. A custom-designed substrate holder, able to accommodate a square substrate with a size of 10 × 10 mm^2, was used for sample fabrication. Its configuration is illustrated in Fig. 1.

DC magnetron sputtering from a NbN-target (NbN, 99.99%) in a pure Ar atmosphere was employed for the deposition of the NbN layers. The NbN thin films were deposited at room temperature onto square Si-substrates (10 × 10 mm^2) coated with a 400 nm thick thermal SiO_2. The base pressure was below $3 \bullet 10^{-5}$ Pa. Gas pressure, discharge power, and target-substrate distance were varied for the deposition processes of the sample, whereas the thickness of the deposited films was always kept constant at 50 nm. The variation of the mentioned process parameters can be found in Table 1.

Perfect conductivity is the first particular hallmark of superconductivity and a prerequisite for a large number of applications of superconductors such as high-current transmission lines or high-field magnets [14]. The phenomenon of perfect conductivity can be detected after a phase transition at a critical temperature T_C. The determination of the critical temperature is, therefore, an important method for characterizing a superconductor. To measure the critical temperature, the NbN films were lowered in liquid helium while their resistance was monitored. To ensure electrical contact, 0.25 mm radius circular Au top electrodes were deposited by DC magnetron sputtering with a stencil mask. The substrate was then attached with silver paste to the solid sample head of the deep temperature probe, which consisted of Copper (Cu). Wire bonding was used to contact the four Au pads with the measuring devices, and contact and lead resistance were eliminated by four-point sensing [15]. To determine the exact temperature of the phase transition during the resistance versus temperature (R-T) measurement, the cryogenic temperature sensor was placed at the same position as the sample, on the backside of the Cu-block.

Since both crystallinity and grain size affect the critical temperature and the critical current density of superconductors [16], a structural analysis of the NbN layers was also conducted. For this purpose grazing incidence x-ray deflection (GIXRD), established in thin-film technology [17,18], was used to examine the important structural properties. The film thickness was analyzed by x-ray reflection (XRR). For both thin film analyses a Rigaku SmartLab 9 kW diffractometer at a wavelength of $\lambda = 1.5418$ Å was used. For the GIXRD measurements a 9 kW copper X-ray source was used in a monochromatic parallel beam configuration focused with a length-limiting slit of 5 mm along the longitudinal axis. A typical GIXRD spectrum of polycrystalline Fm-3 m NbN is shown in Fig. 2. Topographic analyzes of the samples were made possible by atomic force microscopy (AFM). The AFM's ability to characterize nanoscale objects makes it a perfect tool to determine particle sizes and surface roughness. Hence, the sample surface was scanned using a Si AFM tip, attached to a cantilever. The tip was either repelled or attracted due to the atomic forces that occur when interacting with the sample surface. The bending caused by the atomic forces can be detected with the aid of a laser reflected onto the back of the cantilever and towards a photodetector. All AFM measurements were carried out on a SmartSPM 1000 from AIST-NT in a non-contact alternating current mode.

Table 1
Experimental deposition parameters.

Pressure variation @	Distance variation @	Power variation @
37 mm, 50W	0.5 Pa, 50 W	0. 5 Pa, 37 mm
0.5 Pa	10 mm	20 W
1 Pa	15 mm	30 W
1.5 Pa	20 mm	40 W
2 Pa	25 mm	50 W
2.5 Pa	30 mm	60 W
3 Pa	35 mm	70 W
3.5 Pa	40 mm	80 W
4.5 Pa		90 W
5 Pa		100 W

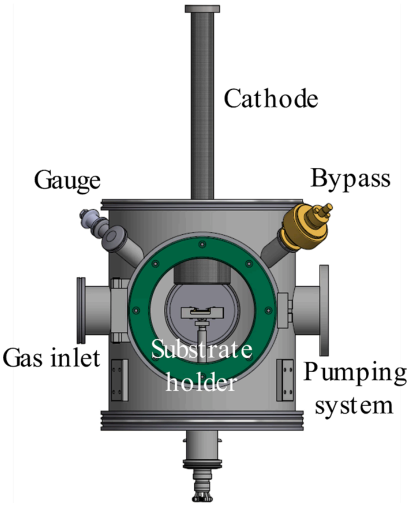

Fig. 1. Homemade sputtering system with 10 mm substrate holder and 2-inch target.

2.2. Measurement of plasma parameters

The plasma diagnostic was performed for the same deposition parameters, i.e. power, gas pressure, and probe-to-target distance, as the ones used for the NbN film deposition. Each process parameter was varied one at a time while keeping the others constant.

The PTP and LP measurements were carried out axially from the target. For the pressure and power variation the PTP was inserted vertically into the deposition chamber, while for the remaining measurements, the PTP and LP were inserted perpendicularly beneath the target, as shown for the LP in Fig. 3b. In both cases, the top of the probe pointed towards the target, yet, the different arrangement of the probe holder results in a different geometry, which in turn influences the energy flux of the plasma. The different installation of the PTP probe for power and pressure measurements in contrast to the distance measurement is due to the heating of the shutter by the plasma. Since the

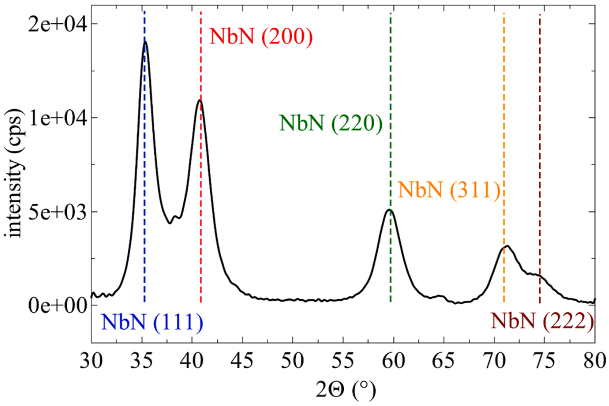

Fig. 2. Deflection spectrum with a grazing incidence angle (GIXRD) of NbN thin film with the following deposition parameters: $p = 0.5$ Pa, $P = 50$ W, $d = 37$ mm (black). The blue straight lines show the theoretical reflection peaks for Fm-3 m NbN. (For interpretation of the references to color in this figure legend, the reader is referred to the web version of this article.).

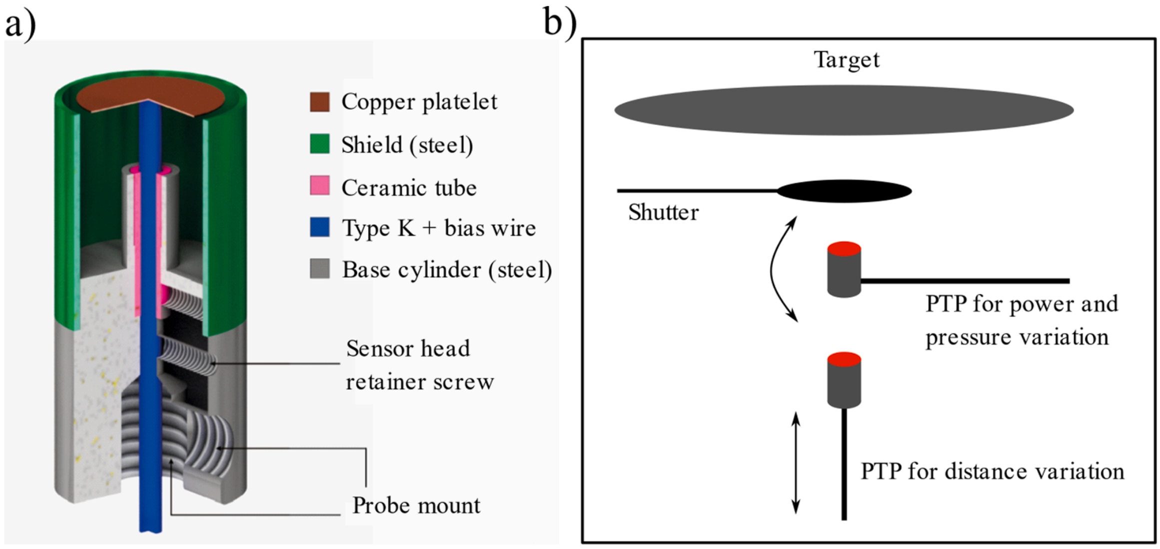

Fig. 3. (a) PTP design (used with permission of S. Gauter, F. Haase, and H. Kersten, Thin Solid Films 669, 8 (2019)). (b) Schematic drawing of the experimental setups of the PTP measurements for different process parameter variations. The PTP is positioned at 37, 67 and 97 mm from the NbN target for the distance variation. For the LP measurements, the experimental setup is analogous the PTP setup for the distance variation.

heat radiation of the shutter would affect the measurements, the probe was rotated 180° for power and pressure measurements, so that it was averted from the target during the cooling phase. This allowed the plasma to burn permanently during the measurement series. Due to the vertical installation of the probe, it was not possible to perform a 180° turn for cooling for the distance variation. Therefore, the plasma had to be switched off for the cooling phase. The PTP was oriented facing towards the cathode target for 20 s, while the plasma was switched off for 120 s, repeating this procedure for each varied process parameter (see Table 1). The LP measurements regarding the effect of power and pressure variation were repeated for probe-to-target distances of 37 mm, 67 mm and 97 mm. Since the magnetic field of the sputter-magnetron influences the LP measurements [13] for small distances (e.g. 37 mm), the influence of the magnetic field on the electrons was considered. For larger distances of 67 mm and 97 mm the magnetic field was expected to be weak and to have a much lower effect on the resulting plasma parameters.

2.2.1. Passive thermal probe

An effective diagnostic tool to record the energy flux towards a surface in a process plasma is the passive thermal probe (PTP). Its design is based on Thornton's idea of 1978 [19] and was recently improved [20]. The probe consisted of a copper plate with a diameter of 11 mm and a thickness of 100 μm (cf. Fig. 3a). On the back, a type K thermocouple (40 μV/K) and a copper bias wire are spot-welded. The probe is shielded by a housing made of stainless steel, so only the energy flux from the half-space above the substrate (probe) is detected. The wires are placed inside a ceramic tube, which is further installed inside a base cylinder. The cylinder is mounted on a vacuum feed-through, so the probe can be inserted into the process chamber by a vacuum flange.

When exposed to the plasma during the sputtering process, the PTP measures a temperature increase resulting from the incoming power towards it. This phase is known as the heating phase. It is mainly dominated by charged and neutral particles reaching the probe, surface processes like film formation, electron-ion recombination or chemical reactions as well as line radiation from the plasma and heat radiation from the target or the chamber walls. Inversely, the probe's temperature decreases when the power to the cathode target is turned off. This temperature course is characterized by the power leaving the probe and is referred to as the cooling phase. The power loss contributions result mainly from heat conduction, convection, and radiation of the probe's surface. To obtain the energy flux during these phases, the overall change in the enthalpy $\dot{H}$ has to be considered [21]:

$$Heating : \dot{H}_h = C_S = P_{in} - P_{out,h} \tag{1}$$

$$Cooling : \dot{H}_c = C_{Sc} = -P_{out,c} \tag{2}$$

where P_{in} is the input power from the plasma source, while $P_{out,h}$ and $P_{out,c}$ are the power losses and $\dot{T}_h$ and $\dot{T}_c$ the time derivatives of the temperature during the heating and cooling phase, respectively. The heat capacity C_S of the PTP is determined beforehand by calibration of the probe in an electron beam, as described in [22].

Only short time periods are investigated around the heating and cooling kinks when the plasma source is switched on and off. Thus, it can be assumed that the outgoing power remains the same during both phases such as $P_{out,h}(T_S) = P_{out,c}(T_S)$. The equations above can be combined, and the incoming power to the probe is obtained as follows:

$$P_{in} = \dot{H}_h - \dot{H}_c = C_S(\dot{T}_h - \dot{T}_c) \tag{3}$$

Based on the probe surface A_S, the incoming energy flux density is calculated:

$$J_{in} = \frac{P_{in}}{A_S} = \frac{C_S}{A_S}(\dot{T}_h - \dot{T}_c) \tag{4}$$

The evaluation method chosen for the measured temperature curves is the kink-method [20], where linear fits are used around the heating kink and cooling kink as demonstrated in Fig. 4a. By subtracting the slopes of the two linear fits, the term $\dot{T}_h$ - $\dot{T}_c$ is obtained. Further parameters like heat capacity C_S and probe surface A_S in Eq. (6) are already known due to calibration and probe manufacturing, respectively. As a result, the energy flux can be easily determined. A detailed description of this evaluation method is given in the literature [20].

2.2.2. Langmuir probe

The Langmuir probe is a widespread and established plasma diagnostic method, which goes back almost a hundred years [13,23]. Its simplicity and easy fabrication allow for a wide range of applications in different plasma environments [24–26]. By bringing an additional

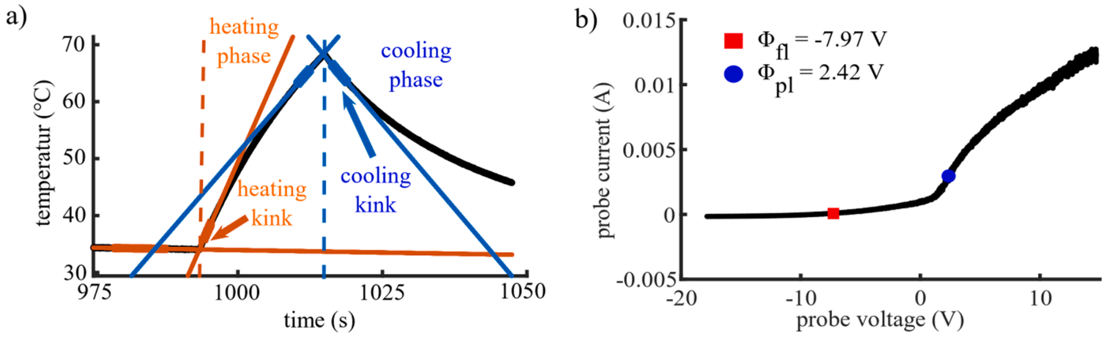

Fig. 4. (a) Example of a PTP measurement for position 37 mm, 50 W magnetron power and 0.5 Pa Ar gas pressure. The heating and cooling kink along with the linear fits are marked in red and blue, respectively. (b) Typical I-V characteristic measured by the LP at 97 mm probe-to target distance, a magnetron power of 50 W and gas pressure of 0.5 Pa. (For interpretation of the references to color in this figure legend, the reader is referred to the web version of this article.).

electrode into the plasma and applying a voltage sweep, a typical current-voltage *(I-V)* characteristic can be obtained. The probe can have different geometries, cylindrical, planar or spherical. In this work, a 2.7 mm long cylindrical tungsten wire of 100 μm diameter is used. The *I-V* characteristic can be employed to determine a variety of plasma parameters, such as the floating potential φ_{fl}, the plasma potential φ_{pl}, the electron temperature T_e, and the current density of the positive ions j_{ion}.

A typical *I-V* characteristic is presented in Fig. 4b. Starting at a high negative voltage, the plasma electrons are repelled and only positive ions can reach the probe. The resulting current is the ion saturation current.

When increasing the probe voltage, more electrons can reach the LP and the floating potential φ_{fl}, which is defined as the zero-crossing point of the *I-V* curve, is reached. Here, the electron current and the ion current flowing towards the probe are equal, resulting in a zero-net current at the probe. Further increase of the voltage increases the electron current towards the probe, which leads to an exponential rise in the electron current due to the Boltzmannfactor. The turning point of this exponential rise marks the plasma potential, after which the electron current saturates. The plasma potential φ_{pl} can be obtained from the maximum of the first derivative of the *I-V* curve. The energy of the impinging positive ions in the plasma is largely defined by the plasma potential and is therefore, an important parameter in this study.

Looking at a semi-logarithmic plot of the *I-V* curve, the electron temperature T_e can be extracted from the slope of exponentially rising current. By combining T_e with the Bohm sheath criterion, the ion current density j_{ion} can be obtained [27].

3. Results and discussion

To better understand the interplay between the superconducting properties of NbN layers and the plasma parameters during deposition, electrical and structural information of the layers as well as plasma data were collected. In order to analyze the critical temperatures of the samples, a four-point measurement was carried out with a fixed current of 10 μA on the outer electrodes, as the RT-probe head (Fig. 5a) was lowered into liquid helium. The superconducting properties of the samples were compared using two parameters that were derived from the RT measurements: the superconducting critical temperature (T_C, taken from the middle point of the resistive transition) and the residual resistivity ratio RRR (ratio of the film resistivity at 300 K to that at 20 K: RRR = $\rho(300\text{ K})/\rho(20\text{ K})$) [28].

3.1. Film and plasma properties versus sputtering pressure

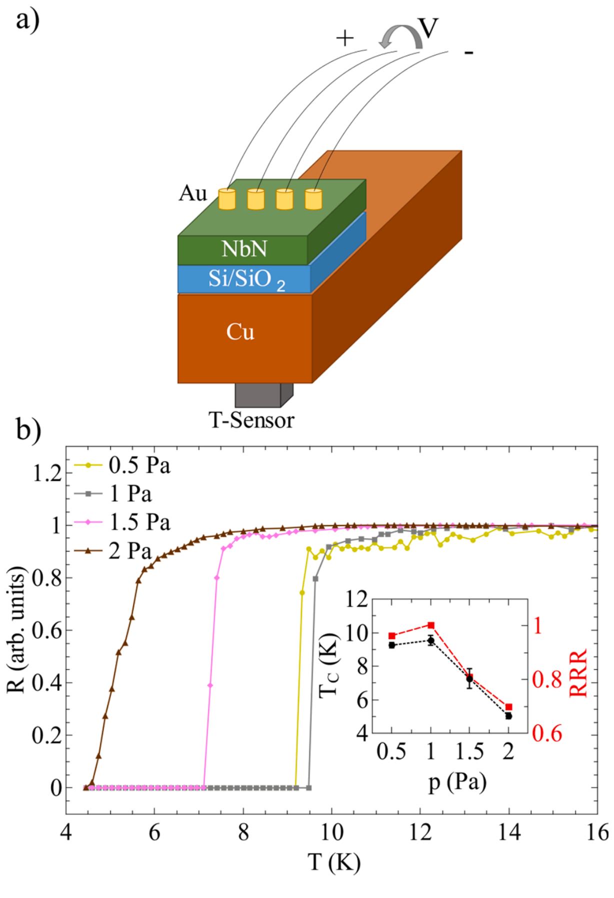

Fig. 5. (a) Schematic illustration of the sample fixed with conductive silver paste on a copper block. (b) RT-measurements for a variation in the deposition pressure for constant distance of 37 mm and deposition power of 50 W. Inset: Calculated T_c (black) and RRR (red) for the measured RT-curves. (For interpretation of the references to color in this figure legend, the reader is referred to the web version of this article.).

Normalized resistance versus temperature dependence of NbN films (50 nm thick) de- posited at four different process pressures are shown in Fig. 5b. The resistance versus temperature measurements were performed three times for each sample. For clarity, only one measurement per pressure variation was shown. The deviations can be seen in the error bars of T_C in the inset. The inset presents the parameters for T_C and RRR derived from the RT measurements. Samples that were deposited at a process pressure higher than 2 Pa showed no superconducting properties and are therefore, not shown in Fig. 5b. A slight increase in the critical temperature is obtained when increasing the pressure from 0.5 Pa to 1 Pa. If the pressure rises further, a sharp drop in T_C and RRR occurs, down to a T_C of 5 K for a 2 Pa process pressure. Previous studies by Iosad et al. [29,30] observed similar relationships between deposition pressure and T_C of superconducting materials. Also, an optimal pressure (~1 Pa) for superconducting material deposition is found in our study, depending on the distance between the substrate and the target. A similar observation for structure and transition temperature between 0.47 Pa and 1.33 Pa was made by Bacon et al. [9]. At this optimum a transition from degrading factors is expected, which is related to destructive bombardment by fast neutrals at low pressure to highly thermalized conditions at high pressure [31]. With a transition temperature of 9.6 K, the optimal result obtained in this work is below the optimal values reported in other recent studies [12], which report up to 14.5 K for ambient temperature deposition. This can be due to two main factors: First, thin films of 50 nm are deposited in this work, which affects the structure and transition temperature. Second, the substrate used is not matched to the crystal lattice of NbN.

An investigation of the RRR for the different process pressures also shows that the conduction process changes from “metallic” (RRR > 1) to “thermally activated” (RRR < 1) for pressures around 1 Pa due to a much stronger grain boundary contribution as the grain size decreases [32]. The influence of the grain boundaries can be explained through a model with superconducting grains in a non-superconducting matrix. Here, the coherence length

$$\xi\ (\mathrm{T}) = 0.74\ \xi_0\sqrt{\frac{\mathrm{T_C}}{\mathrm{T_C} - \mathrm{T}}} \tag{5}$$

is defined for two different conditions, $\xi < \mathrm{d}$ and $\xi > \mathrm{d}$, where d is the diameter of the superconducting grain [33]. Since the superconducting properties are given more weight locally for the case $\xi > \mathrm{d}$, they can be limited to the influence of the grains.

It should be noted here that both Tc and RRR show the same dependence on pressure. Such a correlation between RRR and Tc can be explained using a phenomenological approach of the above expounded model of superconducting grains in a non-superconductive matrix from Deutscher et al. [34]. In this approach the phase transition at the temperature T_C is defined as

$$\frac{1}{\mathrm{T_C}} \approx \frac{1}{\mathrm{T_{C0}}} + \frac{0.1\mathrm{N(E_F)}}{\mathrm{T_{C0}^2 C_{ij}}}. \tag{6}$$

For this model a weakening of the coupling Cij between the grains would lead to $\mathrm{T_C} < \mathrm{T_{C0}}$ and to an increased importance of the hopping conductance between the grains [33], which leads to a reduction in the total conductivity of the film. Therefore, T_C and RRR show the same functional relationship with respect to the grain size. For systems where the coherence length ξ is largely dependent on the grain size, Gurvitch et al. [35] suggested a method of calculating grain sizes by making an estimate of the mean free path l,

$$\mathrm{l} = \upsilon_\mathrm{f} \cdot \tau \tag{7}$$

where v_f is the average Fermi velocity and τ is the relaxation time. The latter can be expressed as a function of the electron phonon coupling constant λ of NbN according to:

$$\frac{\hbar}{\tau} = 2\pi\ k_B\ T\ \lambda \tag{8}$$

Taking into consideration the study by Chockalingam et al. [36] the Fermi velocity v_f for our films can be estimated to $1.44 \bullet 10^6$ m/s and the electron phonon coupling $\lambda = 1.13$, resulting in l (300 K) = 51 Å. Taking RRR = 1 for 1 Pa we find l (10 K) = l (300 K) • RRR = 51 Å and 37.7 Å for a pressure of 0.5 Pa.

The GIXRD method offers a more global analysis of the structural features relevant to the superconducting properties, namely grain size, crystal structure, and crystallinity. Therefore, GIXRD scans are performed with an incidence angle omega of 0.5° from a 2theta in the 20° to 80° range.

The GIXRD patterns of all investigated NbN films show a face centered cubic phase for the deposited NbN (COD 1538667 [37] was used for fitting of the GIXRD patterns). For increasing sputtering pressure, a reduction in crystallinity can be observed (Fig. 6). The grain size of the films is determined by the Halder-Wagner [38] method used on the five reflections of the orientations within the scanning range (Figs. 2 and 6). A maximal grain size is achieved at a sputtering pressure of 1 Pa in agreement with the findings from the R-T measurements described above. The offset in the calculated values between GIXRD and R-T measurements suggests that there is an inhomogeneous distribution of grain sizes in the film. While a global recording of the film is made with a GIXRD analysis, the RT measurement collects the data exclusively from the local current path. Smaller grains which do not contribute to the current transport are, thus, recorded in the statistical averaging of the X-ray data, but remain insignificant in the R-T analysis. A relationship between the transition temperature and the layer thickness is often observed [39] and indicates an increase of the average total grain size with increasing film thickness.

An analysis of the orientation of the cubic structure also shows that we can find a preferential orientation in the (111) direction for a pressure of 1 Pa (gray line, Fig. 6). The ratio between the intensities of the (111) and (200) orientations changes from 1.3 for a process pressure of 0.5 Pa to 2.2 for a pressure of 1 Pa.

The observed variations in crystallization, grain size, and structuring orientation, together with collected data on surface roughness, allow a classification in Thornton’s structure zone diagram (SZD) [40,41]. Due to the high roughness (Fig. 7a) in combination with low crystallization and small grain sizes for high process pressures, it can be concluded that the film displays a porous structure consisting of tapered crystallites separated by pits, as described in zone 1 of the SZD. With decreasing process pressure, a transition into the T-zone can be identified on the basis of decreasing roughness (Fig. 7b), increasing crystallization, and grain sizes. Adatom diffusion processes might occur, but their mobility and, thus, grain boundary migration is limited. The higher structure of the film at a process pressure of 1 Pa also indicates a transition into zone 2 of the SZD, in which the growth of columnar grains is described. Here, the adatom mobility is still high and the surface is smooth. Overall, it can

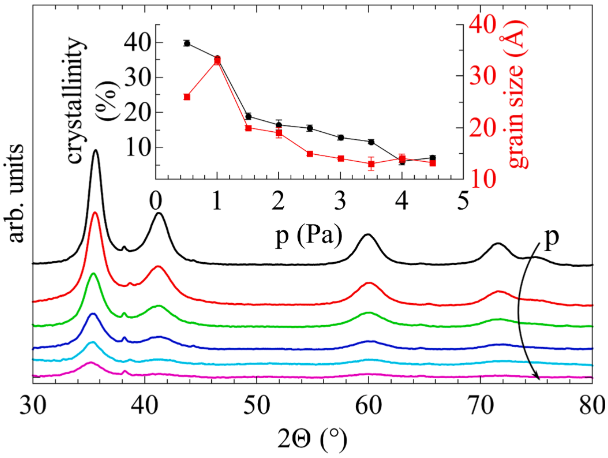

Fig. 6. GIXRD curves for deposition pressures in a 0.5 Pa to 5 Pa range for constant distance of 37 mm and deposition power of 50 W. Inset: Crystallinity (black) and grain size (red) extracted from the GIXRD. (For interpretation of the references to color in this figure legend, the reader is referred to the web version of this article.).

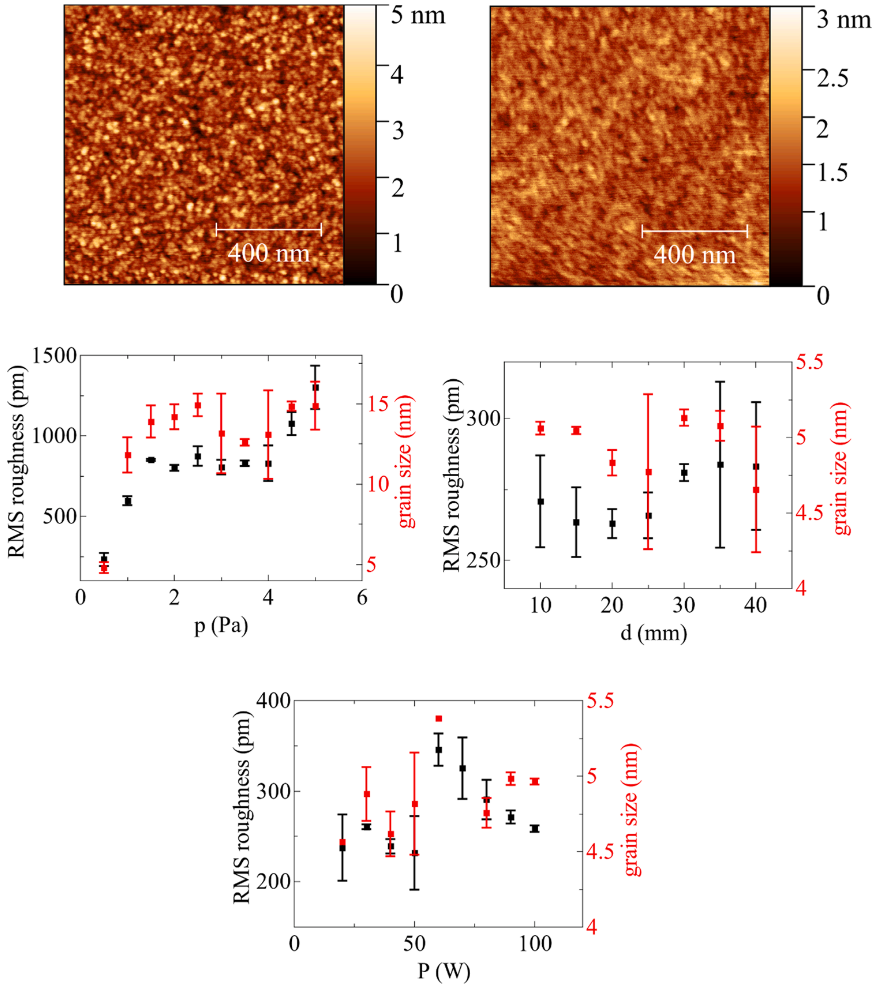

Fig. 7. Roughness of a thin film produced at a deposition pressure of a) 1.5 Pa and b) 0.5 Pa. RMS roughness (black) and grain size (red) dependence on c) the gas pressure, d) substrate-target distance and e) the magnetron power during deposition. (For interpretation of the references to color in this figure legend, the reader is referred to the web version of this article.).

be stated that, as expected according to Thornton et al. [41,42], increasing process pressure has a negative influence on the crystallinity and grain size of the layer.

Similar topography images for NbN films deposited by DC magnetron sputtering have been reported by other working groups, enabling an easier categorization into Thornton's SZD [42]. In addition, the grain size can be extracted from AFM topography measurements. Here, the grain size is determined using Otsu's method [43], which separates the pixels composing an image into two populations (noise and signal, or in this case grains and grain boundaries) using a mathematical method that minimizes the intra-class variance. The evolution of the grain size as a function of pressure, target-sample distance and sputtering power in shown in Fig. 7c–e. As the deposition pressure increases from 0.5 Pa to 2.5 Pa, the grains become larger, with values of 4.8 ± 0.2 nm and 14.9 ± 0.5 nm, respectively (Fig. 7c). When the pressure is further increased the grain size appears unchanged. As the target-substrate distance increases from 10 mm to 40 mm, the grain size remains constant with an average value of 4.94±0.07 nm (Fig. 7d). Similarly, the grain size does not show any significant changes as the power increases from 20 W to 100 W, with an average grain size of 4.87±0.09 nm (Fig. 7e). The increase in grain size with increasing process pressure contrasts with the observations of the XRD and current analysis (Fig. 7d). This can be explained by the different methodology of the analysis methods. XRD depends on the size of the defect-free volume, while AFM determines the size of particles independently of defects, which can consist of several grains. For the influence of the distance (Fig. 7d) and process power (Fig. 7e), the same trends are obtained as with the other analysis methods.

In summary, it can be stated that the morphological properties show a strong dependence on the gas pressure, which affects the kinetic energies of impinging particles especially gas ions and sputtered neutrals. Therefore, the energy influx as well as the NbN deposition rate have been determined for the related pressure variation (Fig. 8).

The results for the energy influx show only a small variation, as seen in Fig. 7.

Beside the weak maximum of about 90 mW/cm^2 at 0.5 Pa, the energy flux remains almost constant during the pressure variation. This is due to a balance between the kinetic energies of sputtered and reflected particles, and their interaction with particles of the background gas:

When increasing the gas pressure, the collision rate between the neutral background gas particles and kinetic particles (e.g. sputtered and reflected particles) increases as well. Thus, the mean free path of the particles from the target and the ions decreases. This leads to energetic losses, resulting in lower energy fluxes of sputtered and reflected particles [44]. However, the total flux of kinetic particles is still high,

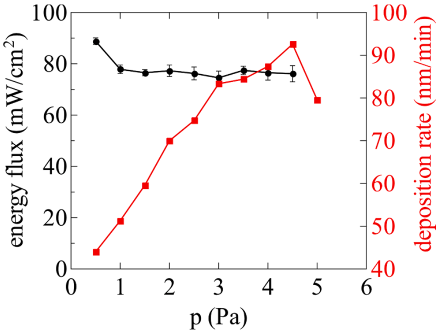

Fig. 8. Energy flux measured by passive thermal probe (PTP) as a function pressure(black). The mean values and the standard deviations are obtained from the two measurements acquired for each process pressure. The deposition rate for sputtered NbN thin films is determined by XRR (red). (For interpretation of the references to color in this figure legend, the reader is referred to the web version of this article.).

leading to an overall constant total energy flux in the pressure range investigated here.

Vice versa, the deposition rate first increases with increasing pressure, since a higher ionization rate and, thus, a higher number of sputtered particles is provided. For pressures between 3 Pa and 4.5 Pa the deposition rate increases just slowly. At higher pressures, the deposition rate decreases due to a decrease in the mean free path. The sputtered neutrals are no longer able to reach the substrate at the same rate as before, and the film thickness and, hence, the deposition rate are reduced [45].

Since the total energy flux showed a relatively constant behavior, it is important to understand the several energetic contributions to the integral energy flux and their correlation to specific film properties. Therefore, plasma parameters are measured by the LP at distances of 37 mm, 67 mm, and 97 mm while varying the pressure, as presented in Fig. 9.

Fig. 9a shows the electron temperature during pressure variation. The increasing gas pressure leads to a higher collision rate between the electrons and the gas particles. As a result, their mean thermal energy and temperature is reduced, which is confirmed by the electron temperature T_e. This trend is reflected in further experimental work [46].

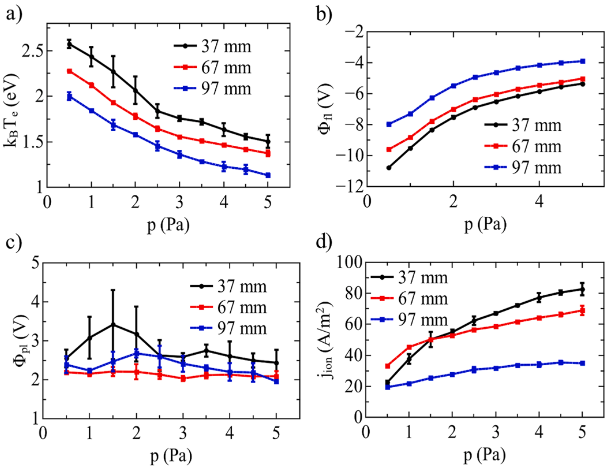

Fig. 9. Plasma parameters as a function of process pressure - the mean values and the standard deviations obtained from the three measurement points for each condition are depicted (squares with error bars). The solid and dashed lines are added as a guide to the eye for the mean values (37, 67 and 97 mm target to probe distance, respectively). (a) electron temperature, (b) floating potential of probe, (c) plasma potential, and (d) current density of positive ions.

The floating potential φ_{fl} shows the same behavior for all probe-to-target distances (Fig. 9b). Yet, for a distance of 37 mm (black curve), its values are more negative than for larger distances. This can be attributed to a stronger magnetic field closer to the magnetron, resulting in a larger amount of electrons being trapped in the plasma torus in front of the target cathode. Similar results on the enormous influence of the magnetron on film properties have already been shown by Zahari et al. [47].

Furthermore, φ_{fl} becomes less negative with increasing pressure for all three probe-to-target distances. This behavior can qualitatively be compared to the ion current density j_{ion} in Fig. 8d. Since the ion density increases with increasing gas pressure it is possible for more positive ions to reach the probe (substrate) surface due to its negative bias voltage.

The plasma potential φ_{pl} in Fig. 9c shows a much less pronounced behavior and almost no dependence of the gas pressure. For a probe-to-substrate distance of 37 mm, a change between 0.5 Pa and 1.5 Pa is noticeable, but the values are still within the error margins. Thus, the plasma potential φ_{pl} can be correlated to the electron temperature T_e according to the Boltzmann relation [48]. Through the electron temperature, valuable information regarding the kinetic energy of particles is provided.

With increasing gas pressure, higher ion and electron densities are expected due to higher collision rates with the gas atoms. Therefore, an increasing ion current density is obtained, as seen in Fig. 9d. In summary, increasing pressure in the range studied results in more electrons and ions being present in the plasma but with reduced kinetic energies.

Plasma properties like the electron temperature T_e and the ion current density j_{ion} are further correlated to morphological and electrical film properties. The crystallinity and grain size shown in Fig. 6 decrease with increasing gas pressure, similarly to the T_e curve. As stated earlier, the number of charged particles in a plasma increases with increasing gas pressure, which is confirmed by the j_{ion} trend. Yet, their kinetic energies and temperatures are reduced due to the decreased mean free path. The sputtered particles undergo an increased collision rate as well, leading to lower kinetic energies and, consequently, to a lower adatom mobility. A limited boundary migration is expected, which results in smaller grain sizes and a lower crystallization rate. For small process pressures, bombardment by fast neutrals becomes the significant destructive process limiting the deposition of high quality NbN thin films.

Since these crystallographic features have an influence on the electrical film properties (e.g. critical temperature), it is possible to correlate them to plasma properties [28,49]. For instance, the critical temperature T_c decreases with increasing gas pressures resembling the behavior for the grain size and electron temperature T_e. Grain size is therefore, an indicator for the critical temperature (Fig. 5b).

3.2. Film and plasma properties versus target substrate distance

The influence of the target-substrate distance on the superconducting properties is shown in Fig. 10. An increase in the distance leads to an increase in the critical temperature, as depicted in the inset of Fig. 10, while RRR displays no dependence on a change in the distance. Comparable observations were also reported by Iosad et al. [30], where a modulation of the mean free path was achieved by adjusting the process pressure, resulting in transition temperatures > 14 K for both an 80 mm and a 40 mm separation. In contrast to the observations of the effect of varying gas pressure, RRR does not appear to have any direct influence on T_c in this case. Although a semiconductor-like type is demonstrated for the conduction flow, the RRR of all NbN samples is below 1 for all target-substrate distances, indicating that the previous assumption of superconducting grains in a non-superconducting matrix as limiting factor is no longer valid. In the case of a distance variation, the electrical

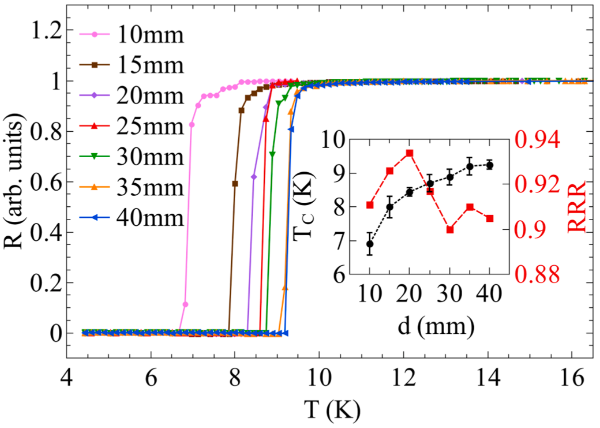

Fig. 10. RT-measurements for a variation in the distance (10 mm - 40 mm) between substrate and target with a constant pressure of 0.5 Pa and power 50 W. Inset: Calculated T_c (black) and RRR (red) for the measured RT-curves. (For interpretation of the references to color in this figure legend, the reader is referred to the web version of this article.).

resistance does not seem to be largely determined by the size of the grains. This absence of correlation between Tc and RRR could be due to an increased bombardment at shorter distances. Due to the mean free path of 33 mm between the neutrals in the gas phase at a pressure of 0.5 Pa, this effect would be stronger at smaller distances and lead to defects formation [50].

An increase in crystallinity can be seen as the target-substrate distance rises (Fig. 11). For distances 30 mm $< d <$40 mm, a saturation appears in the crystallinity. Although growth of larger grains can be detected with increasing distance, this growth seems to have a different dependence on the distance than the crystallinity. The increase in the general crystallinity in the films also indicates a reduction in the defect density.

Furthermore, the energy flux measured by the PTP can be compared to the deposition rate during distance variation (Fig. 12). Due to the different arrangement of the probe holder and the resulting anode geometry (Chapter 2.2), only a qualitative comparison can be made between the PTP measurements of the distance variation and the measurements of the pressure and power variation. The energy flux decrease results from the increased collision rate of sputtered particles at higher probe-to-target distances. Thus, a higher number of sputtered atoms are slowed down and unable to reach the substrate. This leads to thinner films and lower deposition rates.

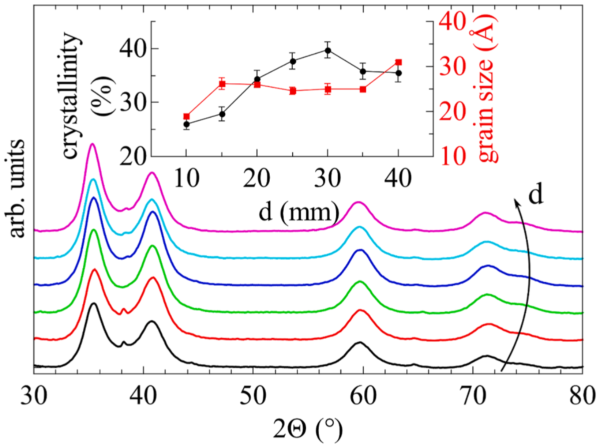

Fig. 11. GIXRD for a substrate-target distance between 10 mm and 40 mm for constant pressure of 0.5 Pa and deposition power of 50 W. Inset: Crystallinity (black) and Grain size (red) extracted from the GIXRD. (For interpretation of the references to color in this figure legend, the reader is referred to the web version of this article.).

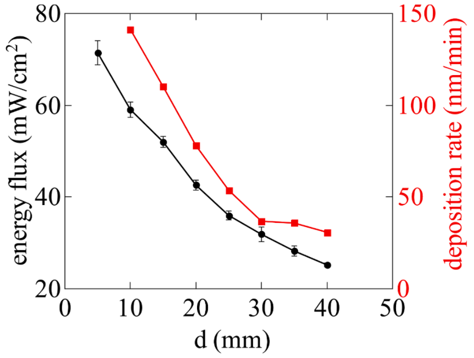

Fig. 12. Energy flux obtained from passive thermal probe (PTP) measurements as a function of the distance d between target and substrate(black). The mean values and the standard deviations are obtained from the two measurements for each distance. The black dashed line shows a fit of the mean values. The deposition rate for sputtered NbN thin films is determined by XRR (red). (For interpretation of the references to color in this figure legend, the reader is referred to the web version of this article.).

The energy flux and consequently, the deposition rate show a quadratic decrease with increasing distances, suggesting that the heat intensity resembles that of a point-like source.

Here, the intensity decreases with increasing distance in a ratio of I $\sim 1/d^2$, with I being the intensity and d the distance between the probe and a point-like source. Since the distance $d = 5$ mm - 40 mm is very small, we can no longer consider a close and comparably large plasma plume as a whole point-source, but instead we need to consider every point of it - especially beneath the race track - as a point-like source [21, 50].

3.3. Film and plasma properties versus sputtering power

When increasing the plasma power of the sputtering process from 20 W to 100 W, only slight variations on the superconducting properties of

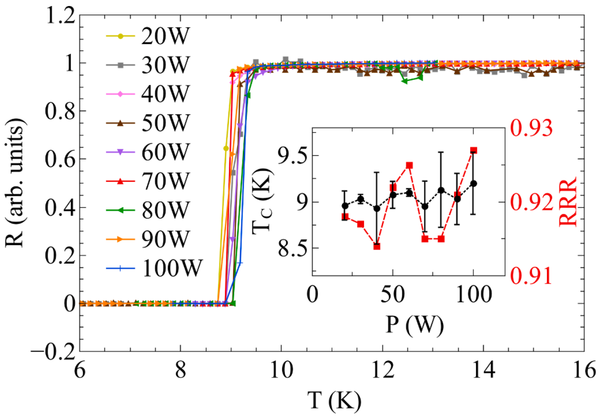

Fig. 13. RT-measurements for a variation in the deposition power (20 W - 100 W) with a constant pressure of 0.5 Pa and distance between target and sample of 37 mm. Inset: Calculated T_c (black) and RRR (red) for the measured RT-curves. (For interpretation of the references to color in this figure legend, the reader is referred to the web version of this article.).

the NbN films can be observed (Fig. 13). Only a marginal increase in T_C with increased sputtering power can be detected while RRR does not display any significant changes. Despite the minimal change in transition temperature, there is a clear linear increase in the deposition rate as a function of the increasing process power. Such an observation is surprising since, according to previous assumptions, the growth of the crystal layers of superconducting NbN is closely linked to the deposition rate [8] (Fig. 15).

At a process pressure of 0.5 Pa and a distance of 37 mm, the structure of the deposited NbN layers is independent of process power, as demonstrated by the GIXRD spectrum (Fig. 14). Neither crystallinity nor grain size show any dependence on sputtering power. This observation is in agreement with the investigation of the influence of the process power on the critical temperature, and confirms that the deposition rate cannot be directly correlated to the transition temperature and crystallinity of the NbN films.

A comparison between the energy flux and deposition rate for increasing magnetron power is shown in Fig. 15. The mean energy flux varies between 42 mW/cm^2 at a power of 20 W and 172 mW/cm^2 at 100 W. Moreover, the deposition rate increases from 15 nm/min at 20 W to 85 nm/min at 100 W. Both the energy flux and deposition rate show a linear increase for increasing power.

The energy flux being understood as a power transfer from the target/cathode to the substrate, a linear increase of the energy flux for increasing magnetron power is expected [20].

At higher power, the target's potential gets more negative compared to the substrate. Due to a higher potential difference, the positive ions accelerated towards the target obtain higher velocities and, thus, a higher kinetic energy. After momentum transfer, more target atoms will be sputtered resulting in a higher deposition rate.

Other plasma parameters like floating and plasma potential, electron temperature, and ion current density are obtained for probe-to-target distances of 37, 67, and 97 mm (Fig. 16).

The electron temperature shows an almost constant trend for $d > 37$ mm as seen in Fig. 16a. At higher probe-to-target distances, the electrons collide with more particles, losing kinetic energy and consequently reducing their temperature. As a result, the electron temperature at 67 mm and 97 mm is lower than at 37 mm.

Furthermore, the electron temperature increases from 2.2 eV at 20 W to about 3.1 eV at the maximum power for a distance of 37 mm. This is reflected by the plasma potential (Fig. 16c) and can be related to the strong presence of the magnetic field.

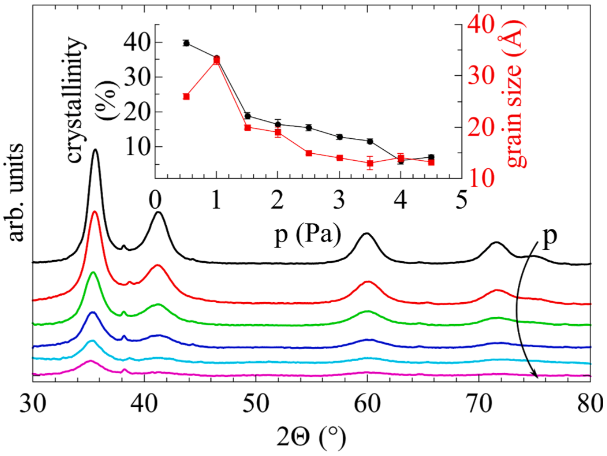

Fig. 14. GIXRD curves for a power range from 20 W to 100 W with a constant pressure of 0.5 Pa and distance between target and sample of 37 mm. Inset: Crystallinity (black) and grain size (red) extracted from the GIXRD. (For interpretation of the references to color in this figure legend, the reader is referred to the web version of this article.).

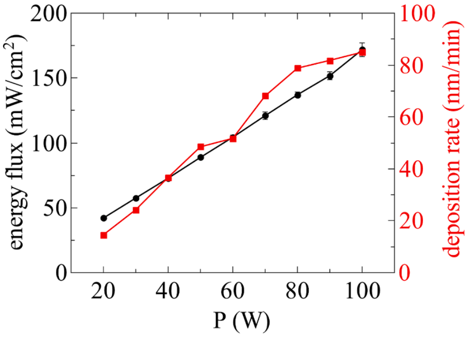

Fig. 15. Energy flux obtained by passive thermal probe (PTP) measurements as a function of deposition power (black). The mean values and the standard deviations are obtained from the two measurements for each deposition power. The black dashed line shows fits of the mean values. The deposition rate for sputtered NbN thin films is determined by XRR (red). (For interpretation of the references to color in this figure legend, the reader is referred to the web version of this article.).

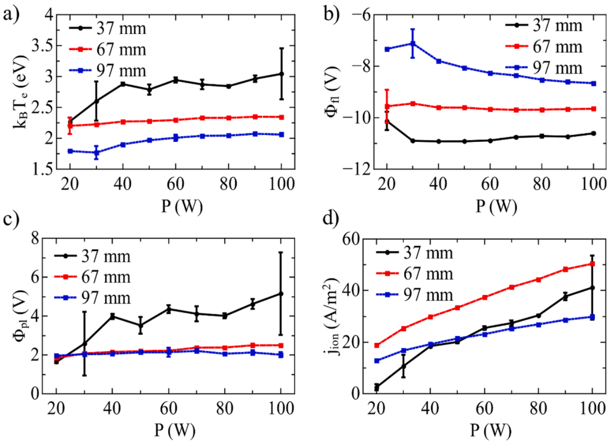

Fig. 16. Plasma parameters as a function of process power- the mean values and the standard deviations obtained from the three measurement points for each condition are depicted (squares with error bars). The solid and dashed lines are added as a guide to the eye for the mean values (37, 67 and 97 mm target to probe distance, respectively). (a) Electron temperature, (b) floating potential of probe, (c) plasma potential, and (d) current density of positive ions.

Since the field strength of the magnetron is stronger at short distances, the floating potential is more negative resulting in a higher number of trapped electrons (Fig. 16b). With increasing magnetron power, the plasma density increases, leading to a higher number of electrons and ions. Yet, the floating potential of all three curves does not show a pronounced behavior, which is inconsistent with previous work on DC magnetron sputtering processes [51].

The plasma potential for distances of $d > 37$ mm behaves analogous to the floating potential, while for a probe-to-target distance of 37 mm it exhibits a total increase of 3.6 eV (1.6 eV to 5.2 eV) with increasing power (Fig. 16c). Here, the effect of the magnetic field is more pronounced, leading to a higher number of electrons in the plasma torus and, thus, a higher plasma density at a distance of 37 mm.

The current density of the positive ions is presented in Fig. 16d. With increasing magnetron power, the velocity and kinetic energy of the ions increases. As a result, a higher number of ions are accelerated towards the probe (substrate) leading to a higher ion current density.

At 37 mm the increase of the current density is steeper (from 2.5 A/$m^2$to 41.13 A/m^2).

This can be attributed to smaller amounts of ions close to the magnetron and its magnetic field.

4. Conclusions

In summary, we show in this work that the analysis of the plasma parameters offers a comprehensive understanding of the effect of sputtering parameters on the layer growth of superconducting NbN. As the characterization of the energy flux alone provides insufficient information, further insight into the plasma parameters can be obtained by means of Langmuir probe measurements. This shows an increase of charged plasma particles with lower kinetic energies, resulting in a strong degradation of the structural layer properties via grain size reduction. This reduction in grain size is directly correlated to the transition temperature of the superconducting thin film. In addition, GIXRD and AFM structural analyses permitted film classification in Thornton's SZD, and demonstrating that the NbN film display the highest crystallinity for a pressure of 1 Pa.

A change in the substrate-target distance lower than the mean free path of the neutrals in the gas phase, induces an increase in the energy flux and a decrease in the transition temperature. The absence of correlation between RRR and T_C and the increase in energy flux suggests a higher defect density due to increased bombardment by neutrals.

The increase in plasma power shows a linear increase in deposition rate and energy flux, which are very highly correlated. No influence on the crystallinity and transition temperature of the layers could not be demonstrated under the given conditions, which together with the change in energy flux and sputtering rate can be explained by an increased amount of target atoms with constant energies.

CRediT authorship contribution statement

Richard Marquardt: Conceptualization, Writing – original draft, Investigation, Conceptualization, Methodology, Software, Visualization. **Julia Cipo:** Investigation, Software, Writing – original draft, Writing – review & editing. **Felix Schlichting:** Software, Investigation, Writing – review & editing. **Gitanjali Kolhatkar:** Data curation, Writing – review & editing. **Hermann Kohlstedt:** Project administration, Validation, Writing – review & editing, Funding acquisition, Supervision. **Holger Kersten:** Conceptualization, Writing – review & editing, Project administration, Validation, Supervision.

Declaration of Competing Interest

The authors declare that they have no known competing financial interests or personal relationships that could have appeared to influence the work reported in this paper.

Acknowledgements

One of the authors (G.K.) is thankful for a postdoctoral fellowship from the Alexander von Humboldt foundation. Funded by the Deutsche Forschungsgemeinschaft (DFG, German Research Foundation) – Project-ID 434434223 – SFB 1461.

References

[1] A. Verevkin, J. Zhang, R. Sobolewski, A. Lipatov, O. Okunev, G. Chulkova, A. Korneev, K. Smirnov, G.N. Gol'tsman, A. Semenov, Detection efficiency of large-active-area NbN single-photon superconducting detectors in the ultraviolet to near-infrared range, Appl. Phys. Lett. 80 (Jun. (25)) (2002) 4687–4689, https://doi.org/10.1063/1.1487924.

[2] G. Reithmaier, J. Senf, S. Lichtmannecker, T. Reichert, F. Flassig, A. Voss, R. Gross, J.J. Finley, Optimisation of NbN thin films on GaAs substrates for in-situ single photon detection in structured photonic devices, J. Appl. Phys. 113 (Apr. (14)) (2013), 143507, https://doi.org/10.1063/1.4800838.

[3] V. Larrey, J. Villegier, M. Salez, F. Miletto-Granozio, A. Karpov, Processing and characterization of high Jc NbN superconducting tunnel junctions for THz analog circuits and RSFQ, IEEE Trans. Appl. Supercond. 9 (Jun. (2)) (1999) 3216–3219, https://doi.org/10.1109/77.783713.

[4] Q. Zhang, H. Wang, X. Tang, W. Peng, Z. Wang, Fabrication and characteristics of all-NbN SQUID series array, IEEE Trans. Appl. Supercond. 30 (Apr. (3)) (2020) 1–3, https://doi.org/10.1109/TASC.2019.2938582.

[5] I. Holzman, Y. Ivry, On-chip integrable planar NbN nanoSQUID with broad temperature and magnetic-field operation range, AIP Adv. 9 (Oct. (10)) (2019), 105028, https://doi.org/10.1063/1.5100259.

[6] S. Leith, M. Vogel, J. Fan, E. Seiler, R. Ries, X. Jiang, Superconducting NbN thin films for use in superconducting radio frequency cavities, Supercond. Sci. Technol. 34 (Jan. (2)) (2021), 025006, https://doi.org/10.1088/1361-6668/abc73b.

[7] C. s Sandu, M. Benkahoul, M. Parlinska-Wojtan, R. Sanjines, F. Lévy, Morphological, structural and mechanical properties of NbN thin films deposited by reactive magnetron sputtering, Surf. Coat. Technol. 200 (2006) 6544–6548, https://doi.org/10.1016/j.surfcoat.2005.11.054. Jun.

[8] M.J. Deen, The effect of the deposition rate on the properties of d.c.-magnetron-sputtered niobium nitride thin films, Thin Solid Films 152 (Sep. (3)) (1987) 535–544, https://doi.org/10.1016/0040-6090(87)90269-0.

[9] D.D. Bacon, A.T. English, S. Nakahara, F.G. Peters, H. Schreiber, W.R. Sinclair, R. B. van Dover, Properties of NbN thin films deposited on ambient temperature substrates, J. Appl. Phys. 54 (Nov. (11)) (1983) 6509–6516, https://doi.org/10.1063/1.331881.

[10] M.S. Wong, W.D. Sproul, X. Chu, S.A. Barnett, Reactive magnetron sputter deposition of niobium nitride films, J. Vac. Sci. Technol. A 11 (Jul. (4)) (1993) 1528–1533, https://doi.org/10.1116/1.578696.

[11] Y.M. Shy, L.E. Toth, R. Somasundaram, Superconducting properties, electrical resistivities, and structure of NbN thin films, J. Appl. Phys. 44 (Dec. (12)) (1973) 5539–5545, https://doi.org/10.1063/1.1662193.

[12] T. Polakovic, S. Lendinez, J.E. Pearson, A. Hoffmann, V. Yefremenko, C.L. Chang, W. Armstrong, K. Hafidi, G. Karapetrov, V. Novosad, Room temperature deposition of superconducting niobium nitride films by ion beam assisted sputtering, APL Mater. 6 (Jul. (7)) (2018), 076107, https://doi.org/10.1063/1.5031904.

[13] J. Benedikt, H. Kersten, A. Piel, Foundations of measurement of electrons, ions and species fluxes toward surfaces in low-temperature plasmas, Plasma Sources Sci. Technol. 30 (Mar. (3)) (2021), 033001, https://doi.org/10.1088/1361-6595/abe4bf.

[14] M. Tinkham, Introduction to Superconductivity, Courier Corporation, 2004.

[15] M.P. MacMartin, N.L. Kusters, A direct-current-comparator ratio bridge for four-terminal resistance measurements, IEEE Trans. Instrum. Meas. 15 (Dec. (4)) (1966) 212–220, https://doi.org/10.1109/TIM.1966.4313542.

[16] J.H. Kim, S.X. Dou, J.L. Wang, D.Q. Shi, X. Xu, M.S.A. Hossain, W.K. Yeoh, S. Choi, T. Kiyoshi, The effects of sintering temperature on superconductivity in MgB_2/Fe wires, Supercond. Sci. Technol. 20 (May (5)) (2007) 448–451, https://doi.org/10.1088/0953-2048/20/5/007.

[17] S. Banerjee, A.A.I. Aarnink, R. van de Kruijs, A.Y. Kovalgin, J. Schmitz, PEALD AlN: controlling growth and film crystallinity, Phys. Status Solidi c 12 (7) (2015) 1036–1042, https://doi.org/10.1002/pssc.201510039.

[18] P.D. Edmondson, Y. Zhang, S. Moll, F. Namavar, W.J. Weber, Irradiation effects on microstructure change in nanocrystalline ceria - phase, lattice stress, grain size and boundaries, Acta Mater 60 (Sep. (15)) (2012) 5408–5416, https://doi.org/10.1016/j.actamat.2012.07.010.

[19] J.A. Thornton, Substrate heating in cylindrical magnetron sputtering sources, Thin Solid Films 54 (Oct. (1)) (1978) 23–31, https://doi.org/10.1016/0040-6090(78)90273-0.

[20] S. Gauter, F. Haase, H. Kersten, Experimentally unraveling the energy flux originating from a DC magnetron sputtering source, Thin Solid Films 669 (2019) 8–18, https://doi.org/10.1016/j.tsf.2018.10.021. Jan.

[21] S. Bornholdt, H. Kersten, Transient calorimetric diagnostics for plasma processing, Eur. Phys. J. D 67 (Aug. (8)) (2013) 176, https://doi.org/10.1140/epjd/e2013-40148-8.

[22] M. Stahl, T. Trottenberg, H. Kersten, A calorimetric probe for plasma diagnostics, Rev. Sci. Instrum. 81 (Feb. (2)) (2010), 023504, https://doi.org/10.1063/1.3276707.

[23] H.M. Mott-Smith, I. Langmuir, The theory of collectors in gaseous discharges, Phys. Rev. 28 (Oct. (4)) (1926) 727–763, https://doi.org/10.1103/PhysRev.28.727.

[24] R.H. Huddlestone, S.L. Leonard, Plasma diagnostic techniques, J. Plasma Phys. 1 (1) (1965) 156, https://doi.org/10.1017/S0022377800003160.

[25] B.B. Sahu, J.G. Han, M. Hori, K. Takeda, Langmuir probe and optical emission spectroscopy studies in magnetron sputtering plasmas for Al-doped ZnO film deposition, J. Appl. Phys. 117 (Jan. (2)) (2015), 023301, https://doi.org/10.1063/1.4905541.

[26] X. Wang, Q. Li, Z. Chen, W. Wang, C. Xie, J. Wang, Q. Gao, W. Peng, X. Geng, G.-N. Luo, A newly designed actively water-cooled Langmuir probe for tokamak devices, Rev. Sci. Instrum. 90 (2019) 6.

[27] A. Piel, Plasma Physics: an Introduction to Laboratory, Space, and Fusion Plasmas, Springer, 2017.

[28] Z. Wang, A. Kawakami, Y. Uzawa, B. Komiyama, Superconducting properties and crystal structures of single-crystal niobium nitride thin films deposited at ambient substrate temperature, J. Appl. Phys. 79 (May (10)) (1996) 7837–7842, https://doi.org/10.1063/1.362392.

[29] N.N. Iosad, A.V. Mijiritskii, V.V. Roddatis, N.M. van der Pers, B.D. Jackson, J. R. Gao, S.N. Polyakov, P.N. Dmitriev, T.M. Klapwijk, Properties of (Nb0.35, Ti0.15) xNi1−x thin films deposited on silicon wafers at ambient substrate temperature,

J. Appl. Phys. 88 (Nov. (10)) (2000) 5756–5759, https://doi.org/10.1063/1.1319653.

[30] N.N. Iosad, N.M. van der Pers, S. Grachev, V.V. Roddatis, B.D. Jackson, S. N. Polyakov, P.N. Dmitriev, T.M. Klapwijk, Texture formation in sputter-deposited (Nb0.7,Ti0.3)N thin films, J. Appl. Phys. 92 (Nov. (9)) (2002) 4999–5005, https://doi.org/10.1063/1.1510589.

[31] M. Wittmer, Properties and microelectronic applications of thin films of refractory metal nitrides, J. Vac. Sci. Technol. A 3 (Jul. (4)) (1985) 1797–1803, https://doi.org/10.1116/1.573382.

[32] F. Marsili, A. Gaggero, L.H. Li, A. Surrente, R. Leoni, F. Lévy, A. Fiore, High quality superconducting NbN thin films on GaAs, Supercond. Sci. Technol. 22 (Aug. (9)) (2009), 095013, https://doi.org/10.1088/0953-2048/22/9/095013.

[33] H.C. Jones, Some properties of granular thin films of high-field superconductors, Appl. Phys. Lett. 27 (8) (1975) 471, https://doi.org/10.1063/1.88532.

[34] G. Deutscher, Y. Imry, L. Gunther, Superconducting phase transitions in granular systems, Phys. Rev. B 10 (Dec. (11)) (1974) 4598–4606, https://doi.org/10.1103/PhysRevB.10.4598.

[35] M. Gurvitch, M. Washington, H. Huggins, J. Rowell, Preparation and properties of Nb Josephson junctions with thin Al layers, IEEE Trans. Magn. 19 (May (3)) (1983) 791–794, https://doi.org/10.1109/TMAG.1983.1062296.

[36] S.P. Chockalingam, M. Chand, J. Jesudasan, V. Tripathi, P. Raychaudhuri, Superconducting properties and Hall effect of epitaxial NbN thin films, Phys. Rev. B 77 (Jun. (21)) (2008), 214503, https://doi.org/10.1103/PhysRevB.77.214503.

[37] R. Kieffer, H. Nowotny, P. Ettmayer, G. Dufek, Neue Untersuchungen über die Mischbarkeit von Übergangsmetallnitriden und-karbiden, Metall (26) (1972) 701.

[38] N.C. Halder, C.N.J. Wagner, Separation of particle size and lattice strain in integral breadth measurements, Acta Cryst. 20 (Feb. (2)) (1966) 312–313, https://doi.org/10.1107/S0365110X66000628.

[39] S. Kubo, M. Asahi, M. Hikita, M. Igarashi, Magnetic penetration depths in superconducting NbN films prepared by reactive dc magnetron sputtering, Appl. Phys. Lett. 44 (Jan. (2)) (1984) 258–260, https://doi.org/10.1063/1.94690.

[40] J.A. Thornton, Influence of apparatus geometry and deposition conditions on the structure and topography of thick sputtered coatings, J. Vac. Sci. Technol. 11 (Jul. (4)) (1974) 666–670, https://doi.org/10.1116/1.1312732.

[41] J.A. Thornton, Influence of substrate temperature and deposition rate on structure of thick sputtered Cu coatings, J. Vac. Sci. Technol. 12 (Jul. (4)) (1975) 830–835, https://doi.org/10.1116/1.568682.

[42] O. Kluth, G. Schöpe, J. Hüpkes, C. Agashe, J. Müller, B. Rech, Modified Thornton model for magnetron sputtered zinc oxide: film structure and etching behaviour, Thin Solid Films 442 (Oct. (1)) (2003) 80–85, https://doi.org/10.1016/S0040-6090(03)00949-0.

[43] N. Otsu, A threshold selection method from gray-level histograms, in: IEEE Transactions on Systems, Man, and Cybernetics, 9, 1979. Art. no. 1.

[44] S.M. Rossnagel, Energetic particle bombardment of films during magnetron sputtering, J. Vac. Sci. Technol. A 7 (May (3)) (1989) 1025–1029, https://doi.org/10.1116/1.576223.

[45] E.G. Sheikin, The pressure dependence of the deposition rate in a magnetron sputtering system, Thin Solid Films 574 (2015) 52–59, https://doi.org/10.1016/j.tsf.2014.11.043. Jan.

[46] S.N. Mazhir, M.K. Khalaf, S.K. Taha, H.K. Mohsin, Measurement of plasma electron temperature and density by using different applied voltages and working pressures in a magnetron sputtering system, IJET 7 (Jun. (3)) (2018) 1177, https://doi.org/10.14419/ijet.v7i3.9459.

[47] F. Zahari, F. Schlichting, J. Strobel, S. Dirkmann, J. Cipo, S. Gauter, J. Trieschmann, R. Marquardt, G. Haberfehlner, G. Kothleitner, L. Kienle, T. Mussenbrock, M. Ziegler, H. Kersten, H. Kohlstedt, Correlation between sputter deposition parameters and *I-V* characteristics in double-barrier memristive devices, J. Vac. Sci. Technol. B 37 (Nov. (6)) (2019), 061203, https://doi.org/10.1116/1.5119984.

[48] K.L. Cartwright, J.P. Verboncoeur, C.K. Birdsall, Nonlinear hybrid Boltzmann-particle-in-cell acceleration algorithm, Phys. Plasmas 7 (Jul. (8)) (2000) 3252–3264, https://doi.org/10.1063/1.874191.

[49] Z. Wang, H. Terai, A. Kawakami, Y. Uzawa, Interface and tunneling barrier heights of NbN/AlN/NbN tunnel junctions, Appl. Phys. Lett. 75 (Jul. (5)) (1999) 701–703, https://doi.org/10.1063/1.124487.

[50] P. Gu, X. Zhu, H. Wu, D. Yang, Regulation of substrate-target distance on the microstructural, optical and electrical properties of CdTe films by magnetron sputtering, Materials 11 (Dec. (12)) (2018), https://doi.org/10.3390/ma11122496.

[51] E. Martines, R. Cavazzana, G. Serianni, M. Spolaore, L. Tramontin, M. Zuin, V. Antoni, Electrostatic fluctuations in a direct current magnetron sputtering plasma, Phys. Plasmas 8 (May (6)) (2001) 3042–3050, https://doi.org/10.1063/1.1369657.

5.3 Energy-dependent film growth of Cu and NiTi

Publication 3

Energy-dependent film growth of Cu and NiTi from a tilted DC magnetron sputtering source determined by calorimetric probe analysis

Authors	F. Schlichting, L. Thormählen, J. Cipo, D. Meyners, H. Kersten
Journal	Surface & Coatings Technology [103]
Technique	Energy flux measurements, scanning electron microscopy, atomic force microscopy, focused ion beam imaging
Own contribution	approximately 40%

Experimental Setup:

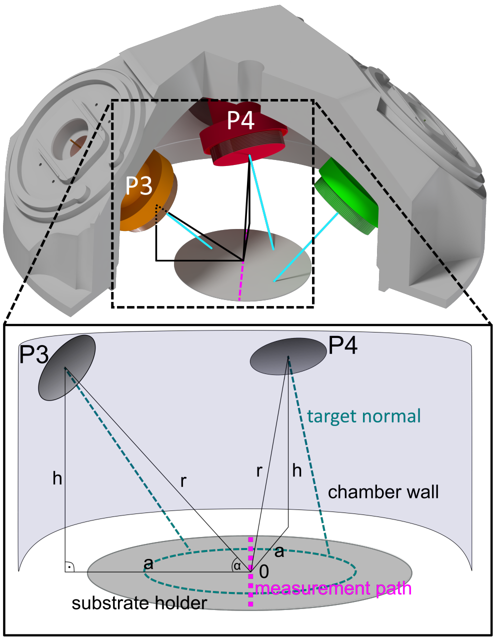

Caption

The Von Ardenne CS400S cluster sputter device has four 4-inch targets arranged perpendicularly above a rotatable substrate holder with a diameter of 200 mm. The targets are tilted at a 45° angle towards the substrate holder. The PTP was moved along the axis of the substrate holder (measurement path) in steps of 10 mm. The two targets P3 and P4 were investigated separately.

Motivation:

Copper (Cu) and nickel-titanium (NiTi) are commonly used metals in the semiconductor industry and for microelectrochemical systems (MEMS). Cu thin films can well be used as electrical conductors or seed layers. NiTi on the other hand is widely used for its shape memory effect. The studied sputter device deposits homogeneous coatings on 200 mm wafers with dcMS by rotating the substrate holder during deposition. However, the size of the substrate holder and the unusual arrangement of the targets gives rise to the question of whether the film properties are evenly distributed over the substrate dimensions without rotating it. Sputter-deposited Cu layers usually have a crystalline structure while NiTi is initially deposited in an amorphous state. As is commonly known the properties and intended functionality of thin films vary with film structure, morphology and growth conditions. The energy balance at the substrate surface serves as a valuable connection between the plasma and film properties.

Main Results:

The energy flux density and deposition rate decrease with increasing probe-to-target distance in a corresponding manner for all measurement points. The Cu thin films show a qualitatively similar bulk growth behaviour over the entire measurement path. A dense film with randomly orientated crystalline grains was measured with FIB imaging. For a low deposition rate also the surface roughness is small. With an increased deposition rate, the surface roughness reaches a plateau-like maximum. The NiTi films' cross-sectional analysis (SEM) shows, however, a significant dependence of the morphology on the energy flux density and the angle of incidence of the film-forming particles. With increasing target distance the films change from compact film to columnar growth. Even the development of an increasing growth angle is visible. The surface roughness exhibits a high dependency on the distance and reflects the change in the growth behaviour. Rotating the substrate holder can homogenize the deposition rate, but can not adjust the film structure change in the inner radii. This can only be accomplished by added tools such as a heat supply.

Surface & Coatings Technology 450 (2022) 129000

Contents lists available at ScienceDirect

Surface & Coatings Technology

journal homepage: www.elsevier.com/locate/surfcoat

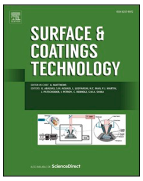

Full Length Article

Energy-dependent film growth of Cu and NiTi from a tilted DC magnetron sputtering source determined by calorimetric probe analysis

Felix Schlichting [a,*,1], Lars Thormählen [b,1], Julia Cipo [a], Dirk Meyners [b], Holger Kersten [a]

[a] *Institute for Experimental and Applied Physics, Kiel University, Leibnizstraße 19, 24098 Kiel, Germany*
[b] *Institute of Material Sciences, Faculty of Engineering, Kiel University, Kaiserstraße 2, 24143 Kiel, Germany*

ARTICLE INFO

Keywords:
Calorimetric plasma diagnostic
Magnetron sputtering
NiTi and Cu coatings
Thin film deposition

ABSTRACT

Plasma-based processes are key applications in microsystems technology and are mainly used for the deposition and modification of thin films. A strong dependence on used equipment and materials can easily affect plasma processes and results in many differences of process characteristics like energy flow and deposition rates. For a deeper understanding of inclined magnetron-deposited thin films, a passive thermal probe was used to investigate the correlation between the film growth of two commonly used metallic target materials (Cu and Ni 46.8/Ti 53.2) and the energy flow from the plasma to the substrate. The special design of the sputtering system with a fixed angle of 45° between targets and substrate allows homogeneous coating of 200mm wafers with 100mm targets. The passive thermal probe measurements were performed radially across the substrate area for two different magnetron positions. Complementary surface and cross-sectional analysis of the deposited layers by atomic force microscopy, focused ion beam technique, and fracture edge analysis by scanning electron microscopy were performed on thin film samples on silicon substrate to investigate the growth rate and structure of the films. The films deposited in these experiments exhibit randomly oriented crystalline grains and heavily position-dependent change in surface topography and morphology from compact films to columnar growth, for Cu and NiTi respectively.

1. Introduction

Plasma-assisted techniques are widely used in microsystems and semiconductor technology for the fabrication of functional films as well as their structuring. Examples of the methods are plasma etching, ion beam etching, reactive ion etching [1], plasma-enhanced chemical vapor deposition (PECVD) [2], and physical vapor deposition (PVD). A much used representative of PVD is magnetron sputtering [3], which is used to deposit a variety of different functional layers on different substrates such as silicon wafers. An important goal is to get as many reliable units per wafer as possible per process run. This demand requires ever larger substrates with a diameter of up to 200mm and more. By using tilted smaller targets in combination with rotating substrates, it is possible to homogeneously coat wafers with larger diameters [4,5]. This method offers companies, and, in particular, research institutions, an advantage in the procurement of targets, their lower costs, a possibility for co-deposition and combinatorial deposition.

The present study focuses on the diagnostic of an Ar plasma used for the fabrication of Cu and NiTi films by tilted DC magnetron sputtering. The deposition experiments are carried out in an industrial cluster sputter device Von Ardenne CS400S using 4 in. targets of the mentioned materials. Thin films made of Cu have proven to be very versatile in their functionality, serving as good electrical conductors or seed layers [6,7]. On the other hand, NiTi films are widely used for their shape memory effect, first shown in [8]. While sputter-deposited Cu layers usually exhibit a crystalline structure [9], Ti 53.2/Ni 46.8 films show an as-deposited amorphous state [10,11]. In general, properties and accessible functionality of thin films vary with film structure and growth conditions which are directly dependent on the configuration of the deposition tool as investigated here.

The energy balance at the substrate surface represents a good link between the plasma and film properties. The total energy influx consists of various contributions, such as plasma radiation, surface interactions, kinetic energy of the particles, but also from loss processes as emitted radiation, heat conduction and convection [12,13]. A versatile diagnostic tool to detect these contributions is the calorimetric probe,

---

* Corresponding author.
E-mail address: schlichting@physik.uni-kiel.de (F. Schlichting).
[1] F. S. and L. T. share co-first authorship and equally contributed to the publication.

https://doi.org/10.1016/j.surfcoat.2022.129000
Received 20 July 2022; Received in revised form 10 October 2022; Accepted 19 October 2022

designed by Thornton in 1978 [14] and developed over the years in different fields [15–17].

2. Experimental

2.1. Setup and sample preparation

The experiments were performed in a cluster physical vapor deposition (PVD) system Von Ardenne CS400S. The deposition tool is equipped with four 100mm balanced magnetron sources in an open field configuration which can be operated by DC or RF, respectively. The magnetron positions are at a fixed 45° angle to each other and to the horizontal axis of the chamber lid (see Fig. 1). A homogeneous coating of 200mm wafers is possible, provided that all inhomogeneities caused by the sputter geometry are compensated by rotation of the substrate holder. However, the basic study presented in this paper aims to identify the inhomogeneities in the plasma energy flow and film properties, which are observed without rotation and therefore must be compensated.

Two of the four target positions, namely P3 and P4, were investigated for two different DC discharge powers of 100W (12.73mW/mm^2 at target) and 300W (38.19mW/mm^2 at target) with copper target and NiTi target, respectively. Since the position P1 and P2 are symmetrical to P3 and P4, an investigation was not carried for all target positions. As DC source a Trumpf TruPlasma DC 3002 generator was used. During the experiments the gas flow was set to 30 sccm Ar, the operational gas pressure was $4.0 \cdot 10^{-3}$mbar, whereas the base pressure of the evacuated chamber was $2 \cdot 10^{-7}$mbar. At the operating pressure the mean free path of the argon gas atoms is about 16mm. Hence, collisions between sputtered particles and sputter gas atoms are expected. Therefore, a potential broadening of the incident angle distribution at the substrate surface due to the collisions must be considered. Except for the substrate rotation, these parameters correspond to the deposition parameters typically used in this chamber for thin film fabrication.

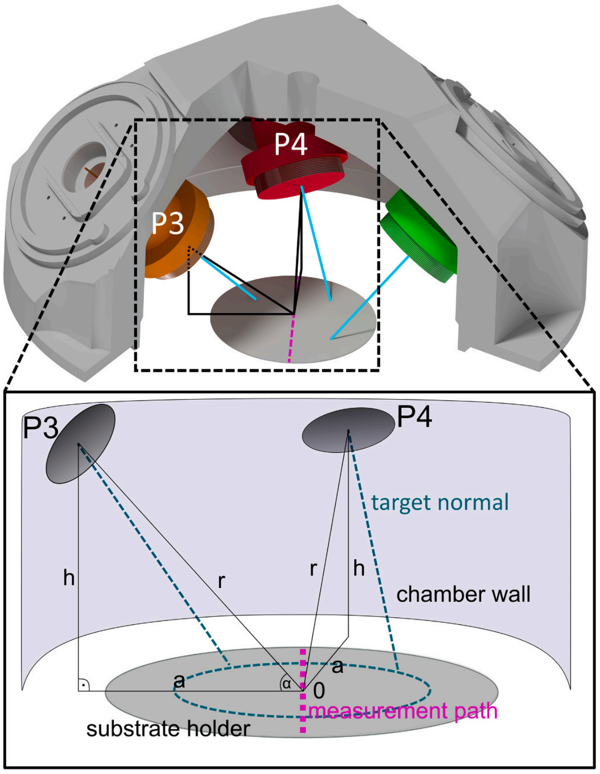

Fig. 1. Construction section of the deposition chamber with three visible tilted magnetron sources. The path of the calorimetric probe across the substrate holder in respect to the two examined targets P3 and P4 is marked by the dotted line. The centered target normals and their respective intersection points at the substrate holder are indicated by straight lines.

For the energy flux measurements a passive thermal probe (PTP) was placed into the deposition chamber in the substrate region. The PTP was mounted on a probe rod and guided over the horizontal center line of the sample plate, where measurements were taken in 10mm lateral steps. The measurement path is shown in Fig. 1. The vertical (h), horizontal (a) and radial distance (r) from the target center to the center of the substrate holder are the same for both targets, due to the radial symmetry of the chamber. To complement the energy flux measurements, samples were prepared for the examination of the thin layers, which have been deposited in a deposition process without the PTP, but at the same height and lateral position as chosen for the PTP. For the following film investigations lithographically prepared silicon samples with native oxide 5mm × 5mm and 10mm × 10mm were placed on the 200 mm sample plate along the PTP measurement path in 10 mm steps. For the deposition of the metal layers, the above mentioned parameters were used. The deposition times were set at 1800 s for Cu and 3600 s for NiTi at 300 W. For the 100 W depositions, the deposition times were twice.

After layer depositing and structuring by lift-off technique, the obtained sharp layer edges were scanned by a surface profiler (Ambios XP200 Profiler) to precisely determine the film thickness for the various sample positions. The results were cross-checked by scanning electron microscopy (SEM) (Zeiss Gemini Ultra55 Plus). Based on the deposition times the film growth rates were calculated. For Cu and NiTi, four of the 10mm × 10mm samples were selected to further investigate the position dependent film growth. Here, layers deposited by magnetron sputtering at target position P4 were examined. The surface topography was imaged using atomic force microscopy (AFM) (AJST-NT SmartSPM 1000) in scan areas of 5μm × 5μm for the Cu layers and 2μm × 2μm for the NiTi layers. To additionally inspect the film structure, cross sectional analysis for Cu and NiTi were carried out. The cross sections of Cu layers were fabricated by focused ion beam (FIB) (FEI Helios NanoLab 600i DualBeam) milling using 30 keV Ga ions. Imaging of the Cu cross sections was processed by rastering the focused ion beam and detecting secondary electron emission. Due to the amorphous structure of sputter-deposited NiTi films, the ion channeling effect is absent and a fracture edge analysis by SEM was conducted for the cross-sectional layer investigation of these samples.

2.2. Passive thermal probe

The concept of the passive thermal probe and the actual design used in these experiments have been presented in much detail before [18–20]. The probe consists of a substrate dummy made of a copper plate with a diameter of 11mm and a thickness of 100 μm. The temperature measurements used to determine the incoming integral energy flux are obtained via a Type K thermocouple, which is spot-welded to the back of the substrate dummy.

By measuring the change in temperature of the probe, a time and energy integrated value of the energy flux density can be calculated. This can be done by various methods. Here, we use the so-called *kink method* [16]. The temperature evolution of the probe is divided into two phases. If the magnetron source is on (i.e. during heating of the probe substrate) the overall change in enthalpy $\dot{H}_h$ of the probe is dominated by the incoming power P_{in}. This is mainly governed by charged and neutral particles impinging on the surface, surface processes like film formation, secondary electron emission or relaxation of meta stable atoms or molecules and heat radiation from the target or chamber walls. When the power source (magnetron plasma) is switched off, the substrate is cooling and its change in enthalpy $\dot{H}_c$ is now governed by the

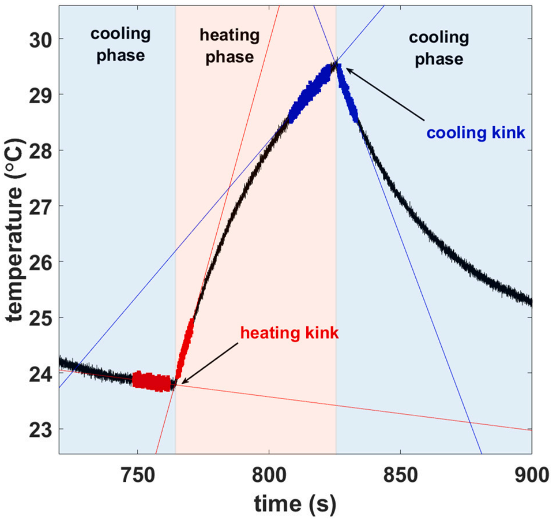

Fig. 2. Example for kink method evaluation of the temperature course, measured for sputtering at target position P3 with Cu target at 300 W. Straight lines indicate linear temperature fits around the thermal kinks.

power $P_{out,\,c}$ leaving the probe.

$$\dot{H}_h = C_s \dot{T}_h = P_{in} - P_{out,h} \tag{1}$$

$$\dot{H}_c = C_s \dot{T}_c = -P_{out,c} \tag{2}$$

Here, C_s is the heat capacity of the probe, which is determined by calibration with an electron beam, as described in [19]. $\dot{T}_h$ and $\dot{T}_c$ are the time derivatives of the temperature during the heating and cooling phase, respectively. During our experiments we kept the heating phase at 60 s and the cooling phase at 120 s.

For the evaluation method displayed in Fig. 2, we only examine short time periods around the two kinks appearing in the temperature course when the plasma source is switched on and off. Here, we can assume that the outgoing power during the respective phases is the same. Therefore, we can combine Eqs. (1) and (2) to calculate the incoming power and, consequently, the experimentally determined energy flux $J_{in,exp}$

$$J_{in} = \frac{P_{in,exp}}{A_s} = \frac{C_s}{A_s}\left(\dot{T}_h - \dot{T}_c\right), \tag{3}$$

where A_s is the probe surface area. For the kink method, as described in [16], linear fits are made around the kinks to determine $\left(\dot{T}_h - \dot{T}_c\right)$. From these two kinks a mean value is obtained as the energy flux density. To compensate an eventual change in the heat capacity of the probe during several deposition experiments due to film growth on the probe, calibration was done before and after each measurement cycle. The first calibration yielded a heat capacity of $C_{s,\,1} = 0.036 \pm 0.0006 J/K$. Calibration after the experiments yielded $C_{s,\,2} = 0.037 \pm 0.0006 J/K$. This slight change did not have any affect on the evaluation of the measurements. Therefore, all presented results were calculated with $C_{s,\,1}$.

3. Theoretical considerations

In order to verify our measuring technique and to interpret the contributions to the total energy flux, the individual contributions have been calculated, supported by simple simulations.

For these considerations the film deposition coming from the Cu target at position P3 was investigated in the centre of the substrate plate. We assume that all arriving Cu particles are contributing to the film formation. A significant part of the energy flux is linked to the incoming particle flux j_N and, thus, also to the number of film forming particles N:

$$N_{Cu} = N_A \cdot \frac{V_p \cdot \rho_{Cu}}{M_{Cu}} = 5.57 \cdot 10^{18}\,\text{particles} \tag{4}$$

where $V_p = A_p \cdot d_f$ denotes the volume of the film grown on the thermal probe. This leads to a particle flux of:

$$j_{N,Cu} = \frac{1}{A_p}\frac{N_{Cu}}{t} = 3.26 \cdot 10^{15}\,\frac{1}{\text{cm}^2 \cdot \text{s}} \tag{5}$$

The values and constants used in Eqs. (4) and (5) are summarized in Table 1.

Using $j_{N,\,Cu}$, the expected energy flux related to the film formation can be determined as follows:

$$J_{cond,theo,Cu} = j_{N,Cu} \cdot \Delta H_{V,Cu} = 1.82\,\frac{\text{mW}}{\text{cm}^2} \tag{6}$$

with $\Delta H_{V,\,Cu} = 3.48\,\text{eV}$ being the heat of condensation per copper atom [21].

To estimate the contribution due to the kinetic energy of the copper atoms reaching the probe at the center of the substrate holder, this part has been determined by simulations based on the SIMTRA code developed at Ghent University [22,23]. With this binary collision Monte Carlo simulation, the experimental setup as seen in Fig. 1 was used to calculate the energy of the incoming particles on the surface of the PTP. The applied power of 300 W results in voltage of +350V at the target, leading to a mean kinetic energy of a single sputtered Cu atom impinging on the substrate of $E_{kin,\,theo,\,Cu} = 5.1\,\text{eV}$.

By multiplying $E_{kin,\,theo,\,Cu}$ with the calculated particle flux, $j_{N,\,Cu}$, a total kinetic energy contribution results in:

$$J_{kin,theo,Cu} = j_{N,Cu} \cdot E_{kin,theo,Cu} = 2.66\,\frac{\text{mW}}{\text{cm}^2} \tag{7}$$

Together with $J_{cond,\,theo,\,Cu}$ the energetic contributions can be added together to a total energy influx of:

$$J_{in,Cu} = 4.48\,\frac{\text{mW}}{\text{cm}^2} \tag{8}$$

This calculated energy flux is lower than the value of $J_{in,exp} = 7.39\,\frac{\text{mW}}{\text{cm}^2}$ measured with the passive thermal probe at the center of the substrate holder under corresponding experimental conditions. However, the total energy influx is a sum of different energetic contributions, with the most important ones being the condensation energy and the kinetic energy of the incoming sputtered target atoms [13]. In addition, the recombination of charge carriers on the floating probe surface contributes minimally, since it results from a diminutive amount of argon ions, which recombine on the surface. The rather small amount of recombining ions is due to a minor ion flux far from the target region towards to probe surface, considering that the gas ionization degree is very small itself. Furthermore, the kinetic energy of the Ar ions may contribute, but is negligible, because the probe is at floating potential [24]. Since the theoretical value for the surface binding energy has been experimentally well confirmed [21] and therefore been used to calculate the

Table 1
Values and constants used for the calculation of incoming particle number for Cu deposition.

Physical data/constant	Value
Probe surface A_p	95mm^2
Deposition time t	1800s
Film thickness d_f	696nm
Molar mass of Cu M_{Cu}	$64\,\frac{\text{g}}{\text{mol}}$
Bulk density of Cu ρ_{Cu}	$8.96\,\frac{\text{g}}{\text{cm}^3}$
Avogadro's constant N_A	$6.022 \cdot 10^{23}\,\frac{1}{\text{mol}}$

condensation energy $J_{cond,\ theo,\ Cu}$, it is very likely for the simulated kinetic energy to be the reason for the lower calculated energy flux compared to our measured value. The complex geometry of the deposition chamber could not be replicated precisely in SIMTRA, due to limitations in the sketching of the chamber in the code.

In order to verify this assumption, the calculations are repeated for the NiTi depositions on position P3 at the centre of the substrate plate, corresponding to the conditions of the Cu depositions from above.

The nominal composition in atomic percentage of the NiTi is 46.8% Ni and 53.2% Ti, which leads to a ratio of 1 Ni atom per 1.14 Ti atoms. This proportion is to be considered in the calculation of the molar mass M_{NiTi}. Further on, the density of the NiTi target has to be considered for the simulations based on the SIMTRA code. Since it does not allow to simulate with a composite target, two simulations with pure Ni and pure Ti targets were performed and a weighted mean was calculated from the results.

Researching the density of different NiTi alloys has shown that the total density increases with higher percentages of Ni. Hence, the density of NiTi with a composition of 55% Ni and 45% Ti is $\rho_{Ni_{55}Ti_{45}} = 6.5\,\frac{\mathrm{g}}{\mathrm{cm}^3}$, for $Ni_{60}Ti_{40}$ the density increases up to $\rho_{Ni_{60}Ti_{40}} = 6.7\,\frac{\mathrm{g}}{\mathrm{cm}^3}$ [25].

Accordingly, the weighted mean is likely higher than the actual density of $Ni_{46.8}Ti_{53.2}$. For our calculations we proceed from a mean density of $\rho_{NiTi} = 6.5\,\frac{\mathrm{g}}{\mathrm{cm}^3}$ as a good approximation for the density of the target.

On the other side, the heat of condensation could not be provided through research, thus, a weighted mean has also been calculated using the atomic percentages of Ni and Ti.

The physical parameters used for the calculations are represented in Table 2. Other relevant values can be found in the above-mentioned Table 1.

In analogy to the previous calculations for copper, the calculated energy influx for NiTi towards the substrate is:

$$J_{inred,NiTi} = 8.18 \cdot 10^{15}\,\frac{\mathrm{eV}}{\mathrm{s \cdot cm^2}} = 1.31\,\frac{\mathrm{mW}}{\mathrm{cm}^2} \tag{9}$$

The calculated particle flux $j_{N,\ Niti}$, the heat of condensation $\Delta H_{V,\ NiTi}$ as well as the simulated kinetic energy $J_{kin,\ theo,\ NiTi}$ of the sputtered particles leading to this energy influx can be found in the appendix in Table 4.

The measured value for the same position, voltage and incidence angle was 4.8 $\frac{\mathrm{mW}}{\mathrm{cm}^2}$. Again, this deviation from the theoretical value can be attributed to the aforementioned reasons of the Cu simulations. Moreover, the weighted mean for the enthalpy of vaporization may not correspond to the actual value of the NiTi film and the density of 6.5 $\frac{\mathrm{g}}{\mathrm{cm}^3}$ may be close to the expected density, but is still an approximation. The exact value is probably smaller. The value for the mass density is also relevant for the simulations and, thus, influences $J_{kin,\ theo,\ NiTi}$.

Yet, the calculations provide results, which are in a comparable magnitude to the experimental ones. This way, we succeeded in developing a simple estimation based on our experimental measurement technique - the passive thermal probe.

Table 2
Parameters of the NiTi depositions.

Physical data	Value
Probe surface A_p	95mm^2
Deposition time t	3600s
Film thickness	414nm
Molar mass of NiTi M_{NiTi}	$54\,\frac{\mathrm{g}}{\mathrm{mol}}$
Density of NiTi ρ_{NiTi}	$6.5\,\frac{\mathrm{g}}{\mathrm{cm}^3}$

4. Results and discussion

All measurements were obtained for the same plasma conditions as mentioned in Section 2.1. Both target materials were used at the two positions (P3, P4) with different DC power (100 W, 300 W). In the following, we will discuss at first the results of the PTP measurements and film thickness measurements for the two target positions. In Section 4.3 we will go into more detail regarding the structure of the deposited films.

4.1. Deposition rate and energy flux for target position P3

Fig. 3 shows again a sketch of the experimental setup in more detail regarding target position P3.

For the PTP measurements the substrate holder was lowered, so that the height h=100 mm of the dummy substrate equals the height of the Si samples, which were subsequently coated for the materials investigation. The horizontal distance is a=145 mm. This amounts to a center of target to center of PTP distance of r=176 mm. At the edges of the substrate holder, e.g. radial positions +100 mm and −100 mm, the distance between the probe and the target center is $r + \Delta r_{P3} = 202\,mm$. So, the distance from the probe to the target center changes significantly across

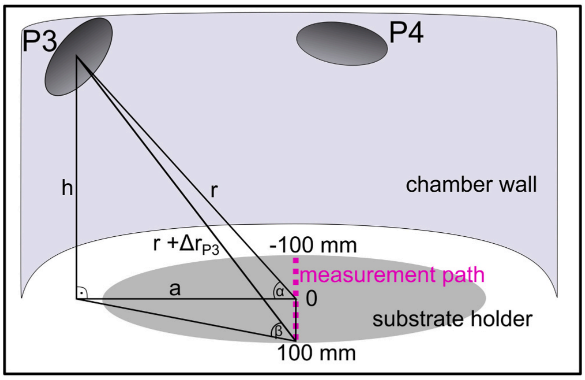

Fig. 3. Sketch of experimental setup. The path of the PTP across the substrate holder in respect to the two examined targets is marked by the dotted line.

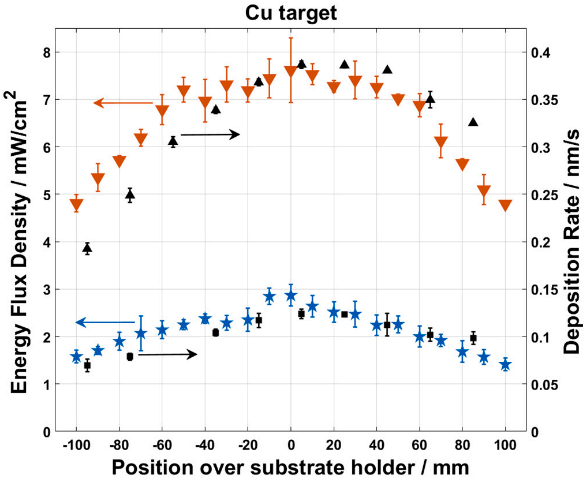

Fig. 4. PTP measurements for Cu target at position P3, obtained for 300 W (red triangle) and 100 W (blue pentagram) magnetron discharge power. The corresponding deposition rates are depicted as well (black triangles and black squares for 300 W and 100 W, respectively).

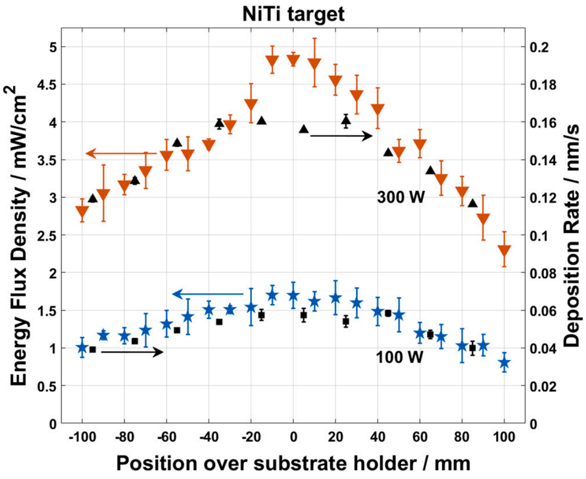

Fig. 5. PTP measurements for NiTi target at position P3, obtained for 300 W (red triangle) and 100 W (blue pentagram) magnetron discharge power, respectively. The corresponding deposition rates are depicted as well.

the substrate region.

In Figs. 4 and 5 the PTP measurements alongside the deposition rate taken for target position P3 for the Cu and NiTi target for both discharge powers are shown. In all of the measurements we take the center of the substrate holder as position 0 mm.

For both targets the energy flux to the probe shows a decrease towards the edges of the substrate holder. This is expected since the distance between the probe and the targets and, therefore, to the plasma plume increases. This decrease in energy flux coincides well with a decrease in film thickness and deposition rate. In Table 5, which can be found in the appendix, the deposition rate and corresponding film thickness for Cu at 300 W and a deposition time of 1800 s are exemplarily shown.

For both measurements the energy flux density and the deposition rate correlate well to each other. The 100 W measurements amount to roughly a third in magnitude to the 300 W measurements, as expected. Overall, the flux density and deposition rate for the Cu target are higher than for the NiTi target. Current-voltage measurements at the targets reveal that increasing the discharge power increases the current applied to the target significantly, while the voltage stays relatively constant compared to the increase in current, i.e. the kinetic energy of the Ar ions impinging on the targets is almost unchanged, while the number of ions striking the targets increases significantly with sputtering power. In Fig. 11 of the appendix these measurements are shown for the two targets. The higher energy flux and deposition rate when comparing the Cu to the NiTi target results from the significantly higher sputter yield of Cu compared to Ni and, especially, Ti [26]. More sputtered particles deliver more energy to the substrate surface. The significance of these different fluxes and deposition rates in terms of impact on the film growth and morphology will be discussed in Section 4.3.

As can be seen in Fig. 4 the energy flux and deposition rate on the right side (0…+100 mm) are slightly higher than on the left of the center of the substrate holder (0…−100 mm). For example, at −75 mm the deposition rate is roughly 0.25 nm/s and at +65 mm it is 0.35 nm/s. So, there is a asymmetry of about 0.1 nm/s around the center position. This difference in deposition rate, however, can be correlated to a different energy flux at these two position. For the −80 mm position of the PTP we have an energy flux density of 5.7 mW/cm^2. At the opposite end on position 60 mm we measured 6.9 mW/cm^2. Still, energy flux and deposition rate behave in a comparable manner across the substrate region. Hence, the energy influx is mainly governed by the arriving and film-forming particles. The asymmetry of the two characteristics with regard to position 0 mm can be explained by the target at position P3 being tilted in a 30° angle towards the +100 mm side of the substrate holder as is implied in the sketch of Fig. 3. This asymmetry does not seem to appear for the NiTi target. The overall lower energy of the incoming particles in comparison to copper seems to lead to less pronounced geometrical factors.

4.2. Deposition rate and energy flux for target position P4

Seen in the previous section, the sputter yield and, therefore, the energy flux at operating power of 100 W does barely exceed 1.5 mW/cm^2 for NiTi at position 0 mm directly beneath the target P3. When investigating target position P4, measurements at 100 W beyond the center position, as seen from P4, were hardly possible due to the low energy flux and, consequently, left out from this work. Therefore, the following section focuses on sputter deposition at 300 W DC power.

When looking at Fig. 3 the target at position P4 is in direction, but slightly off center of the movement of the PTP. The PTP is farthest away from the target at position +100 mm on the substrate holder (target center to PTP center distance: 260 mm) and closest to the target at −100 mm (target center to PTP center distance: 102 mm).

As expected the energy flux during deposition increases when moving the calorimetric probe towards the target. Fig. 6 shows the energy flux density measured across the substrate region for the two targets operated at 300 W, as well as the corresponding deposition rates.

The energy flux at the PTP reaches a maximum of 27 mW/cm^2 for Cu and 17.5 mW/cm^2 for NiTi, respectively. The quadratic fit to the data and the goodness of that fit suggests that we can assume magnetron sputter source as a point source (i.e. $I \sim \frac{1}{r^2}$).

Deposition rate and, consequently, the film thickness decrease in the same manner as the energy flux, see Tables 6 and 7 in the appendix. Assuming a constant film density, the energy per film-forming particle for Cu amounts to the calculated value of 3.48 eV (see Section 3) which is unchanged across the entire substrate position range. This is valid for both targets and positions and favorable for film homogenization by substrate plate rotation.

4.3. Film structure analysis and discussion

The mode of growth, topography and structure of the films is decisive for their quality, function and further processability. Therefore, this chapter focuses on the investigation of arising layer morphology

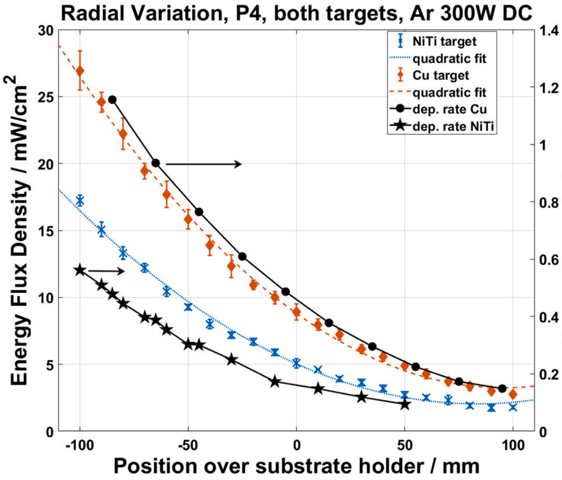

Fig. 6. Energy flux measurements for target position P4 for Cu (red diamond) and NiTi (blue cross) targets and associated deposition rates across the substrate region at 300 W.

observed for Cu and NiTi deposited from target position P4. In order to cover a wide range of energy flux density, the samples of the target position P4 were taken. Based on the results of the energy flux density measurements for P3 and P4 in Figs. 4, 5 and 6, the P3 thin film samples were not investigated since the P3 energy flux density interval is also covered by the measurements of target position P4.

Detailed information regarding the deposition conditions and the different analytical methods used to study the films are provided in Section 3.1. The Cu film cross sections were prepared using the FIB technique, while for the NiTi film cross sections a fracture edge analysis was performed using SEM. The resulting cross sections are illustrated in Fig. 7.

The studied samples of NiTi and Cu were selected at −90 mm, −70 mm, −30 mm and 10 mm positions on the sample plate. The angle of incidence of the film-forming particles ranges from about 60° measured from the horizontal line and at the −90 mm position to about 31° at the 10 mm position.

A strong contrast appears in the FIB images displayed in Fig. 7. This is caused by the known ion channeling effect [27,28] and results from a secondary electron yield variation due to a change of crystallographic orientation within the irradiated sample volume. In the layer thickness range investigated here, there is no evidence of a thickness dependence of the average Cu grain size. Furthermore, a change in the grain orientation can be observed in individual grains (marked positions), which runs through all samples.

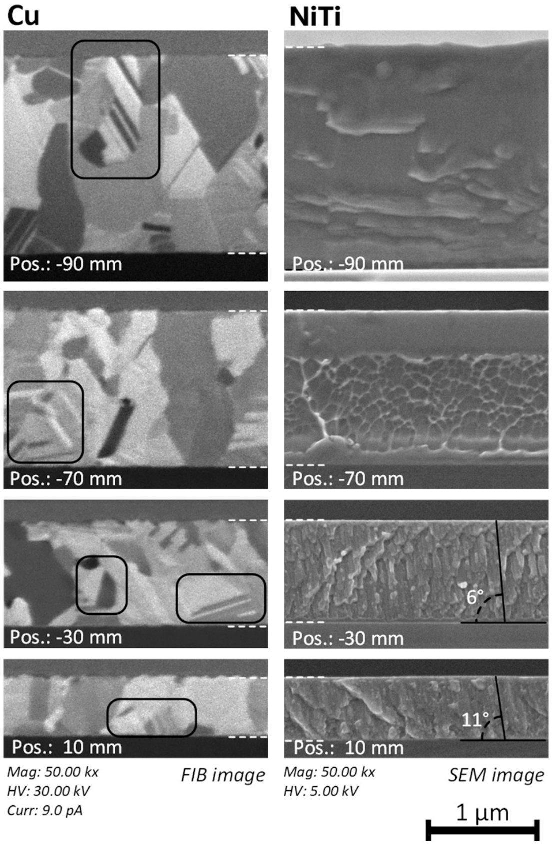

Fig. 7. Combined view of selected images for thin film cross-section study at different substrate positions for Cu (FIB, left) and NiTi (SEM, right). (Cu and NiTi target at position P4, 300W). The area delimited by the white lines shows the thin film under investigation. The areas of the copper samples marked in black show a change in the grain orientation. For NiTi, a change in film growth is observed over the range of sample positions. At sample positions −30 mm and 10 mm tilted columns become apparent.

When looking at the structure zone diagram (SZD) proposed by A. Anders [29] different growth morphologies are divided into zones, depending on a generalized temperature T^* of the films and a normalized energy flux E^*, which are governed by the potential and the kinetic energy of arriving and film forming particles, respectively. As seen in Fig. 6 the energy flux across the substrate holder decreases by about 90% for both targets. Since the Cu films show no change in their morphologies (zone 3, recrystallized grain structure, of the SZD, see Fig. 12 in the appendix), it can be assumed, that there is no significant change in the temperature due to the potential energy of the arriving particles and the change in energy flux does not render a change in growth.

A contrast to the copper films are the resulting fracture edges of the NiTi films shown in Fig. 7 on the right side. The fracture edges can be divided in two different subcategories. The first one concerns the −90 mm and −70 mm positions. The film grows rather dense and shows a smooth break edge. The sample at position −70 mm shows additional structures in the fracture pattern, which may have a cause in the way the fracture was produced. Secondly, looking at the positions −30 mm and 10 mm fractures, it can be seen that the fracture pattern differs remarkably. Inclined columnar structures with a preferred growth direction are formed, which become more refined as the deposition rate reduces from 0.25 nm/s at −30 mm to 0.15 nm/s at 10mm. The inclination of the columns increases from 6° to 11° as the deposition angle develops from 40° to 31°. As NiTi grows amorphously the SZD cannot be applied as it relates to crystal forming films. But the tilted columnar structures are a well-known phenomenon occurring angled material deposition with a high melting point and at low resulting surface diffusion. The resulting growth angle depends on the angle of the incoming film forming atoms and becomes larger with a reducing incident angle a (see Fig. 3) [3]. Recently, inclined columnar structures have also been reported for reactively sputter-deposited TiO_2 layers [30]. These observations support the assumption of a growth behavior of NiTi dependent on the incident angle in this particular case.

In comparison, both materials differ in their bulk growth behavior as seen in the cross sectional analysis in Fig. 7. Whereas copper shows no qualitative changes, the growth behavior of NiTi varies significantly. These differences must also be reflected in the surface topography and roughness. The corresponding AFM images of the selected positions and the determined roughness are shown in Fig. 8 and Table 3.

In the case of Cu, there are two types of surface topography which differ remarkably from each other. In the first case the surface topography of copper exhibits a valley structure with hillocks for samples closer to the target (positions −90 mm and −70 mm). This can be explained by the high deposition rate. Due to the high flux of film formers, Cu grains grow in an obstructive manner and collide at the grain boundaries. Without forming uniform large grains, they start to expand along the grain boundaries and form a random stripe structure.

This pattern becomes less pronounced with increasing distance from the deposition source and changes to the second type of surface topography observed at sample position −30 mm and 10 mm. The strip structure is absent, and the diameter of the hillocks decreases from about 100 nm at position −30 mm to 50 nm at position 10 mm (see Table 3).

As no other parameters were changed, the transition in surface topography from first type to second type must be a result of the growth rate becoming lower and the angle of incidence enlarging with increasing substrate position. Summarizing all sample positions, the surface topography changes to finer structures with increasing substrate position. This is associated with a lowering of growth rate, total energy flux, and film thickness.

On the other hand, NiTi shows a near consistent surface topography. The surface structure in Fig. 8 shows a dominantly growing hillocks structure with varying hillocks sizes for all NiTi samples (see Table 3).

As a measure of the surface roughness, root mean squares (RMS) of height data were calculated from the atomic force microscopy images. Considering the RMS values of AFM height data as a function of sample

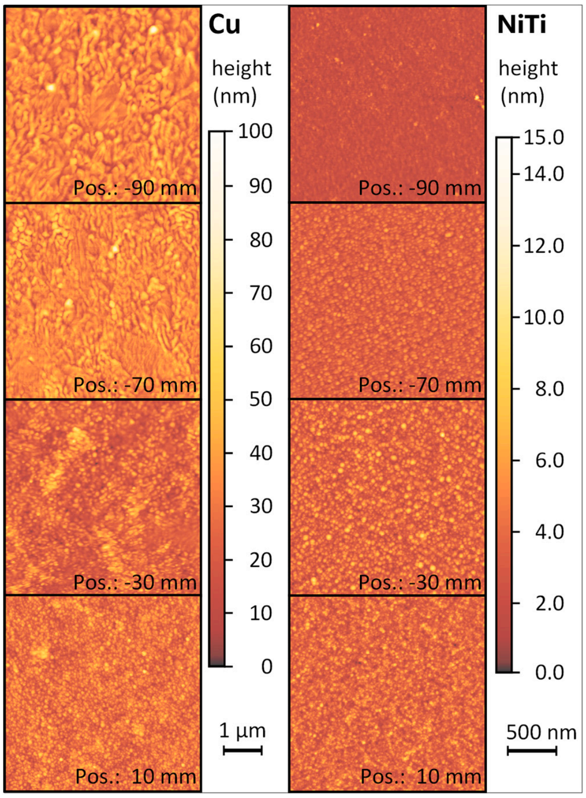

Fig. 8. Selected AFM images to study the thin film topography at different substrate positions [Cu target (left, 1µm scale) and NiTi (right, 500nm scale) at position P4, 300 W.]

Table 3
AFM data for Cu and NiTi deposited at 300W power and target position P4: RMS of height data and average hillocks diameter for 5µm×5µm (Cu) and 2µm×2µm (NiTi) scans.

AFM values for Cu and NiTi 300 W power				
Position/mm	Roughness/nm		Hillocks diameter/nm	
	Cu	NiTi	Cu	NiTi
−90	8.2	0.6	–	–
−70	7.3	0.8	–	35±8
−30	8.0	1.2	96±23	25±7
10	6.9	1.1	55±17	18±3
50	4.7	1.0	53±11	23±16
90	3.7	–	45±24	–

position, it is noticeable that the evolution of surface roughness with deposition rate and angle of incidence is significantly different for NiTi from that found for the Cu depositions.

A comparison of the Cu RMS data with the deposition rate, as seen in Fig. 9, reveals that a plateau occurs in the surface roughness data at about 7.5 nm for high rates above 0.4 nm/s. A possible reason for the differences in roughness of the Cu layers is the phenomenon of statistical roughness and self-shadowing [31]. The resulting roughness for specimens with low surface energy cannot be compensated due to low surface diffusion and increases with thickness to a point where deposition rate and surface energy allows faster surface diffusion. This is indicated by a smaller change in roughness for the samples closer to the target.

For the NiTi layers as displayed by the graph in Fig. 10, the thickest layer exhibits lowest surface roughness of RMS=0.5 nm. Obviously, at position −90 mm the steep angle of incidence promotes smooth layer growth shown in Fig. 7.

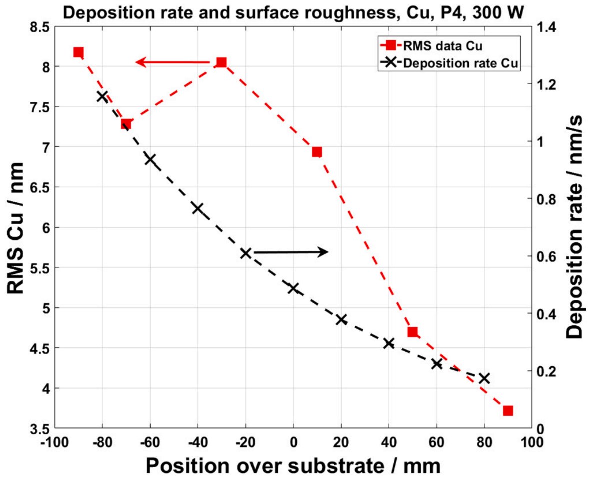

Fig. 9. Deposition rate and RMS height values (Cu target at position P4, 300 W).

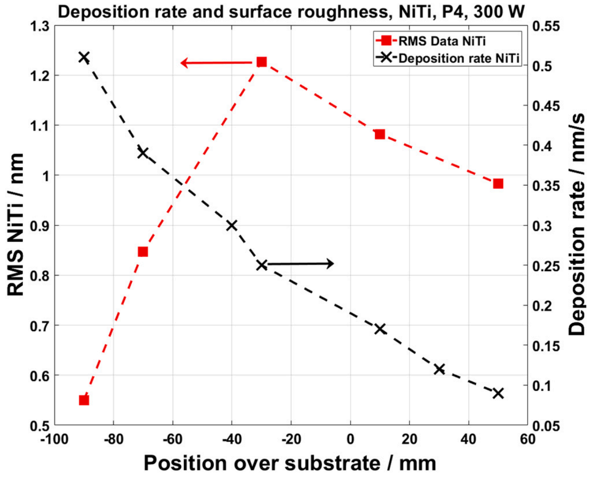

Fig. 10. Deposition rate and RMS height values (NiTi target at position P4, 300 W).

A possible explanation for this behavior is the low thermal conductivity of NiTi (Between 28 W/m·K and 18 W/m·K) [32] compared to Cu (401 W/m·K) [33]. The low heat conduction ensures a growing film near the source of an increasing surface temperature, since the surface energy generated by the film forming atoms cannot be dissipated. This allows the surface atoms to diffuse despite the high deposition rate. The direct consequence is a low surface roughness and a more compact thin film. This can be observed in the roughness values as well as in the cross-section samples in Fig. 7 for the −90 mm as well as for the −70 mm samples. Moving along the sample plate increases the deviation from normal incidence resulting in rougher surfaces reaching a maximum of RMS=1.2 nm under an angle of incidence equal to 40° at position −30 mm. In this substrate region the columnar growth of the film begins, which becomes finer the lower the growth rate and energy flux are, resulting in a slightly reduced roughness for the thinnest layer at sample position 50 mm.

5. Conclusion

The energy flux density from plasma to substrate was spatially measured by a passive thermal probe and correlated to the thin film growth in a tilted magnetron sputtering tool. Cu and Ni 46.8/Ti 53.2 were chosen as representative metallic materials growing crystalline and amorphous, respectively. In general, the geometrical position of the magnetrons in the deposition chamber results in varying conditions across the substrate region. In particular, the variation in energy flux can be well correlated to a change in deposition rate across the substrate.

The theoretically estimated energy fluxes originating from the sputter targets are comparably well in alignment with the measured energy flux at the examined positions. Despite the overestimation of condensation energy (for NiTi) and the difficulty in determining the kinetic energy of the particles via simulation, one can clearly state, that energy flux density mainly is governed by the condensation heat and kinetic energy from incoming particles, while contributions by radiation and recombination on the surface can be neglected. Energy flux coming from the Cu target is persistently higher than the energy flux from the NiTi target mainly because of the higher sputter yield.

The cross sectional analysis of the Cu layers reveals a dense film growth with randomly orientated crystalline grains across the entire substrate plate. The forming surface topography of Cu exhibits a low roughness value for thin samples at low deposition rates, which settles to a constant roughness value for thick films with increasing rate and energy flux. In contrast, the position-dependent angle of incidence of the film-forming particles leads to a significant change in the cross-sectional morphology of the NiTi layers. The deposited NiTi films show an overall change from compact films to columnar growth with the onset of a growth angle as known from oblique angle sputter deposition. The surface roughness of the samples increases with decreasing rate and energy flow.

Based on the chamber and discharge geometry shown in Fig. 1 and the measured fluxes of energy and film formers and deposition rates in Fig. 6 for the static case, it is obvious that in order to homogenize the energy flux and the resulting deposition rate, the substrate holder has to be rotated around its own axis. Depending on the rotational speed and the resulting change in orbital velocity, the deposition rate for the positions near the target will minimize and bring them closer to the values around the axis of rotation. In the case of copper, which shows a qualitatively similar bulk growth behavior over the entire measuring distance, this approach appears promising. Since the surface topography is mainly influenced by the deposition rate, it is expected that an equalization of the rate will also lead to a homogenization of the film surface.

In contrast, NiTi shows two qualitatively different bulk growth behaviors depending on the sample position, energy flux, resulting deposition rate, and deposition angle. To obtain a homogeneous deposition rate, homogenization can be performed by rotating the substrate plate. However, plate rotation cannot compensate for the film structure change in the inner radii of the substrate plate. For this fact, further mechanisms such as an active heat supply are necessary to positively influence the material redistribution by diffusion. For this reason, in a sputtering system with tilted magnetrons, it must be ensured that the rotation of the substrates must not only contribute to homogenization of the energy flux and layer thickness distribution, but also compensate for different growth morphologies induced by a variation in the angle of incidence.

CRediT authorship contribution statement

Felix Schlichting: Conceptualization, Investigation, Formal analysis, Writing – original draft, Writing – review & editing, Visualization, Software. **Lars Thormählen:** Conceptualization, Investigation, Formal analysis, Writing – original draft, Writing – review & editing, Visualization, Project administration. **Julia Cipo:** Investigation, Methodology, Writing – original draft. **Dirk Meyners:** Supervision, Conceptualization, Funding acquisition, Writing – review & editing. **Holger Kersten:** Supervision, Conceptualization, Writing – review & editing.

Declaration of competing interest

The authors declare that they have no known competing financial interests or personal relationships that could have appeared to influence the work reported in this paper.

Data availability

Data will be made available on request.

Acknowledgments

The authors thank Dr. Christiane Zamponi for a fruitful discussion and her insights in cross-sectional layer growth analysis. The authors would also like to thank Prof. Dr. Klaus Rätzke for the intensive discussions and support in the film analysis.

The presented work was financially supported by the German Research Foundation and the Collaborative Research Center CRC1261.

Appendix A

Table 4
Calculated and simulated values for the NiTi depositions.

Physical data	Value
$j_{N,\ NiTi}$	$8.33 \cdot 10^{14}\ \frac{1}{cm^2 \cdot s}$
$\Delta H_{V,\ NiTi}$	4.11eV
$J_{kin,\ theo,\ NiTi}$	5.72eV
$J_{in,\ particle,\ NiTi}$	9.82eV
$J_{in,\ NiTi}$	$1.31\ \frac{mW}{cm^2}$

Table 5
Film thickness and deposition rate for Cu sputtering at 300 W at target position P3.

300 W power Cu target		
Position/mm	Film thickness/nm	Deposition rate/*nm/s*
−95	346±11	0.19
−75	448±13	0.25
−55	549±10	0.31
−35	609±6	0.34
−15	662±7	0.37
5	696±7	0.39
25	694±4	0.39
45	685±2	0.38
65	629±16	0.35
85	585±3	0.33

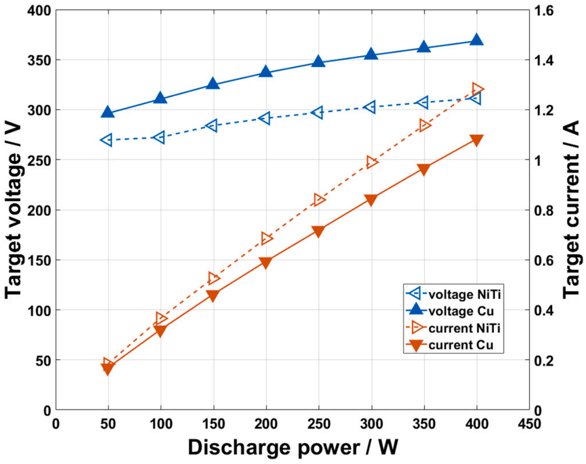

Fig. 11. Voltage and current at the Cu and NiTi target for different discharge powers, respectively.

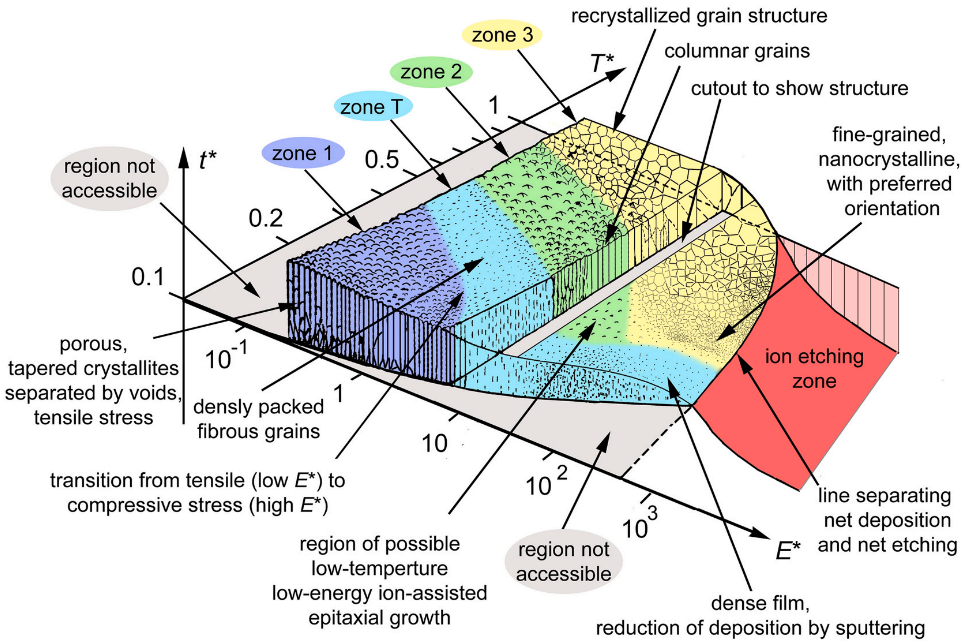

Fig. 12. The extended structure zone diagram taken from [29].

Table 6
Film thickness and deposition rate for Cu target at 300 W at target position P4.

300 W power Cu target		
Position/mm	Film thickness/nm	Deposition rate/*nm/s*
−85	2080±39	1.16
−65	1683±31	0.94
−45	1376±31	0.76
−25	1096±24	0.61
−5	875±15	0.49
15	680±17	0.38
35	532±17	0.30
55	404±18	0.22
75	312±26	0.17
95	268±8	0.15

Table 7
Film thickness and deposition rate for NiTi target at 300 W at target position P4.

300 W power NiTi target		
Position/mm	Film thickness/nm	Deposition rate/*nm/s*
−100	2022±26	0.56
−90	1834±14	0.51
−85	1721±6	0.48
−80	1603±19	0.45
−70	1431±21	0.40
−65	1396±18	0.39
−60	1275±10	0.36
−50	1091±9	0.30
−45	1082±18	0.30
−30	899±88	0.25
−15	623±104	0.17
15	534±28	0.15
35	429±23	0.12
55	339±16	0.09

References

[1] M.J. Madou, Manufacturing techniques for microfabrication and nanotechnology 2, CRC Press/Taylor & Francis, 2012. ISBN 9781420055191.

[2] L. Martinu, O. Zabeida, J. Klemberg-Sapieha, Chapter 9 - Plasma-Enhanced Chemical Vapor Deposition of Functional Coatings, in: P. M. Martin (Ed.), Handbook of Deposition Technologies for Films and Coatings (Third Edition), William Andrew Publishing, Boston, third edition edn., ISBN 978-0-8155-2031-3, 392–465, doi: 10.1016/B978-0-8155-2031-3.00009-0, 2010.

[3] M. Ohring, Materials Science of Thin Films, Second Edition, Academic Press, 2002, https://doi.org/10.1016/B978-012524975-1/50012-4 second edition edn., ISBN 978-0-12-524975-1.

[4] J. Dervaux, P.A. Cormier, P. Moskovkin, O. Douheret, S. Konstantinidis, R. Lazzaroni, S. Lucas, R. Snyders, Synthesis of nanostructured Ti thin films by combining glancing angle deposition and magnetron sputtering: a joint experimental and modeling study, Thin Solid Films. ISSN: 00406090 636 (2017) 644–657, https://doi.org/10.1016/j. tsf.2017.06.006.

[5] H. Zhu, E. Bunte, J. Hüpkes, S.M. Huang, Sputtering of ZnO:Al films from dual tube targets with tilted magnetrons, Thin Solid Films 519 (7) (2011) 2366–2370, https://doi.org/10.1016/j. tsf.2010.10.072. ISSN 00406090.

[6] Y. Pan, Y. Liu, T. Wang, X. Lu, Effect of a Cu seed layer on electroplated Cu film, Microelectron. Eng. 105 (2013) 18–24, https://doi.org/10.1016/j. mee.2012.12.004. ISSN 0167-9317.

[7] K. Mech, R. Kowalik, P. Żabiński, Cu Thin Films Deposited by DC Magnetron Sputtering for Contact Surfaces on Electronic Components, Archives of Metallurgy and Materials (No 4 December).

[8] J.D. Busch, A.D. Johnson, C.H. Lee, D.A. Stevenson, Shape-memory properties in ni-ti sputter-deposited film, J. Appl. Phys. 68 (12) (1990) 6224–6228, https://doi.org/10.1063/1.346914. ISSN 00218979.

[9] M.-T. Le, Y.-U. Sohn, J.-W. Lim, G.-S. Choi, Effect of sputtering power on the nucleation and growth of cu films deposited by magnetron sputtering, Mater. Trans. 51 (1) (2010) 116–120, https://doi.org/10.2320/matertrans.M2009183.

[10] E. Quandt, C. Zamponi, Superelastic NiTi thin films for medical applications, State-of-the-art Research and Application of SMAs 59 (2009) 190–197, https://doi.org/10.4028/www.scientific.net/ AST.59.190.

[11] F. Kahleyss, T. Surmann, C. Zamponi, C. Machai, D. Biermann, E. Quandt, R.L. d. Miranda, Processing and damping properties of sputtered NiTi thin films for tools in machining processes, J. Mater. Eng. Perform. 4 (20) (2011) 500–505, https://doi.org/10.1007/s11665-011-9847-x.

[12] H. Kersten, H. Deutsch, H. Steffen, G.M. Kroesen, R. Hippler, The energy balance at substrate surfaces during plasma processing, Vacuum 63 (3) (2001) 385–431, https://doi.org/10.1016/S0042-207X(01)00350-5. ISSN 0042207X.

[13] H. Kersten, G.M. Kroesen, R. Hippler, On the energy influx to the substrate during sputter deposition of thin aluminium films, Thin Solid Films 332 (1–2) (1998) 282–289, https://doi.org/10.1016/S0040-6090(98)01067-0. ISSN 00406090.

[14] J. A. Thornton, Substrate heating in cylindrical magnetron sputtering sources, Thin Solid Films 54 (23).

[15] K. Ellmer, R. Mientus, Calorimetric measurements with a heat flux transducer of the total power influx onto a substrate during magnetron sputtering, Surface and Coatings Technology 116-119 (1999) 1102–1106, https://doi.org/10.1016/S0257-8972(99)00125-5. ISSN 0257-8972.

[16] S. Gauter, M. Fröhlich, W. Garkas, M. Polak, H. Kersten, Calorimetric probe measurements for a high voltage pulsed substrate (PBII) in a HiPIMS process, Plasma Sources Science and Technology 26 (6), ISSN 13616595, doi: 10.1088/1361-6595/aa6f9e.

[17] F. Haase, D. Manova, D. Hirsch, S. Mändl, H. Kersten, Dynamic determination of secondary electron emission using a calorimetric probe in a plasma immersion ion implantation experiment, Plasma Sources Sci. Technol. 27 (4) (2018) 44003, https://doi.org/10.1088/1361-6595/ aabb2d. ISSN 13616595.

[18] S. Gauter, F. Haase, H. Kersten, Experimentally unraveling the energy flux originating from a DC magnetron sputtering source, Thin Solid Films 669 (2019) 8–18, https://doi.org/10.1016/j. tsf.2018.10.021. ISSN 00406090.

[19] M. Stahl, T. Trottenberg, H. Kersten, A calorimetric probe for plasma diagnostics, Rev. Sci. Instrum. 81 (2) (2010) 23504, https://doi.org/10.1063/1.3276707. ISSN 00346748.

[20] S. Bornholdt, M. Fröhlich, H. Kersten, Calorimetric Probes for Energy Flux Measurements in Process Plasmas, in: Springer International Publishing, Cham, 2014, pp. 197–234.

[21] Y. Kudriavtsev, A. Villegas, A. Godines, R. Asomoza, Calculation of the surface binding energy for ion sputtered particles, Appl. Surf. Sci. 239 (273–278) (apsusc.2004.06.014.), https://doi.org/10.1016/j.

[22] D. Depla, W. Leroy, Magnetron sputter deposition as visualized by Monte Carlo modeling, Thin Solid Films 520 (20) (2012) 6337–6354, https://doi.org/10.1016/ j. tsf.2012.06.032. ISSN 0040-6090.

[23] K.V. Aeken, S. Mahieu, D. Depla, The metal flux from a rotating cylindrical magnetron: a Monte Carlo simulation, J. Phys. D. Appl. Phys. 41 (20) (2008), 205307, https://doi.org/10.1088/0022-3727/41/20/205307.

[24] F. Haase, D. Lundin, S. Bornholdt, H. Kersten, On the impact of electron temperature in magnetron sputtering benchmarked with energy flux measurements, Contributions to Plasma Physics 55 (10) (2015) 701–713, https://doi.org/10.1002/ctpp.201510020. ISSN 15213986.

[25] C. Dellacorte, in: Nickel-Titanium Alloys: Corrosion “Proof” Alloys for Space Bearing, Components and Mechanism Applications, Proceedings of the 40th Aerospace Mechanisms Symposium (216334), 2010, pp. 293–300. ISSN 1757899X.

[26] A.H. Simon, Sputter Processing, in: K. Seshan (Ed.), Handbook of Thin Film Deposition: Techniques, Processes, and Technologies, Third Edition, William Andrew Publishing, Oxford, 2012, pp. 55–88, https://doi.org/10.1016/B978-1-4377-7873-1.00004-8, third edit edn., ISBN 9781437778748.

[27] R.E. Franklin, E.C. Kirk, J.R. Cleaver, H. Ahmed, Channelling ion image contrast and sputtering in gold specimens observed in a high-resolution scanning ion microscope, J. Mater. Sci. Lett. 7 (1) (1988) 39–41, https://doi.org/10.1007/BF01729909. ISSN 02618028.

[28] B.W. Kempshall, S.M. Schwarz, B.I. Prenitzer, L.A. Giannuzzi, R.B. Irwin, F. A. Stevie, Ion channeling effects on the focused ion beam milling of Cu, J. Vac. Sci. Technol. B: Microelectron. Nanometer Struct. 19 (3) (2001) 749, https://doi.org/10.1116/1.1368670. ISSN 0734211X.

[29] A. Anders, A structure zone diagram including plasma-based deposition and ion etching, Thin Solid Films 518 (15) (2010) 4087–4090, https://doi.org/10.1016/j.tsf.2009.10.145. ISSN 0040–6090.

[30] R. Tonneau, P. Moskovkin, J. Muller, T. Melzig, E. Haye, S. Konstantinidis, A. Pflug, S. Lucas, Understanding the role of energetic particles during the growth of TiO2 thin films by reactive magnetron sputtering through multi-scale Monte Carlo simulations and experimental deposition, J. Phys. D: Appl. Phys. ISSN: 13616463 54 (15) (2021) 155203.

[31] D.L. Smith, D.W. Hoffman, Thin-film deposition: principles and practice, Phys. Today 49 (4) (1996) 60, https://doi.org/10.1063/1.2807590.

[32] M.G. Faulkner, J.J. Amalraj, A. Bhattacharyya, Experimental determination of thermal and electrical properties of Ni-Ti shape memory wires, Smart Materials and Structures 9 (5) (2000) 632–639, https://doi.org/10.1088/0964-1726/9/5/307. https:doi:10.1088/0964-1726/9/5/307.

[33] D.R. Lide, CRC handbook of chemistry and physics vol. 85, CRC Press, 2021. ISBN 978-0367712600.

6 Novel concept of a combined plasma diagnostic using RFEA and PTP

Following the previous measurements and also the works of others utilizing the PTP for electrical measurements, the idea was developed to use it as the collector in an RFEA system. By using it as a planar Langmuir probe [88, 101], it was already shown that it is possible to make I-V measurements. The challenge now will be to put a grid system before the PTP while maintaining its usage as a thermal probe. It should not contact any surface since that would lead to unwanted thermal dissipation. But, still, it has to be close to the grid system. Putting the PTP as the collector would make possible the simultaneous measurement of ion energy distribution and the energy flux density towards the collector depending on the scan grid voltage.

The following chapter will overview the first concept design for such a combined diagnostic. It will detail the actual structure and issues that came with it. First measurements in different discharge environments will be shown as proof of principle. The challenges and obstacles will be discussed concerning the probe body's heating and the grids' spacing and insulation. Also, two different electronics were used depending on the plasma environment and ion energies therein. The electronics were already available in the workgroup for ion beam experiments with very high energies. But because it was designed for high voltages, an additional electronic was developed to measure small ion energies as they appear in, for example, rf plasmas.

6.1 Electronics and Software

The electronics described in [92, 93] are used for the thermal probe measurements. A circuit board is kept on the vacuum side and connected to a computer via a 9-pin Sub-D feedthrough. On the outside, a coaxial cable can connect to the bias cable of the PTP. For the RFEA measurements, four-channel electronics are used. The screen, scan and SE repeller grid are fed through a 9-pin Sub-D plug. On the outside of the chamber, coaxial cables are connected to the electronics. The PTP bias is connected to the collector outlet. Figure 6.1 schematically shows all components' wiring. Exemplarily shown is the experimental setup used for measurements in an rf plasma. The combined probe is embedded into the upper grounded electrode.

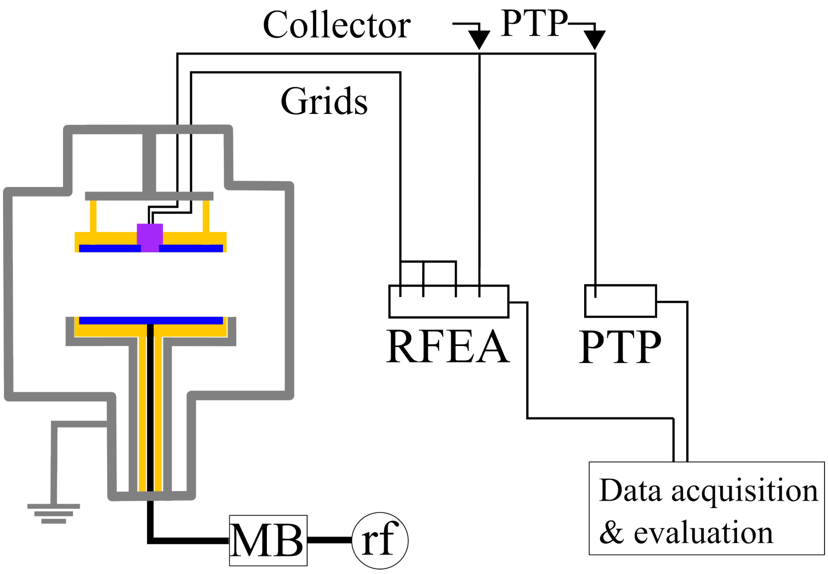

Figure 6.1: Circuit diagram of the setup as used in the rf plasma chamber. The combined diagnostic (purple) is embedded into the grounded electrode. The bias cable of the PTP is connected to the collector output of the RFEA electronics. Screen grid, scan grid and SE repelled are wired directly.

As pointed out earlier, one electronic was already available. With this, the scan grid can be biased with up to 2 kV. The voltage source is built for high positive voltages and measurements in ion beams. It is not very precise for voltages below 100 V. This means that, for example, a voltage sweep from -20 V to 50 V would not be possible. This range, however, is needed if one was to measure in an rf plasma where the ion energies seldom exceed 50 eV. So a second electronic was developed using a passively cooled operational amplifier for each channel. The screen grid and SE repeller always have a constant voltage bias. A voltage sweep from -125 V to 125 V can be applied to the scan grid. At the collector, the current measurements are done via four parallel resistances, which can be patched individually depending on how much current flows. The resistances are $10, 100, 1000$ and $10000\,\Omega$. Two National Instrument© USB-6009 devices are used for data acquisition, and an own LabView© program was written for it. With it, a standard RFEA measurement and the step-wise sweep of the scan grid needed for the combined measurements can be done. As previously discussed, the PTP needs time for heating and cooling. So the temperature change is recorded for static scan grid voltages while the plasma source is switched on (heating phase) and off (cooling phase). The evaluation is done with a Matlab© script.

6.2 First design

As previously stated, the method of the PTP has been developed and improved over the years in our workgroup. It consists of a probe body with a 13 mm diameter and a height of 30 mm. Figure 6.2 (Middle) details the design. The substrate platelet sticks out from the cable duct that goes through the middle. A ceramic tube insulates the cables (thermo couple and bias wire) from the stainless steel body. The protruding substrate/platelet can be adjusted in height and then fixated with a retainer screw. Figure 6.2 (Left) shows the grid holder. It is designed to be placed on the probe body and replace the shield (green). The grids (blue in the figure) have an 11 mm diameter and a latch going at a 90° angle to the sides. The cables are soldered to the latches and led through the bottom outer shield's base or side. The grids are separated from each other by 0.3 mm thick Teflon rings. For better clarity, only one of them is shown in 6.2 (Left).

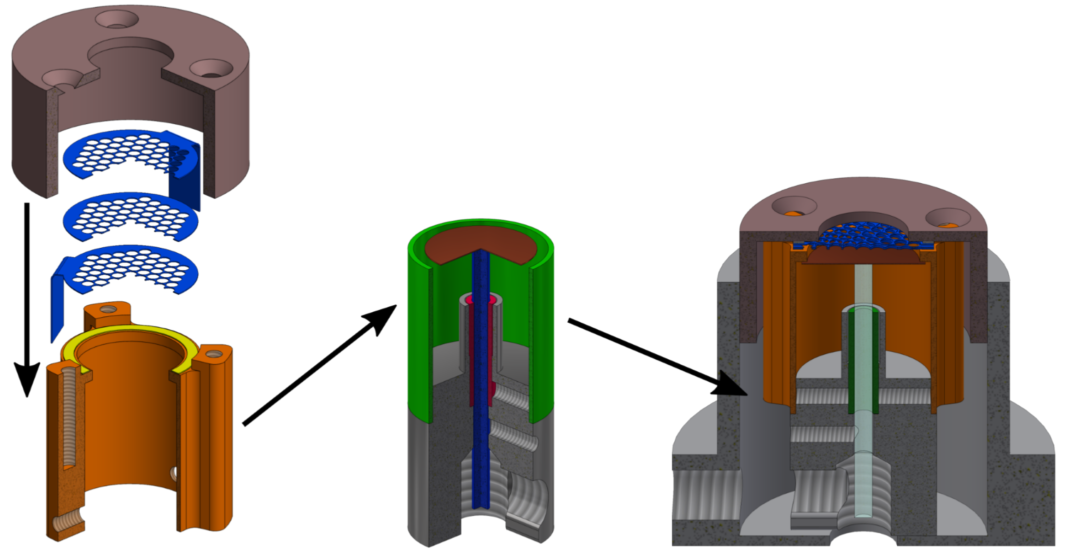

Figure 6.2: (Left) The RFEA grids (blue) are placed on top of the grid holder (orange) and separated by Teflon rings (yellow). The grids are fastened by the orifice cap (brown). (Middle) The grid holder replaces the shield (green) of the PTP. Picture taken from [87]. (Right) The combined grid system and PTP are placed inside the bottom outer shield. Here cable feed-throughs are accessible from the bottom or at a 90° angle.

Usually, the collector is also separated from the grid in front of it (SE repeller) by a thin insulating material, enabling RFEAs with minimal dimensions. In the combined case, the collector/PTP cannot have contact with any material, as was mentioned before. Therefore, the PTP is brought as close as possible to the inner lower edge of the grid holder, getting the distance from the SE repeller to the collector to approximately 0.6 mm. Two Teflon rings are used to separate the grids to equalize the distance between all grids and the collector/PTP.

An interchangeable orifice cap (steel) is screwed on the top and holds the grids. The orifice width can be changed depending on the application. If a fourth grid is used in front of the screen grid, it is grounded by contact with the lid. The bottom outer shield (steel) mounts the probe on a cable feed-through. This can either be done from the bottom or in a 90° angle, depending on the chamber geometry or desired orientation of the probe. The orifice entrance is 1 mm thick which can significantly alter the electric field in front of it. This can be compensated with a grounded grid in front of the screen grid, but only to a certain extent.

As mentioned in section 3.2, a parallel setup of rf-powered and grounded electrodes was built for the author's master thesis[54] with recesses to mount a PTP and an RFEA into it and have the probe surfaces aligned with the plasma-facing side of the grounded electrode. The setup in figure 6.2 (Right) was designed to fit into the grounded electrode. The orifice cap stands out at 5 mm from the upper edge of the bottom outer shield. This way, the orifice surface aligns with the plasma-facing surface of the grounded electrode.

Grid dimensions

The holes in the grids shown in figure 6.2 are not in scale. They are drawn larger for better illustration. The grid transparency and the alignment of the grids play an important role when designing an RFEA [104–108]. The hole diameter and grid distance should not exceed the mean free path of the ions $\lambda_{mfp,i}$. In an rf plasma, this usually ranges from 0.1 up to a few cm.

The first iteration of the grids were fine nickel mesh grids that were spot welded onto the edge of stainless steel rings. The rings had an outer diameter of 11 mm and an inner diameter of 9 mm. These grids had an optical transparency $T_{Ni} = 87\,\%$. In theory, when using three grids, total geometrical transparency T_G would come to $T_G = T_{Ni}^3 = 66\,\%$ [109]. However, the alignment of the grids plays a crucial role, as was found in [108]. In the case of the combined diagnostic, the misalignment and the difficulty in spacing them evenly led to a substantial reduction in the collector current. It was hardly distinguishable from the noise of the electronics and hindered PTP measurement impossible. The same effect was encountered for grids with 0.1 mm diameter holes that were drilled into plane steel discs. The holes were hexagonally distributed with a centre-to-centre distance of 0.15 mm. This way, the grids could be stacked on top of each other with a 120° angle to each other. This would, theoretically, allow for an alignment of the holes. In practice, this was difficult to achieve and did not sufficiently improve the measurements.

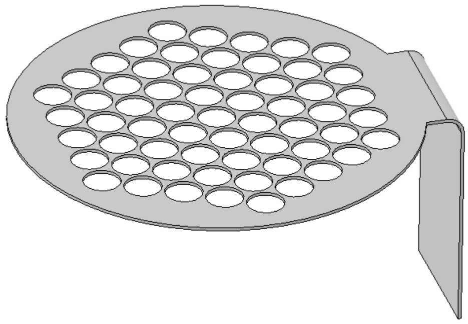

Figure 6.3: Grid with hexagonally aligned holes.

The simulations regarding the alignment of the grids that were done by van den Ven et al. [108], showed a considerable reduction in the total geometrical transparency for misaligned grids. Therefore, a new approach was used. Figure 6.3 shows the custom-made grids used in the first measurements done with the combined diagnostic. The holes are hexagonally aligned and have a diameter of 1.1 mm. The center-to-center distance is 1.25 mm, bringing the optical transparency to $T_{grid} = 57\%$. With this design, a compromise was made between the hole dimension and grid distance and the ability to align the grids and get an evaluable signal at the collector both with respect to current and energy flux density.

6.3 I-V characteristic and IED

After discussing the grids' geometry a few theoretical considerations concerning the determination of the ion energy distribution (IED) have to be made before showing the first measurements.

If only single-charged ions with a minimal velocity v_0 can pass through the RFEA grid system and are contributing to the current measured at the collector, the collector current I_C can generally be written as [71]:

$$I_C = Ae_0 \int_{v_0}^{\infty} v f(v) \mathrm{d}v \tag{6.1}$$

with A the area of the orifice entrance, e_0 the elementary charge. $f(v)$ is the ion velocity distribution assuming a one-directional distribution parallel to the axis of the RFEA grid system. v_0 is the minimum velocity of the incident ions which can pass the potential of the applied scan grid voltage V. In terms of energy, it is the minimum kinetic energy E_0 needed to overcome the potential. Using the relation $E = 1/2 m_i v^2 = e_0 V$ and substituting it in equation 6.1 gives:

$$I_C = Ae_0 \int_{V_0}^{\infty} v \frac{e}{m_i v} f(V) \mathrm{d}V \tag{6.2}$$

with V_0 being the start scan grid voltage. By simply differentiating the collector current the ion energy distribution $f(V)$ depending on the scan grid voltage is obtained:

$$f(V) = -\frac{m_i}{Ae_0^2}\frac{\mathrm{d}I_C}{\mathrm{d}V} \tag{6.3}$$

The reader will have noticed that only the ion energy distribution is mentioned in this work. Whether one uses the ion velocity distribution or the ion energy distribution is at times argued about, since it can be argued that rescaling the scan grid voltage (x-axis) with the relation $v = \sqrt{2eV/m_i}$ would deliver the actual velocity distribution and compress it compared to the energy distribution [70].

And since this work focuses on the feasibility of a combination of two diagnostics and the new possibilities it brings regarding the investigation of the energy balance of species in different plasma environments, a precise determination of the ion velocity distribution is deliberately left out. This is also due to the measurement of energy flux densities which are also done with respect to the scan grid voltage. Therefore, a better comparison between the two is given if the ion energy distribution (IED) is simply derived by differentiating the collector current, displayed in arbitrary units.

6.4 Proof of principle

Figure 6.4 shows the first measurements of the combined diagnostic. The probe was embedded into the grounded electrode of a parallel plate rf plasma and a 6 mm orifice cap was used. The vacuum chamber and placing of the electrodes were detailed in chapter 3.2 and schematically shown in figure 3.4. The plasma is excited with a 13.56 MHz radio-frequency voltage. The working gas is argon at a pressure of 5 Pa. Additionally, a grounded grid was used in front of the screen grid. Previous tests with smaller orifices resulted in a tiny current measured at the collector that could hardly be distinguished from the noise. Therefore, the 6 mm orifice with an extra grounded grid was used. The grounded grid was used to homogenise the electric field of the plasma sheath in front of the probe. With these tests, the versatility of the modular build probe could be verified.

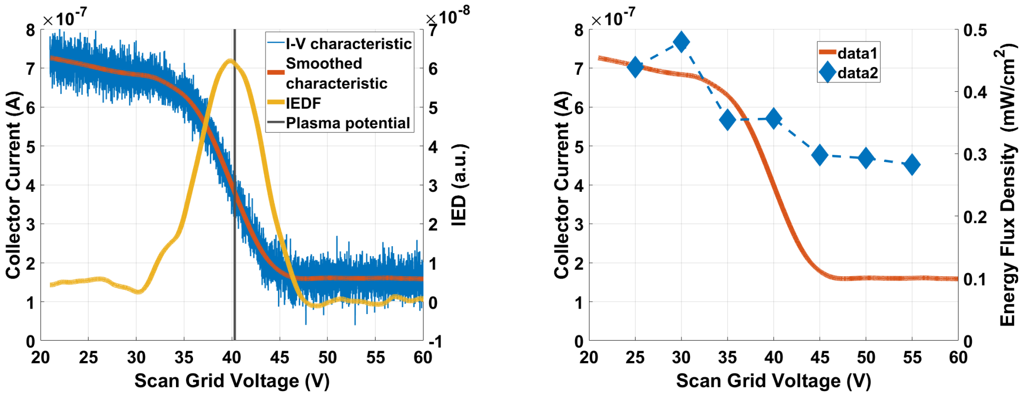

Figure 6.4: Measurements in an rf plasma. The working gas is Ar at 5 Pa. The discharge is powered with 100 W. (Left) RFEA measurements with collector current and IEDF. (Right) Collector current and energy flux density for corresponding scan grid voltage.

Depending on the plasma environment and geometrical placing of the probe inside the chamber, orifice width, grid spacing and grid arrangement can be customised according to requirement. The grids are custom-made stainless steel with hexagonally distributed holes (diameter: 1.1 mm, centre-to-centre: 1.25 mm).

On the left of figure 6.4, the standard RFEA measurement can be seen. Before differentiating the collector current, it is smoothed using a Gaussian convolution with a variable window length. The energy of the ions is mainly governed by the plasma potential since the sheath is assumed to collapse at least once during an rf cycle [110]. Therefore, the floating potential can be neglected and the potential drop across the sheath which accelerates the ions is roughly equal to the plasma potential. The plasma potential was measured using an rf-compensated cylindrical Langmuir probe and displayed in figure 6.4 on the left by a vertical line. The plasma potential is in good accordance with the peak of the IED, which confirms the RFEA functionality. The full width at half maximum (FWHM) of the IED is ≈ 7.6 V. It is a measure for the energy resolution of the probe. Surely, this is not a very high resolution, but suffices for the purpose of showing the working principle and feasibility of the combined diagnostic. In another work of Edelberg et. al. [111] the energy resolution of a self-built compact RFEA with a similar dimension was around 3 eV.

6.5 Combined measurements in a DC magnetron sputter device

For another example, measurements are shown that were conducted in a large multi-target magnetron sputter device. Two 6-inch targets were used. A MgLi target with a Li mass fraction of 14% and a pure Mg target are utilized. These targets are part of an extensive study revolving around the use of lithium in the medicinal therapy of bipolar disorder and depression. A substrate plate was designed to embed the combined diagnostic and a standard PTP separately. Three places at 13, 35 and 55 mm from the centre of the substrate were chosen. To discuss the entire measurement campaign would go beyond the scope of this chapter. Its main goal was the use of the PTP and the RFEA (without energy flux measurements) to determine a rough spatial distribution of ion energy and total energy flux density across the substrate and the difference between the two targets. At this point, only the combined diagnostic measurements are shown which were taken at the outer position (55 mm).

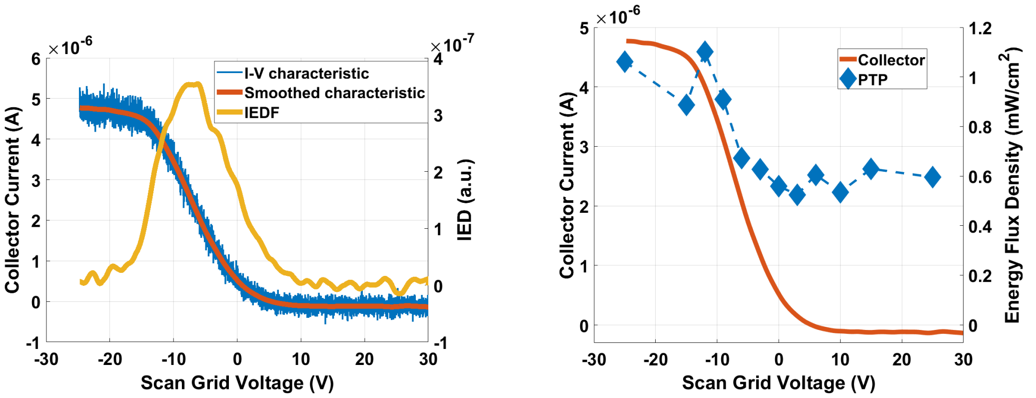

Figure 6.5: Measurements during sputtering using a Mg target. The working gas is Ar at 0.4 Pa. The discharge is powered with 150 W DC. (Left) RFEA measurements with collector current and IEDF. (Right) Collector current and energy flux density for corresponding scan grid voltage.

Figure 6.5 shows the measurements for the pure Mg target and figure 6.6 the measurements for the MgLi target.

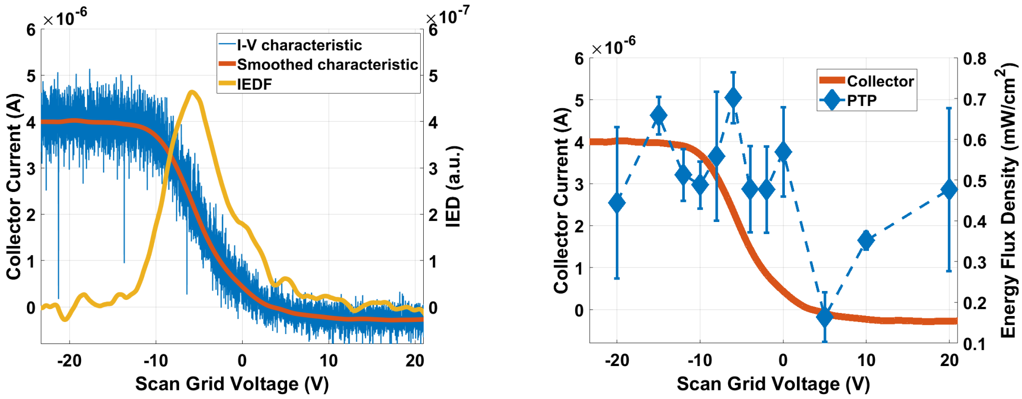

Figure 6.6: Measurements during sputtering using a MgLi target. The working gas is Ar at 0.4 Pa. The discharge is powered with 150 W DC. (Left) RFEA measurements with collector current and IEDF. (Right) Collector current and energy flux density for corresponding scan grid voltage.

As can be seen in figure 6.6 on the right, the error bars of the PTP measurements can be quite large. The deviation comes from the evaluation of the PTP data using the kink method mentioned in chapter 4.2. This evaluation technique always renders two results for one temperature course. One for the heating kink and one for the cooling kink. These two values should not differ too much and the mean value between the two is taken as the energy flux density. In this case, however, these two values in some instances lead to a substantial deviation in the measurements.

When looking at the energy flux density in figure 6.6 (on the right) for scan grid voltages 10 V and 20 V, the difference between the two determined errors can not be explained by changes in the discharge or other outside factors. This comes with the resolution problems of the first design of the combined diagnostics which originates in the alignment of the grids and their spacing. With these very small ion currents and subsequent energy flux densities arriving at the collector, the evaluation of the PTP data is easily prone to error. Another factor for these considerations is the heating of the probe body which has an even bigger influence on the reproducibility and propriety of the combined measurements. The fast heating of the body in this experimental setup only allowed for one PTP measurement for each scan grid step value. Usually, at least two or three PTP temperature courses are taken for each measurement point to allow for a better averaging of the results and error determination. A detailed description of this problem and its implications for the measurements is given in the next section.

6.6 Heating of probe body

One of the main issues with the design of the combined diagnostics was that the probe body heats up to such a degree that the PTP is heated whether or not the plasma is turned on or off. This was especially the case when embedded into the grounded electrode in the rf plasma chamber. The relatively thin stainless steel body radiates enough heat so the PTP can barely detect a temperature difference when the plasma is turned on. As can be seen in the previous section, the ion current is in the range of μA and the measured energy flux densities are in the range of 0.1 mW/cm^2. So if the PTP steadily heats up, the temperature change brought by the energy of the impinging ions can hardly be separated from the noise or be detected at all. Even if that heating process is somewhat linear and on much larger time scales than the measurements themselves. Figure 6.7 shows the temperature course of the PTP during the measurements that were discussed previously and shown in figure 6.4.

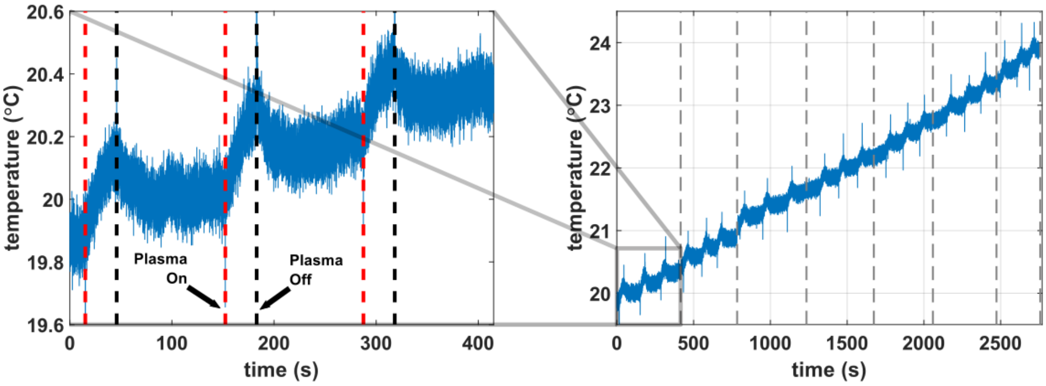

Figure 6.7: Enlarged view (left) of the temperature course (right) of a whole measuring cycle in a 100 W rf plasma for the combined diagnostic. The working gas is Ar at 5 Pa pressure.

The steady rise in the base temperature is clearly visible on the right in figure 6.7. The vertical dashed lines indicate the separate measurements for each step in the scan grid voltage. Three PTP measurements are done for each scan grid step. In other words, the plasma was switched on and off three times for one scan grid measurement point. This yields 6 results for the energy flux density, three each for the heating kink and cooling kink, respectively. From the results, a mean is taken and the standard deviation as an error appraisal. When the temperature change during the heating phase is large enough for a clear distinction from the base temperature, this usually results in high reproducibility of the measurements with only small errors.

During the measurements, however, the base temperature of the PTP rises from

20 °C to about 24 °C. The actual temperature change by turning on the plasma is seen on the left in an enlarged view of the first scan grid step 25 V. For each step the plasma was turned on and off three times. Vertical lines indicate the event times. The plasma was turned on for 30 seconds and the PTP only heats up for about 0.2 °C.

To be able to accurately evaluate PTP measurements the temperature during the cooling phase must reach the starting point it had before the heating phase. In other words, it cools down completely after being heated by the examined energy source. This is especially the case when the incoming energy flux density is very small. When the incoming energy flux is very high and the PTP heats and cools very quickly, an underlying rise in the base temperature could be ignored. However, this is not the case here. In figure 6.7 it can be seen on the left that after the plasma is switched off, the temperature drops only slightly and then starts to rise again. The actual measurement can hardly be distinguished from the underlying rise in temperature which is coming from the gradual heating of the grounded electrode and, subsequently, the probe body.

6.7 Summary

The first measurements in an rf plasma and a DC magnetron sputter system showed the successful combination of the two diagnostics. The simultaneous measurement of ion energy distribution and energy flux density opens up new possibilities in the field of plasma diagnostics. A difficulty with standard PTP measurements is the integral energy flux density that is measured coming from all types of sources. Dividing the total energy flux into individual contributions is a hard-won battle which often requires the use of additional diagnostics or other equipment. With this probe, the energy flux of the ions coming to the collector as well as fast neutrals can be determined directly. The shape and amplitude of the ion energy distribution greatly depend on the plasma parameters such as pressure, plasma potential and sheath width. The maximum of the IED reflects the plasma potential and with pressure change the width of the distribution changes. This is due to the rise of collisions in the plasma bulk and the sheath with rising pressure. According to [112] they can even be used to determine the electron temperature.

To address the issues in this chapter, like grid spacing and alignment as well as the heating of the probe body, a new design of the combined diagnostic is presented in the next chapter.

7 The retarding field thermal probe

Publication 4

A retarding field thermal probe for combined plasma diagnostics

Authors:	F. Schlichting, H. Kersten
Journal:	European Physical Journal Techniques & Instrumentation (submitted)
Technique:	Electrical and energy flux measurements
Own contribution:	approximately 95%

Experimental Setup:

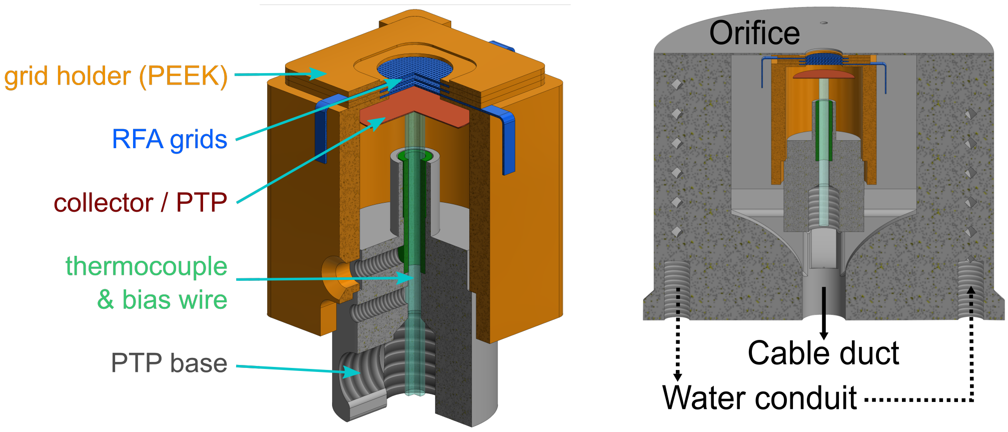

A new design of the combined diagnostic with a water-cooling system is deployed in an ion beam experiment, magnetron sputter device and rf plasma discharge.

Motivation:

The principle of the combined diagnostic has already been proven to work in the previous chapter. However, the first design came with a few challenges. The grid installation and alignment were not easy to accomplish in a reproducible way. Also, the grids' spacing and insulation were subject to reoccurring difficulties. The main cause for the need for a new design, however, was the heating of the probe body which affected the PTP measurements. Only under certain conditions was it possible to fully make use of the simultaneous measurement with RFEA and PTP.

Main Results:

First, the water cooling system was tested and it was shown that the heating of the PTP could be averted. The PTP can be cooled down sufficiently to measure the usually small energy flux density coming from the ions after passing through the RFEA grid system. For the three discharge configurations that were studied, a correlation between the measured ion current and the energy flux density was found. With decreasing ion current to the collector, also the energy flux density decreases. In the ion beam experiments, the energy flux density could be separated into the contributions coming from the ions and fast neutrals originating in charge exchange collisions. In the magnetron and rf discharge, other collisions such as elastic collisions play a more dominant role. So the model, as used in the ion beams, cannot be applied solely. Still, the ratio of ion-to-neutral energy flux density can be determined and help, for instance, in bringing together the examination of thin film properties and accompanying simulations.

RESEARCH

A retarding field thermal probe for combined plasma diagnostics

Felix Schlichting* and Holger Kersten

*Correspondence:
schlichting@physik.uni-kiel.de
Institute for experimental and applied physics, Kiel University, Leibnizstraße 19, 24098, Kiel, Germany
Full list of author information is available at the end of the article

Abstract

The wide variety and ever-growing applications of plasma processes, both in research and industry, require an equally growing diversity and accessibility of suitable plasma diagnostics. The plasma parameters and the tailoring thereof strongly influence the outcome of thin film deposition, plasma etching, or surface treatments, to only name a few. To further enhance the determination of different fluxes of species, their energies, and behavior influencing a surface process, a custom build combination of two commonly used diagnostics was developed. With a retarding field analyzer, one can obtain the ion energy distribution in a plasma by measuring the current at the collector depending on the applied voltage at the scan grid. A passive thermal probe determines the energy flux density coming from a process plasma by measuring the temperature change of a dummy substrate. In this study, we present a retarding field analyzer where the collector is substituted by a passive thermal probe. By doing so, we can determine the energy distribution of the charged ions as well as their energy flux density at a certain potential and the power deposited onto a substrate. Another advantage is that the thermal probe can even measure the power deposited by incoming (fast) neutrals and of the background gas when the ions are kept away by the grids. Hence, combining these two powerful diagnostics yields information neither of them can deliver on their own. The probe has been tested in three different plasma environments: ion beam source, magnetron sputtering and rf discharge plasma.

Keywords: plasma diagnostic; diagnostic combination; ion energy distribution; energy flux density; energy balance

1 Introduction

In plasma diagnostics, one can rely on a vast variety of options depending on the investigated discharge environment. The external parameters such as gas pressure, gas flow, discharge geometry and applied power determine the internal parameters of that environment. These include the potential and kinetic energies of the involved particles (electrons, ions, neutrals and, possibly, precursor radicals) and the energy these particles transfer to a surface and, furthermore, the potentials within the plasma and the force the plasma exerts on a surface [1]. Plasma diagnostics such as optical spectrometry [2], mass spectrometry [3], electrical probe diagnostics [4] or sensitive mechanical probes [5] are commonly used to determine critical plasma parameters.

The focus of this work is on electrical and thermal probes. Electrical probes are commonly used to measure plasma parameters such as plasma potential, electron density and electron temperature, ion energy distribution and magnetic field strength. An important example of these diagnostics is the Langmuir Probe, which despite its simple design, or maybe just because of it, can be used in many different plasma environments [6–8]. Another example is the hairpin probe, which analyzes the amplitude and phase of the rf voltage and current in a resonant circuit [9]. Also, there are magnetic probes that measure the magnetic field strength and direction in the plasma [10], and the retarding field analyzer to determine the ion energy distribution [11]. Thermal probe diagnostics are useful for studying plasma-surface interactions, plasma chemistry, and plasma processing. Examples are bolometers, which are mostly used in confined fusion devices [12]. Additionally, there exist various types of calorimetric probes using thermocouples and temperature measurements to determine energy fluxes onto surfaces in a plasma, based on the principle introduced by Thornton [13]. They can be used to better understand the plasma behaviour for applications such as plasma etching, thin film deposition, and modification.

Recently, also novel and not state-of-the-art methods have been performed. For example, there are thermionic probes, mainly used in magnetically confined fusion devices [14], and optical probes using lasers as trapping systems [15] or Thompson scattering [16], laser-induced fluorescence [17] or microwave interferometry [18].

Most of these diagnostics are invasive, meaning that they change or, at least, minimally disrupt the plasma environment by introducing them. And on their own, they often have limitations concerning the probe placement and obtained results. To get a more comprehensive understanding, multiple diagnostics are often deployed separately. The ever-growing complexity of the processes in which plasmas are used, calls for more multilateral components, which can get results out of minimal invasion, which led to the idea of combining existing diagnostics.

2 Plasma diagnostics

To better understand the abilities (but also shortcomings) of the suggested combined probe techniques, the two diagnostics will be discussed separately. Since both of these diagnostics are well-known and established, we will not go into too much detail.

2.1 Retarding Field Energy Analyser

There are different routes to design a retarding field energy analyzer (RFEA) depending on the requirements for the plasma process investigated. In principle, it consists of a set of vertically aligned grids, acting as filters or lenses for an incoming charged particle flux. As shown in fig. 1, the most commonly used is a three- to four-grid system.

Grids G1, G2, and G3 are designated as the Screen Grid, Scan Grid, and Secondary Electron Repeller Grid (SE Repeller), respectively. Grid G0 is optional. Depending on the size of the Orifice Or, one may use an extra grounded Grid G0 to change the electrical field in front of the RFEA and prevent i.e. the bulk plasma in a rf capacitively coupled plasma (rf-ccp) to spread into the probe. The voltages applied to the different grids are schematically shown in fig. 2.

The negative bias at the Screen Grid prevents electrons from entering the RFEA. Positive ions can pass the Scan Grid in proportion to the applied voltage ramp and

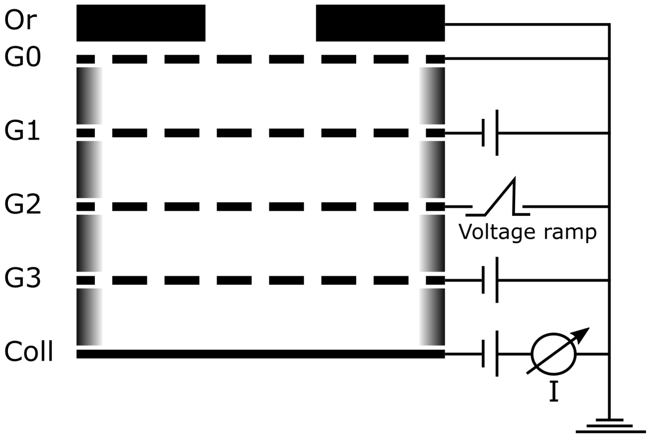

Figure 1: Sketch of a four grid RFEA. Or: Orifice; G0: Grounded Grid; G1: Screen Grid; G2: Scan Grid; G3: Secondary Electron Repeller; Coll: Collector Plate;

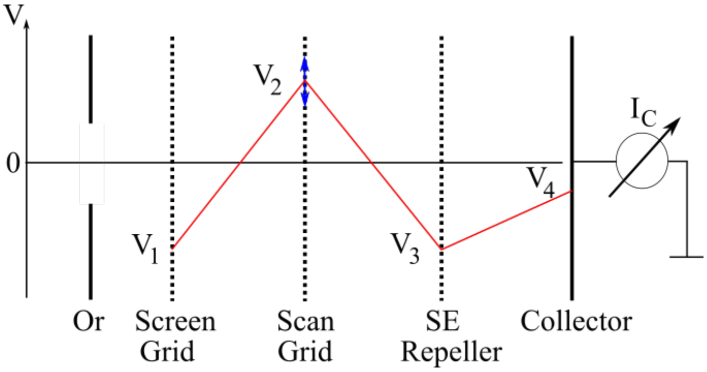

Figure 2: The static voltages $V1$, $V3$ and $V4$ applied to the respective grids and the voltage ramp barrier $V2$, as usually used by an RFEA.

the resulting current I_C is measured at the collector. Upon impact, the ions can release secondary electrons (SE) from the collector and, consequently, distort the measured current. Therefore, $V3$ must have a larger bias than the collector to repel the SEs.

Measuring the voltage ramp and the resulting collector current yields the typical I-V characteristic from which the ion energy distribution (IED) can be calculated by differentiating the curve, as exemplary shown in fig. 3. The ion velocity distribution, and therefore their kinetic energy, is related to the collector current I_C and the Scan Grid voltage U_S [19, 20] like the following

$$f(v) \propto \frac{dI_C}{dU_S}. \tag{1}$$

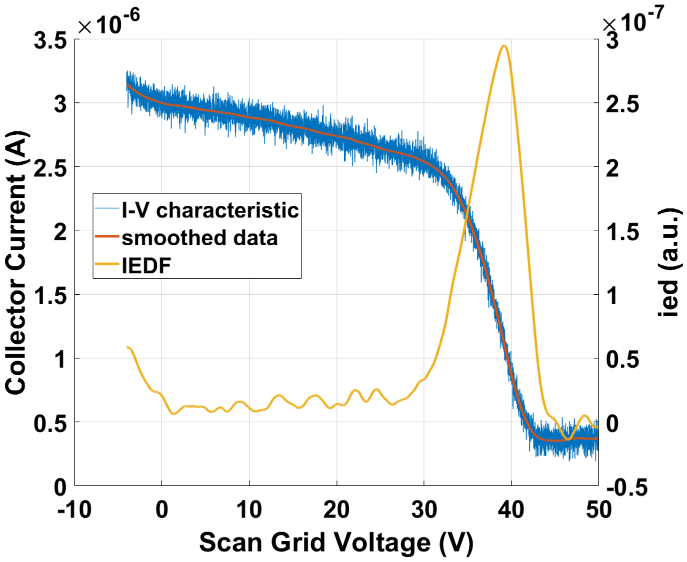

Figure 3: RFEA measurement in a capacitively-coupled rf plasma discharge in an Argon gas environment with 2 Pa and 100 W at powered electrode

By simply differentiating the I-V characteristic, the obtained IED indicates how many ions per unit of time and area are hitting the surface of the collector.

With the possibility of using a different number of grids and spacing them individually, the RFEA is a widely used tool to investigate ion energy distribution in a plasma [11, 21, 22]. But as soon as electrons, their energies, and velocities, neutrals, or overall energy flux densities of species are of interest, additional diagnostics are necessary.

2.2 Passive Thermal Probe

The passive thermal probe (PTP) and the actual design used in these experiments have been presented elsewhere [23, 24]. The probe consists of a substrate dummy with a diameter of 11 mm. Most commonly a 100 μm thick copper plate is used as substrate. One might use different materials with a greater or smaller heat capacity depending on the incoming energy flux density. The temperature measurements used to determine the incoming integral energy flux are obtained via a Type K thermocouple, which is spot-welded to the back of the substrate dummy. A shielded copper wire is additionally welded to the plate to bias the probe and perform current measurements.

By measuring the temperature change of the probe set off by exposing it to a plasma source, a time and energy-integrated value of the energy flux density can be calculated. The evaluation procedure is described in detail in [25]. The typical temperature evolution of the probe during plasma exposure is shown in fig. 4. It can be divided into two phases, the heating phase and the cooling phase. During the heating phase, the plasma source is on and the overall change in enthalpy $\dot{H}_h$ of the probe is dominated by the incoming power P_{in}. Charged and neutral particles impinging on the substrate, surface processes like film formation, secondary electron emission, or relaxation of metastable atoms or molecules as well as heat radiation from a target or chamber walls are the reason for the incoming power (energy influx).

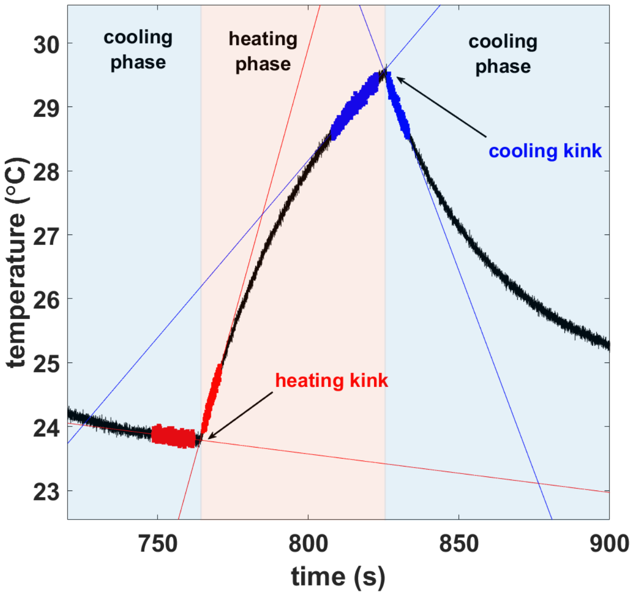

Figure 4: Exemplary depiction of the two phases and the change in temperature of the PTP over time in a magnetron sputter deposition chamber. This measurement was done with a Cu target operated with 300 W DC.

When the plasma source is switched off, the substrate cools down and its change in enthalpy $\dot{H}_c$ is now solely governed by the outgoing power (cooling) $P_{out,c}$. These two phases can be written like this:

$$\dot{H}_h = C_s\,\dot{T}_h = P_{in} - P_{out,h} \tag{2}$$

$$\dot{H}_c = C_s\,\dot{T}_c = -P_{out,c} \tag{3}$$

C_s is the heat capacity of the probe, which can be determined by electron beam calibration [24]. $P_{out,h}$ is the outgoing power during heating. $\dot{T}_h$ and $\dot{T}_c$ are the time derivatives of the temperature during the heating and cooling phases, respectively.

We only examine short periods around the two kinks shown in fig. 4. Here, we can assume that the outgoing power during the respective phases is always the same. Therefore, we can combine equations 2 and 3 to calculate the incoming energy flux density $J_{in,exp}$:

$$J_{in} = \frac{P_{in,exp}}{A_s} = \frac{C_s}{A_s}\left(\dot{T}_h - \dot{T}_c\right), \tag{4}$$

where A_s is the probe surface area. The linear fits are made around the kinks to determine $(\dot{T}_h - \dot{T}_c)$ for each of the kinks. From this difference, a mean is obtained as the energy flux density.

2.3 Combination of both diagnostics: RFEA and PTP

The passive thermal probe has been used in a wide range of environments from low-pressure process plasmas such as rf-ccp sources to high power impulse magnetron sputtering (HiPIMS) systems and ion beam sources or atmospheric pressure plasmas [26–29]. It has proven to be a versatile diagnostic and with the ability to bias the probe it can even be used as a planar Langmuir probe, as shown in [27]. The possibility to apply a bias voltage and to measure the current to the probe led to the idea that this probe should also qualify to be used as a collector in an RFEA system, where it simultaneously would allow to measure the incoming energy flux density from a plasma source depending on the scan grid voltage of the RFEA.

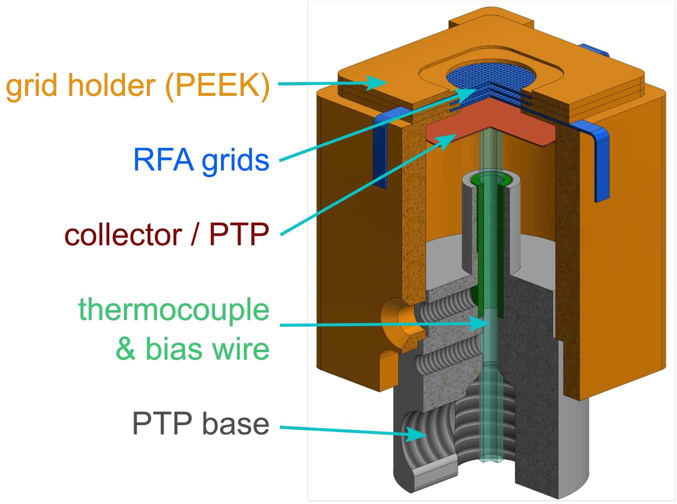

Figure 5: RFEA grid system on top of the PTP base.

For this purpose, the former PTP design [25] is modified to place the grid system in front of the substrate plate, as shown in fig. 5. The grid holder is made from a thermoplastic polymer (PEEK) and is fixed on top of the PTP base. PEEK is thermostable up to around 340 °C and both electrically and thermally insulating. It is also relatively cheap and can be easily processed with a CNC cutter, thus, making it a very suitable material. An expanded and detailed view of the grid holder with the individual grids is displayed in fig. 6. The secondary electron repeller grid is positioned directly on top of the grid holder. Scan grid and screen grid are rotated 90° to each other. This way the protruding latches of the grids can be led to the sides of the holder and connected to the electrical measurement system. Optionally, a fourth grounded grid can be placed in front of the screen grid, as explained above and shown in fig. 2.

The grids themselves have a thickness of 0.2 mm, the same as the grid cutout in the placer. The placers have a thickness of 0.5 mm, which leads to a grid-to-grid distance of 0.3 mm. In hexagonal order, the grid holes have a diameter of 0.4 mm

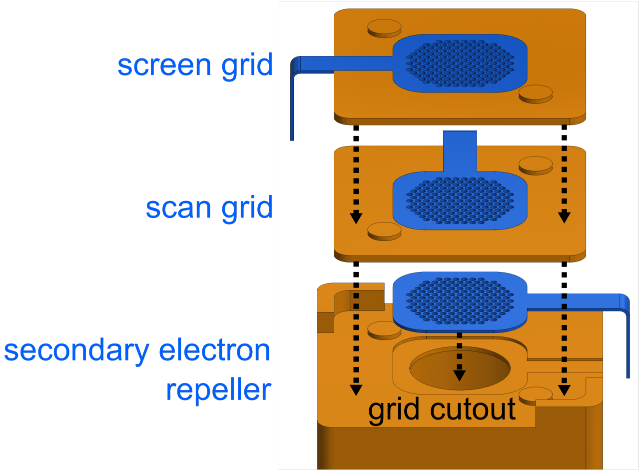

Figure 6: Expanded view of the RFEA grid holder. The grids are fitted into the grid cutouts of the individual placers.

and a 0.5 mm center-to-center distance, thus, creating a 58% optical transparency for each grid. As a whole, the combined diagnostic will now be referenced in the text as a retarding field thermal probe (RFTP).

To adapt the measurement principle of the two separate diagnostics and to be able to combine them, one has to consider that a single RFEA scan may take only a few seconds whereas, in contrast, the PTP measurement may take minutes. The time for the required heating and cooling phases depends on the incoming energy flux and the plasma conditions. With an ion current onto the PTP/collector of only a few mA, which is reduced further with rising scan grid voltage, it can take around 30 seconds to heat the PTP for a few degrees. The respective cooling phase also depends on the environment. The cooling becomes significant considering the housing of the RFTP.

To shield the latches of the grids and the attached wiring from the plasma, the setup in fig. 5 is placed in a stainless steel housing. When exposed to plasma for longer time periods the housing can heat up so much that the heat radiation affects the PTP and thereupon acts as an unquantifiable energy source distorting the measured temperatures. This would even lead to the heating of the probe during the cooling phases. Therefore, the housing can be water-cooled as depicted in fig. 7. The housing is 3D-printed stainless steel with a circular water conduit. Through the cable duct, all wiring can be routed out of the vacuum chamber via a rotary feedthrough. The orifice cap is screwed on top of the housing and serves, simultaneously, as the ground connection to grid G0 (fig. 1) if needed.

As mentioned in the previous chapter, different sizes and materials can be used for the PTP substrate. The standard 11 mm copper platelet has a heat capacity of around 0.03 J/K. When the incoming ion currents are relatively small, leading only to a slight change in temperature of the probe (collector), experiments are performed with a Tantal substrate of 5 mm diameter, resulting in a smaller heat capacity of $C_S = 0.00758 \pm 0.00017$ J/K. This enables the probe to respond more sensitively to small temperature changes.

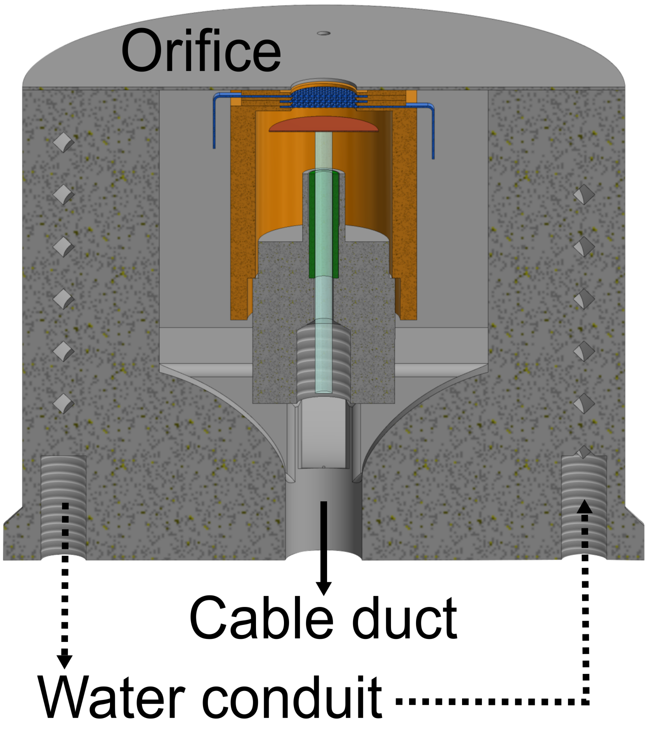

Figure 7: RFTP with water-cooled housing. The housing and orifice cap is made of stainless steel.

3 Examples for experimental tests of the RFTP

The idea of the cooled housing is to stabilize the temperature inside the RFTP and of the PTP substrate so that the outgoing power from the PTP during the measurement is constant and that there are no external heating sources other than the incoming ions or neutrals passing through the RFEA.

To demonstrate this effect, fig. 8 shows temperature courses with and without water cooling, respectively. The RFTP was embedded in the grounded electrode of a rf-ccp parallel plate discharge in an argon plasma. The powered electrode was driven with 50 W and the plasma was ignited for 30 minutes and after another 10 min, the gas was turned off. During the measurements, there was no voltage applied to the RFEA grids. Without cooling there is an almost linear increase in temperature. After the plasma and even after the gas is turned off, the temperature still rises. This is due to the disturbing effect of the heated housing on the temperature measurements. In contrast, a cooled housing results only in a minimal temperature change while the plasma is ignited and cools the probe afterward. Depending on the water temperature, the probe will be cooled to the equivalent temperature. Since this cooling factor stays constant throughout all measurements, it can be ignored for the evaluation of the PTP temperature courses.

Coming back to the time duration of the two diagnostics mentioned in the previous chapter, it is now possible to have sufficient time to cool the PTP and, therefore, be able to determine the incoming energy flux of ions passing through the RFEA

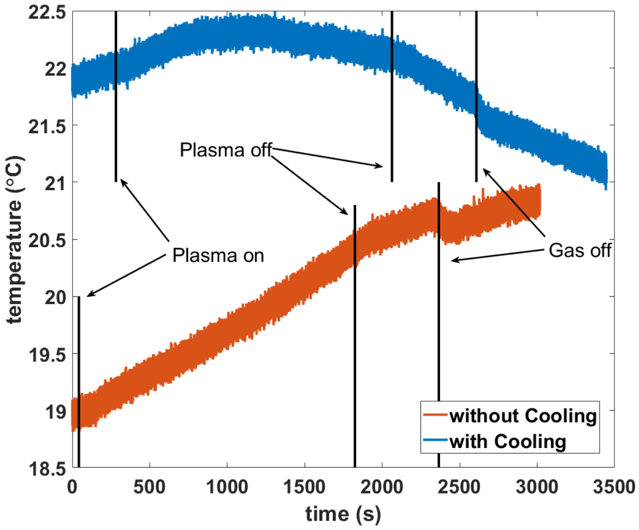

Figure 8: Temperature courses of the PTP substrate with and without water cooling of the housing. Event times are indicated by vertical lines.

for a given grid voltage configuration. Hence, to obtain corresponding RFEA and PTP data, first, a standard RFEA scan is performed, and then, subsequently, PTP measurements are performed for fixed scan grid voltages in well-defined steps, while the other grid voltages remain constant. Then, the ion current to the collector and the energy flux density can be compared for the corresponding scanning range. In the following, such measurements are shown for several different discharge conditions.

The electronic devices for temperature, voltage, and current measurements are custom build. The PTP has its own electronic and vacuum lead-through. The additional BNC bias cable is separated from the temperature measurements and can be connected to the collector output of the RFEA electronics. The RFEA electronic has four BNC outputs for the three grids and the collector, with two outputs for fixed voltages (screen grid and SE repeller) and two outputs with additional possibilities of current measurements and sweeping bias voltages.

3.1 Ion Beam

For a distinct and controlled environment in terms of ion energy and plasma density, measurements were performed in an ion beam. Here, ions and electrons are produced in an electron cyclotron resonance (ECR) discharge as described in [30]. With the use of an anode ring around the discharge the ions can be accelerated up to $U_{anode} = 1200$ V. Two different setups were used: the smaller vertically aligned source (VIB) [31] and a larger horizontal ion beam (HIB) [32].

3.1.1 Vertical ion beam

Fig. 9 shows typical measurements in the vertical setup. Here, the distance of the RFTP to the ion source cannot be changed due to geometrical limitations and is about 0.2 m.

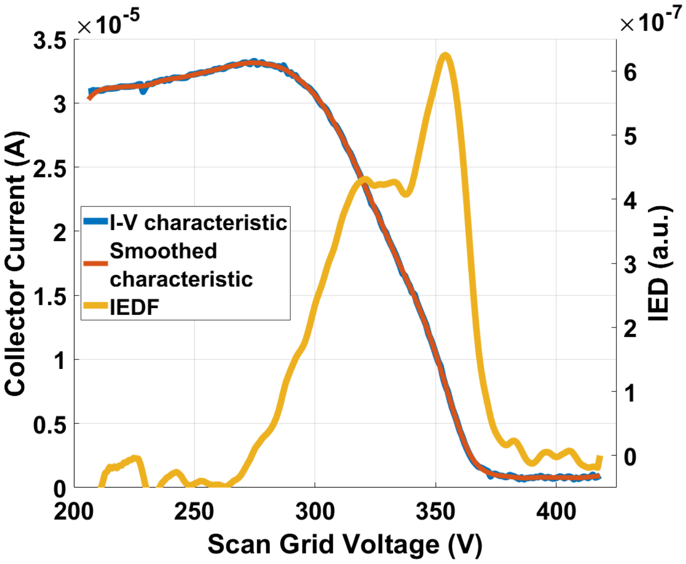

(a) RFEA measurement in vertical ion beam experiment

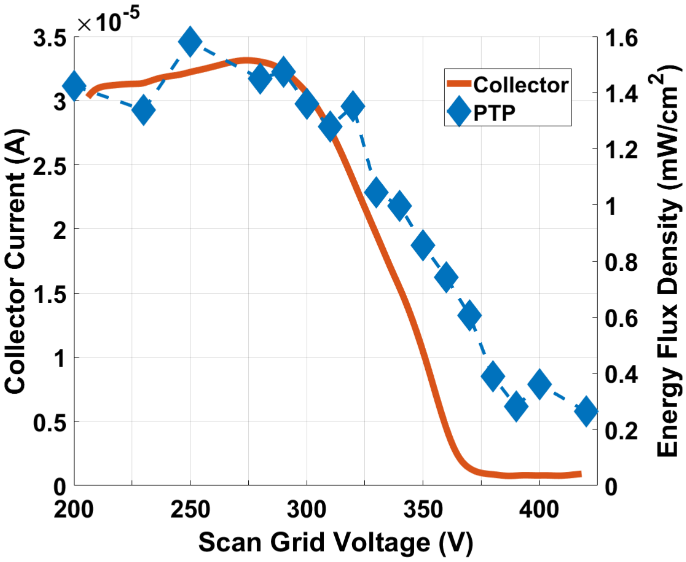

(b) Corresponding energy flux density with measured collector current

Figure 9: RFEA (a) and RFTP (b) measurements in a vertical ECR ion beam. The working gas is Argon at $2.6 \cdot 10^{-2}$ Pa. The anode voltage of the source is $U_{anode} = 300$ V.

The RTFP is placed in the center of the chamber facing the ion beam and the orifice is changed to 4 mm diameter. The grounded grid is left out. Fig. 9a shows the RFEA measurements in the same way as discussed in the previous chapter. The maximum measured ion current is at roughly $30\,\mu$A, much higher than in an rf plasma. The total energy of the ions is $E_{ion} = e(U_{anode} + U_{pp1} - U_{pp2})$ [32]. The sheath potential drop in the ion source is $U_{pp1} = +(60 \pm 10)$ V. The plasma potential of the secondary plasma $U_{pp2} = +(15 \pm 5)$ V in the chamber is highly dependent on the working gas pressure and the anode voltage of the source [31].

This can be seen in the RFEA measurements in fig. 9a, where the peak of the IED is at approximately 360 V whereas the anode voltage is $U_{anode} = 300$ V. Of course, not all ions and their potential energy are wholly affected, leading to the plateau in the IED and the rather large width of the distribution.

The measured energy flux density (EFD), seen in fig. 9b, also drops at the same voltage as the ion current. It amounts to roughly $J_{in,max} = 1.45$ mW/cm^2 (average of measurement points of the PTP for scan grid voltage < 300 V). Looking at fig. 9b the residual EFD above 375 V scan grid voltage is at around $J_{in,min} = 0.38\, mW/cm^2$ (average of measurement points for scan grid > 360 V). This residual energy flux density can be attributed to fast neutrals originating in charge exchange collisions.

The charge exchange collisions of the ions in the beam with the background gas atoms result in fast, energetic neutral atoms. For ions with energies $E_i > 100$ eV the approximated net cross section for these collisions is $\sigma_{cx}(E_i) = 5.75 \cdot 10^{-19}(E_i/eV)^{-0.1}$ m^2 [31] when using the energy dependent cross sections given by Phelps [33]. For ions with an energy of $E_{ion} = 360$ eV and gas pressure of $2.6 \cdot 10^{-2}$ Pa, the mean free path for charge exchange collisions was determined to $\lambda_{cx,vib} = 0.49$ m.

Assuming that only ions and fast neutrals contribute to the total energy flux density J_{in}, the contribution of ions will be [31]

$$\frac{J_{in,ions}(z)}{J_{in,max}(z)} = exp(-\frac{z}{\lambda_{cx,vib}}) = 0.66 \tag{5}$$

for $z = 0.2\, m$. The proportion calculated with the measured energy flux density from fig. 9b is

$$\frac{J_{in,max} - J_{in,min}}{J_{in,max}} = 0.74 \tag{6}$$

which is in good accordance with the theoretical approximation. Hence, the energy flux density due to the ions is $J_{in,ions} = 1.07$ mW/cm^2.

The proximity to the ion source did not allow for measurements above the aforementioned anode voltage. For larger energies, the ion beam plume pushes too much into the RFTP. The thereby growing space charge between the grids of the RFEA can result in breakdowns between the Screen and Scan Grid.

3.1.2 Horizontal ion beam

To avoid this phenomenon, a second ion beam setup, mentioned earlier, was investigated. Here the ion source is oriented horizontally inside a larger vacuum vessel with a length of 1.6 m and a diameter of 0.65 m [32]. At the opposite end of the ion beam source, the RFTP can be placed in the center facing the ion beam. To alter the distance a rod is used which also serves as the cable feedthrough. In this setup, it was possible to apply up to 750 V to the anode. The distance of the RFTP to the ion source was $z = 0.9$ m. The measurements are shown in fig. 10.

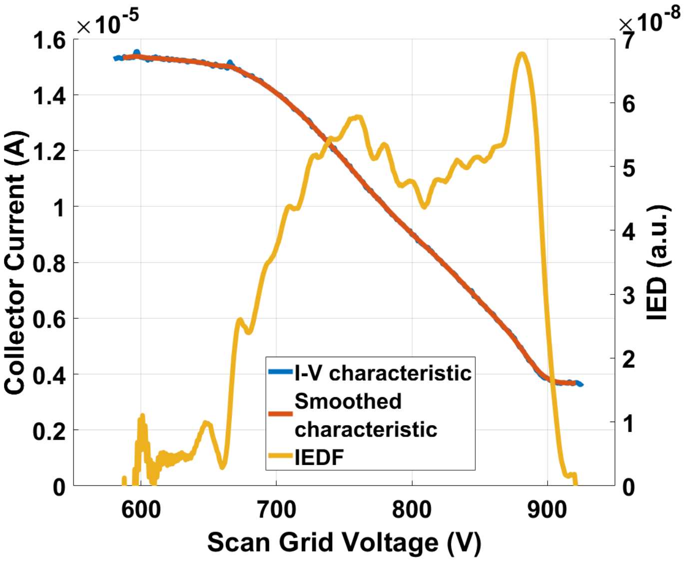

(a) RFEA measurement in horizontal ion beam experiment

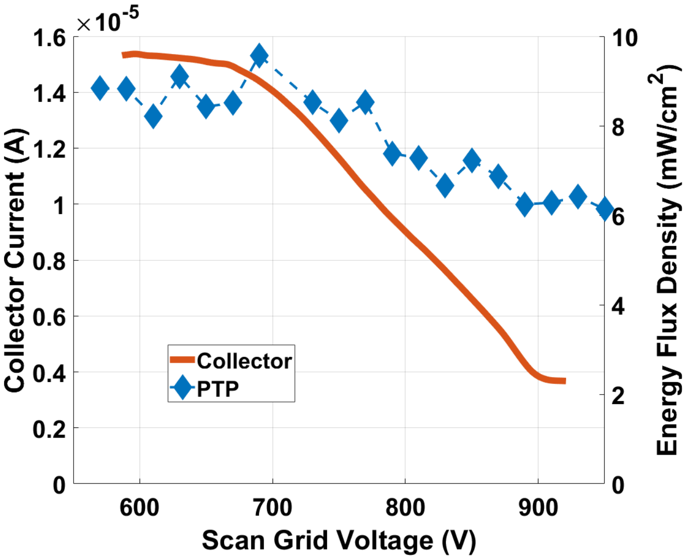

(b) Corresponding energy flux density with measured collector current

Figure 10: RFEA (a) and RFTP (b) measurements in a horizontally orientated ECR ion beam source. The working gas is Argon at $1.76 \cdot 10^{-2}$ Pa. The anode grid voltage of the source is 750 V.

The larger distance to the source allowed for higher ion energies to be investigated. The ion beam, however, diverges in its diameter as it extends further into the chamber. This can be observed in fig. 10a, where the collector current drops from around 700 V until the scan grid voltage reaches 900 V. There are two peaks in the IED at 750 V and 880 V and the plateau is much more pronounced than in the VIB measurements. There is no reasonable explanation for this higher energy of the ions in the beam. A thermionic cathode has been placed in front of the ion beam source to prevent breakdowns inside the chamber. However, this could not fully be averted which leads to a distortion (small peaks) in the measured collector current, which can be seen in the upper left corner of fig. 10a in the collector current. Measurements taken for lower anode voltages reveal that the apparent high energy peak shifts to higher scan grid voltages and gets more pronounced if the anode voltage is higher. Fig. 11 shows the measured ion energy distributions for anode voltages of 300 V, 500 V, 600 V and 800 V. Additionally, the measured I-V characteristic for $U_{anode} = 800$ V is displayed. Again, small peaks coming from breakdowns inside the chamber can be observed, especially around scan grid voltages of 900 V, leading to this pronounced peak in the corresponding IED. This also indicates some limitations of the probe concerning the hole diameter of the grids and the grid distance in the RFEA system.

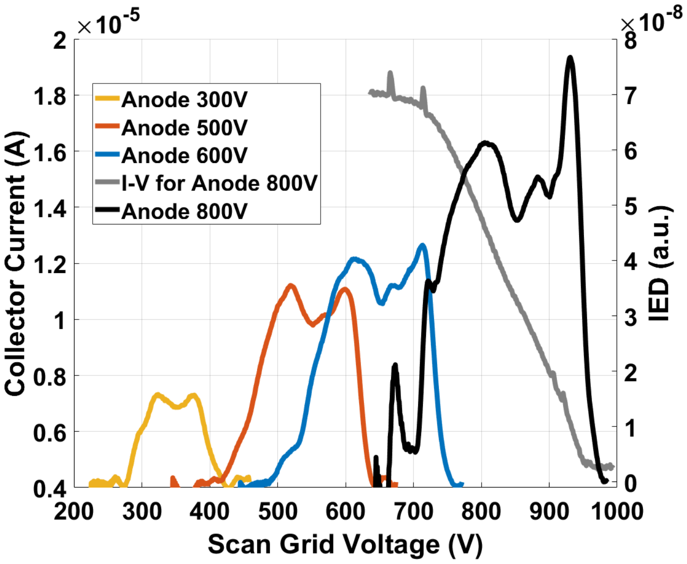

Figure 11: Measurements for different anode voltages showing the effect of breakdowns inside the chamber on the measured current and, subsequently, the IED

In the following the ion energy will be taken from the first peak in fig. 10a. In the horizontal ion beam experiment, the plasma potential inside the source is $U_{pp1} = +(60 \pm 10)$ V, since this setup uses the same ECR plasma source as in the VIB. The plasma potential in the chamber, however, is found to be $U_{pp2} = +(40 \pm 10)$ V [32], measured for an anode potential of $U_{anode} = 1200$ V. Therefore, the total ion energy in this setup would be expected to be around the anode potential. The energy flux density taken from the PTP measurements in fig. 10b follows the collector current. Here, in contrast to the vertical ion beam experiment, the residual EFD is still significantly higher. For ions with an energy of 750 eV and gas pressure of $1.76 \cdot 10^{-2}$ Pa the mean free path for charge exchange collisions comes to $\lambda_{cx,hib} = 0.79$ m. This results in a partial contribution of the ions to the energy flux density of

$$\frac{J_{in,ions}(z)}{J_{in,max}(z)} = exp(-\frac{z}{\lambda_{cx,hib}}) = 0.32 \tag{7}$$

for $z = 0.9$ m. The maximum EFD is around 8.8 mW/cm^2 (averaged over the first 7 measurement points for scan grid < 700 V) above the remaining 6.3 mW/cm^2 (averaged over the 4 last measurement points for scan grid > 900 V). This results in a measured ion contribution of

$$\frac{J_{in,max} - J_{in,min}}{J_{in,max}} = 0.28. \tag{8}$$

The contribution of ions to the maximum energy flux density coming to the collector is thereby $J_{in,ions} = 2.5$ mW/cm^2. Axial Faraday cup measurements in this setup provide an ion beam current density of $j_{beam,FC} = 1.2\ \mu$A/mm^2 for $z = 0.86$ m and $U_{anode} = 800$ V [34]. The orifice of the RFTP used in the HIB experiment has a diameter of $d_{or} = 6$ mm. Taking the maximum ion current measured at the collector of the RFTP from fig. 10 as $I_{coll,max} = 15\,\mu$A, the ion current density measured at the collector is $j_{coll} = I_{coll,max} \,/\, A_{or} = 0.53\,\mu$A/mm^2. Since the experimental conditions are comparable, the electrical transparency of the RFTP approximately is $j_{coll} \,/\, j_{beam,FC} = 44\,\%$. The transparency would be higher if we take into account the smaller distance and higher anode voltage with which the Faraday cup measurements were obtained.

3.2 Magnetron Discharge

Next, measurements are performed in a high-power impulse magnetron sputter (HiPIMS) system [35]. The target cathode is operated with an 800 W DC power supply. The measurement electronics are not equipped to deliver a time resolution for a single pulse in such a system. A carbon target was used in an Argon atmosphere at 0.36 Pa. The distance of the RFTP to the rectangular 10×30 cm carbon target is 10 cm. A 6 mm orifice of the RFTP was used.

For all magnetron discharge configurations that are used in a wide variety of scientific and industrial applications for processing substrate surfaces (e.g. thin film deposition in microelectronics or hard coatings), the energy balance at the substrate of arriving species (charged or neutral) is of utmost importance [36–39].

The film forming neutral atoms, which are ejected from the target surface, mainly influence the properties of the desired films. The energy needed for surface diffusion influencing the structure of the film [40] mainly comes from bombarding ions of the inert working gas [41]. For these considerations, the RFTP enables the user to determine the energy balance between ions and neutrals at a specific location.

Examples of related measurements are shown in fig. 12. The ion current arriving at the collector is comparable to that one in a rf plasma (next chapter) even though the magnetron is operated at such a high power. This is due to the large area of the target. The incoming energy flux density is much smaller though at a maximum of roughly $J_{in,max} = 1.1$ mW/cm^2 and only $J_{in,min} = 0.18$ mW/cm^2 still above 25 V Scan Grid voltage when all charged species are repelled by the probe. This results in an ion-to-neutral ratio of

$$\frac{J_{in,max} - J_{in,min}}{J_{in,max}} = 0.83. \tag{9}$$

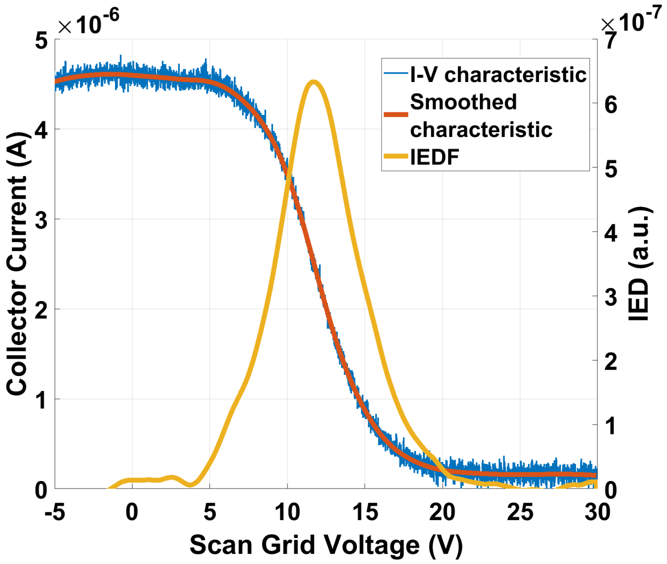

(a) RFEA measurement in HiPIMS magnetron discharge

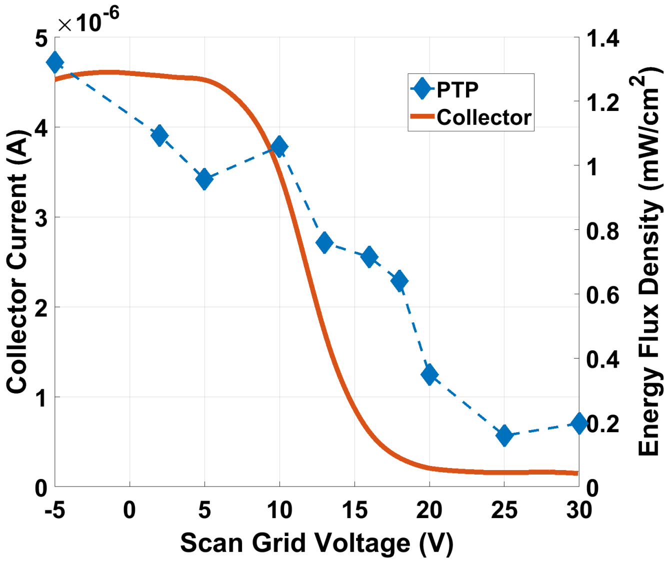

(b) Corresponding energy flux density with measured collector current

Figure 12: RFEA (a) and RFTP (b) measurements in a HiPIMS system. The working gas is Argon with 0.36 Pa with 55 sccm gas flow. The carbon target was operated at 800 W DC.

When looking only at charge exchange collisions, as was done in the previous chapter, the mean free path for charge exchange collisions is $\lambda_{cx,ms} = 0.27$ m. With this estimation, the partial contribution of ions to the total energy flux density would be

$$\frac{J_{in,ions}(z)}{J_{in,max}(z)} = exp(-\frac{z}{\lambda_{cx,ms}}) = 0.69 \tag{10}$$

for $z = 0.1$ m.

The discrepancy in the ratios is expected, since other collisions, especially elastic collisions, play an important role in magnetron discharges. In addition to low-energy argon ions and neutral argon atoms impinging on the substrate (collector), other species such as carbon ions or carbon clusters from the target may also be present in the plasma and can arrive at the substrate. This, of course, is dependent on the operating conditions of the magnetron discharge.

To estimate the contribution of each of these species to the energy balance at the substrate (collector) one could resort to simulations using, for example, a binary collision approximation Monte-Carlo method. Up to now, these kinds of simulations are mostly used to discuss the thin film properties of ex-situ examined film deposited under corresponding conditions [39, 42, 43]. Hence, the RFTP can be used as a useful link between simulations and ex-situ investigations, as it provides quantifiable and localized measurements of ion and neutral energy flux densities.

3.3 RF Plasma

Last, measurements have been performed in a rf-ccp parallel plate discharge. The RFTP is embedded into the grounded electrode. The RFTP orifice has a 6 mm diameter and the grounded first grid G0 is used to shield the bulk plasma from the grid system. Grounded and powered electrodes are in a distance of 5 cm, and the powered electrode is driven with a 13.56 MHz voltage at 100 W power. The working gas is argon at a 2 Pa pressure.

Fig. 13 shows typical measurements for a scan grid sweep from 0 V - 50 V. Fig. 13a shows the I-V characteristic, i.e. the collector current depending on scan grid voltage. Also shown is the smoothed characteristic, resulting from a spline fit method, and the ion energy distribution (IED). Fig. 13b shows the measured energy flux density (EFD) together with the collector current. The energy flux arriving at the collector decreases with the rising scan grid voltage. Ions are steadily reflected at the scan grid and the measured current drops. Simultaneously, the incoming energy due to energetic ions drops with the ion current. However, unlike the collector current, there is still a significant amount of energy flux $J_{in,min} = 5.75$ mW/cm^2 measured above 40 V, even though the charge carriers are blocked from the collector. The incoming EFD drops from roughly $J_{in,max} = 7$ mW/cm^2 to 5.75 mW/cm^2.

Since the RFTP housing is at a constant temperature, additional heat radiation from the holder can be ruled out. Of course, some heat radiation from the plasma might reach the PTP, but the remaining EFD comes from fast neutrals of the plasma bulk originating in charge exchange collisions and possibly a small percentage of recombined ions. Measurements with a cylindrical Langmuir probe inside the plasma bulk revealed a plasma potential of $\Phi_{Pl} = 30$ V and an electron density $n_e = 2.9 \cdot 10^{16}$ m^{-3}. The plasma potential is a good indicator for the RFEA measurements as the ions are accelerated, which is indicated in their energy distribution. Typically, rf plasmas have relatively low ionization rates, shown by the rather small electron density. This in turn confirms, however, why the remaining EFD should come from neutrals passing through the RFEA grid system at such a high rate.

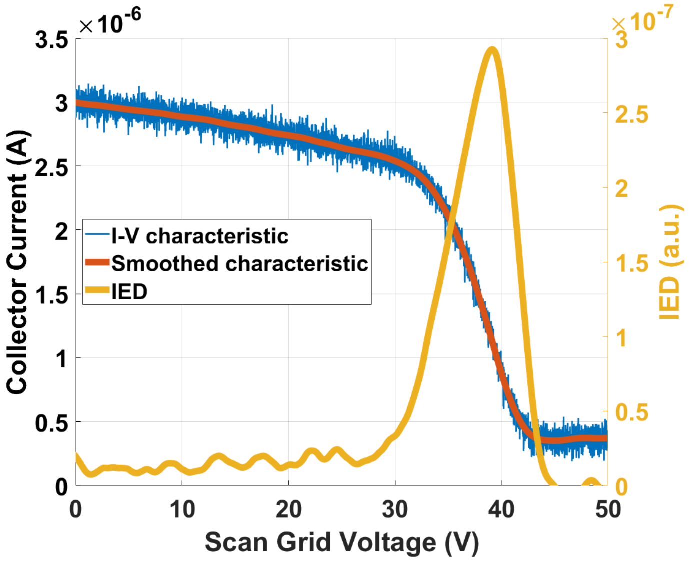

(a) RFEA measurement in rf-ccp parallel plate plasma environment. Operating pressure is 2 Pa Argon and power is 100 W at driven electrode

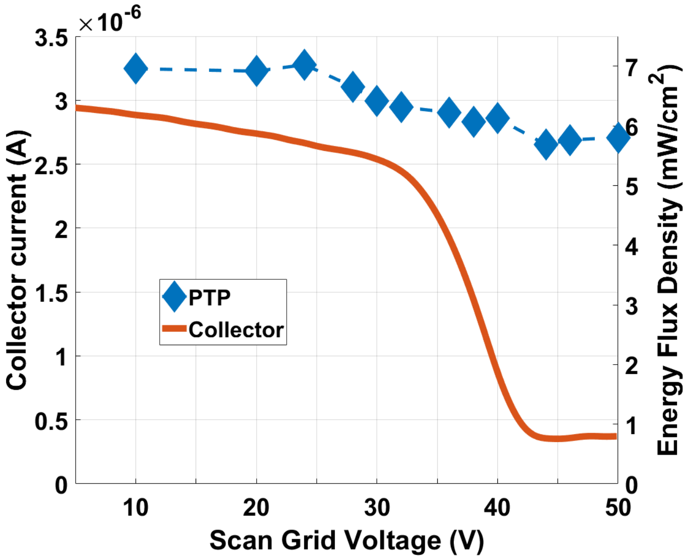

(b) Corresponding energy flux density with measured collector current

Figure 13: RFEA (a) and RFTP (b) measurements in rf-ccp parallel plate discharge

Here, as was also discussed for the magnetron discharge, different types of energetic collisions are responsible for the remaining incoming energy flux $J_{in,min}$. Elastic collisions of ions with neutral gas molecules in the sheath can lead to energy loss and broadening of the ion energy distribution.

Within the plasma itself, charge exchange collisions can lead to the formation of fast neutrals. Overall, the EFD is much higher than in magnetron discharge as well as the relationship between ion and neutral contribution, which is

$$\frac{J_{in,max} - J_{in,min}}{J_{in,max}} = 0.18. \tag{11}$$

The influence of collisions is much more pronounced and the energy balance at the grounded electrode is much more dominated by (fast) neutrals.

4 Conclusions

This newly designed plasma diagnostic (RFTP) presented here opens up new possibilities in the field of analyzing the energy spectrum of particles and flows in a broad range of different plasma environments. Ion energy distribution functions can be determined and correlated to their energy flux density. Additionally, the energy flux density of (fast) neutrals originating from charge exchange collisions can be determined.

In the case of ion beam experiments, where charge exchange collisions are important, the measurements coincide with the theoretical model. For plasma environments where elastic and other collisions play a more dominant role, the individual contributions of collisions to the overall energy balance at the collector are more difficult to quantify by using only this probe. However, the RFTP diagnostic presented here proves a valuable addition to the field of plasma probe diagnostics, since it gives new insight into the energy balance of species in the plasma.

Competing interests

The authors declare that they have no competing interests.

Author's contributions

FS: Conceptualization, Investigation, Analysis, Writing. HK: Conceptualization, Supervision. All authors have read and approved the final manuscript.

Acknowledgements

The magnetron discharge measurements were done at the Surface Science & Coating Technologies Group at Empa, Switzerland. The authors thank Kerstin Thorwarth and Sebastian Siol for their assistance and the provision of the experimental setup.

References

1. Benedikt, J., Kersten, H., Piel, A.: Foundations of measurement of electrons, ions and species fluxes towards surfaces in low-temperature plasmas. Plasma Sources Science and Technology **30**(3) (2021). doi:10.1088/1361-6595/abe4bf
2. Hanna, A.R., Fisher, E.R.: Investigating recent developments and applications of optical plasma spectroscopy: A review. Journal of Vacuum Science & Technology A **38**(2), 020806 (2020). doi:10.1116/1.5141844
3. Benedikt, J., Hecimovic, A., Ellerweg, D., von Keudell, A.: Quadrupole mass spectrometry of reactive plasmas. Journal of Physics D: Applied Physics **45**(40), 403001 (2012). doi:10.1088/0022-3727/45/40/403001
4. Demidov, V.I., Ratynskaia, S.V., Rypdal, K.: Electric probes for plasmas: The link between theory and instrument. Review of Scientific Instruments **73**(10), 3409–3439 (2002). doi:10.1063/1.1505099
5. Spethmann, A., Trottenberg, T., Kersten, H., Hey, F.G., Grimaud, L., Mazouffre, S., Bock, D., Tajmar, M.: Force probes for development and testing of different electric propulsion systems. EPJ Techn Instrum **9**(1), 4 (2022). doi:10.1140/epjti/s40485-022-00079-w
6. Klindworth, M., Arp, O., Piel, A.: Langmuir probe diagnostics in the IMPF device and comparison with simulations and tracer particle experiments. J. Phys. D: Appl. Phys. **39**(6), 1095–1104 (2006). doi:10.1088/0022-3727/39/6/015
7. Singh, S.B., Chand, N., Patil, D.S.: Langmuir probe diagnostics of microwave electron cyclotron resonance (ECR) plasma. Vacuum **83**(2), 372–377 (2008). doi:10.1016/j.vacuum.2008.05.030
8. Irimiciuc, S.A., Chertopalov, S., Lancok, J., Craciun, V.: Langmuir probe technique for plasma characterization during pulsed laser deposition process. Coatings **11**(7), 762 (2021). doi:10.3390/coatings11070762
9. Piejak, R.B., Godyak, V.A., Garner, R., Alexandrovich, B.M., Sternberg, N.: The hairpin resonator: A plasma density measuring technique revisited. Journal of Applied Physics **95**(7), 3785–3791 (2004). doi:10.1063/1.1652247
10. Lovberg, R.H.: The use of magnetic probes in plasma diagnostics. Annals of Physics **8**(3), 311–324 (1959). doi:10.1016/0003-4916(59)90001-6
11. Gahan, D., Dolinaj, B., Hopkins, M.B.: Comparison of plasma parameters determined with a langmuir probe and with a retarding field energy analyzer. Plasma Sources Science and Technology **17**(3), 035026 (2008). doi:10.1088/0963-0252/17/3/035026
12. Meister, H., Bernert, M., Biel, W., Han, M., Ingesson, L.C., Mukai, K., Penzel, F., Peterson, B.J., Reichle, R., Reinke, M.L., Schmitt, S., Zhang, D.: Bolometer developments in diagnostics for magnetic confinement fusion. Journal of Instrumentation **14**(10), 10004 (2019). doi:10.1088/1748-0221/14/10/C10004

13. Thornton, J.A.: Substrate heating in cylindrical magnetron sputtering sources. Thin Solid Films **54**(1), 23–31 (1978). doi:10.1016/0040-6090(78)90273-0
14. van den Berg-Stolp, J., Classen, I.G.J., van der Meiden, H.J., Vernimmen, J.W.M., Brons, S., van Rooij, G.J.: Inducing thermionic emission from lanthanum hexaboride probes in magnum-PSI. Nuclear Materials and Energy **29**, 101097 (2021). doi:10.1016/j.nme.2021.101097
15. Schneider, V., Kersten, H.: An optical trapping system for particle probes in plasma diagnostics. Review of Scientific Instruments **89**(10), 103505 (2018). doi:10.1063/1.5051065
16. Hübner, S., Palomares, J.M., Carbone, E.A.D., van der Mullen, J.J.A.M.: A power pulsed low-pressure argon microwave plasma investigated by thomson scattering: evidence for molecular assisted recombination. J. Phys. D: Appl. Phys. **45**(5), 055203 (2012). doi:10.1088/0022-3727/45/5/055203
17. Vaudolon, J., Mazouffre, S.: Indirect determination of the electric field in plasma discharges using laser-induced fluorescence spectroscopy. Physics of Plasmas **21**(9) (2014). doi:10.1063/1.4895532
18. Dittmann, K., Küllig, C., Meichsner, J.: 160 GHz gaussian beam microwave interferometry in low-density rf plasmas. Plasma Sources Sci. Technol. **21**(2), 024001 (2012). doi:10.1088/0963-0252/21/2/024001
19. Baloniak, T., Reuter, R., Flötgen, C., von Keudell, A.: Calibration of a miniaturized retarding field analyzer for low-temperature plasmas: geometrical transparency and collisional effects. Journal of Physics D: Applied Physics **43**(5), 055203 (2010). doi:10.1088/0022-3727/43/5/055203
20. Böhm, C., Perrin, J.: Retarding-field analyzer for measurements of ion energy distributions and secondary electron emission coefficients in low-pressure radio frequency discharges. Review of Scientific Instruments **64**(1), 31–44 (1993). doi:10.1063/1.1144398
21. Enloe, C.L.: High-resolution retarding potential analyzer. Review of Scientific Instruments **65**(2), 507–508 (1994). doi:10.1063/1.1145167
22. Sharma, S., Gahan, D., Kechkar, S., Daniels, S., Hopkins, M.B.: A spatially resolved retarding field energy analyzer design suitable for uniformity analysis across the surface of a semiconductor wafer. Review of Scientific Instruments **85**(4) (2014). doi:10.1063/1.4870900. 043509
23. Gauter, S., Haase, F., Kersten, H.: Experimentally unraveling the energy flux originating from a DC magnetron sputtering source. Thin Solid Films **669**, 8–18 (2019). doi:10.1016/j.tsf.2018.10.021
24. Stahl, M., Trottenberg, T., Kersten, H.: A calorimetric probe for plasma diagnostics. Review of Scientific Instruments **81**(2), 023504 (2010). doi:10.1063/1.3276707
25. Gauter, S., Fröhlich, M., Garkas, W., Polak, M., Kersten, H.: Calorimetric probe measurements for a high voltage pulsed substrate (PBII) in a HiPIMS process. Plasma Sources Sci. Technol. **26**(6), 065013 (2017). doi:10.1088/1361-6595/aa6f9e
26. Sahu, B.B., Yin, Y., Gauter, S., Han, J.G., Kersten, H.: Plasma engineering of silicon quantum dots and their properties through energy deposition and chemistry. Phys. Chem. Chem. Phys. **18**(37), 25837–25851 (2016). doi:10.1039/C6CP05647D
27. Zahari, F., Schlichting, F., Strobel, J., Dirkmann, S., Cipo, J., Gauter, S., Trieschmann, J., Marquardt, R., Haberfehlner, G., Kothleitner, G., Kienle, L., Mussenbrock, T., Ziegler, M., Kersten, H., Kohlstedt, H.: Correlation between sputter deposition parameters and *I-V* characteristics in double-barrier memristive devices. Journal of Vacuum Science & Technology B **37**(6), 061203 (2019). doi:10.1116/1.5119984
28. Lundin, D., Stahl, M., Kersten, H., Helmersson, U.: Energy flux measurements in high power impulse magnetron sputtering. J. Phys. D: Appl. Phys. **42**(18), 185202 (2009). doi:10.1088/0022-3727/42/18/185202
29. Hansen, L., Kohlmann, N., Kienle, L., Kersten, H.: Correlations between energy flux and thin film modifications in an atmospheric pressure direct current microplasma. Thin Solid Films **765**, 139633 (2023). doi:10.1016/j.tsf.2022.139633
30. Zeuner, M., Scholze, F., Neumann, H., Chassé, T., Otto, G., Roth, D., Hellmich, A., Ocker, B.: A unique ecr broad beam source for thin film processing. Surface and Coatings Technology **142-144**, 11–20 (2001). doi:10.1016/S0257-8972(01)01144-6
31. Trottenberg, T., Schneider, V., Kersten, H.: Measurement of the force on microparticles in a beam of energetic ions and neutral atoms. Physics of Plasmas **17**(10), 103702 (2010). doi:10.1063/1.3489795
32. Spethmann, A., Trottenberg, T., Kersten, H.: Instrument for spatially resolved simultaneous measurements of forces and currents in particle beams. Review of Scientific Instruments **86**(1), 015107 (2015). doi:10.1063/1.4905534
33. Phelps, A.V.: The application of scattering cross sections to ion flux models in discharge sheaths. Journal of Applied Physics **76**(2), 747–753 (1994). doi:10.1063/1.357820
34. Spethmann, A., Trottenberg, T., Kersten, H.: Spatially resolved momentum flux measurements for thruster plume diagnostics. (2013)
35. Sarakinos, K., Alami, J., Konstantinidis, S.: High power pulsed magnetron sputtering: A review on scientific and engineering state of the art. Surface and Coatings Technology **204**(11), 1661–1684 (2010). doi:10.1016/j.surfcoat.2009.11.013
36. Seeger, S., Harbauer, K., Ellmer, K.: Ion-energy distributions at a substrate in reactive magnetron sputtering discharges in ar/h2s from copper, indium, and tungsten targets. Journal of Applied Physics **105**(5), 053305 (2009). doi:10.1063/1.3086618
37. Rudolph, M., Lundin, D., Foy, E., Debongnie, M., Hugon, M.-C., Minea, T.: Influence of backscattered neutrals on the grain size of magnetron-sputtered TaN thin films. Thin Solid Films **658**, 46–53 (2018). doi:10.1016/j.tsf.2018.05.027
38. Schell, V., Müller, C., Durdaut, P., Kittmann, A., Thormählen, L., Lofink, F., Meyners, D., Höft, M., McCord, J., Quandt, E.: Magnetic anisotropy controlled fecosib thin films for surface acoustic wave magnetic field sensors. Applied Physics Letters **116**(7), 073503 (2020). doi:10.1063/1.5140562
39. Farhadizadeh, A., Kozák, T.: The importance of discharge voltage in DC magnetron sputtering for energy of sputtered and backscattered atoms on the substrate: Monte-Carlo simulations. Vacuum **196**, 110716 (2022). doi:10.1016/j.vacuum.2021.110716
40. Anders, A.: A structure zone diagram including plasma-based deposition and ion etching. Thin Solid Films

518(15), 4087–4090 (2010). doi:10.1016/j.tsf.2009.10.145

41. Gudmundsson, J.T.: Physics and technology of magnetron sputtering discharges. Plasma Sources Science and Technology **29**(11), 113001 (2020). doi:10.1088/1361-6595/abb7bd
42. Bultinck, E., Bogaerts, A.: Particle-in-cell/monte carlo collisions treatment of an ar/o2 magnetron discharge used for the reactive sputter deposition of tiox films. New Journal of Physics **11**(10), 103010 (2009). doi:10.1088/1367-2630/11/10/103010
43. Ellmer, K., Welzel, T.: Reactive magnetron sputtering of transparent conductive oxide thin films: Role of energetic particle (ion) bombardment. Journal of Materials Research **27**(5), 765–779 (2012). doi:10.1557/jmr.2011.428

8 Use of the RFTP in an HiPIMS application

During a short stay at the laboratory for Surface Science & Coating Technologies at Empa in Dübendorf, Switzerland, the retarding field thermal probe was used to investigate a High Power Impulse Magnetron Sputter (HiPIMS) device. The experimental chamber has 4 circularly aligned 10 × 30 cm targets perpendicular to the centre of the vacuum chamber. A service flange can be used to replace one of the targets and access the vacuum chamber. The schematic setup alongside a picture of the RFTP inside the chamber is shown in figure 8.1. The additional PTP, also shown in figure 8.1, will be addressed later in this chapter.

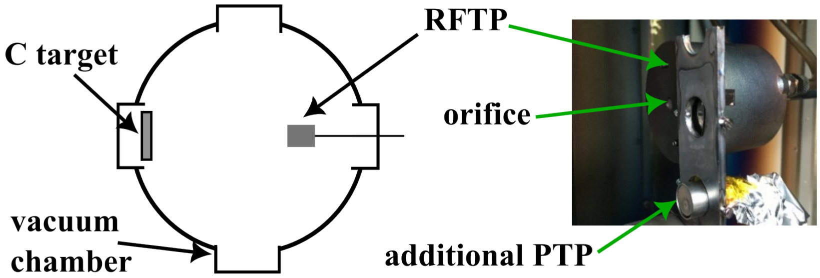

Figure 8.1: (Left) Schematic drawing of the vacuum chamber with the RFTP opposite the C target. (Right) Picture of the RFTP within the vacuum chamber with an additional PTP placed alongside it.

The distance of the RFTP to the C target is 10 cm and is it located slightly above the centre of the target. Various measurements in HiPIMS mode and DC mode were made which will be addressed in the following sections. For all measurements, the working gas is argon at 0.36 Pa with a 55 sccm gas flow. First, a power and pulse length variation is presented, done in HiPIMS mode. During the course of the measurement campaign, it was found that, due to the close proximity of the probe to the target, the first grid (screen grid) could not fully prevent the plasma from entering the grid system. This led to distortions in the collector current and a broadening of the IED and was noticeable in HiPIMS mode. The problem could be solved by alternate wiring of the grids leading to a better energy resolution of the RFTP but also had a negative effect in regard to the secondary electrons emitted from the collector. Last, the measurements presented in the previous chapter for DC mode are discussed in more detail and correlated to the additional PTP.

8.1 Voltage and pulse length variation

In the following, the ion energy distribution (IED) measurements are discussed that were done in HiPIMS mode with the RFTP. The screen grid and collector are biased at −60 V and the SE repelled grid at −70 V. The scan grid is sampled from 0 V to 25 V. The standard pulse width was 3 ms (333 Hz frequency) with a 20 μs high-power pulse length. The custom-built RFTP electronics are not able to resolve such short pulses. So, time-averaged measurements were done with a measurement length of 512 s per scan. A standard scan over a 30 V span (from −5 V to 25 V scan grid voltage) would then result in roughly 6500 data points and 3900 samples per setpoint.

The voltage variation measurements are shown in figure 8.2. The voltage is varied from 700 V to 1 kV with the standard pulse width and high-power pulse length. In this variation, the peak current at the target during the pulse increases from 18 A to 190 A.

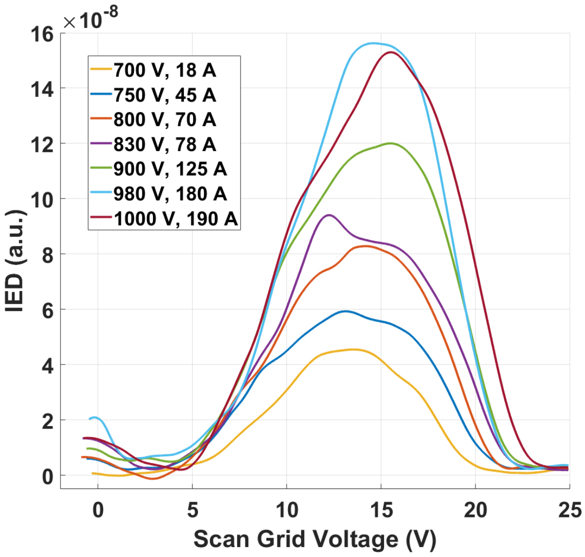

Figure 8.2: Measured IEDs for a target cathode power variation. The legend states voltage and peak current. The collector current is left out for clarity.

The measured collector currents were deliberately left out from figure 8.2 for clarity of the figure. But as expected the maximum collector current measured for scan grid voltages below 5 V increased with increasing target voltage. In table 8.1 these maximum currents are listed alongside the corresponding target voltage for a few selected voltages. As can be seen, the current roughly quadruples over the voltage variation from 700 V to 1 kV, whereas the peak current measured at the target during a pulse increases tenfold. An increase in target voltage has little to no effect on the ion energy distribution. Only the ion flux is increased leading to more ions reaching the collector.

target voltage (V)	peak target current (A)	max. collector current (μA)
700	18	0.43
800	70	0.88
900	125	1.35
1000	190	1.68

Table 8.1: Selected target voltage, peak target current and corresponding collector current during the standard HiPIMS mode.

The RFEA measurements for the pulse length variation are shown in figure 8.3. The high-power pulse was increased from 20 μs (yellow) to 40 μs (blue), 50 μs (purple) and 70 μs (green). The pulse width was held constant at 3 ms (333 Hz frequency) and the target voltage was 750 V.

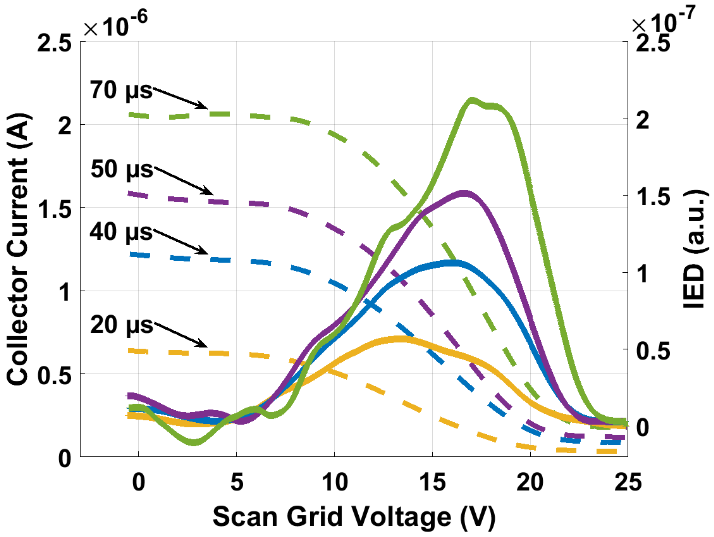

Figure 8.3: High-power pulse length variation. Frequency is kept constant at 333 Hz. Target voltage is 750 V.

An increase in pulse length has a stronger effect on the ion energy distribution than the target voltage. The peak of the IED shifts from 13 V to around 18 V. The increase in collector current correlates to the increase in high-power pulse length. However, the energy resolution of the grid system is strongly affected by the bulk plasma entering the RFTP which leads to a full width at half maximum (FWHM) of 8 V to 10 V.

8.2 Grid wiring and SE repeller grid bias variation

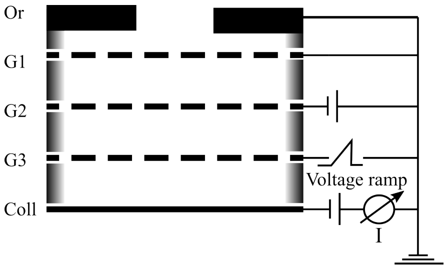

Figure 8.4: Alternate wiring of the grids.

To address the problem of the plasma entering the grid system and distorting the collector current, the grids are wired according to figure 8.4. This was necessary since a negative bias voltage at the first grid could be measured when opening the shutter in front of the target. This was true for both DC mode and HiPIMS mode. Grid G1 is grounded. Grid G2 now serves as the screen grid and the voltage scan is done at grid G3. With this wiring, there is no grid serving as the secondary electron repeller. The screen grid and collector are biased at −30 V and the scan grid is sampled from 0 V to 30 V. With this setup a pressure and frequency variation was investigated. The results of which are shown in figure 8.5 on the left and right, respectively.

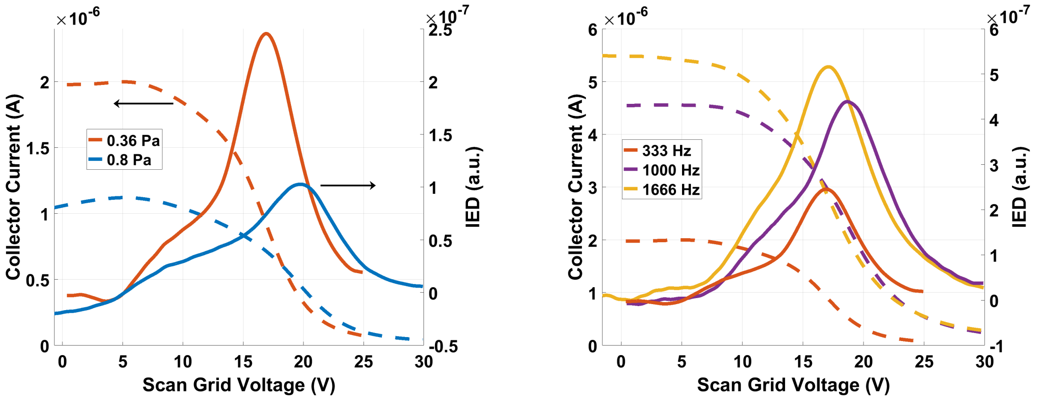

Figure 8.5: (Left) pressure and (Right) frequency variation using the alternate wiring of the grids in HiPIMS mode, 750 V, 45 A, working gas Argon.

As expected the increase in working gas pressure leads to a reduction in measured collector current and a broadening of the IED due to increased collision rate in the bulk plasma. A higher pulse frequency increases the collector current but has seemingly no effect on the peak of the ion energy distribution.

The IEDs shown in figure 8.5, however, exhibit an apparent difference with respect to the ones from the previous section and the standard wiring of the grids. Their FWHM is smaller but also their shape is changed. The FWHM for the pressure variation measurement is ≈ 5 V. But there is a noticeable hump in the rising left flank of all IEDs in figure 8.5. This comes from the missing secondary electron repeller grid. The SEs that are emitted from the collector upon impact by the incoming ions are not brought back to the collector. This leads to a distortion in the measured collector current. To demonstrate this effect and emphasize the importance of the SE repeller grid in an RFEA system, a stepwise reduction of the bias voltage and the resulting IEDs is shown in figure 8.6. The target is operated in DC mode, with 800 W power and 0.36 Pa Ar pressure. The screen grid and collector are biased at -60 V and the SE repeller bias is reduced from -55 V to 0 V in steps of 5 V. The emergence of a second peak and the steady broadening of the IED are clearly visible. The actual peak can not be distinguished anymore.

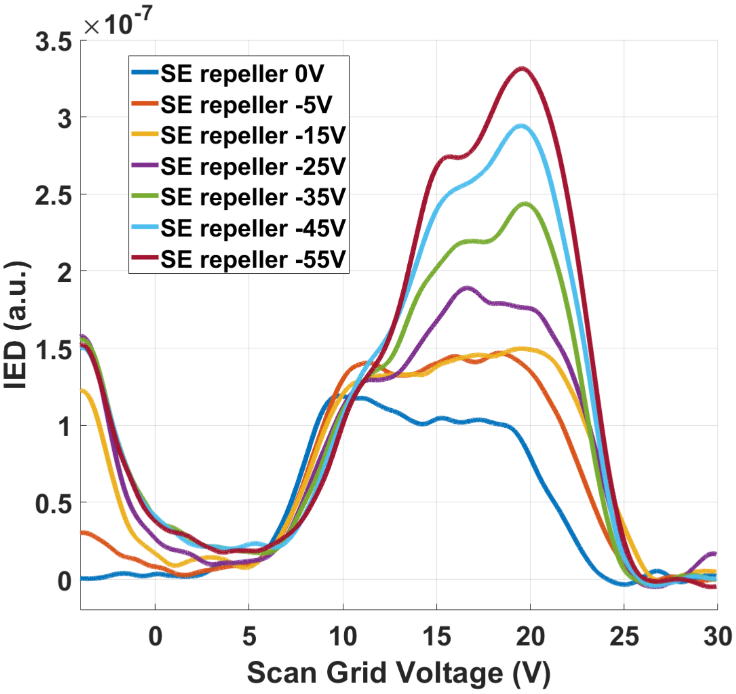

Figure 8.6: Stepwise reduction of the secondary electron repeller grid voltage in DC mode, 800 W

8.3 RFTP and additional PTP

In the previous chapter in publication 4, section 3.2, RFTP measurements were presented that were conducted in this device. The target is operated at 800 W DC power and the working gas is Argon with $3.6 \cdot 10^{-2}$ Pa and 55 sccm gas flow. As a reminder the presented results of the RFEA and RFTP measurements are shown in figure 8.7. The grids are wired as described in the previous section 8.2.

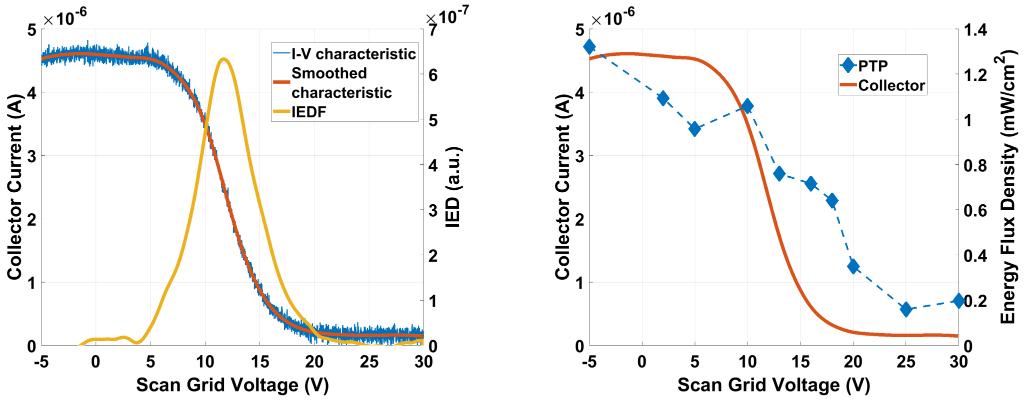

Figure 8.7: RFEA (left) and PTP (right) measurements during sputtering using a C target, taken from submitted publication 4 (chapter 7 of this work).

From these measurements, the partial contribution of ions to the total measured energy flux of the RFTP is 0.83.

The additional PTP, shown in figure 8.1, was used to investigate the ion contribution to the energy flux density without a grid system and to compare it with the ion contribution measured with the RFTP. A standard PTP was used, as described in section 4.2, consisting of a copper platelet with a 100 μm thickness and an 11 mm diameter. The heat capacity of the probe was calibrated to 0.0269 J/K. The probe was biased at −20 V, −40 V and −60 V to gradually repel electrons from the probe. The measurements are shown in figure 8.8. With increasing negative bias voltage, more electrons are repelled from the probe, but ions are accelerated towards it. Hence, the energy

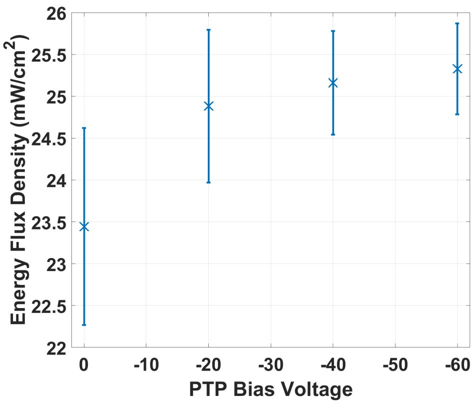

Figure 8.8: PTP bias variation in DC mode with 800 W power and 0.36 Pa Ar at 25 sccm gas flow.

slowly increases as well. In figure 8.8 the 0 V bias voltage measurement was done with a floating PTP substrate. Since it is not shielded in any way, the standard PTP is exposed to all energy fluxes inside the chamber coming from energetic species, radiation, combination on the surface, etc. At floating potential, there is a net zero current to the probe. The PTP inside the RFTP is shielded from electrons, slow neutrals, heat radiation and, depending on the scan grid voltage, ions. The PTP/collector in the RFTP is biased at −60 V.

Taking the energy flux density at 0 V bias $J_0 = 23.44$ mW/cm^2 and subtracting it from the energy flux density at −60 V bias $J_{-60} = 25.33$ mW/cm^2 should leave an ion contribution of $J_{ion,PTP} = 1.9$ mW/cm^2. This rather simple subtraction should be valid since the contribution of the kinetic energies of ions and electrons to the total energy flux in a DC magnetron sputter source is small compared to the contribution by sputtered particles [113]. Biasing the probe does not affect the sputtered particles, so the contribution is the same for all measurements shown in figure 8.8. At floating potential one expects the contribution of recombination to be higher than at a biased probe. But still,

The ion contribution measured with the RFTP is $J_{ion,RFTP} = 0.83 \cdot 1.1$ mW/cm^2 = 0.91 mW/cm^2. In chapter 7 section 3.1.2 a comparison was made between the measured ion current density j_{coll} at the collector and ion current density measurements done with a Faraday cup, $j_{beam,FC}$. From the ratio, a statement could be made about the actual electrical transparency of the grid system of the RFTP. The ratio between the two current densities is

$$\frac{j_{coll}}{j_{beam,FC}} = 0.44. \tag{8.1}$$

The ratio between the two ion contributions to energy flux density comes to

$$\frac{J_{ion,RFTP}}{J_{ion,PTP}} = 0.48. \tag{8.2}$$

To bring this together, two points can be made. First, the assumption that, at a −60 V bias voltage, the energy flux density at the PTP increases with increasing ion flux towards the probe can be confirmed and compared to the electrical transparency of the grids established with Faraday cup measurements. Second, the agreement between the two ratios once more establishes the transparency of the used grid system and the reproducibility of measurements done with the RFTP.

9 Conclusion and Outlook

The presented thesis has been dedicated to shedding light on the complexity of the energy balance in plasma-surface interactions using thermal and electrical diagnostic techniques and exploring the possibilities of simultaneous measurement and combination of these diagnostics. Through a well-structured exploration, this research has made substantial contributions to the field of plasma physics, advancing our understanding regarding the energy balance of the involved species of technological plasmas and their potential applications.

The initial chapters laid the foundation with a concise yet comprehensive overview of the underlying theory. This theoretical grounding paved the way for a deeper exploration into the generation of plasmas, encompassing methodologies like radio-frequency (rf) plasmas, ion beam technology and magnetron sputtering devices. A broader context was established for understanding the subsequent experimental investigations.

The core of this research was anchored in the application of diagnostics in a variety of different plasma environments. The Langmuir probe (LM), retarding field energy analyzer (RFEA) and passive thermal probe (PTP) emerged as crucial tools in the determination of plasma characteristics. These diagnostics bridged the gap between theoretical concepts and empirical observations, enabling a more nuanced understanding of plasma-surface interactions. The detailed analysis of plasma generation techniques and the different possibilities of characterization of plasma parameters and their effect on a surface has unveiled valuable insights into each method's specific features and characteristics, crucial for optimizing their applications.

The next phase of the thesis concentrated on conducting experiments in thin film deposition setups, employing both PTP and LM probe diagnostic techniques. The three publications from these experiments have demonstrated the importance of plasma diagnostics in technological plasma processes, elucidating the connections between plasma parameters and thin film properties. This contributed to improving the efficiency and precision of these depositions, fostering their practical application.

In the first publication, a notable correlation emerged between plasma parameters and the electrical behavior of memristive devices determined with PTP an LM probe. Within the limits of the target race track the desired resistive switching of the active NbO_x layer is present. Under the race track and towards the edges of the substrate this switching mechanism vanishes. A superimposition between the energy flux density (impacting the film properties like stochiometry and morphology) and the plasma parameters (like plasma potential and electron temperature) is believed to facilitate the desired properties of the NbO_x layer in the devices.

The second publication presented a comprehensive study investigating the influence of pressure, power and distance variations on the critical temperature T_C and residual resistivity ratio (RRR) of superconducting thin NbN films. Through the utilization of the PTP and LM probe, this study showed the correlation between grain size and crystallization (governed by ion and electron densities and energies) and T_C and RRR. It helped to pave the way for establishing a reproducible and reliable way of depositing superconducting NbN thin films.

The third publication showcased the utilization of the passive thermal probe to correlate energy flux densities with thin film growth and morphology, particularly within the context of Cu and NiTi films in a tilted magnetron sputter device. The NiTi film's change in morphology across the 200 mm substrate holder showed that actually intended rotation of the substrate holder can homogenize the deposition rate, but can not compensate for the film structure change apparent in the inner radii.

One of the major accomplishments of this research was the development of a novel combined diagnostic approach, utilizing a combination of the RFEA and the PTP. The synergistic effect of the combination provided a deeper insight into the complex ion energy distribution and ion and neutral flux within the plasma, which was previously unattainable through individual diagnostic techniques. The PTP, serving as the collector of the RFEA grid system, can be used to measure the energy flux density of incoming ions and neutrals depending on the scan grid voltage. This could be shown in a proof of principle measurement in an rf plasma and in additional measurements done in a DC magnetron sputter device. However, the first design had some issues regarding the resolution of the grid system and the heating of the probe body which were thoroughly addressed.

As a further development, building upon the success of the combined diagnostic, the improved design with water cooling and a well-defined grid structure was introduced. This enhancement further strengthened the diagnostic capabilities and unlocked the diagnostics' potential for measurements across multiple plasma environments. The water cooling improved the thermal stability inside the probe and allowed for measurements of small temperature changes at the PTP/collector. The improved grid system addressed prior concerns of resolution and reproducibility, paving the way for more accurate and reliable measurements. The submitted publication has highlighted the effectiveness of the upgraded diagnostic setup, showcasing its potential as a valuable tool for advanced plasma diagnostics in rf plasmas, ion beam experiments and magnetron sputter discharges. The ion current measured at the collector correlates with the energy flux density. While the collector current disappears there is still energy flux density coming from fast neutrals. This ratio of ion-to-neutral energy flux can be used, for instance, to investigate the influence of charge exchange collisions in ion beam experiments. The simultaneous measurement of ion energy distribution and the resulting energy flux density is a new way to gain insight into the plasma-surface interaction.

The last chapter's exploration of the combined RFEA and PTP diagnostic inside of a High Power Impulse Magnetron Sputtering (HiPIMS) device further established the reliability of the probe and its widespread usage. Variations in frequency and pulse length revealed a few areas for improvement regarding the resolution of the probe but also highlighted the significance of the secondary electron repeller grid, emphasizing the complex interaction of diagnostic components and the challenging influence they wield in determining plasma parameters. Finally, the additional measurements with a standard PTP once again demonstrate the application possibility of the RFTP as an additional diagnostic yielding results others can not.

In conclusion, this PhD thesis has made significant contributions to the field of plasma physics, particularly in the area of technological plasmas and their applications in thin film deposition processes. The successful combination of RFEA and PTP has proven to be a valuable approach for investigating the energy balance in plasma-surface interactions. As technological plasmas continue to gain prominence in various research and industries, the insights from this work provide implications for the advancement of plasma-based technologies and their applications in materials science, nanotechnology, and beyond.

As a final consideration, some thoughts are provided for future possibilities in the advancement and application of the combined diagnostic:

- Energy resolution of the grid system can be advanced by using even smaller grid holes and varying the grid distances. Simulations of the probe body and the ion paths and electric field inside it could also provide valuable insights.
- The distance of the PTP/collector to the grids and its shielding inside the probe body can be a point of advancement by minimizing the possibility of collisions and influence from other heat/energy sources.
- The material used as PTP/collector can be varied to study its effect on the ion energy distribution (keyword: Secondary electron repeller grid).
- Different PTP materials could also be used to study their individual secondary electron emission in dependence on the incoming ion energy.
- With suitable electronics the probe could be embedded into the driven electrode of a rf plasma and used to investigate the typical two-peaked ion energy distribution and the effect it has on the energy flux density.

List of Figures

Bibliography

[1] M. A. Lieberman and A. J. Lichtenberg, *Principles of plasma discharges and materials processing*, 2nd (Wiley-Interscience, Hoboken, N.J, 2005).

[2] F. Chen, *Introduction to Plasma Physics and Controlled Fusion*, 3rd (Springer International Publishing : Imprint: Springer, 2016).

[3] B. Schmidt and K. Wetzig, *Ion beams in materials processing and analysis*, OCLC: ocn840900154 (Springer, Wien ; New York, 2013).

[4] K. Wasa, I. Kanno, and H. Kotera, eds., *Handbook of sputter deposition technology: fundamentals and applications for functional thin films, nanomaterials and MEMS*, 2nd ed (William Andrew, Waltham, MA, 2012).

[5] A. A. Fridman and L. A. Kennedy, *Plasma physics and engineering*, 2nd (CRC Press, Boca Raton, FL, 2011).

[6] I. Langmuir, "Oscillations in Ionized Gases", Proceedings of the National Academy of Sciences **14**, 627–637 (1928).

[7] R. Hippler, ed., *Low temperature plasma physics: fundamental aspects and applications*, 2nd (Wiley-VCH, Berlin, 2008).

[8] U. Stroth, *Plasmaphysik: Phänomene, Grundlagen und Anwendungen*, 2nd (Springer Spektrum, Berlin [Heidelberg], 2018).

[9] A. Piel, *Plasma physics: an introduction to laboratory, space, and fusion plasmas* (Springer, Heidelberg ; New York, 2010).

[10] E. H. P. Debye, "Zur Theorie der Elektrolyte", Physikalische Zeitschrift **24**, 185–206 (1923).

[11] N. Krall and A. Trivelpiece, *Principles of Plasma Physics*, International series in pure and applied physics (McGraw-Hill, 1973).

[12] D. Bohm, "Minimum ionic kinetic energy for a stable sheath", in *The characteristics of electrical discharges in magnetic fields* (McGraw-Hill, New York, NY, 1949) Chap. 3, p. 77.

[13] J. Pelletier and A. Anders, "Plasma-based ion implantation and deposition: a review of physics, technology, and applications", IEEE Transactions on Plasma Science **33**, 1944–1959 (2005).

[14]C. D. Child, “Discharge From Hot Cao”, Physical Review (Series I) **32**, 492–511 (1911).

[15]I. Langmuir, “The Effect of Space Charge and Residual Gases on Thermionic Currents in High Vacuum”, Physical Review **2**, 450–486 (1913).

[16]M. Lieberman, “Dynamics of a collisional, capacitive RF sheath”, IEEE Transactions on Plasma Science **17**, 338–341 (1989).

[17]B. H. Bransden and C. J. Joachain, *Physics of atoms and molecules*, 2nd (Prentice Hall, Harlow, England ; New York, 2003).

[18]R. B. Brode, “The Quantitative Study of the Collisions of Electrons with Atoms”, Reviews of Modern Physics **5**, 257–279 (1933).

[19]Y.-K. Kim and M. E. Rudd, “Binary-encounter-dipole model for electron-impact ionization”, Physical Review A **50**, 3954–3967 (1994).

[20]J. Kaur et al., “Electron impact ionization cross sections of atoms”, Canadian Journal of Physics **93**, 617–625 (2015).

[21]R. Rejoub, B. G. Lindsay, and R. F. Stebbings, “Determination of the absolute partial and total cross sections for electron-impact ionization of the rare gases”, Physical Review A **65**, 042713 (2002).

[22]I. H. Hutchinson, *Principles of Plasma Diagnostics*, 2nd edition (Cambridge University Press, Cambridge, 2005).

[23]A. V. Phelps, “The application of scattering cross sections to ion flux models in discharge sheaths”, Journal of Applied Physics **76**, 747–753 (1994).

[24]T. Trottenberg, V. Schneider, and H. Kersten, “Measurement of the Force on Microparticles in an Energetic Ion Beam”, IEEE Transactions on Plasma Science **38**, 774–780 (2010).

[25]I. Langmuir, “The Interaction of Electron and Positive Ion Space Charges in Cathode Sheaths”, Physical Review **33**, 954–989 (1929).

[26]J. A. Thornton, “Influence of apparatus geometry and deposition conditions on the structure and topography of thick sputtered coatings”, Journal of Vacuum Science and Technology **11**, 666–670 (1974).

[27]I. Adamovich et al., “The 2022 Plasma Roadmap: low temperature plasma science and technology”, Journal of Physics D: Applied Physics **55**, 373001 (2022).

[28]G. S. Oehrlein, “Surface processes in low pressure plasmas”, Surface Science **386**, 222–230 (1997).

[29]S. Samukawa and et al., “The 2012 Plasma Roadmap”, Journal of Physics D: Applied Physics **45**, 253001 (2012).

[30] J. Friedrich, *The plasma chemistry of polymer surfaces: advanced techniques for surface design* (Wiley-VCH, Weinheim, 2012).

[31] A. Anders, “A structure zone diagram including plasma-based deposition and ion etching”, Thin Solid Films **518**, 4087–4090 (2010).

[32] H. Kersten et al., “The energy balance at substrate surfaces during plasma processing”, Vacuum **63**, 385–431 (2001).

[33] M. J. Druyvesteyn and F. M. Penning, “The Mechanism of Electrical Discharges in Gases of Low Pressure”, Reviews of Modern Physics **12**, 87–174 (1940).

[34] E Kawamura et al., “Ion energy distributions in rf sheaths; review, analysis and simulation”, Plasma Sources Science and Technology **8**, R45–R64 (1999).

[35] K. Ellmer and T. Welzel, “Reactive magnetron sputtering of transparent conductive oxide thin films: Role of energetic particle (ion) bombardment”, Journal of Materials Research **27**, 765–779 (2012).

[36] G. Betz and K. Wien, “Energy and angular distributions of sputtered particles”, International Journal of Mass Spectrometry and Ion Processes **140**, 1–110 (1994).

[37] T. Lill, V. Vahedi, and R. A. Gottscho, “Etching of Semiconductor Devices”, in *Materials Science and Technology*, edited by R. W. Cahn, P. Haasen, and E. J. Kramer, 1st ed. (Wiley, Nov. 2019), pp. 1–25.

[38] S. Kasi et al., “Inelastic processes in low-energy ion-surface collisions”, Surface Science Reports **10**, 1–104 (1989).

[39] P. Sigmund, “Sputtering by ion bombardment theoretical concepts”, in *Sputtering by Particle Bombardment I*, Vol. 47, edited by R. Behrisch, Series Title: Topics in Applied Physics (Springer Berlin Heidelberg, Berlin, Heidelberg, 1981), pp. 9–71.

[40] D. Rosenberg and G. K. Wehner, “Sputtering Yields for Low Energy He^+-, Kr^+-, and Xe^+-Ion Bombardment”, Journal of Applied Physics **33**, 1842–1845 (1962).

[41] N. Laegreid and G. K. Wehner, “Sputtering Yields of Metals for Ar^+ and Ne^+ Ions with Energies from 50 to 600 ev”, Journal of Applied Physics **32**, 365–369 (1961).

[42] J. F. Ziegler, M. Ziegler, and J. Biersack, “SRIM – The stopping and range of ions in matter (2010)”, Nuclear Instruments and Methods in Physics Research Section B: Beam Interactions with Materials and Atoms **268**, 1818–1823 (2010).

[43] X. Z. Yao and D. Y. Jiang, “Effect of secondary electron emission on sheath potential in an electron cyclotron resonance plasma”, Journal of Applied Physics **81**, 2119–2123 (1997).

[44] R. G. Lye and A. J. Dekker, “Theory of Secondary Emission”, Physical Review **107**, 977–981 (1957).

[45] B. N. Chapman, *Glow discharge processes: sputtering and plasma etching* (Wiley, New York, 1980).

[46] C. Kittel, *Introduction to solid state physics*, 8th ed (Wiley, Hoboken, NJ, 2005).

[47] G. Hua and D. Li, "Electron work function: a novel probe for toughness", Physical Chemistry Chemical Physics **18**, 4753–4759 (2016).

[48] A. V. Keudell, "Surface processes during thin-film growth", Plasma Sources Science and Technology **9**, 455–467 (2000).

[49] J. A. Thornton, "Substrate heating in cylindrical magnetron sputtering sources", Thin Solid Films **54**, 23–31 (1978).

[50] E. Husain and R. S. Nema, "Analysis of Paschen Curves for air, N2 and SF6 Using the Townsend Breakdown Equation", IEEE Transactions on Electrical Insulation **EI-17**, 350–353 (1982).

[51] H. Takikawa and H. Tanoue, "Review of Cathodic Arc Deposition for Preparing Droplet-Free Thin Films", IEEE Transactions on Plasma Science **35**, 992–999 (2007).

[52] J. R. Roth, *Industrial plasma engineering, Volume 1, Principles* (CRC Press, Boca Raton, Florida, 1995).

[53] R. P. Brinkmann, "From electron depletion to quasi-neutrality: the sheath–bulk transition in RF modulated discharges", Journal of Physics D: Applied Physics **42**, 194009 (2009).

[54] F. M. Georg, "Aufbau einer Sondendiagnostik zur Untersuchung von Plasma-Wand-Wechselwirkung", MA thesis (CAU Kiel, 2016).

[55] M. Zeuner et al., "A unique ECR broad beam source for thin film processing", Surface and Coatings Technology **142-144**, 11–20 (2001).

[56] T. Trottenberg et al., "Non-Electrostatic Diagnostics for Ion Beams", Contributions to Plasma Physics **52**, 584–592 (2012).

[57] J. Asmussen, "Electron cyclotron resonance microwave discharges for etching and thin-film deposition", Journal of Vacuum Science & Technology A: Vacuum, Surfaces, and Films **7**, 883–893 (1989).

[58] A. Spethmann, T. Trottenberg, and H. Kersten, "Instrument for spatially resolved simultaneous measurements of forces and currents in particle beams", Review of Scientific Instruments **86**, 015107 (2015).

[59] W. D. Gill and E. Kay, "Efficient Low Pressure Sputtering in a Large Inverted Magnetron Suitable for Film Synthesis", Review of Scientific Instruments **36**, 277–282 (1965).

[60] J. T. Gudmundsson, "Physics and technology of magnetron sputtering discharges", Plasma Sources Science and Technology **29**, 113001 (2020).

[61] J. J. Licari and L. R. Enlow, *Hybrid microcircuit technology handbook: materials, processes, design, testing, and production*, 2nd ed, Materials science and process technology series (Noyes Publications, Westwood, N.J, 1998).

[62] J. Musil et al., “Reactive magnetron sputtering of thin films: present status and trends”, Thin Solid Films **475**, 208–218 (2005).

[63] J. Sellers, “Asymmetric bipolar pulsed DC: the enabling technology for reactive PVD”, Surface and Coatings Technology **98**, 1245–1250 (1998).

[64] V. Kouznetsov et al., “A novel pulsed magnetron sputter technique utilizing very high target power densities”, Surface and Coatings Technology **122**, 290–293 (1999).

[65] D. M. Mattox, *The foundations of vacuum coating technology*, 2nd (William Andrew Applied Science Publishers, Oxford [England] ; Cambridge, MA, 2018).

[66] P. M. Martin, *Handbook of deposition technologies for films and coatings: science, applications and technology*, 3rd ed (Elsevier, Amsterdam, 2010).

[67] H. M. Mott-Smith and I. Langmuir, “The Theory of Collectors in Gaseous Discharges”, Physical Review **28**, 727–763 (1926).

[68] J. E. Allen, “Probe theory - the orbital motion approach”, Physica Scripta **45**, 497–503 (1992).

[69] J. Benedikt, H. Kersten, and A. Piel, “Foundations of measurement of electrons, ions and species fluxes toward surfaces in low-temperature plasmas”, Plasma Sources Science and Technology **30**, 033001 (2021).

[70] C. Böhm and J. Perrin, “Retarding-field analyzer for measurements of ion energy distributions and secondary electron emission coefficients in low-pressure radio frequency discharges”, Review of Scientific Instruments **64**, 31–44 (1993).

[71] S. G. Ingram and N. S. J. Braithwaite, “Ion and electron energy analysis at a surface in an RF discharge”, Journal of Physics D: Applied Physics **21**, 1496–1503 (1988).

[72] D. Rafalskyi, S. Dudin, and A. Aanesland, “Magnetized retarding field energy analyzer measuring the particle flux and ion energy distribution of both positive and negative ions”, Review of Scientific Instruments **86**, 053302 (2015).

[73] J. S. Halekas et al., “Electron heat flux in the near-Sun environment”, Astronomy & Astrophysics **650**, A15 (2021).

[74] J. Ballestrín, G. Burgess, and J. Cumpston, “Heat flux and temperature measurement technologies for concentrating solar power (CSP)”, in *Concentrating Solar Power Technology* (Elsevier, 2012), 577–e4.

[75] C. Killer et al., “Characterization of the W7-X scrape-off layer using reciprocating probes”, Nuclear Fusion **59**, 086013 (2019).

[76]Z. Huang et al., "Upgrade of an integrated Langmuir probe system on the closed divertor target plates in the HL-2A tokamak", Plasma Science and Technology **24**, 054002 (2022).

[77]A. Omelcenko et al., "Thin-film calorimetry: In-situ characterization of materials for lithium-ion batteries", International Journal of Materials Research **108**, 904–919 (2017).

[78]H. Wulfmeier et al., "Thin-Film Calorimetry: Analytical Tool for In-Situ Characterization of Lithium Ion Batteries", Journal of The Electrochemical Society **162**, A727–A736 (2015).

[79]R. Gardon, "An Instrument for the Direct Measurement of Intense Thermal Radiation", Review of Scientific Instruments **24**, 366–370 (1953).

[80]K. Ellmer and R. Mientus, "Calorimetric measurements with a heat flux transducer of the total power influx onto a substrate during magnetron sputtering", Surface and Coatings Technology **116-119**, 1102–1106 (1999).

[81]H Kersten et al., "Investigations on the energy influx at plasma processes by means of a simple thermal probe", Thin Solid Films **377-378**, 585–591 (2000).

[82]M. Stahl, T. Trottenberg, and H. Kersten, "A calorimetric probe for plasma diagnostics", Review of Scientific Instruments **81**, 023504 (2010).

[83]S. Bornholdt and H. Kersten, "Transient calorimetric diagnostics for plasma processing", The European Physical Journal D **67**, 176 (2013).

[84]F. Haase, H. Kersten, and D. Lundin, "Plasma characterization in reactive sputtering processes of Ti in Ar/O2 mixtures operated in metal, transition and poisoned modes: a comparison between direct current and high-power impulse magnetron discharges", The European Physical Journal D **71**, 245 (2017).

[85]T. Kewitz, M. Fröhlich, and H. Kersten, "Analysis of passive calorimetric probe measurements at high energy influxes", EPJ Techniques and Instrumentation **4**, 1 (2017).

[86]L. Hansen et al., "Understanding the energy balance of a surface barrier discharge for various molecular gases by a multi-diagnostic approach", Journal of Applied Physics **129**, 053308 (2021).

[87]S. Gauter et al., "Calorimetric investigations in a gas aggregation source", Journal of Applied Physics **124**, 073301 (2018).

[88]F. Haase et al., "Dynamic determination of secondary electron emission using a calorimetric probe in a plasma immersion ion implantation experiment", Plasma Sources Science and Technology **27**, 044003 (2018).

[89] L. Hansen et al., "Conventional and non-conventional diagnostics of a stable atmospheric pressure DC normal glow microplasma discharge intended for in situ TEM studies", Plasma Sources Science and Technology **31**, 035013 (2022).

[90] L. Hansen et al., "Correlations between energy flux and thin film modifications in an atmospheric pressure direct current microplasma", Thin Solid Films **765**, 139633 (2023).

[91] S. Bornholdt, "Particle and energy fluxes during plasma based deposition of nanostructured materials", PhD thesis (Christian-Albrechts-Universität zu Kiel, 2013).

[92] F. Haase, "A calorimetric study of plasma based thin film deposition applications", PhD thesis (Christian-Albrechts-Universität zu Kiel, 2018).

[93] S. Gauter, "Calorimetric investigation on plasma and ion beam sources used for thin film deposition", PhD thesis (Christian-Albrechts-Universität zu Kiel, 2018).

[94] R. F. Egerton, *Physical Principles of Electron Microscopy: An Introduction to TEM, SEM, and AEM*, 2nd ed. 2016 (Springer International Publishing : Imprint: Springer, Cham, 2016).

[95] D. B. Williams and C. B. Carter, *Transmission electron microscopy: a textbook for materials science*, 2nd ed, Cambridge library collection (Springer, New York, 2008).

[96] I. M. Watt, *The principles and practice of electron microscopy*, 2nd ed (Cambridge University Press, Cambridge ; New York, 1997).

[97] H. Stanjek and W. Häusler, "Basics of X-ray Diffraction", Hyperfine Interactions **154**, 107–119 (2004).

[98] P. J. Eaton and P. West, *Atomic force microscopy*, OCLC: ocn455831540 (Oxford University Press, Oxford ; New York, 2010).

[99] J. Gupta et al., "Focused ion beam imaging of grain growth in copper thin films", Applied Physics Letters **61**, 663–665 (1992).

[100] C. A. Volkert and A. M. Minor, "Focused Ion Beam Microscopy and Micromachining", MRS Bulletin **32**, 389–399 (2007).

[101] F. Zahari et al., "Correlation between sputter deposition parameters and *I-V* characteristics in double-barrier memristive devices", Journal of Vacuum Science & Technology B **37**, 061203 (2019).

[102] R. Marquardt et al., "Correlation between properties of direct current magnetron sputtered thin niobium nitride films and plasma parameters", Thin Solid Films **742**, 139046 (2022).

[103] F. Schlichting et al., "Energy-dependent film growth of Cu and NiTi from a tilted DC magnetron sputtering source determined by calorimetric probe analysis", Surface and Coatings Technology **450**, 129000 (2022).

[104]E. A. Edelberg et al., “Energy distribution of ions bombarding biased electrodes in high density plasma reactors”, Journal of Vacuum Science & Technology A: Vacuum, Surfaces, and Films **17**, 506–516 (1999).

[105]T. Baloniak et al., “Calibration of a miniaturized retarding field analyzer for low-temperature plasmas: geometrical transparency and collisional effects”, Journal of Physics D: Applied Physics **43**, 055203 (2010).

[106]K. Landheer et al., “Note: Laser-cut molybdenum grids for a retarding field energy analyzer”, Review of Scientific Instruments **88**, 066108 (2017).

[107]M. Cavenago, L. Bellan, and M. Comunian, “Analysis of grid size and ion temperature effects in retarding field energy analyzers (RFEA)”, AIP Advances **8**, 125221 (2018).

[108]T. H. M. Van De Ven et al., “Analysis of retarding field energy analyzer transmission by simulation of ion trajectories”, Review of Scientific Instruments **89**, 043501 (2018).

[109]A. W. Molvik, “Large acceptance angle retarding-potential analyzers”, Review of Scientific Instruments **52**, 704–711 (1981).

[110]J Schulze et al., “Charge dynamics in capacitively coupled radio frequency discharges”, Journal of Physics D: Applied Physics **43**, 225201 (2010).

[111]E. A. Edelberg et al., “Compact floating ion energy analyzer for measuring energy distributions of ions bombarding radio-frequency biased electrode surfaces”, Review of Scientific Instruments **70**, 2689–2698 (1999).

[112]D Gahan, B Dolinaj, and M. B. Hopkins, “Comparison of plasma parameters determined with a Langmuir probe and with a retarding field energy analyzer”, Plasma Sources Science and Technology **17**, 035026 (2008).

[113]S. Gauter, F. Haase, and H. Kersten, “Experimentally unraveling the energy flux originating from a DC magnetron sputtering source”, Thin Solid Films **669**, 8–18 (2019).

Acknowledgments

In the completion of this work, I equally relied on the help and support of colleagues, friends and family.

First, I would like to thank Holger Kersten for the opportunity to work in his group and finish my PhD. Starting as a master's student, I always felt in good hands and Holger left no stone unturned for me to be able to continue my work. His expertise and knowledge always helped and guided me and his friendliness and joy left no day without laughter.

The same goes for the entire workgroup AG Plasmatechnologie. From colleagues to friends, the last years brought about support in the daily questions and hardships of the work in experimental physics and also much-needed companionship and cheerfulness in the well-remembered activities outside of work. Here, I want to especially thank Thomas Trottenberg, Luka Hansen and Mathis Klette for the countless answered questions and overcoming hurdles.

Also, I'd like to thank Michael Poser for his support in all things electronics and the soldering of circuit boards and Volker Rohwer for his help with the technical applications of the experimental chambers. Furthermore, without Michael Brix, Frank Brach and the entire workshop at the IEAP the combined diagnostic would not be as is. The drilling of the fine grids and the exact fabrication of the grid holders was a remarkable service.

For my time at the faculty of engineering, I would like to thank Finn Zahari, Richard Marquardt, Julia Cipo, Lars Thormählen and Dirk Meyners. I will always remember and cherish the collaborations and the insight and knowledge I gained from them.

The measurements at Empa in Switzerland were made possible by Kerstin Thorwarth and Sebastian Siol. Thank you for the opportunity and support during my short stay in Zurich.

Last, but definitely not least, I thank my wife, Kerrin Schlichting, for her continuous help and support during the long work hours, especially in the last few months. You kept our family going and had my back, always and unconditionally. I love you very much!

Eidesstattliche Erklärung

Hiermit versichere ich an Eides statt, dass ich die vorliegende Arbeit selbsständig und ohne fremde Hilfe angefertigt habe, abgesehen von der Beratung durch den Betreuer. Ausschnitte, welche wörtlich oder sinngemäß auf Arbeiten anderer Autoren beruhen, sind als solche klar gekennzeichnet. Ich versichere außerdem, dass ich keine andere als die angegebene Literatur verwendet habe. Diese Versicherung schließt alle in dieser Arbeit enthaltenen Grafiken, Skizzen, bildlichen Darstellungen und dergleichen ein. Die Arbeit als Ganzes wurde bisher keiner anderen Prüfungsbehörde vorgelegt. Teile dieser Arbeit wurden bereits in begutachteten wisschenschaftlichen Fachzeitschriften veröffentlicht und sind als solche gekennzeichnet. Die in den Veröffentlichungen angeführten Quellenverweise sind in den Veröffentlichungen selbst und nicht zusätzlich im Literaturverzeichnis dieser Arbeit aufgeführt. Abschließend erkläre ich, dass diese Arbeit unter Einhaltung der Regeln guter wissenschaftlicher Praxis der Deutschen Forschungsgemeinschaft entstanden ist und mir niemals ein akademischer Grad entzogen worden ist.

Ort, Datum

Unterschrift